Monte Carlo-based investigation of absorbed dose energy dependence of various detectors used in radiotherapy

By

Subhalaxmi Mishra

HLTH 09 2012 04 004

Tata Memorial Centre, Mumbai

A thesis submitted to the

Board of Studies in Health Sciences

In partial fulfillment of requirements

for the Degree of

DOCTOR OF PHILOSOPHY

of

HOMI BHABHA NATIONAL INSTITUTE

August, 2018

Homi Bhabha National Institute[1]

Recommendations of the Viva Voce Committee

As members of the Viva Voce Committee, we certify that we have read the dissertation prepared by Subhalaxmi Mishra entitled "Monte Carlo-based investigation of absorbed dose energy dependence of various detectors used in radiotherapy" and recommend that it may be accepted as fulfilling the thesis requirement for the award of Degree of Doctor of Philosophy.

Chairman - Dr. J. P. Agarwal	10/5/19	**Date:**
Guide / Convener - Dr. T. Palani Selvam	T. Palani	**Date:** 10/05/2019
Examiner - Dr. Paul Ravindran	B. Ravi	**Date:** 10/5/2019
Member 1- Dr. S. D. Sharma		**Date:** 10/5/2019
Member 2- Dr. D. D. Deshpande		**Date:** 10/5/2019

Final approval and acceptance of this thesis is contingent upon the candidate's submission of the final copies of the thesis to HBNI.

I/We hereby certify that I/we have read this thesis prepared under my/our direction and recommend that it may be accepted as fulfilling the thesis requirement.

Date: 10/05/2019

Place: Mumbai, India

T. Palani

Dr. T. Palani Selvam

Guide

[1] This page is to be included only for final submission after successful completion of viva voce.

STATEMENT BY AUTHOR

This dissertation has been submitted in partial fulfillment of requirements for an advanced degree at Homi Bhabha National Institute (HBNI) and is deposited in the Library to be made available to borrowers under rules of the HBNI.

Brief quotations from this dissertation are allowable without special permission, provided that accurate acknowledgement of source is made. Requests for permission for extended quotation from or reproduction of this manuscript in whole or in part may be granted by the Competent Authority of HBNI when in his or her judgment the proposed use of the material is in the interests of scholarship. In all other instances, however, permission must be obtained from the author.

(Subhalaxmi Mishra)

DECLARATION

I, hereby declare that the investigation presented in the thesis has been carried out by me. The work is original and has not been submitted earlier as a whole or in part for a degree / diploma at this or any other Institution / University.

(Subhalaxmi Mishra)

Annexure 1

CERTIFICATION ON ACADEMIC INTEGRITY

1. I Smt. Subhalaxmi Mishra, HBNI Enrolment No. **HLTH09201204004** hereby undertake that, the Thesis titled "***Monte Carlo-based investigation of absorbed dose energy dependence of various detectors used in radiotherapy***" is prepared by me and is the original work undertaken by me and free of any plagiarism. That the document has been duly checked through a plagiarism detection tool and the document is plagiarism free.

2. I am aware and undertake that if plagiarism is detected in my thesis at any stage in future, suitable penalty will be imposed as per the applicable guidelines of the Institute/UGC.

Mishra 10/5/2019

(Smt. Subhalaxmi Mishra)

Signature of the Student

(with date)

T. Palani

Endorsed by the PhD Supervisor

(I certify that the work done by the Researcher is plagiarism free)

Signature: T. Palani

Name: Dr. T. Palani Selvam

Designation: Assoc. Prof. HBNI;
Head, CRP&QAS

Department/Centre: RPAD, BARC

Name of the CI/OCC: TMC

List of Publications arising from the thesis

Journal

1. "Monte Carlo-based beam quality and phantom scatter corrections for lithium formate dosimeter for high energy brachytherapy dosimetry", **Subhalaxmi Mishra,** T. Palani Selvam, *J. Med. Phys*, **2017**, 42(2), 72-79.
2. "Phantom scatter correction of radiochromic films in high-energy brachytherapy dosimetry: a Monte Carlo study", **Subhalaxmi Mishra,** T. Palani Selvam, *Radiol. Phys Tecnol.* **2015**, 8(2), 215-223.
3. "Monte Carlo-based beam quality and phantom scatter corrections for solid-state detectors in ^{60}Co and ^{192}Ir brachytherapy dosimetry", **Subhalaxmi Mishra,** T. Palani Selvam, J. *Appl Clin. Med. Phys*, **2014**, 15(6), 295-305.
4. "Monte Carlo-based investigation of absorbed-dose energy dependence of radiochromic films in high energy brachytherapy dosimetry", **Subhalaxmi Mishra,** T. Palani Selvam, *J. Appl Clin. Med. Phys*, **2014**, 15(1), 351-362.
5. "Monte Carlo calculation of beam quality correction for solid-state detectors and phantom scatter correction at ^{137}Cs energy", Palani Selvam T, **Subhalaxmi Mishra**, Vishwakarma RS, *J. Appl. Clin. Med. Phys*, **2014**, 15(1), 339-350.
6. "Monte Carlo-based investigation of water-equivalence of solid phantoms at ^{137}Cs energy", Ramkrishna S. Vishwakarma, T. Palani Selvam, Sahoo Sridhar, **Subhalaxmi Mishra** and G. Chourasiya, *J. Med. Phys*, **2013**, 38(4), 158-164.

Manuscripts Communicated

1. "In-phantom depth-dependent photon energy response and phantom scatter corrections for low energy brachytherapy sources", **Subhalaxmi Mishra** and T. Palani Selvam, *Biomed. Phys. Eng. Express* (submitted).

Conferences proceedings:

1. "Monte Carlo study of response of solid state detectors for radiotherapy electron beams", **Subhalaxmi Mishra** and T. Palani Selvam. Proceedings of 39th Annual conference of the Association of Medical Physicists of India (AMPICON 2018), November 2-4, (2018). Oral Presentation
2. "Monte Carlo study of water-equivalence of various solid phantom materials for ^{131}Cs, ^{125}I and ^{103}Pd low energy brachytherapy sources", **Subhalaxmi Mishra** and T. Palani Selvam, Proceedings of 38th Annual conference of the Association of Medical Physicists of India (AMPICON **2017**), November 4-7, (2017). Oral Presentation
3. "Influence of phantom materials on ^{192}Ir brachytherapy dosimetry using air as a detector material: a Monte Carlo study", **Subhalaxmi Mishra** and T. Palani Selvam, Proceedings of 36th Annual conference of the Association of Medical Physicists of India (AMPICON 2015), November 20-22, (**2015**). Poster Presentation
4. "Absorbed dose energy dependence of radiochromic films in high energy brachytherapy dosimetry – an EGSnrc study", **Subhalaxmi Mishra** and T. Palani Selvam, Proceedings of 34th Annual conference of the Association of Medical Physicists of India (AMPICON 2013), November 13-16, (**2013**). Oral Presentation

5. “Monte Carlo-based energy response study of indigenously developed LiMgPO4: Tb phosphor”, **Subhalaxmi Mishra**, T. Palani Selvam, Bhushan Dhabekar, A. K. Singh and M. Chaougaonkar, Proceedings of 32nd Annual conference of the Association of Medical Physicists of India (AMPICON 2011), November 16-19, (**2011**). Oral Presentation

(Subhalaxmi Mishra)

DEDICATED TO

My husband Shri Bibekananda Mishra

&

My daughters Miss Ritisha Mishra

and Miss Rinisha Mishra

ACKNOWLEDGEMENT

First and foremost, I would like to express my special appreciation and thanks to my guide Dr. T. Palani Selvam, Associate Prof. Homi Bhabha National Institute (HBNI), and Head, CRP&QAS, Radiological Physics & Advisory Division (RP&AD), Bhabha Atomic Research Centre (BARC), who has been a great mentor for me and for encouraging my research work. I owe my deep sense of gratitude for his constant support and advices during my work.

I express my gratitude to Dr. D. Datta, Head, RP&AD, BARC, Dr. Pradeepkumar K. S., Associate Director, HS&EG, BARC, Dr. K. B. Sainis former Director Bioscience Group, BARC, Dr. Y. S. Mayya former Head, RP&AD, BARC, Mumbai, India, for their encouragement, supports and for allowing me to pursue my PhD project.

I would also like to thank my doctoral committee members, Dr. J. P. Agarwal, Dr. S. D. Sharma, Dr. D. D. Deshpande and Dr. S. K. Shrivastava for their brilliant comments and suggestions during the progress of the work.

I would like to thank my colleagues Smt. Vandana Shrivastava, Shri Sridhar Sahoo, Shri R. S. Vishwakarma and Shri. Arghya Chattraj, RP&AD, BARC for their support and help.

Words cannot express how grateful I am to my family and parents, for all the sacrifices that they have made and their prayer for me, which sustained me so far. I would like to thank everybody who was important in the successful realization of this thesis, as well as apologize that I could not mention everyone personally. Last but not the least I thank the supreme soul almighty for giving me strength to complete my thesis in time.

(Subhalaxmi Mishra)

CONTENTS

ABSTRACT

A radiation detector is a device that measures directly or indirectly the quantity absorbed dose. In general, detectors are calibrated in ^{60}Co beam and used for measurements in radiotherapy applications. Therefore, the energy response correction factor needs to be applied if the detector is used in a different beam quality. In this thesis, in-phantom depth-dependent absorbed-dose energy dependence of a given detector at a given beam quality is addressed by beam quality correction and were calculated as function of distance along the transverse axis of the brachytherapy sources in the water phantom using Monte Carlo-based EGSnrc code system. The present study also calculates the energy response correction factors of different detectors such as diamond, LiF, $Li_2B_4O_7$, Al_2O_3, Plastic Scintillator and Lithium Formate for the radiotherapy electron beams as a function of depth in water. In addition the most appropriate Δ parameter was investigated for thin micro diamond detector and electron fluence perturbation correction factors were studied for other solid-state detectors for the radiotherapy electron beams.

For clinical dosimetry applications, the medium of interest for measuring absorbed dose with any dosimeter is water. While water provides excellent reproducibility and comparability of measurements worldwide, the precise and reproducible placement of radiation detectors in water is a challenge and may be the cause of measurement errors. Hence, liquid water is often replaced by solid phantoms for measurement purposes. However, the solid phantoms are not truly water-equivalent in case of brachytherapy and their influence on the dosimetry should be taken into account. In this thesis, for a given detector, the influences of solid water phantoms were addressed by phantom scatter correction. This study also includes calculation of the mean energies of photons in solid phantoms and water phantom for different brachytherapy sources.

SYNOPSIS

Radiotherapy is the use of radioactive isotopes, X-rays and particles (electrons, protons etc.) for treatment of cancer. The success of radiotherapy depends on the accuracy of the prescribed dose delivery. Various detectors are used to determine absorbed dose. Energy dependence of radiation detectors is an important property for determination of absorbed dose. The overall energy dependence of a detector is composed of two parts. One is the intrinsic energy dependence and the other is absorbed dose energy dependence. The intrinsic energy dependence relates the reading of the detector to the dose to the sensitive volume of the detector. Absorbed-dose energy dependence of a given detector at a given beam quality is addressed by beam quality correction which is based on absorbed dose to the medium at the point of measurement and absorbed dose to the sensitive material of the detector obtained for the beam quality under consideration and reference radiation. The reference beam quality is generally telecobalt radiotherapy beam. It may be noted that intrinsic energy dependence can be determined through measurements whereas absorbed dose energy dependence of the detectors can only be calculated. Radiation transport using Monte Carlo methods serves as a powerful tool to calculate beam quality correction.

In radiotherapy, water is recommended as the reference medium for dosimetry and provides excellent reproducibility and comparability of measurements. But, the precise and reproducible placement of detectors in water is a challenge and may cause measurement errors. Hence, water is often replaced by solid phantoms which have several advantages such as it can be machined, to accommodate the source and detector in a precise geometry facilitating an accurate measurement and reproducibility, water proofing etc. However, in the case of brachytherapy, the solid phantoms are not truly water-equivalent and their influence on the dosimetry should be taken into account when solid phantoms are used for

measurement purposes. Monte Carlo is a perfect tool to address the influence of solid water phantom on dosimetry. This study also includes the calculation of mean energies of photons in solid phantoms and water phantom for different brachytherapy sources.

For radiotherapy photon beams such as ^{60}Co, 6 MV – 18 MV Compton scattering is the predominant interaction in water and the detector materials. Hence, the response of the detector can be understood by using electron density information of the detector materials. However, in case of electron beams, electron density information of the detector materials is not sufficient to understand the response of the detector as the electrons will undergo multiple scattering in the detector materials. Hence, for electron beams, investigation of cavity theory is important to understand the response of the detector. Such investigations can be done using Monte Carlo methods.

The objective of the present study undertaken for the thesis was:

- To determine in-phantom distance-dependent beam quality correction for a given detector for various brachytherapy sources by using Monte Carlo methods. The detectors investigated in this study are diamond, phosphors (LiF, $Li_2B_4O_7$, Al_2O_3), Plastic Scintillator, Lithium Formate and different radiochromic Films such as EBT, EBT2, RTQA, XRT, HS and XRQA. The brachytherapy sources included in the investigation are:
    - High energy brachytherapy sources (^{60}Co, ^{137}Cs, ^{192}Ir and ^{169}Yb)
    - Low energy brachytherapy sources (^{131}Cs, ^{125}I and ^{103}Pd)

  However, for ^{169}Yb and ^{125}I sources the absorbed dose energy response correction factors were reported by Selvam and Biju (2010) for LiF, $Li_2B_4O_7$, Al_2O_3, Diamond, Silicon diode and air detectors. Hence, the present study doses not include the LiF, $Li_2B_4O_7$, Al_2O_3, and Diamond detectors for calculation of beam quality correction for ^{169}Yb and ^{125}I sources.

- To calculate detector-specific, solid phantom-to-water phantom conversion factor i.e phantom scatter corrections, $k_{phan}(r)$ for various solid phantoms as a function distance along transverse axis of the sources (r) in the phantom material for the above brachytherapy sources by using Monte Carlo methods. The solid phantoms investigated are PMMA (polymethyl methacrylate), polystyrene, solid water, virtual water, plastic water, plastic water (LR), RW1, RW3, A150 and WE210.
- To determine the response of different detectors as a function of depth in a water phantom for radiotherapy electron beams (6 MeV, 9 MeV, 12 MeV, 15 MeV and 18 MeV). In addition, Spencer-Attix cavity theory characterized by a parameter Δ, which is the kinetic energy of an electron that is sufficient to cross the cavity, was investigated for thin micro diamond detector and electron fluence perturbation correction factors were studied for other solid-state detectors (LiF, $Li_2B_4O_7$, Al_2O_3, Plastic Scintillator and Lithium Formate) for radiotherapy electron beams.

The calculations are based on Monte Carlo-based EGSnrc code system. This thesis comprises of seven Chapters organized as follows:

Chapter 1: Introduction

This Chapter introduces the overview of different radiotherapy treatments, rationale of radiotherapy treatments and the need for accuracy in treatment dose delivery. Various detectors used to quantify absorbed dose in radiotherapy are summarized. This Chapter also provides a brief introduction to the basic physics of interaction of radiation with matter and the occurrence of quantitative probabilities of each of these mechanisms as a function of energy. Generally, photons and electrons are considered as the main choice for the treatment

in radiotherapy. The major photon interaction processes with matter are: Photoelectric absorption, Compton scattering, Pair production and Rayleigh scattering. When the photon travels through the matter, they can undergo one or a combination of the above processes depending on their energy and atomic number of the medium. When electrons pass through a medium they interact through Coulomb forces with atomic nuclei and orbital electrons. Coulomb interactions between the incident electron and orbital electrons of an absorber result in ionizations and excitations of absorber atoms. These collisional energy losses are characterized by collision stopping powers. Coulomb interactions between the incident electron and nuclei of the absorber atom result in electron scattering and energy loss of the electron through bremsstrahlung production. These types of energy losses are characterized by radiative stopping powers. The type of interaction depends on the energy of the incident electron, impact parameter and the atomic radius. This Chapter is useful for better understanding of interactions of radiation with matter and also for later discussion of the results. This Chapter ends with literature survey and aim of the thesis.

Chapter 2: Monte Carlo Methods for radiation transport

In this Chapter, an overview of fundamental principles of the Monte Carlo technique and its application to radiotherapy is briefly discussed. A short description about the transport of electron and photon using Monte Carlo method was discussed. Various Monte Carlo codes available are also outlined. Overview of the code used in this study i.e EGSnrc code system and its user-codes FLURZnrc, DOSRZnrc and SPRRZnrc are described. This Chapter ends with the variance reduction techniques of particular importance in the simulations of this study.

Chapter 3: Calculation of mean energies of brachytherapy sources in various phantoms

In this Chapter, fluence-weighted mean energies, $\bar{E}_{fl}$, and detector-kerma weighted mean energies, $\bar{E}_k$ were calculated for high energy (^{192}Ir, ^{60}Co, ^{137}Cs and ^{169}Yb) and low energy (^{131}Cs, ^{125}I and ^{103}Pd) brachytherapy sources in the different solid phantoms and water phantom by using the following equations:

$$\bar{E}_{fl} = \frac{\sum_i E_i \Phi(E_i) dE}{\sum_i \Phi(E_i) dE}$$

$$\bar{E}_k = \frac{\sum_i E_i^2 \Phi(E_i) \left(\frac{\mu_{en}}{\rho}(E_i)\right)_{\text{det}} dE}{\sum_i E_i \Phi(E_i) \left(\frac{\mu_{en}}{\rho}(E_i)\right)_{\text{det}} dE}$$

Where E_i is the kinetic energy of ith photon in keV, $\Phi(E_i)$ is the differential photon fluence spectrum at E_i about dE. $\left(\frac{\mu_{en}}{\rho}(E_i)\right)$ is the mass energy absorption coefficient of the detector at E_i. Monte Carlo-based FLURZnrc user-code of EGSnrc code system was used for the above calculation. This Chapter is helpful to understand and discuss the results of following two Chapters (4 and 5).

Chapter 4: Beam quality corrections for brachytherapy sources

Beam quality correction for a brachytherapy source of beam quality Q can be defined as follows:

$$k_{QQ_0}(r) = \frac{f(Q)}{f(Q_0)} = \frac{\left[\frac{D_{wat}}{D_{det}}\right]_Q}{\left[\frac{D_{wat}}{D_{det}}\right]_{Q_0}}$$

where the numerator presents water-to-detector dose ratio at Q, and the denominator represents the same dose ratio at ^{60}Co beam energy. Numerator of $k_{QQ_0}(r)$ corrects for the difference in the energy absorption properties of water and detector at brachytherapy beam

quality Q at r, and the denominator of $k_{QQ_0}(r)$ corrects for the same, but at reference beam quality Q_0. The present study calculates the beam quality correction, $k_{QQ_0}(r)$ for brachytherapy sources using Monte Carlo-based EGSnrc code system. The results of the present study indicate that, effective atomic number (Z_{eff}) of detectors and mean energy in the phantoms play a major role on the $k_{QQ_0}(r)$ values. For detectors with Z_{eff} close to that of water, $k_{QQ_0}(r)$ values were close to unity. For detectors with lesser Z_{eff} than that of water, values are much larger than unity and for detectors with higher Z_{eff} than that of water, values are smaller than unity.

In this Chapter, investigation of $k_{QQ_0}(r)$ is presented separately for high energy and low energy brachytherapy sources separately.

High energy brachytherapy sources

High energy brachytherapy sources such as ^{192}Ir, ^{60}Co, ^{137}Cs and ^{169}Yb, allow a higher dose to tissues at larger distances from the sources. These sources are commonly used for an effective treatment of cervical, breast, uterine cervix, head & neck and skin cancers. $k_{QQ_0}(r)$ is about unity and is distance-independent for diamond, Plastic Scintillator, LiF, Lithium Formate, $Li_2B_4O_7$, EBT, EBT2 (lot 020609 and lot 031109), RTQA and HS detectors for ^{60}Co and ^{137}Cs sources. For ^{192}Ir source, the values of $k_{QQ_0}(r)$ are unity (within 1%) and are distance-independent for the detectors Lithium Formate, $Li_2B_4O_7$, EBT and EBT2 (lot 031109). All the investigated detectors showed distance-dependent $k_{QQ_0}(r)$ values for ^{169}Yb source.

Low energy brachytherapy sources

Low energy photon emitting brachytherapy sources are being used with increasing frequency for interstitial implants in tumors, especially prostate and breast. For a given source, all the investigated detectors exhibit similar trend of $k_{QQ_0}(r)$ and is independent of distance. Lithium formate, $Li_2B_4O_7$, EBT, EBT2 detectors showed lesser energy response corrections than other investigated detectors. For EBT film, values are about 8 %, 7 % and 6 % larger than unity for ^{131}Cs, ^{125}I and ^{103}Pd sources, respectively. It is observed that values of EBT and EBT2 (lot 031109) are identical for all the above sources. This is because of the fact that these two films have very similar compositions except their structure. For EBT and EBT2 (lot 031109) films, values are about 6 %, 5 % and 3 % smaller than unity for ^{131}Cs, ^{125}I and ^{103}Pd sources, respectively. Except these above films, remaining investigated films such as RTQA, XRT, XRQA and HS showed higher energy response correction factors. For example, RTQA, XRT and XRQA films showed under response (i.e values are smaller than unity) of about 40 %, 93 % and 96 %, respectively. Whereas, HS film showed over response of about 70 % i.e values are larger than unity by 70 %.

Chapter 5: Phantom scatter corrections for brachytherapy sources

Phantom scatter correction, $k_{phan}(r)$ can be calculated at a brachytherapy beam quality *Q* for a given solid-state detector by using the following relation:

$$k_{phan}(r) = \left[D_{\det, Q}(r) / D_{\det,\ phan, Q}(r) \right]$$

where, $D_{\det,Q}(r)$ and $D_{\det,phan,Q}(r)$ are the absorbed dose to a given detector material in water and in the solid phantom at *r* a distance for brachytherapy source of beam quality *Q*, respectively. Note that, $k_{phan}(r) = 1$ implies the phantom material is water-equivalent.The

phantoms where the $k_{phan}(r)$ values deviate from unity within ±3 % at clinically relevant distances i.e up to 10 cm for high energy sources (^{192}Ir, ^{60}Co, ^{137}Cs, ^{169}Yb) and up to 5 cm for low energy sources (^{131}Cs, ^{125}I and ^{103}Pd) were also considered as water-equivalent phantoms. In the present study, in-phantom depth-dependent $k_{phan}(r)$ of various solid phantoms were calculated for brachytherapy sources using the Monte Carlo-based EGSnrc code system. In this Chapter, investigation of $k_{phan}(r)$ is presented separately for high energy and low energy brachytherapy sources.

High energy brachytherapy sources

For ^{60}Co and ^{137}Cs sources, phantoms such as solid water, virtual water, RW1, RW3 and WE210 are water-equivalent at all distances (1-15 cm) for all the solid-state detectors other than XRT and XRQA films. For ^{192}Ir source, phantoms such as solid water, virtual water, RW3 and WE210 are water-equivalent in the distance range of 1-15 cm for all the solid state detectors other than Al_2O_3, XRT and XRQA. For ^{169}Yb source, none of the investigated phantom is water-equivalent.

Low energy brachytherapy sources

Plastic water (LR) and A150 phantoms were water equivalent solid phantoms among the investigated phantom materials. However, solid phantom materials such as solid water, virtual water and WE210 are not water-equivalent phantoms for distances larger than 1 cm. It is interesting to note that, unlike for high energy sources (^{60}Co, ^{137}Cs, ^{192}Ir and ^{169}Yb), $k_{phan}(r)$ values did not change with detector type for low energy sources (^{131}Cs, ^{125}I and ^{103}Pd) at all distances.

Chapter 6: Response of solid state detectors in radiotherapy electron beams

In the present study, we have investigated the response of various detectors (diamond, LiF, Al_2O_3, $Li_2B_4O_7$, Plastic Scintillator and Lithium Formate) as a function of depth in the water phantom for radiotherapy electron beams (6 MeV, 9 MeV, 12 MeV, 15 MeV and 18 MeV). Absorbed dose to detector and absorbed dose to water were scored as a function of central axis depth in the water phantom. Using the dose results, ratio of dose-to-water and dose-to-detector was calculated. This dose ratio represents the response of the detector. It was observed that, for a given detector the response does not change significantly with depth. The maximum variation in the response as a function of depth is about 7 % for a given beam energy.

To obtain the suitable Δ, (the Spencer-Attix cavity characterized by this parameter Δ and is the kinetic energy of an electron that is sufficient to cross the cavity), that best characterizes the detector thickness, the electron energy that corresponds to the CSDA range and mean chord length of the detector were considered. But the penetration depth could be substantially less than the CSDA range due to extensive multiple scattering. Hence a variety of Δ were investigated. By comparing the results with the dose-ratio calculations as a function of depth, the most appropriate Δ parameter for each detector was determined. It is observed that, Δ values of about 200 - 300 keV are appropriate for all the investigated detectors.

Chapter 7: Summary, conclusion and future work

This Chapter summarizes the major findings of the thesis and outlines the scope for future work. In this thesis, detector-specific, depth dependent, beam quality correction, $k_{QQ_0}(r)$, and phantom scatter correction, $k_{phan}(r)$, were calculated for different detectors as a function of distance along the transverse axis of the brachytherapy sources using the Monte Carlo-based EGSnrc code system. Effective atomic number of detectors and mean energy in the phantoms play a major role on the $k_{QQ_0}(r)$ values. For a given detector, $k_{phan}(r)$ values depend on distance from the brachytherapy sources for the investigated phantom materials, but the degree of deviation from unity depends on the type of solid phantom and the brachytherapy source. In order to understand the results for brachytherapy sources, the variations in the primary and scattered component of collision-kerma, were studied. The total linear attenuation coefficient (μ) data and the macroscopic cross section data of individual photon interactions (Photoelectric absorption, Compton scattering, Pair production and Rayleigh scattering) in the energy range of 10 keV - 1.25 MeV were analysed for the investigated solid phantom materials using the state-of-the art XCOM.

The scope for future work includes: (1) Energy response studies can be extended for various detectors used in hardontherapy (proton, carbon ion beams etc) (2) Intrinsic energy dependence can also be studied for different detectors and brachytherapy sources. This study can be extended for other detectors and brachytherapy sources. General-purpose Monte Carlo codes that model radiation transport can be used to calculate the absorbed-dose energy dependence, but cannot be used to calculate the intrinsic energy dependence since the process of detection can not modeled. Intrinsic energy dependence can be determined through measurements.

List of Figures

Figure 4.1 **(a)** Monte Carlo-calculated $k_{QQ_0}(r)$ values for XRT and XRQA films are shown as a function of distance along the transverse axis of the ^{60}Co source **(b)** Values of mass-energy-absorption coefficients of film-to-water.

Figure 4.2 Beam quality correction, $k_{QQ_0}(r)$ for ^{137}Cs brachytherapy source **(a)** solid-state detectors (LiF, $Li_2B_4O_7$, diamond, Lithium Formate, Plastic Scintillator, Al_2O_3) **(b)** radiochromic films (EBT2 (lot 020609), XRT, XRQA).

Figure 4.3 Beam quality correction, $k_{QQ_0}(r)$ of radiochromic films (EBT2 (lot 020609), XRT, XRQA, RTQA and HS) presented for ^{192}Ir source.

Figure 4.4 Beam quality correction, $k_{QQ_0}(r)$ of radiochromic films (EBT2 (lot 020609), XRT, XRQA, RTQA and HS) presented for ^{169}Yb source.

Figure 4.5 Beam quality correction, $k_{QQ_0}(r)$, presented for the investigated detectors as a function of distance along the transverse axis of **(a)** ^{131}Cs source **(b)** ^{125}I source **(c)** ^{103}Pd source.

Figure 5.1 Phantom scatter correction, $k_{phan}(r)$, presented for Al_2O_3 detector in polystyrene and plastic water phantoms as a function of distance along the transverse axis of the ^{60}Co source.

Figure 5.2 Phantom scatter correction, $k_{phan}(r)$, presented as a function of distance along the transverse axis of the ^{60}Co brachytherapy source for different solid-state detectors LiF, $Li_2B_4O_7$, diamond, Lithium Formate, Plastic Scintillator and water **(a)** PMMA, **(b)** A150.

Figure 5.3 Phantom scatter correction, $k_{phan}(r)$, presented as a function of distance along the transverse axis of the ^{60}Co source for different radiochromic films **(a)** PMMA **(b)** A150.

Figure 5.4 Phantom scatter correction, $k_{phan}(r)$, presented as a function of distance along the transverse axis of the ^{137}Cs source for different solid-state detectors **(a)** Polystyrene, **(b)** Plastic water, **(c)** PMMA, **(d)** A150.

Figure 5.5 Phantom scatter correction, $k_{phan}(r)$, presented for the ^{137}Cs brachytherapy source for different radiochromic films **(a)** Polystyrene, **(b)** Plastic water**, (c)** PMMA, and **(d)** A150.

Figure 5.6 Phantom scatter correction, $k_{phan}(r)$, presented as a function of distance along the transverse axis of the ^{192}Ir source for Al_2O_3 detector **(a)** virtual water, solid water, RW3 and WE210 phantoms **(b)** in 40 cm dia x 40 cm height and 50 cm dia x 50 cm height A150 phantoms.

Figure 5.7 Phantom scatter correction, $k_{phan}(r)$, presented as a function of distance along the transverse axis of the ^{192}Ir brachytherapy source for solid-state detectors $Li_2B_4O_7$, LiF, diamond, Plastic Scintillator, Lithium Formate, Al_2O_3 and water in **(a)** PMMA **(b)** Polystyrene **(c)** RW1 **(d)**Plastic water **(e)** A150.

Figure 5.8 Phantom scatter correction, $k_{phan}(r)$, presented as a function of distance along the transverse axis of the ^{192}Ir brachytherapy source for different radiochromic films **(a)** Polystyrene**, (b)** Plastic water, **(c)** PMMA **(d)** A150.

Figure 5.9 Phantom scatter correction, $k_{phan}(r)$, presented as a function of distance along the transverse axis of the ^{169}Yb source for different solid-state detectors **(a)** solid water / virtual water / WE210 **(b)** PMMA **(c)** Polystyrene **(d)** RW1**(e)** RW3 **(f)** Plastic water **(g)** A150.

Figure 5.10 Phantom scatter correction, $k_{phan}(r)$, presented as a function of distance along the transverse axis of the ^{169}Yb brachytherapy source for different phantoms **(a)** EBT and EBT2 (lot 031109) **(b)** EBT2 (lot 020609) **(c)** RTQA **(d)** HS **(e)** XRT **(f)** XRQA.

Figure 5.11 Phantom scatter correction, $k_{phan}(r)$, presented for the investigated detectors as a function of distance along the transverse axis **(a)** ^{131}Cs **(b)** ^{125}I **(c)** ^{103}Pd brachytherapy sources.

Figure 5.12 Phantom scatter correction, $k_{phan}(r)$, presented for EBT2 film in the investigated phantoms as a function of distance along the transverse axis **(a)** ^{131}Cs **(b)** ^{125}I **(c)** ^{103}Pd brachytherapy sources.

Figure 5.13 Macroscopic cross section normalized to total macroscopic cross section as a function of photon energy **(a)** Photoelectric Absorption **(b)** Compton scattering. Data are based on XCOM.

List of Tables

presented. Also shown in this table are the values of ratio of mass-energy-absorption coefficients of detector to water calculated at the ^{60}Co energy (1.25 MeV) and the values of ratio of <*Z*/*A*> of films to water.

Table 4.2 Beam quality correction, $k_{QQ_0}(r)$, presented for diamond, Al_2O_3, $Li_2B_4O_7$, LiF, Lithium Formate and Plastic Scintillator detectors as a function of distance *r* along the transverse axis of ^{60}Co brachytherapy source.

Table 4.3 Beam quality correction, $k_{QQ_0}(r)$, presented for radiochromic films EBT, EBT2 (lot 020609 and lot 031109), RTQA and HS film.

Table 4.4 Monte Carlo-calculated values of beam quality correction $k_{QQ_0}(r)$ .The data are presented as a function of distance along the transverse axis of the ^{137}Cs RTR source.

Table 4.5 Monte Carlo-calculated values of beam quality correction $k_{QQ_0}(r)$ for EBT, EBT2 (lot 031109), RTQA and HS presented for the ^{137}Cs RTR source.

Table 4.6 Beam quality correction, $k_{QQ_0}(r)$, presented for diamond, Al_2O_3, $Li_2B_4O_7$, LiF, Lithium Formate and Plastic Scintillator detectors as a function of distance *r* along the transverse axis ^{192}Ir brachytherapy source.

Table 4.7 Beam quality correction, $k_{QQ_0}(r)$, presented for Lithium Formate and Plastic Scintillator detectors for ^{169}Yb brachytherapy source.

Table 4.8 Beam quality correction, $k_{QQ_0}(r)$, presented for the investigated detectors for the brachytherapy sources ^{131}Cs, ^{125}I and ^{103}Pd.

Table 4.9 Self-attenuation factors for ^{131}Cs and ^{103}Pd sources for LiF and Al_2O_3 detectors.

Table 6.3 Energy response correction, $f_{^{60}Co}^{E}$ and detector response, $\frac{\overline{D}_{med}(E)}{\overline{D}_{\det}(E)}$ of diamond, LiF, $Li_2B_4O_7$, Al_2O_3, Plastic Scintillator and Lithium Formate detectors calculated at different depths for 6 MeV electron beam.

Table 6.4 Energy response correction, $f_{^{60}Co}^{E}$ and detector response, $\frac{\overline{D}_{med}(E)}{\overline{D}_{\det}(E)}$ of diamond, LiF, $Li_2B_4O_7$, Al_2O_3, Plastic Scintillator and Lithium Formate detectors calculated at different depths for 9 MeV electron beam.

Table 6.5 Energy response correction, $f_{^{60}Co}^{E}$ and detector response, $\frac{\overline{D}_{med}(E)}{\overline{D}_{\det}(E)}$ of diamond, LiF, $Li_2B_4O_7$, Al_2O_3, Plastic Scintillator and Lithium Formate detectors calculated at different depths for 12 MeV electron beam.

Table 6.6 Energy response correction, $f_{^{60}Co}^{E}$ and detector response, $\frac{\overline{D}_{med}(E)}{\overline{D}_{\det}(E)}$ of diamond, LiF, $Li_2B_4O_7$, Al_2O_3, Plastic Scintillator and Lithium Formate detectors calculated at different depths for 15 MeV electron beam.

Table 6.7 Energy response correction, $f_{^{60}Co}^{E}$ and detector response, $\frac{\overline{D}_{med}(E)}{\overline{D}_{\det}(E)}$ of diamond, LiF, $Li_2B_4O_7$, Al_2O_3, Plastic Scintillator and Lithium Formate detectors calculated at different depths for 18 MeV electron beam.

Table 6.8 Diamond detector response, $\left(\frac{\overline{D}_{water}(E)}{\overline{D}_{diamond}(E)}\right)_{d_{max}}$ at a depth of d_{max} and Spencer-Attix stopping power ratios at different Δ values for radiotherapy electron beams.

Table 6.9 Electron fluence perturbation correction factors, $\gamma(p)$ calculated for LiF, $Li_2B_4O_7$, Al_2O_3, Plastic Scintillator and Lithium Formate detectors calculated at a depth of d_{max}, for Δ=300 keV for the investigated radiotherapy electron beams.

Glossary

3D-CRT Three-dimensional conformal radiotherapy

AEIT Approximate Efficiency Improving Techniques

CSDA Continuous Slowing Down Approximation

EPR Electron Paramagnetic resonance

EGSnrc Electron-Gamma Shower developed by National Research Council of Canada

$\overline{E}_{fl}$ Fluence-weighted mean energy

$\overline{E}_{k}$ Detector-kerma weighted mean energy

f(Q) Absorbed dose energy dependence

HDR High-dose rate

IGRT Image guided radiotherapy

IMRT Intensity modulated radiotherapy

$k_{bq}(Q)$ Intrinsic energy dependence

$k_{phan}(r)$ Phantom scatter correction

$k_{QQ_0}(r)$ Beam quality correction

LDR Low-dose rate

Linac Medical Linear accelerator

L_{Δ} Restricted mass collision stopping power

MDR Medium-dose rate

MOSFET Metal-Oxide Semiconductor Field Effect Transistor

NTCP Normal Tissue Complication Probability

OSL Optically stimulated luminescence

PDR	Pulsed-dose rate
PMMA	Polymethyl methacrylate
PRESTA	Parameter Reduced Electron-Step Transport Algorithm
RNG	Random Number Generator
S	Linear stopping power
S/ρ	Mass stopping power
SRS	Stereotactic radio surgery
SRT	Stereotactic radiotherapy
TCP	Tumor Control probability
TLD	Thermoluminescent dosimeter
VRT	Variance Reduction Techniques
Z	Atomic number
$\mathbf{Z_{eff}}$	Effective atomic number
<Z/A>	Electron density
μ	Linear attenuation coefficient
μ/ρ	Mass attenuation coefficient
$\gamma(p)$	Perturbation correction factor

CHAPTER 1

Introduction

1.1 Radiotherapy

Radiotherapy is one of the four approaches for the treatment of cancer. The other three approaches are surgery, chemotherapy and immuno therapy. Radiation therapy may be used alone or in combination with surgery, chemotherapy, and/or immuno therapy. Radiotherapy is the use of radiation to treat cancer. It has been estimated that the addition of radiotherapy to cancer treatment improves 5 year survival by 16 % (Barton et al 1995). In comparison, the 5 year survival contribution from chemotherapy drugs is estimated as 2 % (Morgan et al 2004) making radiotherapy second only to surgery in its effectiveness. The most common types of cancer that radiation therapy is used for are brain tumors, head and neck cancers, lung cancer, breast cancer, prostate cancer, skin cancer, rectal cancer, cervix cancer, uterine cancer, lymphomas, and sarcoma etc. Radiotherapy can be given by the following methods:

1.1.1 External beam radiotherapy (Teletherapy)

External beam radiotherapy is used for most cancer patients requiring radiotherapy. External beam therapy, also known as Teletherapy, is a method of delivering a beam or several beams of high-energy x-rays or electrons to the tumor of the patient. It directs the radiation to the tumor from outside the body i.e, radiation is delivered from an external source which is present outside the patient body. These high energy x-rays or electrons deposit dose to the tumor and destroy the cancer cells. In external beam radiotherapy, several energies of X-rays are being used (Johns and Cunningham 1983, Attix 1986, Gerig et al 1994, Khan 2010) for example, orthovoltage (superficial) X-rays are used for treating skin cancer and superficial structures. Whereas megavoltage X-rays are used to treat deep-seated tumors. High-energy electrons are also been used in radiation therapy (Jackson 1970, Karzmark 1987) for treating superficial tumors (less than 5 cm deep) such as skin and lip cancers,

chest wall irradiation for breast cancer, administering boost dose to nodes, and the treatment of head and neck cancers.

Cobalt units which produce stable, dichromatic beams of 1.17 and 1.33 MeV from radioactive isotope ^{60}Co are used in Radiotherapy. The Cobalt unit has largely been replaced by the medical linear accelerator (Linac), which generates megavoltage X-rays and electrons. But Cobalt treatment is still in use worldwide, since the machinery is relatively cheaper, reliable and simple to maintain compared to the Linac. The photographs of ^{60}Co and Linac units are shown in Fig. 1.1.

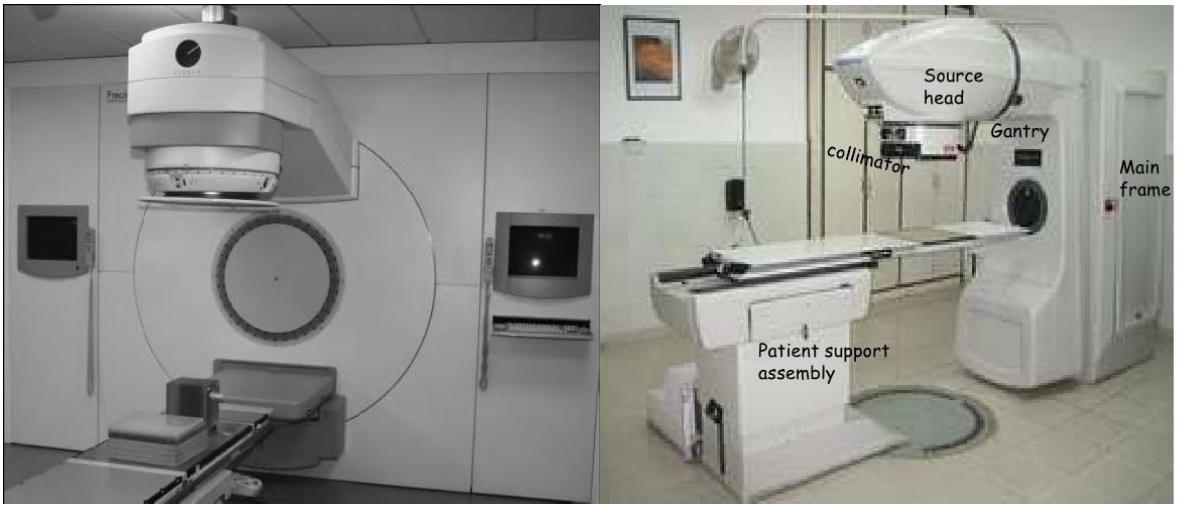

(a) (b)

Fig. 1.1 Photographs of a) medical linear accelerator b) Cobalt unit.

There are several techniques available for external beam therapy (Teh et al 1999, Webb 2003, Reco and Clifton 2008, Gupta and Anand 2012) such as conventional radiotherapy, three-dimensional conformal radiotherapy (3D-CRT), intensity modulated radiotherapy (IMRT), Image guided radiotherapy (IGRT), Stereotactic radiotherapy (SRT), Stereotactic radio surgery (SRS) etc. Recently, Protons and carbon ions are also being used (Jakel et al

2003). Although hadron therapy has shown many advantages over electron and photon beams (e.g. more precision of dose and high effectiveness of treatment), its use is still limited due to its complexity and the high cost of the devices required for the beam production.

1.1.2 Brachytherapy

Brachytherapy is the delivery of radiation dose using radioactive sources positioned in close proximity to the tumour for treatment of cancer. The word 'brachy' originates from the Greek word 'Brachios' meaning 'short'. Brachytherapy can be used alone or in combination with external beam radiotherapy (Pierquin et al 1987, Brenner 1997, Dale and Jones 1998, Joslin et al 2001). The main advantage of brachytherapy technique is that it delivers localized high dose to the tumor volume with steep dose gradients inside or outside the tumor region. The dose outside the volume falls off very rapidly, thereby giving less integral dose (Simon 1963, Williamson 1977, Perez et al 1986, Turesson 1990). Since the sources are fixed in the target, the problem of organ movement is also reduced. Hence, the dose delivered in brachytherapy is absorbed more locally and protects healthy tissues to a higher extent than external beam therapy. The energies used in brachytherapy applications depend upon the radioisotopes used and are in general much lower compared to the External beam radiotherapy (Dutreix and Wambersie 1975, Chen and Nath 2001) ^{137}Cs, ^{60}Co, ^{192}Ir and ^{169}Yb are good for intracavitary and interstitial applications. Radioisotopes such as ^{198}Au, ^{125}I and ^{103}Pd are used for permanent implants. For treatment of eye cancer beta sources such as ^{90}Sr and ^{106}Ru are also used. Electronic brachytherapy is a relatively new form of brachytherapy, in which instead of using radioisotopes, a kilovoltage X-ray tube is used for the treatment of skin and breast cancers.

In general, brachytherapy treatments are classified into four categories with respect to the dose rate of the source such as low-dose rate (LDR) brachytherapy, medium-dose rate (MDR) brachytherapy, high-dose rate (HDR) brachytherapy and pulsed-dose rate (PDR) brachytherapy. LDR brachytherapy involves implanting radiation sources that emit radiation at a rate less than 2 Gy/h. MDR brachytherapy is characterized by a medium rate of dose delivery, ranging between 2 Gy/h to 12 Gy/h. When the rate of dose rate exceeds 12 Gy/h it is known as HDR brachytherapy which is most commonly used. PDR brachytherapy involves short pulses of radiation, typically once in an hour, to simulate the overall rate and effectiveness of LDR treatment. The photographs of HDR and LDR units are shown in Fig. 1.2.

(a) (b)

Fig. 1.2 Photographs of a) HDR b) LDR brachytherapy units.

1.1.3 Rationale of radiotherapy and the need for accuracy

Radiotherapy relies on the delivery of therapeutic doses of radiation to the tumor volume and minimizing dose to the surrounding normal tissues. In order to maintain a high TCP

(Tumor Control Probability - curve A) we must deliver as much dose as possible to the target in order to kill all of the viable cancer cells. While doing this we also damage the surrounding normal tissues which must be minimized to give a low NTCP (Normal Tissue Complication Probability- curve B) as shown in the Fig. 1.3.

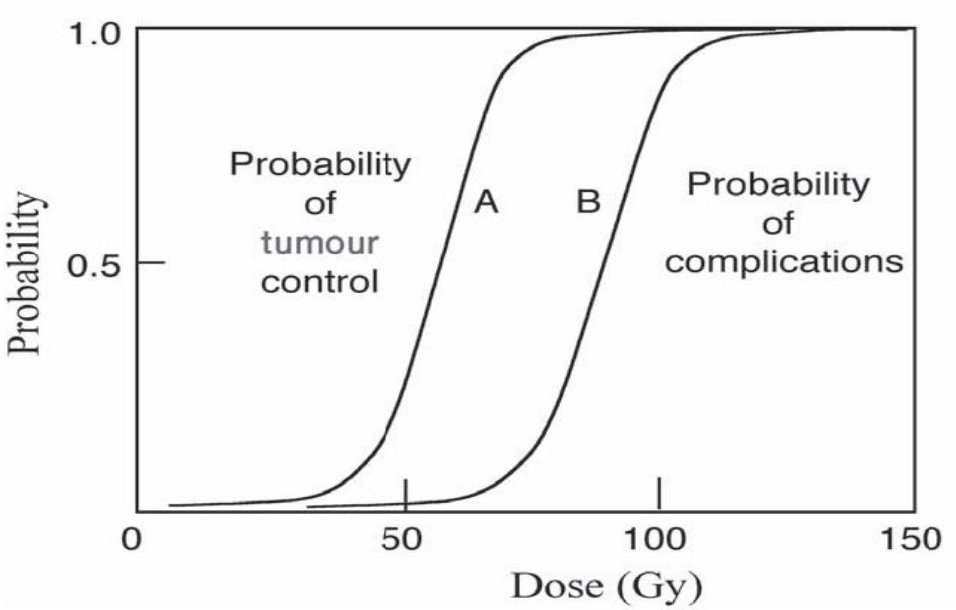

Fig.1.3. Generalized dose-response curve for tumor and normal tissues. In this case a small change in dose has a much greater effect on the normal tissue than on the tumor itself (Adapted from Podgorsak 2005).

In practice a dose must be chosen that gives a given level of cure with acceptable complication levels. Due to the gradient of the respective curves at the dose level, any uncertainty in dose means that the response can be greater in the normal tissues than for the tumor. The radiation dose delivered to the target and surrounding tissues is one of the major predictors of radiotherapy treatment outcome. Hence, it is an essential need to have greater accuracy in the delivery and reporting of radiotherapy doses. It is generally assumed that the dose must be delivered within an uncertainty of less than ± 3.5 % of the prescribed dose to

ensure the treatment aims are met (Sipila 1994). In clinical situations with best practice this is around 5 % (Svensson 1984, Knöös T and McClean 2007).

1.1.4 Detectors used in Radiotherapy

A radiation detector is a device that measures directly or indirectly the quantity absorbed dose. Radiation detectors are used for a variety of measurements in radiotherapy such as quality assurance of the equipment, verification of treatment delivery, output measurement of the machine, measurement of beam parameters etc. In this context, the desirable properties of a detector will be characterized by accuracy and precision, environmental (temperature, pressure, humidity) correction, dose linearity, dose or dose rate dependence, energy response, directional dependence and spatial resolution etc (Attix 1986, Knoll 2000, Yin 2003). For radiotherapy purposes the detector should be robust and produce measurements with high precision and accuracy. As dose is generally measured as dose-to-water, the ideal detector should be water equivalent. A water equivalent detector would not suffer from variations in stopping power ratios or mass energy absorption coefficient ratios with variation in energy. It should also have a dose response (detector signal per mean absorbed dose in the detector) independent of radiation quality as much as possible since the energy spectrum varies with position in the tissue or phantom used for measurement. There are numerous types of detectors, each with specific benefits and intended situations of usage. Obviously, not all dosimeters can satisfy all characteristics. Hence, the choice of dosimeter must be made judiciously taking into account the requirement of measurement situation.

The main types of detectors used in radiotherapy are ionization chambers, semiconductor detectors, thermoluminescent detector (TLD), diamond detector, electron paramagnetic resonance (EPR) detectors, Plastic Scintillators, radiochromic and radiographic films etc. A single probe with synthetic diamond as the radiation sensing element could be used for both photon and electron beams dosimetry in large as well as in small radiation fields (Planskoy 1980). Small-size ion chambers are mostly used and are recommended for clinical electron and photon beam calibration. They are accurate and precise and also provide instant readout of the result. Diode detectors have small size, instant readout, high spatial resolution and are highly sensitive to radiation as a result of the high density of silicon compared to air, but they have few major drawbacks such as non tissue equivalent, temperature dependent, sensitivity changes with accumulated dose (Essers and Mijnheer 1999, Yin et al 2002). Most commonly used TLDs in medical applications are LiF:Mg,Ti, LiF:Mg,Cu:P and $Li_2B_4O_7$:Mn, because of their close to tissue equivalence property. Other TLDs are also used because of their high sensitivity. Those are $CaSO_4$:Dy, Al_2O_3:C and CaF_2:Mn. TLDs are available in various forms such as powder, chips, rods and ribbons. The major drawbacks of TLDs are no instant readout, accurate results require care, readout is time consuming, require calibration before being used (Cameron et al 1968, Horton 1987). Alanine dosimeter produces free radicals when exposed to irradiation and can be measured using EPR. Alanine dosimeters are close to water equivalent and shows insignificant energy dependence (Bradshaw et al 1962, Desrosiers et al 2008). Lithium Formate monohydrate detector is also a promising EPR dosimeter. Compared to alanine detector, it exhibits higher sensitivity and equally limited energy dependence for clinical megavoltage photon beams. Radiochromic and radiographic films are used in radiotherapy dosimetry (Azam et al 1998, Sujatha et al 2007). The properties and features of both films are different. Dosimetry with radiochromic

films have a few advantages over radiographic films, such as easy to use, elimination of the need for darkroom facilities, film cassettes or film processing, dose rate independence, better energy characteristics (except for low energy photons) and insensitivity to ambient conditions. Other detectors used in radiotherapy are gel detectors, chemical detector, metal-oxide semiconductor field effect transistor (MOSFET) detectors, optically stimulated luminescence (OSL) detectors and Plastic Scintillators etc.

1.2 Interaction of radiation with matter

1.2.1 Interaction of photon with matter

The major interaction processes (see Fig. 1.4) which the photons can undergo when interacting with matter are Photoelectric absorption, Compton scattering, Pair production and Rayleigh scattering.

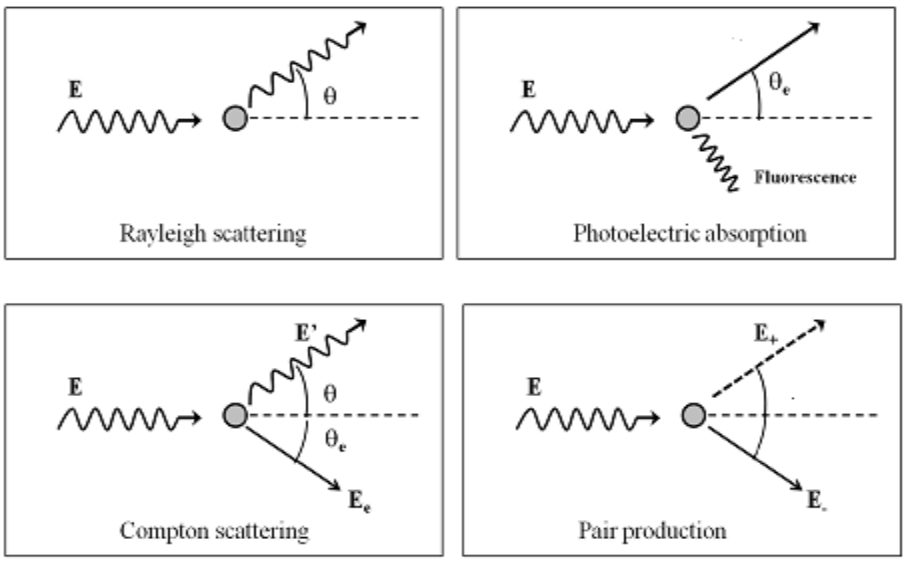

Fig. 1.4 Schematic diagram of photon interaction processes. E is the incident photon energy, E' is the scattered energy of the photon, E_e is the energy of the electron. E_+ and E_- are the

kinetic energy of positron and electron, respectivey. θ and θ_e are the scattering angles of photon and recoil electron, respectively(adapted from Podgorsak 2005).

1.2.1.1 Photoelectric absorption

The Photoelectric absorption is the predominant mode of interaction for photons of low energy, in the energy range of few keV to around 0.1 MeV. In this process, the incident photon interacts with a tightly bound electron (inner shells such as K, L, M or N) and it is completely absorbed and the electron called photoelectron is ejected from the atom (see Fig. 1.4). Photoelectric absorption occurs when the incident photon energy is higher than the binding energy of the electron. A part of the photon energy is used to overcome the binding energy of the atom and the residual energy is transferred as kinetic energy of the photoelectron. Hence, the kinetic energy of the photoelectron is given by:

$$E_e = h\upsilon - E_B \qquad (1.1)$$

where E_e is the kinetic energy of the photoelectron, $h\upsilon$ is the energy of the incoming photon and E_B is the binding energy of the electrons in the atomic shell. As result of the emission of the electron, the atom is left in an excited state with a vacancy in the ionized shell. This vacancy is quickly filled through the capture of an outer orbital electron therefore, one or more characteristic X-ray photons (fluorescent photons) are generated followed by Photoelectric absorption. In some fraction of the cases, the emission of Auger electrons may substitute for the characteristic X-ray in carrying away the atomic excitation energy (Podgorsak 2005). The probability of occurrence of the Photoelectric absorption varies roughly with the energy of the incident photon and the atomic number (Z) of the medium, as follows:

$$\tau_{PE} \propto \frac{Z^n}{(h\upsilon)^3} \tag{1.2}$$

where τ_{PE} is the cross section in cm^{-2}. n is the exponent which varies between 3 and 4 over the photon energy region of interest. Photoelectric absorption is predominant for photons of relatively low energy and for high Z materials. The angular distribution of the emitted electrons depends on the energy of the incident photon. For low photon energy, the electrons are predominantly ejected at 90^0 relative to the incident photon direction. With increasing photon energy, the electrons are emitted in more forward directions (Attix 1986).

1.2.1.2 Compton scattering

The Compton scattering is the dominant mode of interaction in the energy range from several hundred keV to several MeV and therefore it represents the major mechanism of interaction for most photon energies used in radiotherapy. When the Compton scattering occurs, the incident photon transfers a part of its energy to an electron and is deflected through an angle θ with respect to its original direction (see Fig. 1.4). In contrast to the Photoelectric absorption, the incoming photon interacts with a loosely bound electron, i.e. an outer shell electron in case of Compton scattering (Podgorsak 2006). In this collision, the photon transfers a part of its energy to the electron, which departs at an angle θ with a kinetic energy given by:

$$E_k = h\upsilon - h\upsilon' = h\upsilon \frac{\frac{h\upsilon}{m_0 c^2}(1-\cos\theta)}{1+\frac{h\upsilon}{m_0 c^2}(1-\cos\theta)} \tag{1.3}$$

where $h\upsilon$ and $h\upsilon'$ are the energy of the incident and scattered photons, respectively. E_k is the kinetic energy of the recoil electron (Compton), m_0 is the rest mass energy of the electron and c is the velocity of light in vacuum. Energy and momentum conservation constraints can be used to derive the relation between the energy of incident and scattered photons as:

$$h\upsilon' = \frac{h\upsilon}{1+\left(\frac{h\upsilon}{m_0c^2}\right)(1-\cos\theta)} \tag{1.4}$$

This relation shows that the energy of the scattered photon depends not only on the energy of incident photon but also on its scattering angle θ. It is clearly observed from this equation that as the energy of the scattered photon increases, the photon is deflected more and more along the forward directions. For a given incident photon energy, the minimum energy of the scattered photons (corresponding to a maximum energy for the scattered electron) corresponds to $\theta = 180^0$. The scattering angle θ of the photon and recoil angle Φ of the emitted electron are related as follows:

$$\cot\Phi = \left(1+\frac{h\upsilon}{m_0c^2}\right)\tan\frac{\theta}{2} \tag{1.5}$$

It is interesting to notice from equation 1.5 that the electron angle is thus always confined to the forward direction ($0 \le \Phi \le 90^0$), whereas the photon can be scattered to any direction. As the energy of the incident photon increases, the electrons tend to be scattered in a more forward directions and the transfer of the energy to the electrons also increases. Compton scattering is the only type of interaction that is not highly dependent on the Z of the medium, but it depends on the incident energy and the density of the material. In particular, the

probability of occurrence of Compton scattering decreases with increasing photon energy and it shows to be proportional to the material density.

1.2.1.3 Pair production

Pair production refers to the creation of an electron and a positron pair from a photon in the field of an atomic nucleus (see Fig. 1.4). For this interaction to occur, the photon energy should be greater than the rest mass energy of the electron-positron pair, i.e, $E \geq 2m_0c^2 = 1.02$ MeV. For this effect to occur, three quantities energy, charge and momentum must be conserved. To conserve the linear momentum the effect cannot occur in free space. The angular distribution of the electrons and positrons produced in pair production is peaked increasingly in the forward direction with increasing incident photon energy *hv* (Evans 1955). For photon energies close to the threshold energy $2m_0c^2$, the created electron and positron travel almost in opposite directions to each other. For energy above this threshold, the pair can travel in a more forward direction. The probability of occurrence of the pair production process is governed by the theory of Bethe and Ashkin (1953). According to this formalism, the probability increases rapidly as the photon energy increases and it is also strongly dependent on the atomic number as Z^2:

$$\tau_{PP} \propto Z^2 \log E \qquad (1.6)$$

1.2.1.4 Rayleigh scattering

In Rayleigh scattering the photon is scattered by bound atomic electrons. The atom is neither excited nor ionized. The atom as a whole absorbs the transferred momentum but its

recoil energy is very small and the incident photon scattered with relatively small scattering angle θ has essentially the same energy as the original photon. In this process the photon loses none of its energy and only deflected through a small angle θ (sees Fig. 1.4). The probability of occurrence of this process decreases with the incident photon energy, but it increases with the atomic number of the medium as follows:

$$\tau_{RS} \propto \frac{Z^2}{(h\upsilon)^2} \tag{1.7}$$

The relative importance of the Rayleigh scattering is in the low energy regime, but it contributes only a few percent or less to the total attenuation cross section. It does not contribute to the kerma or dose, since no energy is transferred during this interaction.

1.2.1.5 Attenuation coefficient

When the photon travels through the matter, they can undergo one or a combination of the above processes depending on their energy and atomic number of the medium. Incident photons can also be transmitted out of the medium without undergoing any interaction. If we consider *N* photons traversing a distance *dl* in a material of density ρ, then if *dN* particles experience interactions with the material, we can define the linear attenuation coefficient (macroscopic cross section) μ (cm^{-1}) as

$$\mu = \frac{1}{dl}\frac{dN}{N} \tag{1.8}$$

The probability that a particle at a normal incidence in a material of thickness *dl* undergoes an interaction is μdl. It is the product of the atomic density *N* and the total cross section σ_{total}

$$\mu = N\sigma_{total} = \frac{\rho N_A}{A}\sigma_{total} \tag{1.9}$$

Based on this coefficient, the number of photons passing a certain thickness *x* of a medium decreases following an exponential function as follows:

$$N = N_0 e^{-\mu x} \tag{1.10}$$

where N_0 is the incident number of photons. In general, the total linear attenuation coefficient is represented as the sum of attenuation coefficients for all individual interactions that a photon of given energy may undergo with atoms of a specific material. As discussed above, the interactions of interest in the therapeutic energy range are basically three (Photoelectric absorption, Compton scattering and pair production).

$$\mu = \mu_{PE} + \mu_{CE} + \mu_{PP} = \frac{\rho N_A}{A}\left(\tau_{PE} + \tau_{CS} + \tau_{PP}\right) \tag{1.11}$$

where $\mu_{PE,}$ μ_{CE} and μ_{PP} denote the linear attenuation coefficient for the Photoelectric absorption, Compton scattering and pair production, respectively. The corresponding cross section for theses interactions are denoted by $\tau_{PE,}$ τ_{CS} and τ_{PP}, respectively.

As seen from equation 1.9, μ of a given material is directly proportional to the density of the material. In order to eliminate the density dependence, the mass attenuation coefficient, μ/ρ (where the ρ is the mass density of the medium), is used instead. The mass attenuation coefficient can be divided into two parts, namely the energy transfer coefficient (μ_{tr}/ρ) related to the transfer of energy to charged particles and the energy absorption coefficient

(μ_{en}/ρ) which applies to the energy absorbed in the medium. It can also happen that a part of the energy transfer to the electrons is not deposited locally within the medium along the electron track, being lost by emission of bremsstrahlung photons. This fact is described by the mass energy absorption coefficient (μ_{en}/ρ) which is given by:

$$\frac{\mu_{en}}{\rho} = (1-g)\frac{\mu_{tr}}{\rho} \qquad (1.12)$$

where g is the fractional energy of the electrons that is lost as bremsstrahlung. g is negligible for low energy photons but significant for high energy photons and high atomic number materials.

1.2.2 Interaction of electron with matter

Electrons are used directly as beams for cancer therapy and also responsible for the energy deposition in matter by photon beams. Contrary to photons which can pass through the matter with no interactions at all, a charged particle is surrounded by its Coulomb electric force field that interacts with orbital electrons (collision loss) and the nucleus (radiative loss) of all atoms it encounters as it penetrates into matter. The energy transfer from the charged particle to matter in each individual atomic interaction is generally small. Hence, a charged particle undergoes a large number of interactions before its kinetic energy is spent. Compared to heavy charged particles, electrons and positrons have a different behaviour when passing through matter. Because of their small mass, electrons (and positrons) can lose a large fraction of their energy in a single collision with an atomic electron (which have equal mass as the incident electron) and, they can also be scattered into relatively large angles. Coulomb interactions between the incident electron and orbital electrons of an

absorber result in ionizations and excitations. These collisional energy losses are characterized by collision (ionization) stopping powers. Coulomb interactions between the incident electron and nuclei of the absorber atom result in electron scattering and in production of bremsstrahlung photons. These types of energy loss are characterized by radiative stopping powers. In general, energy losses are described by stopping power and scattering is described by scattering power. The types of charged particle interactions are elastic and inelastic collisions with the atomic electron and nuclei.

1.2.2.1 Elastic collision with atomic electron and nuclei

In elastic collision the total kinetic energy of the system is conserved, i.e., the total kinetic energy before the interaction is equal to the total kinetic energy of the products after the interaction. For example, when the target particle in a collision simply recoils, the interaction is elastic and the energy lost by the incident charged particle appears as the recoil energy of the target particle. Such elastic collisions take place when the incident particle does not have adequate energy to excite or ionize or disintegrate the target atom.

1.2.2.2. Inelastic collision with atomic electron and nuclei

In inelastic collision some part of the kinetic energy of the charged particle is used up to change the internal state of the target atom, which therefore, does not appear as the kinetic energy of the resultant products. Inelastic collision of charged particle with atomic electron results in ionization and excitation of the medium. When the charged particle has sufficiently lost its energy and is not having enough energy to cause ionization, they lose

energy by elastic collisions with the atoms of the medium and are finally thermalized in the medium (Podgorsak 2005).

Inelastic collision of charged particle with the nuclei of the medium results in radiative collisions. The electrons are deflected and accelerated rapidly by the electric field of the atomic nucleus, leading to the emission of bremsstrahlung photons. The probability of occurrence of this interaction varies nearly Z^2 and increases with the energy and the inverse square of the mass of the particle. Hence, the radiative process is much more important for electrons than for heavy charged particles. The bremsstrahlung radiation is characterized by a continuous energy spectrum where the maximum energy that a bremsstrahlung photon can reach corresponds to the energy of the electron producing the radiation.

1.2.2.3 Stopping power

Energetic electrons experience thousands of collisions as they traverse in the medium before coming to rest. The stopping power is a property of the material in which a charged particle propagates. The rate of energy loss per unit of path length by a charged particle in a medium is called the linear stopping power, $S = -(dE/dx)$. The mass stopping power, S/ρ, is defined as the linear stopping power divided by the density of the absorbing medium. Division by the density of the absorbing medium eliminates the dependence of the mass stopping power on mass density. Typical units for the linear and mass stopping powers are MeV.cm^{-1} and MeV cm^2.g^{-1}, respectively. The total mass stopping power $(S/\rho)_{tot}$ for a charged particle is the sum of the radiative and collision stopping powers, i.e.

$$(S/\rho)_{tot} = (S/\rho)_{col} + (S/\rho)_{rad} \qquad (1.13)$$

The losses by ionization due to the collisions (soft and hard) are accounted by $(S/\rho)_{col}$ and the losses by radiative interactions are accounted by $(S/\rho)_{rad}$ (ICRU 1984, ICRU 1993, Rohlf 1994).

Radiative stopping power

It results from charged particle Coulomb interaction with the nuclei of the absorber. Only light charged particles (electrons and positrons) experience appreciable energy losses through these interactions (bremsstrahlung production).

Collision (ionization) stopping power

It results from charged particle Coulomb interactions with orbital electrons of the absorber. Both heavy and light charged particles experience these interactions that result in energy transfer from the charged particle to orbital electrons, i.e., excitation and ionization of absorber atoms. $(S/\rho)_{col}$ has an important role in radiation dosimetry, The theory of the mass collision stopping power for heavy charged particles, electrons and positrons as a result of soft and hard collisions combines the Bethe theory (Bethe and Ashkin 1953, Hale 1974, Greening 1985, Podgorsak 2006) for soft collisions with the stopping power as a result of energy transfers due to hard collisions. The result of this, for a heavy charged particle with mass *M* and velocity v, collision mass stopping power can be as follows (Podgorsak 2006):

$$\frac{S_{col}}{\rho} = 4\pi \frac{N_A Z}{A} \left(\frac{e^2}{4\pi\varepsilon_0} \right)^2 \frac{z^2}{m_e v^2} \left\{ \ln \frac{2m_e c^2}{I} + \ln \beta^2 - \ln\left(1-\beta^2\right) - \beta^2 - \frac{C_K}{Z} - \delta \right\} \qquad (1.14)$$

where m_e is the mass of the electron, $\beta = v/c$ is the ratio of the electron velocity v to the velocity of light c, $\tau = E_0/(m_e c^2)$ is the ratio of kinetic energy of the electron to its rest mass energy, $N_A Z/A$ the number of electrons per gram of medium and I the mean excitation energy of the atoms. δ is the density effect arises because of the shielding of distant electrons i.e polarization of orbital electrons by the electric field of the moving electron. The term C_k/Z is the shell correction. The stopping power varies slowly with particle energy and is proportional to the atomic number Z of the material. Also, it can be seen that the collision stopping power varies as $(1/v^2)$, i.e. inversely proportional to the energy of the electron. The mass stopping power of light charged particles such as electrons and positrons is given by a modified version of the Bethe-Bloch formula, as follows (Podgorsak 2006):

$$\frac{S_{col}}{\rho} = 2\pi r_e^2 \frac{N_A Z}{A} \frac{m_e c^2}{\beta^2} \left\{ \ln \frac{E_K}{I} + \ln(1+\tau/2) + F^{\mp}(\tau) - \delta \right\} \qquad (1.15)$$

The function $F^{-}(\tau)$ is given for electron as (Podgorsak 2006)

$$F^{-}(\tau) = (1-\beta^2)\left[1 + \tau^2/8 - (2\tau+1)\ln 2\right] \qquad (1.16)$$

And the function $F^{+}(\tau)$ is given for positrons as (Podgorsak 2006)

$$F^{+}(\tau) = 2\ln 2 - \left(\frac{\beta^2}{12}\right)\left[23 + \frac{14}{(\tau+2)} + \frac{10}{(\tau+2)^2} + \frac{4}{(\tau+2)^3}\right] \qquad (1.17)$$

Where r_e is the classical electron radius, $\boldsymbol{\tau}$ is the electron or positron kinetic energy normalized to $m_e c^2$, i.e., $\tau = E_K/m_e c^2$ and β is the electron or positron velocity normalized to c, i.e., $\beta = \upsilon/c$.

The rate of bremsstrahlung production by light charged particles traveling through an absorber is expressed by the mass radiative stopping power S_{rad} (in MeV.cm^2/g) as follows (Podgorsak 2006):

$$S_{rad} = \alpha r_e^2 Z^2 \frac{N_A}{A} B_{rad} E_i \qquad (1.18)$$

Where E_i is the initial total energy of the light charged particle, i.e., $E_i = E_{Ki} + m_e c^2$, B_{rad} is a slowly varying function of Z and E_i.

Restricted stopping power

The concept of restricted mass collision stopping power, L_Δ is introduced to calculate the energy transferred to a localized region of interest as in case of radiotherapy. By limiting the energy transfer to secondary charged (δ rays) particles to a threshold (often denoted as Δ), highly energetic secondary particles are allowed to escape the region of interest. The restricted stopping power is lower than the unrestricted stopping power. In radiation dosimetry, the use of the mass collision stopping power $(S/\rho)_{col}$ may overestimate the dose because $(S/\rho)_{col}$ incorporates both hard and soft collisions. L_Δ is defined as the linear rate of energy loss due to only those collisions in which the energy transfer does not exceed a specified threshold value Δ, i.e

$$L_\Delta = \left(\frac{dE}{dx}\right)_\Delta \qquad (1.19)$$

It is usually expressed in units of keV/μm. The choice of the energy threshold Δ depends on the problem at hand. For dosimetric measurements involving air-filled ionization chambers

with a typical electrode separation of 2 mm a frequently used threshold value is 10 keV (Note, the range of a 10 keV electron in air is of the order of 2 mm).

1.2.2.3 Range of charged particles

The path of heavy charged particles in an absorbing medium is rectilinear because they transfer only small amounts of energy in individual ionizing collisions with orbital electrons and suffer small angle deflections in elastic collisions. However, electrons with kinetic energy E_K can lose energy up to $E_K/2$ in individual ionizing collisions and energy up to E_K in individual radiative collisions (Evans 1955). Since they can also be scattered with very large scattering angles, their path through the absorbing medium is tortuous. Hence, the electron which is moving through the medium loses its kinetic energy gradually and continuously. This approach is often referred to as the continuous slowing down approximation (CSDA). However, it is known that the collisions which occur along the path of an electron are governed by probability theories and there statistical fluctuations. So a number of identical particles traveling under identical conditions do not lose the same energy as they pass a given region or interval. This phenomenon is called energy straggling. Similarly, range straggling reflects the existence of different path lengths for particles of identical energies, as consequence of the statistical variations in the rates of energy loss. Based on the CSDA approximation, range can be calculated as follows:

$$R_{CSDA} = \int_0^{E_{Ki}} \frac{dE}{S_{tot}(E)} \qquad (1.20)$$

Where R_{CSDA} is the CSDA range of the charged particle in the absorber, E_{Ki} is the initial kinetic energy of the charged particle, $S_{tot}(E)$ is the total stopping power of the charged particle as a function of the kinetic energy E_K. In general, R_{CSDA} is a very good approximation to the average range, R of the charged particle in the absorbing medium for heavy charged particles, because of the essentially rectilinear path.

1.2.3 Basic dosimetric quantities

In the context of the present work, the characterization of electron and photon beams which are presented in the following Chapters are based on some of the radiometric quantities (ICRU 1980, ICRU 1998) described below.

Fluence (Φ)

The particle fluence Φ gives the number of particles dN that cross a sphere of unit cross-sectional area dA, *i.e*

$$\Phi = \left(\frac{dN}{dA} \right) \qquad (1.21)$$

It is usually expressed in units of cm^{-2}. An additional definition of fluence, simplifying the description of the radiation field, was introduced by Attix (1986) and it is called planar fluence. The planar fluence is defined as the number of particles crossing a giving plane per unit area and, contrarily to the fluence, this quantity depends on the angle of incidence of the particle beam.

Energy fluence (Ψ)

The energy fluence ψ, which is a measure of the total amount of energy entering or leaving a small volume, is defined as:

$$\Psi = \left(\frac{dR}{dA} \right) \tag{1.22}$$

where *dR* denotes the radiant energy incident on a spherical volume of cross-sectional area *dA*. The unit for energy fluence is Jm^{-2}. Radiant energy, *R*, means the energy (excluding rest mass energy) of the particles emitted, transferred or received by all the particles striking the spherical volume.

Kerma (K)

The quantity kerma (from the kinetic energy released per unit mass) refers to the kinetic energy of charged particles, e.g., electrons and positrons, which have been liberated by uncharged particles such as photons. The unit of kerma is J/kg (Gray). If dE_{tr} is the sum of the initial kinetic energies of all charged particles liberated by uncharged particles within a volume element *dV* of a material containing a mass dm ($=\rho dV$) of that material, the kerma *K* is given by:

$$K = \left(\frac{dE_{tr}}{dm} \right) \tag{1.23}$$

If we consider uncharged particles of a given energy E and if the fluence of these uncharged particles at the position of the volume element dV is Φ, the kerma K is related to Φ as follows:

$$K = \Phi E\left(\frac{\mu_{tr}}{\rho}\right) = \Psi\left(\frac{\mu_{tr}}{\rho}\right) \qquad (1.24)$$

where μ_{tr}/ρ, is the mass energy transfer coefficient of the material with energy E.

Absorbed dose (D)

The absorbed dose, D is probably the key quantity in respect to the clinical effects of the radiation interaction with matter. According the ICRU Report (1998), absorbed dose is defined as the mean energy imparted $d\epsilon$ by the ionizing radiation to the absorbing material of mass dm:

$$D = \left(\frac{d\varepsilon}{dm}\right) \qquad (1.25)$$

The unit for dose is J/kg. The SI unit for absorbed dose is Gray (Gy): 1 Gy = 1 J/ kg. The absorbed dose, D in the medium may be expressed as:

$$D = \Phi(S/\rho)_{col} \qquad (1.26)$$

where Φ is the fluence of electrons. The concept of kerma deals only with primary interactions in matter, absorbed dose deals with all the interactions taking place in the medium.

Exposure (*X*)

Let us consider a volume element *dV* filled by air of mass *dm* at a point in a photon radiation field. If *dQ* is the absolute value of the total charge of ions of one sign produced in air when all the electrons and positrons liberated or created by photons in the air-filled volume element dV are completely stopped in this volume, then exposure *X* is defined as:

$$X = \left(\frac{dQ}{dm} \right) \tag{1.27}$$

The SI unit for exposure is C/ kg. The quantity *X* is only defined in air for photons.

1.3 Literature review

Energy dependence of radiation detectors including films has been investigated by several authors for diamond (Rustgi 1995, Laub 1997, Bucciolini et al 2003,), LiF TLD (Holt et al 1975, Olivera et al 1994a and 1994b, Mobit et al 1996a and 1996b, Mobit et al 1998, Medich and Munro 2010), Al_2O_3 (Akselrod et al 1993, Aznar et al 2005, Scarboro and Kry 2013), Plastic Scintillators (Williamson et al 1999, Beddar et al 2005, Ebenau et al 2016) and different radiochromic films (Butson et al 2004, 2005, 2006a and 2006b, Chiu-Tsao et al 2005, Ebert et al 2009). Most of these studies were limited to therapeutic energy range (100 keV-10 MeV) and some studies were also carried out for lower X-ray energies i.e diagnostic energy range (75kVp-125kVp). However, limited data are available for energy response corrections for different solid state detectors and radiochromic films especially for brachytherapy sources. In general, photon energy response corrections were determined in air for a given beam quality. However, in a previously published study, Meigooni et al

(1988a) pointed out that LiF:Mg,Ti TLD exhibits an over-response with photon energy of ^{192}Ir brachytherapy source that varies with the depth in the phantom due to the shift of the photon energy spectrum to lower energies with increasing depths in the phantom material. This over-response from the change in the spectra at different depths (due to multiple scattering) was estimated to be as much as 8.5% at a depth of 10 cm as compared to a value at 1 cm depth which was confirmed by another study (Pradhan and Quast 2000). Hence, it was recommended to determine in-phantom depth-dependent photon energy response corrections for a given detector (Pradhan 2010). Selvam and Biju (2010) have reported the relative absorbed dose energy response correction, R of LiF, $Li_2B_4O_7$, Al_2O_3, Diamond, Silicon diode and air detectors as a function of distance along the transverse axis of the ^{169}Yb and ^{125}I sources using Monte Carlo-based EGSnrc code system. Medich and Munro (2010) also reported the absorbed dose energy correction factors of LiF TLD detector for ^{169}Yb source as a function of distance r and polar angle θ i.e $f(r,\theta)$ at different locations in the phantom using Monte Carlo-based MCNP5 code. In this thesis, in-phantom depth-dependent absorbed-dose energy dependence of a given detector at a given beam quality is addressed by beam quality correction which is based on absorbed dose to the medium at the point of measurement and absorbed dose to the sensitive material of the detector obtained for the beam quality (brachytherapy sources) and reference radiation. The reference beam quality is generally telecobalt radiotherapy beam. Radiation transport using Monte Carlo methods serves as a powerful tool to calculate beam quality correction. In this thesis, Beam quality corrections were calculated as function of distance along the transverse axis of the brachytherapy sources in the water phantom using Monte Carlo-based EGSnrc code system. However, for ^{169}Yb and ^{125}I sources, the calculation of beam quality correction does not

include LiF, $Li_2B_4O_7$, Al_2O_3 and Diamond detectors since it was already reported by Selvam and Biju (2010).

For clinical dosimetry applications, the medium of interest for measuring absorbed dose with any dosimeter is water and recommended as the reference medium for dosimetry radiotherapy (Nath et al 1995, Rivard et al 2004). While water provides excellent reproducibility and comparability of measurements worldwide, the precise and reproducible placement of radiation detectors in water is a challenge and may be the cause of measurement errors. Hence, liquid water is often replaced by solid phantoms for measurement purposes. Solid phantom have several advantages over liquid water phantom for example solid phantoms can be machined, to accommodate the source and detectors in a precise geometrical configuration, facilitating an accurate measurement and reproducibility in source-detector geometry, water proofing, precise positioning of detectors etc. However, in the case of brachytherapy, the solid phantoms are not truly water-equivalent and their influence on the dosimetry should be taken into account when solid phantoms are used for measurement purposes. The question of water equivalent solid phantom materials has been studied by several authors for ^{192}Ir brachytherapy sources (Meli et al 1988, Williamson 1991, Ballester et al 2001 and 2004, Song et al 2009, Tedgren et al 2009, Schoenfeld et al 2015) as well as for low energy brachytherapy sources (Meigooni et al 1988b, Reniers et al 2004, Song et al 2009, Schoenfeld et al 2017). Meigooni et al 1988b compared the solid phantom materials solid water, PMMA and polystyrene with water both by measurement using TLD-100 and Monte Carlo method for ^{125}I brachytherapy source. In recent times, Schoenfeld et al (2015 and 2017) investigated water-mimicking solid phantom materials for brachytherapy dosimetry using Monte Carlo method. The authors followed the approach of Tedgren et al

(2009) and the selection criterion of water equivalent solid phantom materials was done by comparing the radial distributions of the absorbed dose to water in the water-mimicking phantom and in real water. Song et al (2009) introduced solid phantom-to-water phantom conversion factor that converts the dose measured in the solid phantom material to that in water phantom. The phantom material investigated was ice and found that the value of these conversion factor was highly dependent on the composition of the phantom material and the photon energy spectrum at that depth in the phantom material. Monte Carlo is a perfect tool to address the influence of solid water phantom on dosimetry. In this thesis, the influences of solid water phantoms for a given detector were addressed by phantom scatter correction using Monte Carlo method. This study also includes the calculation of mean energies in solid phantoms and water phantom for different brachytherapy sources.

In general, detectors are calibrated in ^{60}Co beam and used for measurements in megavoltage photon and electron beams. Therefore, the energy response correction factor needs to be applied if the detector is used in a different beam quality. The energy response correction factor of different detectors was studied by several authors for high energy electron beams. Holt et al (1975), Olivera et al (1994a and 1994b) have studied the energy correction factor of LiF thermoluminescent dosimeters (TLD) and found a strong dependence of the energy correction factor on the electron beam energy that varies in the range of 1.02–1.14. Horowitz (1981) has reviewed the energy dependence of LiF TLD in electron beams. Mobit et al (1996a and 1996b) determined the energy correction factor of LiF TLD by using both experimental and Monte Carlo simulations. They found that the energy correction factor varies from 1.036 for 4 MeV electron beams to 1.021 for 20 MeV electron beams at the depth of maximum dose (d_{max}) in PMMA phantom. The data reported indicate that the energy correction factors of LiF TLD in electron beams depend on the average electron

energy incident on the phantom surface, the electron energy spectrum incident on the detector surface, the size and density of the detector etc. Mobit et al (1998) calculated energy correction factor for $Li_2B_4O_7$ detector in megavoltage electron beams using Monte Carlo methods and found that the energy correction factor varies from 0.981 for 2 MeV electron beams to 0.99 for a 20 MeV electron beams. Wang and Rogers (2007) studied the energy response of a thin diode detector and found that the energy dependence is less than 2 % at d_{ref} for electron beam energies from 6 to 18 MeV. Their study also investigated the most appropriate Δ parameter (the kinetic energy of an electron that is sufficient to cross the cavity, i.e the electron energy that corresponds to a CSDA range or the mean chord length of the detector thickness) for which the Si diode of thickness 0.06 mm behaved almost as an ideal Spencer-Attix cavity for radiotherapy electron beams. However, Mobit et al (2000) found that for intermediate sized detectors LiF and CaF_2 of thicknesses 1 mm, Burlin cavity theory is valid. The authors demonstrated that the total electron fluence (primary electrons and δ-rays) in these solid state detector materials is significantly different from that in water for the same incident electron energy and depth of irradiation. Thus the Spencer–Attix assumption that the electron fluence energy spectrum in the cavity is identical in shape to that in the medium is violated. Differences in the total electron fluence give rise to electron fluence perturbation correction factors which were up to 5 % less than unity for CaF_2 and less than 1 % for LiF. Generally, not only the density of the cavity perturbs the electron fluence but also the atomic number differences between the medium and cavity are responsible for the large electron fluence perturbation correction factors for detectors. In this thesis, energy correction factors of different detectors such as diamond, LiF, $Li_2B_4O_7$, Al_2O_3, Plastic Scintillator and Lithium Formate were calculated for the radiotherapy electron beams as a function of depth in water. In addition the most appropriate Δ parameter was

investigated for thin micro diamond detector and electron fluence perturbation correction factors were studied for other solid-state detectors for the radiotherapy electron beams.

1.4 Aim of the thesis

The objectives of the present study are the followings:

- To determine in-phantom depth-dependent beam quality correction for a given detector for various brachytherapy sources by using Monte Carlo methods. The detectors investigated in this study are diamond, phosphors (LiF, $Li_2B_4O_7$, Al_2O_3), Plastic Scintillator, Lithium Formate and different radiochromic Films such as EBT, EBT2, RTQA, XRT, HS and XRQA. The brachytherapy sources included in the investigation are high energy brachytherapy sources (^{60}Co, ^{137}Cs, ^{192}Ir and ^{169}Yb) and low energy brachytherapy sources (^{131}Cs, ^{125}I and ^{103}Pd). However, for ^{169}Yb and ^{125}I sources the absorbed dose energy response correction factors were reported by Selvam and Biju (2010) for LiF, $Li_2B_4O_7$, Al_2O_3, Diamond, Silicon diode and air detectors. Hence, the present study dose not includes LiF, $Li_2B_4O_7$, Al_2O_3 and Diamond, detectors for calculation of beam quality correction for ^{169}Yb and ^{125}I sources.
- To calculate detector-specific, solid phantom-to-water phantom conversion factor i.e phantom scatter corrections, $k_{phan}(r)$ for various solid phantoms as a function distance along transverse axis of the sources (r) in the phantom material for the above brachytherapy sources using Monte Carlo methods. The solid phantoms investigated are PMMA (polymethyl methacrylate), polystyrene, solid water, virtual water, plastic water, plastic water (LR), RW1, RW3, A150 and WE210.

- To determine the response of different detectors as a function of depth in a water phantom for radiotherapy electron beams (6 MeV, 9 MeV, 12 MeV, 15 MeV and 18 MeV). In addition, Spencer-Attix cavity theory characterized by a parameter Δ, which is the kinetic energy of an electron that is sufficient to cross the cavity, was investigated for diamond and electron fluence perturbation correction factors were studied for LiF, $Li_2B_4O_7$, Al_2O_3, Plastic Scintillator and Lithium Formate detectors for the above electron beams.

CHAPTER 2

Monte Carlo method for radiation transport

2.1 Overview of Monte Carlo Technique

Monte Carlo simulations provide estimated solutions to analytically intractable mathematical problems via computational methods (Fishman 1996). The Monte Carlo method was originally proposed by Stan Ulam and John Von Neumann during the Second World War with the aim of developing atomic weapons (Eckhardt et al 1987). The first application of the method was idealized by Wilson in 1952 for the study of the production of electromagnetic cascades in the area of high energy physics (Wilson 1952). This study established the base for the development of Monte Carlo codes focused on the simulation of radiation transport. Since then, the method has been evolved into many different areas (high energy physics, nuclear reactor analysis, medical imaging, radiation shielding etc.) as an alternative of experimental approaches. There is tremendous increase in the applications of Monte Carlo methods in the medical physics field (Andreo 1991, Rogers 2006).

2.2 Monte Carlo transport of photons

The physical processes of electron and photon interactions with matter are well-established and discussed in Section 1.2.1 of Chapter 1. Fig. 2.1 presents a flow diagram for a Monte Carlo simulation of photon transport. The mean free path of megavoltage photons in a tissue–like medium is on the order of decimeters, thus relatively few photon interactions occur within typical simulation geometry. Therefore it is reasonable to treat each photon interaction individually. For Monte Carlo transport of photon, consider a particle obtained from a source, with a certain position, energy and direction. A random number is drawn in order to determine a distance to the next particle interaction, which will depend on the type of particle, its energy and the medium in which the particle is located. The particle is transported along its direction for a distance determined by the random number drawn. A new random number is drawn in order to determine the type of interaction the particle

should undergo using a cross section database. The type of interaction will again depend on the type of particle, its energy and the medium in which the interaction takes place. Depending on the type of interaction, the particle may change its direction and/or energy, moreover new particles may be generated as a consequence of the interaction. This is again determined by drawing random numbers and using a cross section data base. This process is repeated until the primary particle either reaches predetermined cut-off energy or leaves the boundaries of the system. The process is then conducted for all secondary particles generated, which in turn may give rise to additional particles, created along its path. A new primary particle is subsequently drawn from the source and the same procedure is repeated (Rogers and Bielajew 1990).

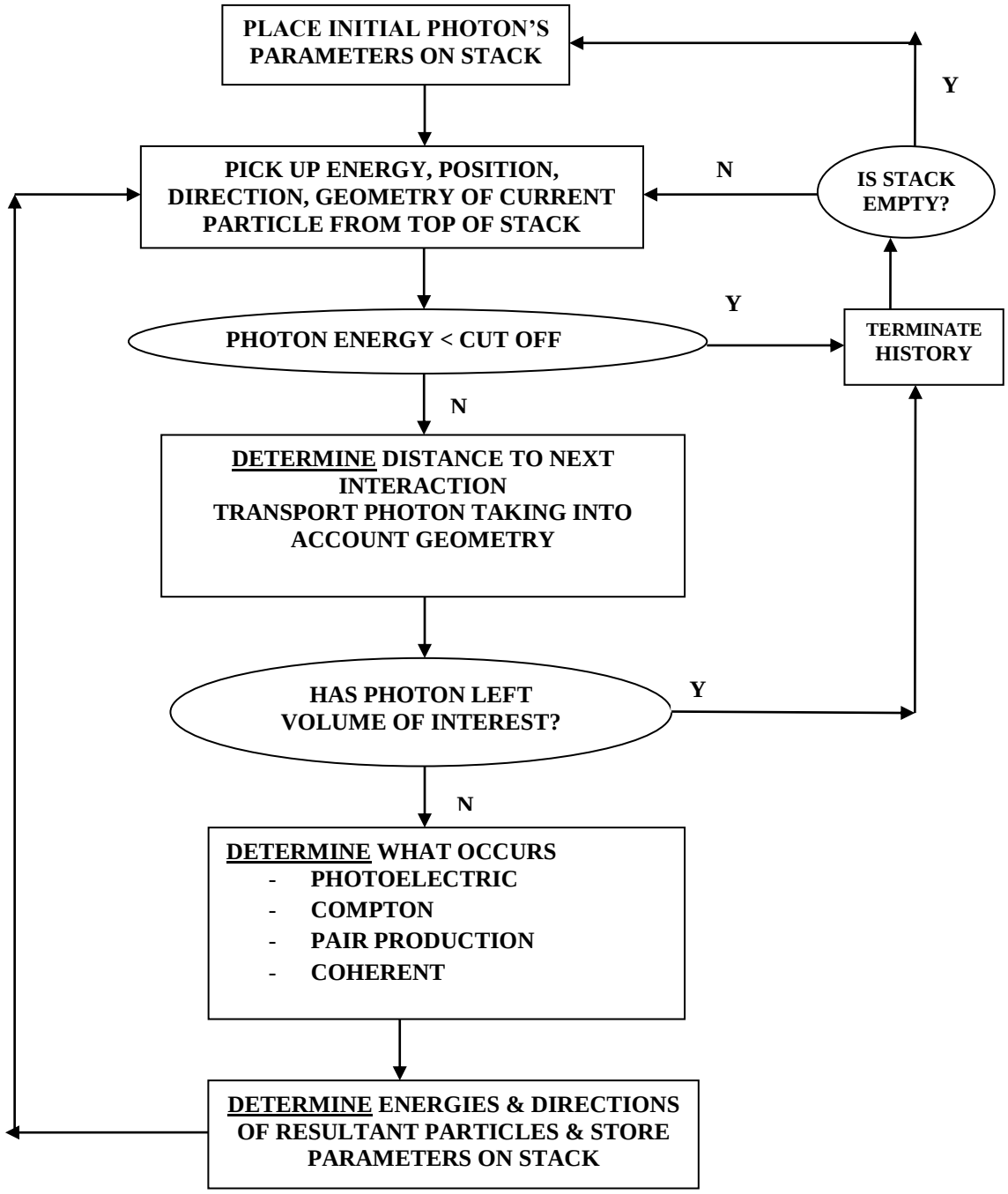

Fig. 2.1 Logic flow of a Monte Carlo simulation of photon transport. DETERMINE means that the quantities of interest are found by sampling from the relevant probability distribution using one or more random numbers (Adapted from Rogers and Bielajew 1990).

The photon transport algorithms used in Monte Carlo simulations of the radiation transport can be summarized as a process consisting of the following steps (Cashwell and Everett 1959):

1. Source Routine
2. Path Length Routine
3. Photon Interaction Routine
4. Geometry and Scoring Routine

1. Source Routine

Source routine generates photons well defined in energy, position and direction coordinates.

Photon energy: Discrete random sampling techniques are used for simulating photons of energy E_i with yield Y_i. In case the source photons exhibit continuous energy spectrum as is the case with bremsstrahlung spectrum of photons emitted by a β emitter, stratified sampling is used to assign photon energies. The energy range is divided into a number of bins and a pre-assigned number of photon histories N_i are generated in the i^{th} bin with energy E_i.

Position coordinates: For point source, position coordinates (x, y, z) are assigned with respect to a specified Cartesian coordinate system. For volume source, points are simulated by generating photons uniformly distributed in a volume of a parallelepiped enclosing the source region. Employing Monte Carlo Rejection sampling technique, the photons falling inside the source volume are accepted and traced further and those falling outside are rejected.

Direction: The probability density function for isotropic distribution can be interpreted as choosing a point with uniform density on the surface of a sphere of unit radius.

2. Path Length Routine

The law governing the distance to interaction is exponential probability law. i.e, probability that no interaction occurs for a photon traveling a distance $x = e^{-\mu x}$. Probability that an interaction occurs in the distance between x *to* $x + dx$ is, $p(x)dx = \mu e^{(-\mu x)}dx$. Sampling distance x from the cumulative probability $P(x)$:

$$R = P(x) = \int_0^s p(x)dx \tag{2.1}$$

$$R = \mu \left| \frac{e^{-\mu x}}{-\mu} \right|_0^s = 1 - e^{-\mu s} \qquad or \qquad s = \frac{\ln(1-R)}{-\mu} = \frac{-\ln R}{\mu} \tag{2.2}$$

The interaction point (x,y,z) at a distance `$s$` in the direction cosines of (u,v,w) from the initial point (x_i,y_i,z_i) is determined as:-

$$x = x_i + u.s \tag{2.3.a}$$

$$y = y_i + v.s \tag{2.3.b}$$

$$z = z_i + w.s \tag{2.3.c}$$

This procedure is suitable for homogeneous medium.

For the heterogeneous media a photon may cross one or more boundaries separating different media and a part of the path length may fall in other media. Coleman technique (Colemon 1968) is used to assign correct probabilities of crossing any number of boundaries.

Step 1. The potential site of an interaction is determined as:

$$S = \frac{-\ln R}{\mu_{\max}} \tag{2.4}$$

where, μ_{max}, is attenuation coefficient that is greater than or equal to that of any of the regions.

Step 2. Determine the medium (i^{th}) containing the probable point of interaction (x,y,z) and its total attenuation coefficient μ_i.

Step 3. If $\left(R \le \frac{\mu_i}{\mu_{\max}} \right) \rightarrow$ the interaction site is accepted.

Step 4. Else, the photon is allowed another flight beginning with the point reached & continuing with the same direction & energy (step 1).

3. Photon Interaction Routine

As described in detail in Section 1.2.1 of Chapter 1, based on the energy of the photon and the type of medium, the important photon interactions are Rayleigh scattering, Photoelectric absorption, Compton scattering and Pair production. In this Section, Monte Carlo simulation of these interactions is explained. The type of interaction is determined by random sampling from their individual relative probabilities (μ_i/μ_T), where, μ_i is the probability of individual interactions and μ_T (= μ_{pe}+ μ_{coh}+ μ_c+ μ_{pp}) is the total interaction probability. Here, μ_{pe} is the probability for Photoelectric absorption, μ_{coh} is the probability of Rayleigh scattering (coherent scattering), μ_c is the probability of Compton scattering and μ_{pp} is the probability of pair production that the photon may undergo. For example, to sample the type of interactions the photon will undergo, let us assume that the probability that the photon will undergo Rayleigh scattering is 5 %, Photoelectric absorption is 20 %, Compton scattering is 70% and pair production is 5 %. Then, if the random number $R \le 0.05$ the particle will undergo Rayleigh scattering, if R lies between 0.05 and 0.25 the particle will undergo Photoelectric absorption, if R lies between 0.25 and 0.95 the particle will undergo Compton scattering and if $R \ge 0.95$ the particle will undergo pair production interaction. Let us assume that R lies between 0.25 and 0.95 and the particle has undergone Compton scattering then:

Compton scattering (Incoherent scattering)

The energy of the scattered photon ($h\upsilon'$) can be sampled from $h\upsilon$ and a random number, R as suggested by Cashwell & Everett (1959).

$$h\upsilon' = \frac{h\upsilon}{1+sR+(2h\upsilon - s)R^3} \; where, s = \frac{h\upsilon}{(1+0.5625h\upsilon)} \tag{2.5}$$

Polar angle θ can becomputed from $h\upsilon$ and $h\upsilon'$:

$$\cos\theta = 1+\frac{1}{h\upsilon}-\frac{1}{h\upsilon'} \tag{2.6}$$

Azimuthal angle φ is randomly sampled between 0 and 2π. New direction cosines $(\bar{u},\bar{v},\bar{w})$ of the scattered photon are computed from sampled values of θ and φ. Scattered photon is traced again as any fresh photon.

Direction Parameters after Compton scattering

The formulae for the final direction parameters of a particle after scattering through an angle Ψ from an incident direction cosines (*u,v,w*) may be determined from the simple principle of elementary complex variables which states that the (*x + iy*). (*cos θ + i sin θ*) is a complex number whose vector is rotated through an angle θ from that of (*x + iy*). Let $(\bar{u},\bar{v},\bar{w})$ be the direction cosines of incident line of flight with $\bar{\gamma}$ & ϕ be the polar and azimuthal angles. Consider $(\bar{u},\bar{v},\bar{w})$ as a point on the unit sphere.

$$\begin{aligned} &u^2+v^2+w^2=1 \\ &\bar{u}=\bar{\rho}\cos\bar{\phi} \\ &\bar{v}=\bar{\rho}\sin\bar{\phi} \\ &\bar{w}=\cos\bar{\gamma}, \quad \bar{\rho}=\sin\bar{\gamma}=\sqrt{1-\bar{w}^2} \end{aligned} \tag{2.7}$$

4. Geometry and Scoring Routine

A geometric routine is designed to decide whether a particle, during its transport in the system, is inside a particular medium of the system, escaped into another medium, deflected from the original direction (the new direction parameters of the particle are determined), entered the region of interest (particle scored with specified parameters) or escaped from the system.These steps are repeated until particles have left the defined simulation geometry or if their energy falls below a specified energy which is the energy where particles are assumed to be stopped and locally absorbed in the medium.

2.3 Monte Carlo Transport of electrons

The simulation of charged particles transport by analog Monte Carlo techniques is incompatible for most applications. Unlike photons, which deposit their energy at discrete points along their path, electrons and positrons lose their energy in a nearly continuous set of interactions. As known, they have a considerably smaller mean free path length and undergo an Enormous number of interactions with the electrons and atomic nuclei in the medium until they are locally absorbed. As example, a fast electron can typically undergo around 10^5 - 10^6 collisions with surrounding matter, for most of which the electron's directions and energies are only slightly changed (Berger 1963). Because of this large number of interactions, an event-by-event simulation of electron transport is not a suitable technique. It would lead to unacceptable long simulation times in order to reach an acceptable statistical uncertainty of the calculated quantities. To solve this difficulty, Berger (1963) developed the condensed history technique for transport of electrons (positrons) in 1963. This technique is the fundamental element of the algorithms which simulate the transport of electrons by Monte Carlo methods. In this method, large numbers of collision processes are condensed to a single electron step. The cumulative effect of the individual

interactions is taken into account by appropriate change of particle's energy and direction of motion at the end of the step. This approach is motivated by the fact that most electron collisions are elastic or semi-elastic and for most cases only minor changes in particle's energy and direction of flight occurs.

According to this technique, the electron trajectory is broken into a series of steps, usually known as condensed steps or multiple scattering steps. In each step, electron undergoes interactions which lead to very small energy loss. These steps are chosen to be long enough to encompass many collisions (so that multiple scattering theories are valid) but short enough that the mean energy loss in any one step is small (so that the approximations necessary for the multiple scattering theories are satisfied). The energy loss and angular deflection of the electron during each of the steps can then be sampled from probability distributions based on the appropriate multiple-scattering theories. In this method, changes in the electron energy and/or direction are statistically grouped.

According to Berger (1963), the condensed history technique is of two types:

- Class I - The effects on the primary particle caused by all interactions (soft and catastrophic) are grouped together for each condensed-history step. When a secondary particle is generated, the primary particle step does not depend directly on the parameters of the secondary particle, although a relation through the cross sections is obviously present (conservation of energy and momentum on a macroscopic scale).
- Class II - The effects of only a subset of the interactions for each type and treat the effects of the remaining interactions on an individual basis. For example, for collisional energy loss a continuous energy-loss model is used which groups together the effects of all interactions that produce knock-on electrons with energy below

some arbitrary threshold energy. Individual treatment is given to those relatively rare "catastrophic" interactions which create secondary particles (δ-ray and a bremsstrahlung) above the same arbitrary energy. These discrete interactions cause the primary electron to lose energy and be deflected.

Class I is the simple form of electron Monte Carlo calculation which is the continuous slowing down approximation (CSDA) model. The name arises because the electron is thought of as continuously losing energy along its path, although the algorithm takes finite steps and the energy appears to drop in discrete steps. In Class I, no secondary particles are produced and the unrestricted total stopping power is used to account for the energy loss in each step. In the CSDA model, all angular deflections are treated using a multiple-scattering theory. In Class I algorithm, the creation of the knock on electron does not explicitly affect the direction of the primary electron. Class II algorithms are in principle more accurate than Class I because correlations between primary and secondary particles are included. In the Class II model, an electron of initial energy E_0 travels a distance t and then creates a knock-on electron of energy E_δ. Immediately after creating the knock-on, the energy of the primary electron is $E_0 - tL_{col}^{AE} - E_\delta$ where L_{col}^{AE} is the collision stopping power restricted to secondaries with energies less than AE (energy threshold for the production of secondary electrons) and tL_{col}^{AE} is the energy loss in continuous processes and deposited along the path *t*. The creation of the knock-on causes the primary electron to change direction. In the Class I model, the electron travels a step length *t* and creates an electron somewhere along the path. The energy at the end of the step is not explicitly affected by the creation of the knock-on electron but is decreased by sampling from an energy-loss distribution (Roger and Bielajew 1990, Bielajew 2000).

In a first step of Monte Carlo transport of electrons (positrons), the distance between two catastrophic events is sampled based on the total cross section of inelastic and radiative processes. The electron is then transported in condensed steps. In each condensed step, the particle position, direction and energy is modified. At the next discrete interaction site, the interaction type (δ-ray or bremsstrahlung above defined energy threshold Δ) is selected and the energy and angular changes are sampled from the appropriate differential cross sections. This procedure is repeated until the electron comes to rest or it leaves the simulated geometry. At the end of each condensed step, the angular deviation of the particle due to multiple scattering is selected based on theories of multiple scattering (Moliere 1948, Goudsmit and Saunderson 1940). Fig. 2.6 presents a logic-flow diagram for electron transport simulations using either a Class I or a Class II algorithm.

The condensed history technique uses straight steps for the electron transport. This approximation is not accurate as electrons follow curved paths. Thus, some corrections of the condensed step, s, are therefore required for the calculation of the true and real curved trajectory of the electron. Additionally to the correction of the path length curvature, the lateral displacement ρ of the electron due to multiple scattering must be taken into account. Selection of the size of each electron step for a particular Monte Carlo simulation is important. The size of the step can affect dramatically both the accuracy and the computation time. A reduction in the electron step size can result in accurate results, since in this case all the corrections required for the calculation of the true curved trajectory of the electron would be avoided. However, the calculation time would increase dramatically. On the other hand, reducing the step size can also lead to the violation of fundamental constraints of the multiple-scattering theories (Kawrakow 2000a and 2000b).

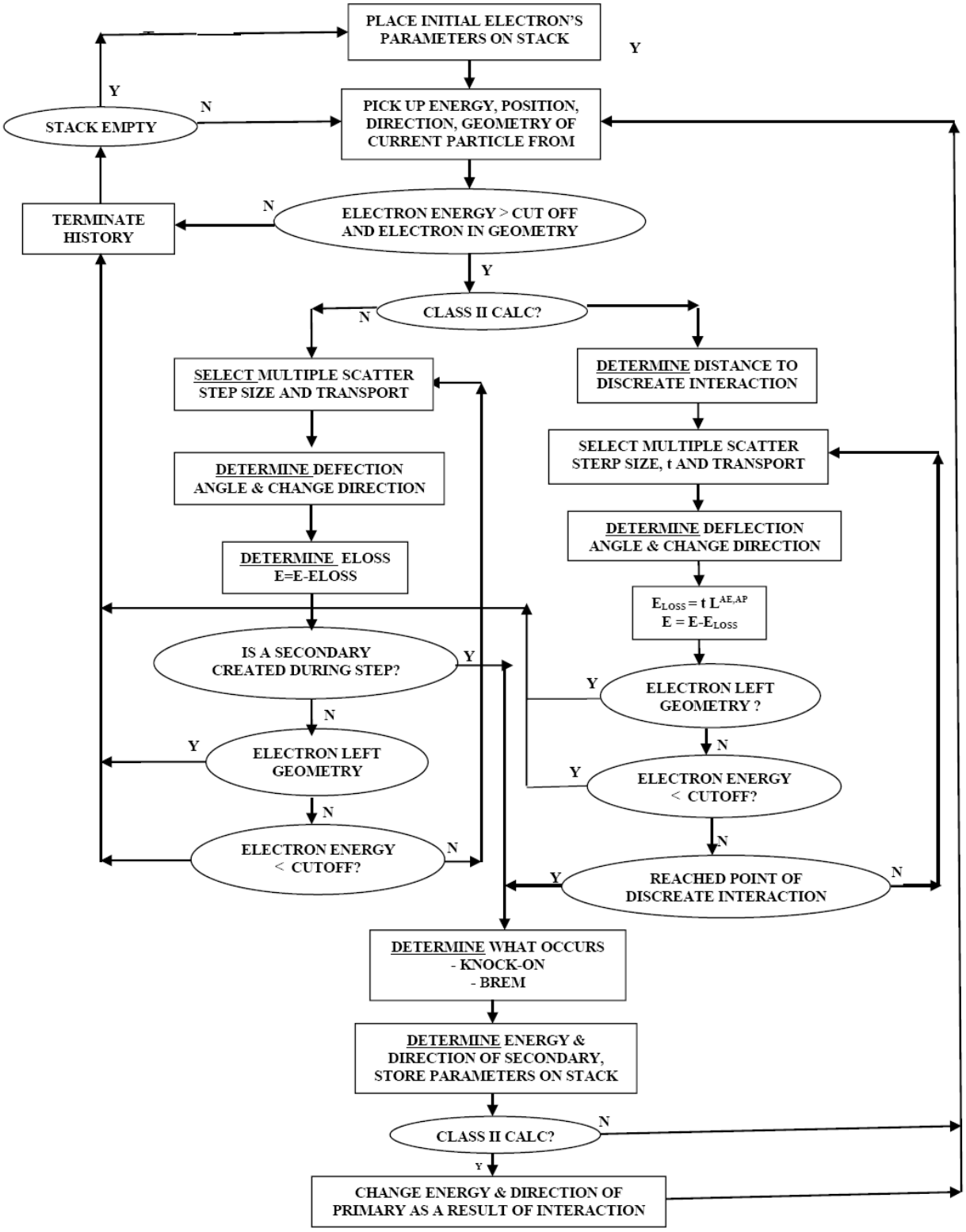

Fig 2.2 Logic flow for Class I and Class II Monte Carlo algorithms for simulating electron transport (Adapted from Rogers and Bielajew 1990).

Another special aspect of Monte Carlo simulation of electron transport is the presence of interfaces between different materials and/or scoring regions. In this situation a boundary crossing algorithm must be used. As the condensed history technique relies on the multiple scattering theory, it is limited by the fundamental constraints of these theories, namely their strict application in infinite or semi-infinite geometries. The presence of a boundary, dividing two different regions, two regions composed of different materials, can result in incorrect energy deposition calculation.

2.4 Variance Reduction Techniques and Efficiency Improvements

The efficiency, ε of a Monte Carlo simulation can be defined as:

$$\varepsilon = \frac{1}{\sigma^2 T} \tag{2.8}$$

where σ^2 is the variance of the simulated result and T is the CPU simulation time needed to reach this variance. The time T is directly proportional to the number of simulated histories N, while the variance is inversely proportional to N. Thus, the efficiency is independent of the number of histories N.

There are two different ways to improve the efficiency of a given calculation: (1) decreasing σ^2 for a given T (2) decreasing T for a given N without changing the variance. Several techniques, referred as variance reduction techniques, have been developed to increase the efficiency, not only reducing the variance, but also decreasing the time to achieve it.

There are two types of variance reduction techniques which increase the efficiency. The first type is known as Approximate Efficiency Improving Techniques (AEIT) which increases the efficiency by making approximations to the transport simulation. For example, using high-energy transport cut offs (ECUT and PCUT) so that a particle is discarded (not transported) once its energy reaches below the set cut offs and its energy is deposited locally.

Another example of AEIT is the use of range rejection which allows the user to terminate the history of an electron when its residual CSDA range is such that it cannot possibly reach another region and deposit energy in that region. However this technique introduces a bias by terminating an electron's history preliminary, in which the possibility of a bremsstrahlung production and its escape from the region is eliminated. To control this approximation an energy threshold is defined, ESAVE above which no range rejection is done. An intelligent choice of this energy must depend on *Z* of the medium and is essentially made based on knowing the approximate fraction lost to bremsstrahlung in a specific material.

The second type of technique is Variance Reduction Technique (VRT) which improves the efficiency without changing the underlying physics of the simulation and does not introduced any bias. When implemented correctly, they are guaranteed to produce the same result as without using these VRTs. Some of the common VRTs are photon forcing, bremsstrahlung splitting, Russian Roulette, bremsstrahlung cross section enhancement, photon splitting, exponential transforms, correlated sampling, importance and/or stratified sampling, cross section enhancement etc. Generally, in particle splitting VRT, one can split a particle into *N* identical particles, each of the daughter particles gets *1/N* of the statistical weight of the original particle. Each daughter particle can then be transported separately thus improving the information gain and efficiency. The splitting can be applied in two different ways: uniform bremsstrahlung splitting (UBS) and directional bremsstrahlung splitting (DBS). Russian Roulette is the reverse of particle splitting in which at any time one can terminate a particle trajectory with a given probability *p* (i.e. play a RR game with the particle where the survival probability is p). If the particle survives, its statistical weight is increased by *1/p*. A particle surviving a RR game represents all other particles killed in the

game. A typical application of this VRT is to avoid transporting particles that contribute nothing or very little to the quantity of interest. Pathlength biasing is a technique to decrease or increase the path length of a photon in order to improve statistics in a specific region of interest. This technique of pathlength biasing is an exponential transformation of photon path lengths. This technique is efficient for studies related to dose buildup region of photon beams and deep penetration problems. Photon forcing is a technique to force an interaction within the geometry between the current point and the point where the photon exits the geometry. Consider a photons passing through a geometry (or region) with a thickness of X mean free path. Fraction of photons interacting in the geometry will be $1 - e^{-X}$ and the fraction of photons leaving without interaction will be e^{-X}. Now split the photon into an interacting portion (with weight $1-e^{-X}$) and a non-interacting portion (with weight e^{-X}). Transport the non-interacting portion to end of geometry (or region) and force the interacting portion mean free path to interact between 0 and X. This technique is useful for calculations involving very thin geometries for example studying the contribution of scattered photons in an ion chamber (Rogers 1984, Rogers and Bielajew 1986 and 1990).

2.5 Overview of EGSnrc Code System

The Monte Carlo code used in this study is EGSnrc code system (Kawrakow et al 2010). The EGSnrc, an acronym of Electron-Gamma Shower, is a general-purpose package of Monte Carlo codes used for the simulation of the coupled transport of electrons and photons through an arbitrary geometry and for particle energies ranging from a few tens of keV up to a few hundred GeV (Kawrakow et al 2010). It can handle particle transport of electrons (and positrons) and photons. The EGSnrc code system has been benchmarked in the radiotherapy energy range for dosimetry.

In this code, the transport of photons is performed in an analog manner. Regarding to the electron and positron transport, the EGSnrc code uses a Class-II scheme based on the condensed history model. In this mechanism individual treatment is given to those relatively rare "catastrophic" interactions which create secondary particles (bremsstrahlung or delta rays) above the user defined threshold energy Δ. Moller scattering is used for electron-electron interaction and Bhabha scattering is used for electron-positron interactions. This code includes a specific electron-transport algorithm which selects automatically the optimum step-size, saving time to the user. This algorithm is called PRESTA, an acronym that stands for Parameter Reduced Electron-Step Transport Algorithm (Bielajew and Rogers 1987). This algorithm allows the use of fewer, larger electron steps, increasing the speed of the simulation without compromising the accuracy of a simulation. It has been shown that the original PRESTA underestimates lateral deflections and longitudinal straggling and produces a singularity in the distribution describing the lateral spread of electrons in a single condensed history. Even though the original PRESTA may be accurate enough for high energies (where elastic scattering is weak), it is not recommended for low energy applications. The code includes now a new version of this algorithm, the PRESTA-II, to overcome these limitations. The size of the condensed step is controlled by the parameter ESTEPE which limits the fractional loss of energy for the continuous process. In order to ensure the convergence for the correct special distribution, the condensed steps may be of small sizes, corresponding to values of ESTEPE within 1 % and 4 % using the original PRESTA algorithm and 25 % for the PRESTA-II algorithm. A new electron transport algorithm, EXACT, is implemented in EGSnrc in which electrons are transported in single elastic scattering mode when they are within a user-defined distance from a region boundary. In EGSnrc, the energy thresholds for the production of secondary electrons and photons are

referred as AE and AP, respectively. These values are selected by the user. Their choice depends on the problem and it has a high influence on the speed of the EGSnrc calculation. Additionally to the threshold of discrete events, the code have others energy threshold which can affect the speed and accuracy of the simulations. These parameters are “the cutoff energies” ECUT and PCUT for electrons/positrons and photons, respectively. These cutoff energies represent the energy below which the transport of the particle is terminated and the energy is locally deposited. Similarly to AE and AP values, ECUT and PCUT also have influence on the accuracy and time consuming of a simulation.

Prior to all simulations the cross section databases for photon and electron interactions are initialized. The data sets are provided in look-up tables for the materials found in the simulation geometries. These tables can be generated with the PEGS4 program, the cross section data preprocessor for EGSnrc. Specifically, PEGS4 generates energy dependent photon attenuation coefficients and electron stopping powers based on experimental data and theoretical cross section calculations. By specifying elemental composition, density and energy range, data tables are generated for use in the EGSnrc simulation.

For many years the standard method for calculating uncertainties was the batch method. The calculation was done in N separate batches and for any scored quantity X, the value X_i was determined for each batch i, separately. The estimate of the uncertainty in the average X was:

$$S_{\bar{X}} = \sqrt{\frac{\sum_{i=1}^{N}(X_i - \bar{X})^2}{N(N-1)}} \qquad (2.9)$$

where, N is the number of batches, X_i is the value of X in batch i, X is the mean value of X evaluated over all batches and $S_{\bar{X}}$ is an estimate of the uncertainty on the mean value of the quantity of interest. The problems with batch method are the uncertainty on the uncertainty

is large, unless very careful, correlations between particles are ignored (e.g. bremsstrahlung splitting) and an extra location was needed to store X_i for each batch (for example 128x128x128 voxels requires 20,971,520 extra locations for 10 batchs).

In EGSnrc, statistics are handled by grouping scored quantities on a history by-history basis (Walter et al 2002) in which all these above difficulties were removed. Now the uncertainties $S_{\bar{X}}$ at the 1σ level are determined for each scored quantity X_i (energy fluence or dose to a voxel) as statistically independent events, such that

$$S_{\bar{X}} = \sqrt{\frac{1}{N-1}\left(\frac{\sum_{i=1}^{N} X_i^{\,2}}{N} - \left(\frac{\sum_{i=1}^{N} X_i}{N}\right)^2\right)} \qquad (2.10)$$

where N is the total number of independent events and is always equal to the total number of primary histories. Using this method, a statistical dose uncertainty for each region can be calculated as a function of initial history number. Since the sample size is large, the uncertainty is reduced, grouping by primary histories ensures that correlations between particles in phase space sources are accounted for and keep track of 2 rather than N_{batch} locations.

EGSnrc code system consists of several user-codes dedicated to address specific situations. These user-codes allow to model specific geometry, set-up various particle sources (e.g. parallel beam of photons with certain spectral distribution, seed sources), and the scoring of quantities sufficient for most of the problems. The user-codes of EGSnrc code system are BEAMnrc (for simulating head of a linear accelerator) (Rogers et al 2016), DOSRZnrc (scores dose in an arbitrary geometry composed of cylinders i.e RZ-geometry) (Rogers et al 2010), DOSXYZnrc (calculates dose to rectilinear voxels of a homogeneous or

heterogeneous geometries) (Walters et al 2016), SPRRZnrc (allows the calculation of stopping power ratios) (Rogers et al 2010), FLURZnrc (calculates fluences and particle spectra) (Rogers et al 2010), g (Calculates quantities such as μ_{tr}, μ_{en} and g i.e the average fraction of energy lost to radiation needed for the calculation of μ_{en}), examin (displays photon cross section data actually used by EGSnrc), CAVRZnrc (calculates various factors of interest when using cavity ion chambers such as A_{att} and A_{scat} and A_{wall}) (Rogers et al 2010). For spherical geometry there are two special user-codes CAVSPHnrc (spherical analogue of CAVRZnrc, designed for ion chamber calculations) and EDKnrc (calculates deposition kernels for both mono-energetic and poly-energetic sources). In the present study user-codes DOSRZnrc, SPRRZnrc and FLURZnrc (Rogers et al 2010) were used.

CHAPTER 3

Calculation of mean energies of brachytherapy sources in various phantoms

Fluence-weighted mean energies, $\bar{E}_{fl}$, and detector-kerma weighted mean energies, $\bar{E}_k$ of photons were calculated for high energy (^{192}Ir, ^{60}Co, ^{137}Cs and ^{169}Yb) and low energy (^{131}Cs, ^{125}I and ^{103}Pd) brachytherapy sources in different solid phantoms (PMMA, polystyrene, solid water, virtual water, RW1, RW3, plastic water, A150 and WE210) and in water phantom by using the equations 3.1 and 3.2. Monte Carlo-based FLURZnrc (Rogers et al 2010) user-code of EGSnrc code system (Kawrakow et al 2010, Rogers et al 2010) was used for the above calculation. The energy degradation in different phantoms is important to understand the absorbed dose for any detector in a given phantom. This Chapter is helpful to understand and discuss the results of following two Chapters (4 and 5).

3.1 Fluence-weighted mean energy

Spectral distributions of radiation can be described in terms of fluence, $\Phi(E)$ or energy fluence, $\psi(E)=E*\Phi(E)$, differential in energy. Fluence-weighted mean energies of photons, $\bar{E}_{fl}$ can be calculated by using the following equation:

$$\bar{E}_{fl} = \frac{\sum_i E_i \Phi(E_i) dE}{\sum_i \Phi(E_i) dE} \tag{3.1}$$

where E_i is the kinetic energy of i^{th} photon in MeV, $\Phi(E_i)$ is the differential photon fluence spectrum at E_i about dE.

3.2 Detector-kerma weighted mean energy

Detector-kerma weighted mean energies of photons, $\bar{E}_k$ can be calculated for a given beam using the following equation:

$$\bar{E}_k = \frac{\sum_i E_i^2 \Phi(E_i) \left(\frac{\mu_{en}}{\rho}(E_i) \right)_{\text{det}} dE}{\sum_i E_i \Phi(E_i) \left(\frac{\mu_{en}}{\rho}(E_i) \right)_{\text{det}} dE} \tag{3.2}$$

where E_i is the kinetic energy of i^{th} photon in MeV, $\Phi(E_i)$ is the differential photon fluence spectrum at E_i about dE. $\left(\frac{\mu_{en}}{\rho}(E_i)\right)_{\text{det}}$ is the mass energy absorption coefficient of the detector at E_i.

3.3 Brachytherapy sources investigated

3.3.1 High energy brachytherapy sources

Generally, ^{169}Yb, ^{137}Cs, ^{192}Ir and ^{60}Co are considered as high energy brachytherapy sources because all of them emit relatively high-energy photons (Perez-Calatayud 2009). ^{192}Ir source is the most widely used source for high dose rate (HDR) brachytherapy treatment worldwide. The high specific activity of ^{192}Ir makes it practical to fabricate miniature size of sources with high activities (Karaiskos et al 1998, Daskalov et al 1998). This allows very short treatment durations and dose optimizations. Recently, due to the technological advancements ^{60}Co sources became available with miniaturized geometrical dimensions as ^{192}Ir sources (Strohmaier and Zwierzchowski 2011, Ballester et al 2005). ^{60}Co HDR unit is gaining importance owing to its longer half-life (5.26 years) as compared to ^{192}Ir (74 days). A typical source replacement interval for ^{192}Ir is 25 times as compared to just a single one for ^{60}Co which results in reducing the operating costs. ^{137}Cs is a low dose rate (LDR) brachytherapy source which is most widely used for gynecological cancer treatment (Williamson 1998, Ballester et al 2000). The low specific activity of ^{137}Cs does not allow the production of miniature sources of very high activity (e.g., 370 GBq) for HDR remote afterloading brachytherapy applications. Thus it is only appropriate to be used as a LDR source. The ^{169}Yb decays by electron capture to ^{169}Tm and emits X-rays and γ-rays with an average energy of 93 keV and half life of 32 days. It has a higher initial dose rate and dose homogeneity. These parameters make the ^{169}Yb source suitable to be used in brachytherapy

applications (Loft et al 1992, Lazarescu and Battista 1997). ^{169}Yb has been investigated as an alternative to ^{125}I for permanent interstitial implants. The brachytherapy source models investigated in this study are:

^{60}Co source

The geometric design and dimensions of the BEBIG ^{60}Co source (model Co0.A86) are shown schematically in Fig.3.1 (Granero et al 2007).

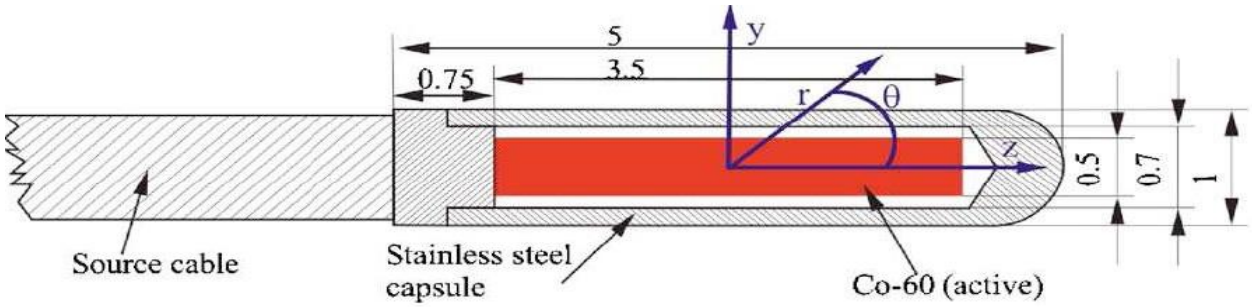

Fig.3.1 Schematic view of ^{60}Co brachytherapy source (model Co0.A86). All the dimensions are in millimeters.(Adapted from Granero et al 2007).

The source is composed of a central cylindrical active core made of metallic Cobalt, 3.5 mm in length and 0.5 mm in diameter. The active core is covered by a cylindrical stainless-steel capsule 0.15 mm thick with an external diameter of 1 mm. The source consists of a rounded tip. The total length of the source is 5 mm.

^{137}Cs source

The geometric design and dimensions of the RTR ^{137}Cs source are shown in Fig. 3.2 (Perez-Calatayud et al 2005). The RTR source is a stainless steel cylinder of 2.09 cm in length and with an external diameter of 0.3 cm. The active part is composed of an extruded gold wire, 0.08 cm in diameter and 1.5 cm in length, placed asymmetrically with respect to the transversal source axis. This source is modeled accurately using DOSRZnrc user-code of EGSnrc code system for further calculations.

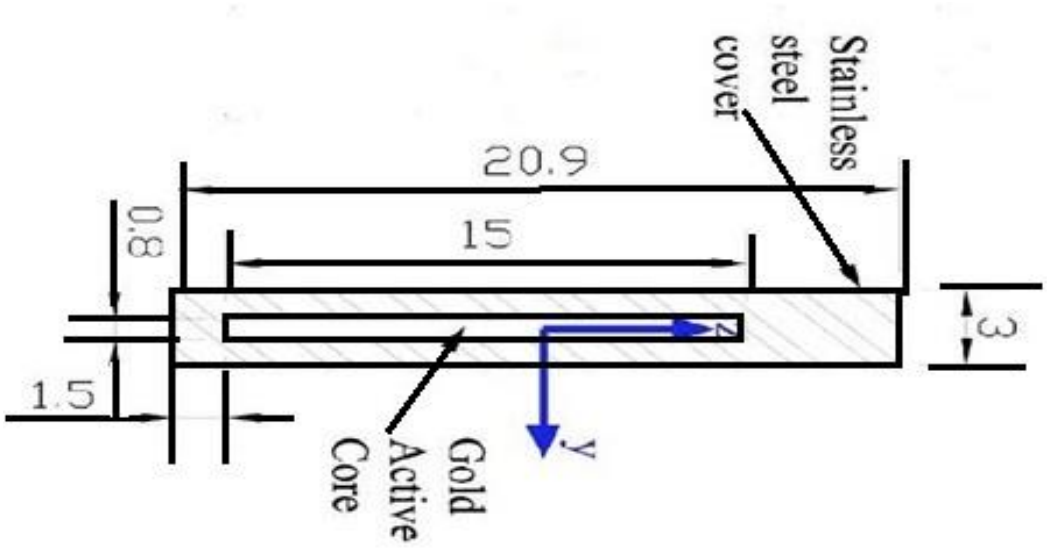

Fig. 3.2 Schematic view of the RTR ^{137}Cs brachytherapy source. All dimensions are in mm (Adapted from Perez-Calatayud et al 2005).

^{192}Ir source

The geometric design and dimensions of the MicroSelectron HDR ^{192}Ir source are shown schematically in Fig. 3.3 (Daskalov et al 1998).

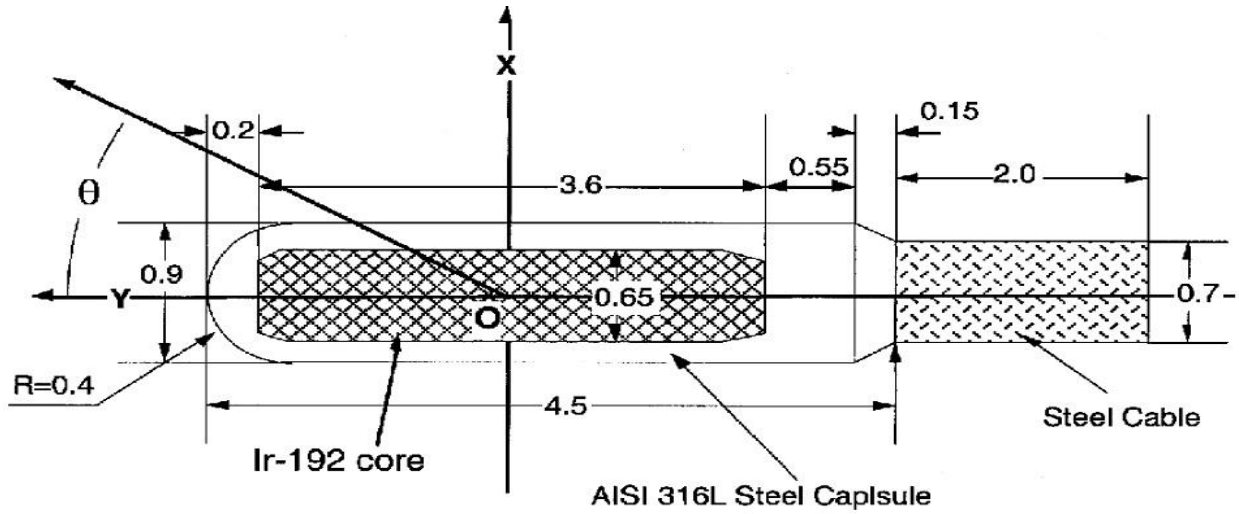

Fig. 3.3 Schematic design of MicroSelectron HDR ^{192}Ir brachytherapy source (Adapted from Daskalov et al 1998).

The source consists of a pure iridium metal (density 22.42 g/cm^3) cylinder of 0.65 mm diameter and 3.6 mm long within which the radioactive ^{192}Ir is uniformly distributed. The source core has rounded edges, allowing the capsule thickness at the distal source tip of 0.20 mm. The outer capsule diameter, the maximum capsule length, and the maximum rigid length (including cable-to-capsule welding) are 0.90, 4.50, and 4.95 mm, respectively. The source capsule is welded to a 200 mm long woven steel cable with a diameter of 0.70 mm. The remaining cable length (approximately 1305 mm) has a cross-sectional diameter equal to that of the capsule 0.90 mm.

^{169}Yb source

A graphical depiction of the HDR 4140 is presented in Fig. 3.4 (Medich et al 2006). The source consists of Ytterbium oxide (density 6.9 mg/mm^3) cylinder of 0.73 mm diameter and 3.6 mm length. The outer stainless steel encapsulation (density 7.8 mg/mm^3) capsule outer diameter, inner diameter and length are 0.90, 0.73, and 4.8 mm, respectively. The source capsule has 0.5 mm thick hemispherical welded end and 0.75 mm thick solid plug. The stainless steel actual cable length is 2100 mm with an outer diameter of 0.9 mm.

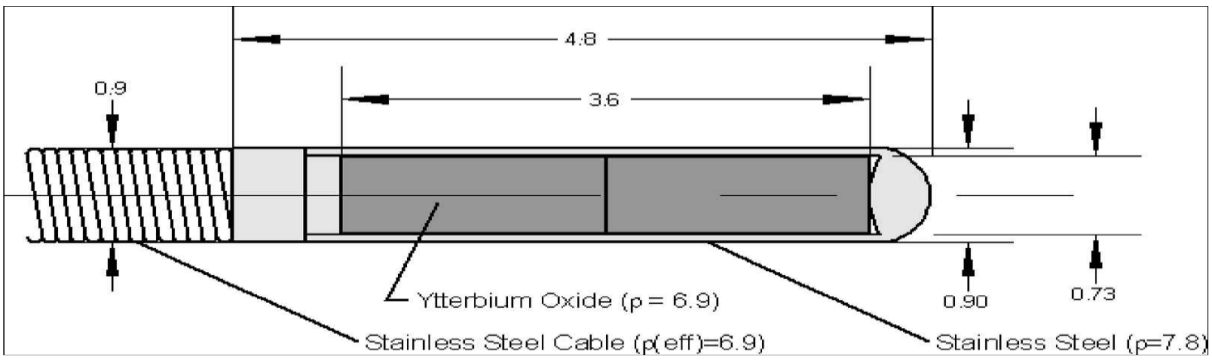

Fig.3.4 Schematic design of the model HDR 4140 ^{169}Yb HDR brachytherapy source (Adapted from Medich et al 2006).

3.3.2 Low energy brachytherapy sources

Low energy photon emitting brachytherapy sources are being used with increasing frequency for interstitial implants in tumors, especially prostate and breast (Crook 2011, Keller et al 2005, Beaulieu et al 2012). Permanent implantation of ^{125}I and ^{103}Pd brachytherapy seeds has become an accepted and well-documented method for the treatment of prostate cancer (Peter et al 2001, Kent et al 2003). Another shorter half-life radioisotope ^{131}Cs is now a days commonly used in prostate brachytherapy as well as for treatment of tumors in the breast, head and neck, lung, and pancreas.

^{125}I source

The SelectSeed source dimensions and structural details are presented in Fig. 3.5 (Karaiskos et al 2001). The active element consists of a cylindrical silver rod (density 10.5 g/cm^3) that is 3.4 mm long and 0.51 mm in diameter. Its edges are free of bur and it is coated with a radioactive silver halide layer (AgCl/AgI/Ag^{125}I) of 3 μm thickness. This active silver core is encapsulated in a hollow titanium tube (density 4.51 g/cm^3) that is 4.5 mm long and 0.8mm in external diameter with a thickness equal to 50 μm. Laser welding, using hemispherical shaped end welds of radius 0.4 mm, seals the tube.

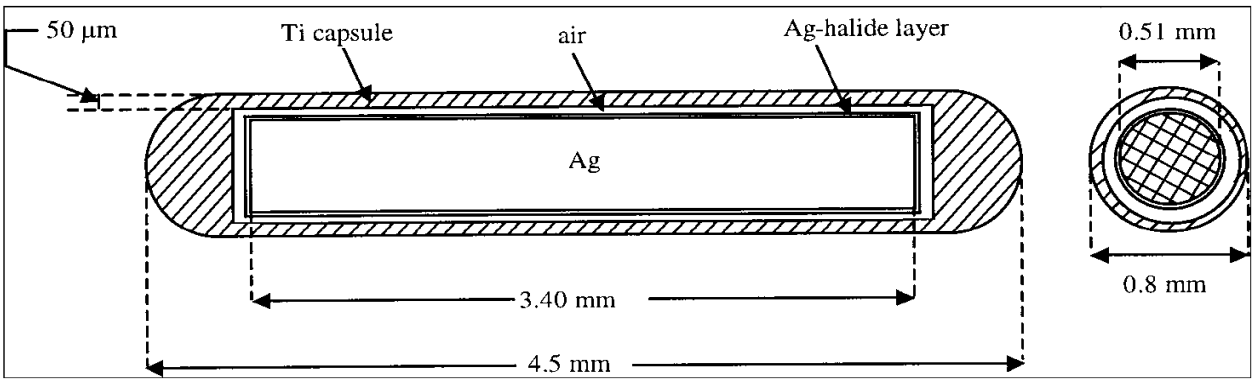

Fig. 3.5 Schematic diagram of the SelectSeed ^{125}I interstitial brachytherapy seed source design (Adapted from Karaiskos et al 2001).

^{131}Cs source

The CS-1 source dimensions are presented in Fig. 3.6 (Rivard et al 2007). It consists of a gold (density of 19.3 g/cm^3) marker that is a 4.0 mm long cylindrical rod with a 0.125 mm radius. The gold marker is housed in a Pyrex/ceramic (density of 2.4 g/cm^3) tube whose inner side is coated with ^{131}Cs. The housing has an inner radius of 0.20 mm (0.15 mm with coating) and an outer radius of 0.31 mm with a length of 4.0 mm. This housing is placed in a Ti (density of 4.54 g/cm^3) capsule with an inner radius of 0.355 mm, an outer radius of 0.415 mm and an outer length of 4.52 mm with an end weld thickness of 0.1 mm. The void within the capsule is filled with argon. The overall source length is 4.52 mm and the active length is 4 mm.

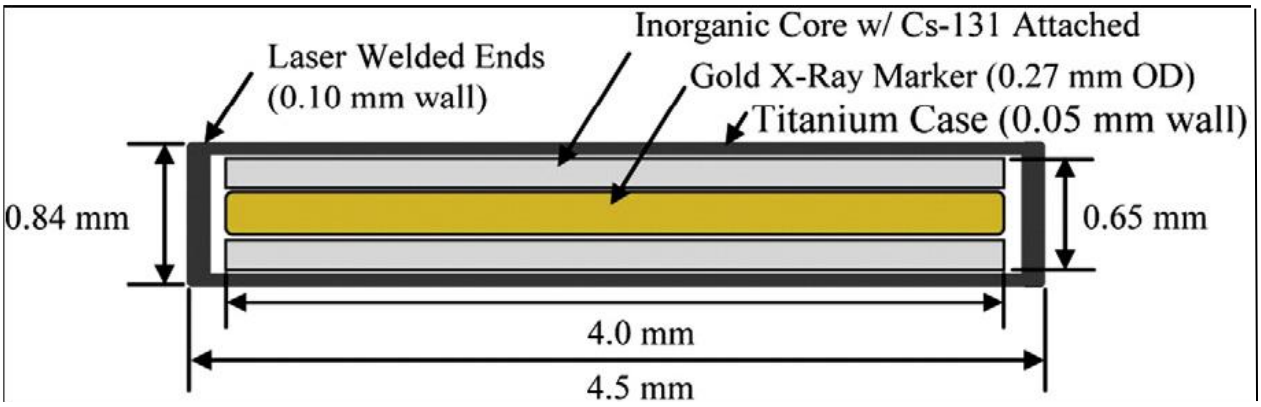

Fig. 3.6 Schematic diagram of ^{131}Cs brachytherapy source (Adapted from Rivard et al 2007).

^{103}Pd source

Fig.3.7 shows the geometry of the IRA ^{103}Pd source (Sadeghi et al 2008). The source capsule consists of a 0.05 mm thick titanium capsule (density =4.54 g/cm^3) with an external length and diameter of 4.8 and 0.8 mm, respectively. This source has an effective active length of 3 mm. The end caps, which were laser welded on the wall of the capsule, have an average thickness of 0.9 mm along the seed longitudinal axis and 0.7 and 0.8 mm inner and

outer diameters, respectively. The source consists of a cylindrical silver core (density =10.5 g/cm^3) 3 mm long, 0.5 mm diameter, onto which a 0.5 nm layer of ^{103}Pd has been uniformly adsorbed.

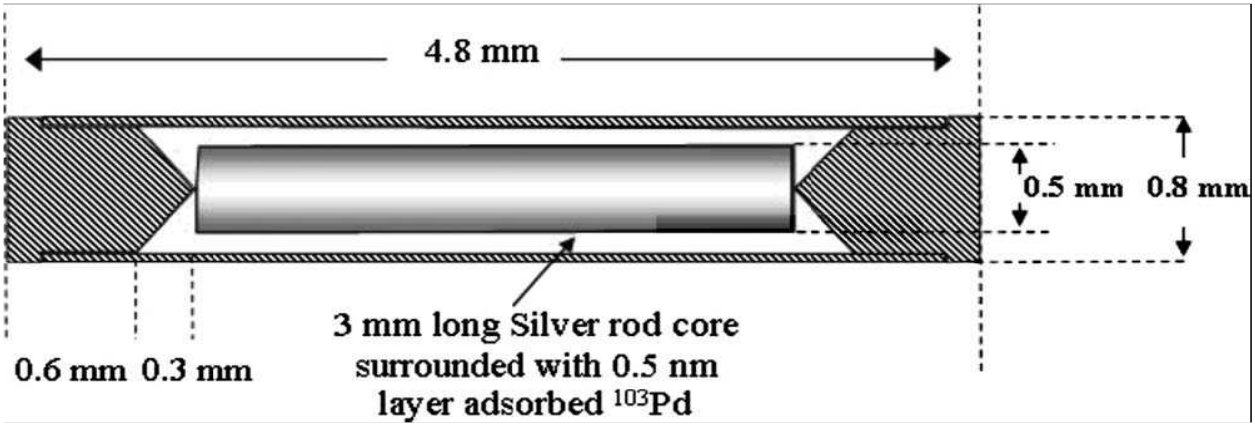

Fig. 3.7 Schematic diagram of IRA ^{103}Pd source (Adapted from Sadeghi et al 2008).

The sources such as BEBIG ^{60}Co, Microselectron ^{192}Ir, 4140 ^{169}Yb and SelectSeed ^{125}I which have a rounded tip at the end could not be simulated in DOSRZnrc code exactly. For these sources the rounded end was approximated as flat end. The details of the investigated brachytherapy sources are presented in Table 3.1.

Table 3.1 Details of the investigated brachytherapy sources.

Source	Manufacturer	Model	Type	Half-life	Average energy(MeV)
^{60}Co	Eckert & Ziegler, BEBIG GmbH, Germany	Co0.A86	HDR	5.26 years	1.2500
^{137}Cs	Radiation Therapy Resources, USA	RTR	LDR	30 years	0.6620
^{192}Ir	Nucletron, Netherland	Micro-Selectron	HDR	74 days	0.3800
^{169}Yb	Implant Science Corporation	4140	HDR	32 days	0.0930
^{131}Cs	IsoRay Medical Inc, USA	CS-1	LDR	9.7 days	0.0273
^{125}I	Isotron, Isotopentechnik GmbH, Berlin, Germany	SelectSeed	LDR	60 days	0.0284
^{103}Pd	IsoAid, Port Richey, FL, USA	IRA1	LDR	17 days	0.0207

3.4 Detectors investigated

Various solid-state detectors considered in this work were diamond, LiF, $Li_2B_4O_7$, Al_2O_3, Plastic Scintillator, Lithium Formate and various radiochromic films. The composition, Z_{eff} (effective atomic number), $\langle Z/A \rangle$ (represents electron density) and ρ (mass density) of these solid-state detectors are listed in Table 3.2 as below:

Table 3.2 Elemental composition, mass fraction, mass density ρ, electron density $\langle Z/A \rangle$ and effective atomic number (Z_{eff}) of the investigated solid-state detectors LiF, $Li_2B_4O_7$, Al_2O_3, diamond, Plastic Scintillator and Lithium Formate.

	Composition (weight fraction)									
Material	H	Li	B	C	O	F	Al	Z_{eff}	$\langle Z/A \rangle$ (mol/g)	ρ (g/cm^3)
Diamond	--	--	--	1.0	--		--	6	0.496	3.5
LiF	--	0.268	--	--	--	0.732	--	8.27	0.462	2.635
$Li_2B_4O_7$	--	0.082	0.257	--	0.661	--	--	7.4	0.485	2.44
Al_2O_3	--	--	--	--	0.471	--	0.529	10.2	0.491	3.97
Plastic Scintillator	0.085	--	--	0.915	--	--	--	5.67	0.541	1.032
Lithium Formate	0.0432	0.0992	--	0.1716	0.6859	--	--	7.23	0.514	1.48

The radiochromic film models included in the present study are HS (Devic et al 2004, 2006), EBT (Sutherland and Rogers 2010), EBT2 (lot 031109) (Sutherland and Rogers 2010), RTQA (Butson et al 2007), EBT2 (lot 020609) (Sutherland and Rogers 2010), XRT (Devic et al 2004, 2006) and XRQA (Ebert et al 2009). The above films were listed in order of their increasing atomic number (Z). The composition and structural details of these investigated films were taken from the published studies. The composition and values of Z_{eff}, $\langle Z/A \rangle$ and ρ of these radiochromic films are presented in Table 3.3. Table 3.4 presents the structural details of the investigated radiochromic films.

Table 3.3 Elemental composition, mass fraction, mass density ρ, electron density $< Z/A >$ and effective atomic number (Z_{eff}) of the investigated radiochromic films.

	Composition (weight fraction)											
Material	H	C	N	O	Li	Cl	K	Br	Cs	Z_{eff}	<Z/A> (mol/g)	ρ (g/cm^3)
Polyster	0.042	0.625	--	0.333	--	--	--	--	--	6.64	0.52	1.35
Adhesive	0.094	0.656	--	0.249	--	--	--	--	--	6.26	0.546	1.2
Surface	0.065	0.323	0.216	0.205	0.023	0.168	--	--	--	9.9	0.527	1.2
	Composition of active layers											
EBT	0.094	0.574	0.132	0.164	0.008	0.029	--	--	--	7.06	0.545	1.1
EBT2 (lot 020609)	0.096	0.578	0.002	0.278	0.009	0.017	0.006	0.013	--	9.17	0.538	1.2
EBT2 (lot 031109)	0.095	0.597	0.002	0.261	0.009	0.023	0.013	--	--	7.44	0.539	1.2
RTQA	0.091	0.537	0.127	0.142	0.019	0.084	--	--	--	8.28	0.541	1.1
XRT	0.078	0.462	0.115	0.143	--	--	--	0.076	0.126	26.59	0.523	1.75
HS	0.090	0.570	0.160	0.180	--	--	--	--	--	6.28	0.544	1.08
XRQA	0.064	0.381	0.055	0.138	0.040	--	--	0.134	0.223	34.52	0.501	1.2

Table 3.4 Structural details of investigated radiochromic films. All the dimensions are in μm.

	EBT	EBT2	RTQA	XRT	HS	XRQA
Polyster	97	50	97	97	97	97
Adhesive	--	25	12	--	--	--
Active	17	--	--	30	40	25
Surface	6	5	3	--	--	10
Active	17	30	17	--	--	25
Polyster	97	175	97	97	97	97

3.5 Solid phantoms investigated

The solid phantoms investigated in this study are PMMA, polystyrene, solid water, virtual water, RW1, RW3, plastic water, plastic water (LR), A150 and WE210. Table 3.5 presents the composition and values of Z_{eff}, $<Z/A>$ and ρ of the above investigated phantoms including water. The compositions of these solid phantoms were taken from the published

studies. The atomic composition and density details of RW1 and virtual water phantoms were taken from the published studies (Reniers et al 2004, Murphy et al 2004). The data on the remaining phantoms were taken from a study by Seco et al (2006).

Table 3.5 Elemental composition, mass fraction, mass density ρ, electron density < Z/A > and effective atomic number (Z_{eff}) of water and the investigated solid phantoms.

	Element	Z	A	Water	Solid water	A150	WE210	RW3	RW1	Plastic Water (LR)	Plastic Water	Virtual Water	PMMA	Polystyrene
Composition and mass fraction	H	1	1.008	0.1119	0.081	0.1013	0.0821	0.0759	0.132	0.0791	0.0930	0.077	0.08054	0.07742
	C	6	12.01		0.672	0.7755	0.6633	0.9041	0.794	0.5362	0.6282	0.687	0.59985	0.92258
	N	7	14.01		0.024	0.0351	0.0221			0.0174	0.0100	0.023		
	O	8	15.99	0.8881	0.199	0.0523	0.2065		0.038	0.2721	0.1794	0.189	0.31961	
	F	9	18.998			0.0140		0.008						
	Mg	12	24.31						0.009	0.0929				
	Cl	17	35.46		0.001		0.004		0.027	0.0023	0.0096	0.001		
	Ti	22	47.87											
	Ca	20	40.08		0.023	0.1840	0.022	0.012			0.0795	0.023		
	Br	35	79.9								0.0003			
ρ (g/cm^3)				1	1.036	1.127	1.006	1.045	0.97	1.029	1.013	1.03	1.19	1.06
< Z/A > (mol/g)				0.555	0.54	0.547	0.540	0.536	0.565	0.538	0.545	0.538	0.539	0.538
Z_{eff}				7.4	7.38	10.92	7.42	6.47	6.62	8.56	9.37	7.38	6.47	5.7

3.6 Monte Carlo calculations

The values of $\bar{E}_{fl}$ and $\bar{E}_{k}$ were calculated using FLURZnrc user-code of EGSnrc code system (Kawrakow et al 2010). In the Monte Carlo calculations of $\bar{E}_{fl}$, the photon fluence spectrum was scored in 0.2 mm thick and 0.5 mm high cylindrical shells, along the

transverse axis of the sources (distances, 1 cm–15 cm) in a 20 cm radius and 40 cm hight cylindrical water phantom. For the Monte Carlo calculation of $\bar{E}_k$, the fluence spectrum was calculated as above at a distance of 10 cm from the brachytherapy sources. The fluence spectrum was then converted to collision kerma to detector by using the mass-energy absorption coefficients of detectors.

For generating the PEGS4 dataset needed for the Monte Carlo calculations, AE = 0.521 MeV (kinetic energy of the electron is 0.01 MeV) and AP = 0.01 MeV was set for high energy brachytherapy sources (^{169}Yb, ^{137}Cs, ^{192}Ir and ^{60}Co) and AE = 0.512 MeV and AP = 0.001 MeV was set for low energy brachytherapy sources (^{131}Cs, ^{125}I and ^{103}Pd), where the parameters AE and AP were the low-energy thresholds for the production of knock-on electrons and secondary bremsstrahlung photons, respectively. The photon transport cut off energy PCUT was chosen 10 keV for high energy brachytherapy sources and 1 keV for low energy brachytherapy sources in the Monte Carlo calculations. Similarly, ECUT was set 0.521 MeV (10 keV kinetic energy) for high energy brachytherapy sources and 0.512 MeV for low energy brachytherapy sources. Up to 10^8 photon histories were simulated. The 1σ statistical uncertainties on the calculated FLURZnrc-based collision kerma values were less than 0.2 %.

3.7 Fluence-weighted mean energies of photons for brachytherapy sources

The Monte Carlo-calculated $\bar{E}_{fl}$ values were presented in Table 3.6 - 3.9 for high energy brachytherapy sources ^{60}Co, ^{137}Cs, ^{192}Ir and ^{169}Yb, respectively.

Table 3.6 Monte Carlo-calculated fluenc-weighted mean energies *of photons, $\bar{E}_{fl}$ (MeV) as a function of distance along the transverse axis of the ^{60}Co brachytherapy source in different phantoms including water.*

Distance, *r* (cm)	Water	PMMA	Polystyrene	Plastic water	RW1	RW3	Virtual water	Solid water	A150	WE210
1	1.149	1.134	1.146	1.152	1.151	1.149	1.150	1.149	1.140	1.152
2	1.057	1.026	1.049	1.063	1.061	1.056	1.058	1.058	1.036	1.061
3	0.972	0.927	0.958	0.982	0.974	0.969	0.973	0.972	0.943	0.980
4	0.896	0.842	0.877	0.913	0.900	0.891	0.899	0.897	0.861	0.905
5	0.832	0.770	0.807	0.851	0.831	0.824	0.835	0.830	0.792	0.841
6	0.774	0.709	0.746	0.796	0.774	0.766	0.778	0.776	0.731	0.785
7	0.723	0.656	0.693	0.751	0.726	0.715	0.728	0.726	0.681	0.735
8	0.682	0.612	0.649	0.712	0.683	0.672	0.687	0.684	0.637	0.694
9	0.644	0.575	0.608	0.678	0.646	0.636	0.650	0.648	0.602	0.659
10	0.612	0.546	0.576	0.648	0.614	0.603	0.620	0.615	0.569	0.626
11	0.585	0.517	0.550	0.623	0.587	0.577	0.594	0.589	0.543	0.599
12	0.563	0.495	0.528	0.603	0.564	0.556	0.571	0.567	0.522	0.578
13	0.547	0.477	0.511	0.585	0.548	0.539	0.555	0.549	0.503	0.559
14	0.532	0.462	0.498	0.573	0.533	0.523	0.542	0.534	0.490	0.547
15	0.520	0.455	0.486	0.562	0.523	0.512	0.530	0.524	0.481	0.536

Table 3.7 Monte Carlo-calculated fluenc-weighted mean energies, *$\bar{E}_{fl}$ (MeV) as a function of distance along the transverse axis of the ^{137}Cs brachytherapy source in different phantoms including water.*

Distance, *r* (cm)	Water	PMMA	Polystyrene	Plastic water	RW1	RW3	Virtual water	Solid water	A150	WE210
1	0.566	0.557	0.563	0.568	0.567	0.566	0.567	0.566	0.559	0.568
2	0.516	0.499	0.510	0.521	0.517	0.514	0.517	0.516	0.505	0.519
3	0.471	0.449	0.462	0.480	0.472	0.469	0.473	0.472	0.457	0.475
4	0.433	0.407	0.421	0.445	0.435	0.430	0.436	0.433	0.416	0.439
5	0.401	0.371	0.387	0.414	0.401	0.398	0.404	0.402	0.383	0.407
6	0.374	0.342	0.358	0.390	0.374	0.370	0.375	0.375	0.355	0.380
7	0.351	0.318	0.334	0.369	0.351	0.347	0.353	0.351	0.331	0.357
8	0.332	0.299	0.313	0.351	0.330	0.326	0.334	0.333	0.311	0.338
9	0.315	0.282	0.295	0.334	0.315	0.311	0.318	0.316	0.295	0.322
10	0.302	0.267	0.281	0.322	0.300	0.296	0.304	0.302	0.281	0.307
11	0.289	0.256	0.267	0.311	0.288	0.284	0.292	0.291	0.269	0.296
12	0.279	0.246	0.258	0.302	0.277	0.274	0.282	0.281	0.260	0.286
13	2.714	0.239	0.249	0.295	0.269	0.266	0.275	0.273	0.251	0.277
14	0.265	0.232	0.243	0.289	0.264	0.259	0.269	0.268	0.246	0.271
15	0.260	0.228	0.239	0.285	0.259	0.255	0.263	0.264	0.242	0.268

Table 3.8 Monte Carlo-calculated fluence-weighted mean energies *of photons, $\bar{E}_{fl}$ (MeV) as a function of distance along the transverse axis of the ^{192}Ir brachytherapy source in different phantoms including water.*

Distance, *r* (cm)	Water	PMMA	Polystyrene	Plastic water	RW1	RW3	Virtual water	Solid water	A150	WE210
1	0.325	0.320	0.324	0.327	0.325	0.324	0.325	0.325	0.321	0.326
2	0.295	0.285	0.292	0.299	0.295	0.294	0.296	0.294	0.288	0.296
3	0.270	0.257	0.265	0.276	0.270	0.269	0.271	0.270	0.262	0.272
4	0.249	0.234	0.242	0.258	0.270	0.247	0.250	0.250	0.240	0.252
5	0.233	0.216	0.223	0.242	0.232	0.229	0.233	0.233	0.223	0.235
6	0.218	0.200	0.208	0.230	0.217	0.215	0.220	0.219	0.208	0.221
7	0.206	0.188	0.195	0.220	0.205	0.203	0.208	0.207	0.196	0.210
8	0.197	0.178	0.184	0.210	0.195	0.193	0.198	0.197	0.186	0.200
9	0.189	0.169	0.175	0.203	0.187	0.185	0.190	0.189	0.178	0.192
10	0.182	0.162	0.168	0.196	0.179	0.177	0.184	0.183	0.171	0.186
11	0.175	0.156	0.161	0.192	0.173	0.171	0.178	0.176	0.165	0.179
12	0.170	0.152	0.156	0.186	0.168	0.166	0.172	0.172	0.160	0.174
13	0.166	0.147	0.152	0.183	0.164	0.162	0.169	0.168	0.156	0.171
14	0.163	0.145	0.148	0.180	0.161	0.159	0.165	0.165	0.153	0.167
15	0.161	0.142	0.147	0.178	0.159	0.156	0.163	0.163	0.151	0.165

Table 3.9 Monte Carlo-calculated fluence-weighted mean energies *of photons, $\bar{E}_{fl}$ (MeV) as a function of distance along the transverse axis of the ^{169}Yb brachytherapy source in different phantoms including water.*

Distance, *r* (cm)	Water	PMMA	Polystyrene	Plastic water	RW1	RW3	Virtual water	Solid water	A150	WE210
1	0.103	0.101	0.102	0.106	0.103	0.103	0.103	0.103	0.102	0.104
2	0.097	0.094	0.094	0.103	0.097	0.097	0.098	0.098	0.096	0.098
3	0.093	0.089	0.089	0.102	0.093	0.093	0.095	0.095	0.092	0.095
4	0.091	0.086	0.085	0.101	0.089	0.090	0.092	0.092	0.089	0.092
5	0.088	0.083	0.082	0.101	0.087	0.087	0.090	0.090	0.087	0.090
6	0.087	0.081	0.079	0.101	0.085	0.085	0.089	0.089	0.085	0.089
7	0.086	0.079	0.077	0.101	0.084	0.084	0.088	0.088	0.084	0.088
8	0.085	0.078	0.075	0.101	0.083	0.083	0.087	0.087	0.083	0.087
9	0.084	0.077	0.074	0.101	0.081	0.082	0.086	0.086	0.082	0.087
10	0.083	0.076	0.073	0.101	0.081	0.081	0.086	0.086	0.081	0.086
11	0.083	0.075	0.072	0.101	0.080	0.080	0.085	0.085	0.081	0.086
12	0.082	0.075	0.071	0.101	0.080	0.080	0.085	0.085	0.081	0.086
13	0.082	0.074	0.070	0.102	0.079	0.079	0.085	0.085	0.081	0.085
14	0.082	0.074	0.070	0.102	0.079	0.079	0.085	0.085	0.080	0.085
15	0.082	0.074	0.069	0.103	0.079	0.079	0.085	0.085	0.080	0.085

It is observed that, for high energy brachytherapy sources (^{60}Co, ^{137}Cs, ^{192}Ir and ^{169}Yb) the value of $\bar{E}_{fl}$ decresases as a function of *r* in various phantoms. $\bar{E}_{fl}$ decreases with distance due to degradation in the photon energy after scattering. The degree of decrease depends on the type of the phantom as well as the type of source. For the ^{60}Co source, the decrease in $\bar{E}_{fl}$ is higher in PMMA, polystyrene and A150 phantom as compared to other phantoms. For example, $\bar{E}_{fl}$ decreases from 1.134 MeV to 455 keV in PMMA, from 1.146 MeV to 486 keV in polystyrene and from 1.140 MeV to 481 keV in A150 phantom when the distance is increased from 1 cm to 15 cm. For phantoms such as water, RW1, RW3 and solid water, $\bar{E}_{fl}$ decreases from about 1.15 MeV to 520 keV in the above distance range. For the virtual water and WE210 phantoms, $\bar{E}_{fl}$ decreases from about 1.150 MeV to 530 keV and in case of plastic water from 1.152 MeV to 562 keV in the above distance range.

For ^{137}Cs source, the phantoms such as water, virtual water, RW1 and solid water, $\bar{E}_{fl}$ decreases from about 565 keV to 260 keV when the distance is increased from 1 cm to 15 cm. In the case of plastic water phantom, $\bar{E}_{fl}$ decreases from 570 keV to 285 keV in the above distance range. The values of $\bar{E}_{fl}$ at 15 cm are 228 keV and 239 keV, respectively, for PMMA and polystyrene phantoms. For ^{192}Ir source, decrease in $\bar{E}_{fl}$ is higher for PMMA, A150 and polystyrene phantoms as compared to other phantoms. $\bar{E}_{fl}$ decreases from about 320 keV to 140 keV when the distance is increased from 1 cm to 15 cm. For phantoms such as water, WE210, virtual water, and solid water, $\bar{E}_{fl}$ decreases from about 325 keV to 160keV in the above distance range. For RW1 and RW3 phantoms, $\bar{E}_{fl}$ decreases from

about 325 keV to 156 keV in the above distance range. For plastic water phantom, $\overline{E}_{fl}$ decreases from 327 keV to 178 keV when the distance is increased from 1 cm to 15 cm.

For ^{169}Yb source, decrease in $\overline{E}_{fl}$ is higher for PMMA and polystyrene phantoms as compared to other phantoms. $\overline{E}_{fl}$ decreases from about 106 keV to 70 keV when the distance is increased from 1 cm to 15 cm. For phantoms such as water, WE210, virtual water, and solid water, $\overline{E}_{fl}$ decreases from about 107 keV to 85 keV in the above distance range. For RW1 and RW3 phantoms, $\overline{E}_{fl}$ decreases from about 107 keV to 79 keV in the above distance range. In case of plastic water phantom, $\overline{E}_{fl}$ decreases from 108 keV to 103 keV when the distance is increased from 1 cm to 15 cm.

For low energy brachytherapy sources such as ^{131}Cs, ^{125}I and ^{103}Pd, it was found that, $\overline{E}_{fl}$ values did not vary significantly with distance for any of the investigated sources and solid phantoms. Table 3.10 presents the Monte Carlo-calculated values of $\overline{E}_{fl}$ as a function of distance, r for ^{131}Cs, ^{125}I and ^{103}Pd brachytherapy sources for all the investigated solid phantoms. The maximum change in $\overline{E}_{fl}$ values was observed only in PMMA and polystyrene phantoms compared to remaining investigated phantoms. For example, the change in $\overline{E}_{fl}$ values at a distance of 1 cm to that of 5 cm in PMMA phantom were about 4 %, 3 % and 2 % for ^{131}Cs, ^{125}I and ^{103}Pd sources, respectively. Similarly, for polystyrene phantom, the change in $\overline{E}_{fl}$ values were about 6 %, 4 % and 3 % for ^{131}Cs, ^{125}I and ^{103}Pd sources, respectively at a distance of 1 cm to that of 5 cm.

Table 3.10 fluence-weighted mean energies *of photons, $\overline{E}_{fl}$ (MeV) presented for different solid phantoms including water as a function of distance along the transverse axis of the investigated low energy brachytherapy sources ^{131}Cs, ^{125}I and ^{103}Pd.*

Source	distance (cm)	water	Solid water	A150	WE210	RW3	RW1	Virtual water	PMMA	Polystyrene
^{131}Cs	0.5	0.0300	0.0301	0.0300	0.0300	0.0300	0.0300	0.0300	0.0300	0.0299
	1	0.0300	0.0300	0.0300	0.0300	0.0300	0.0300	0.0300	0.0299	0.0296
	2	0.0294	0.0299	0.0294	0.0294	0.0294	0.0294	0.0294	0.0293	0.0291
	3	0.0292	0.0300	0.0292	0.0292	0.0292	0.0292	0.0292	0.0290	0.0287
	4	0.0291	0.0291	0.0291	0.0291	0.0291	0.0291	0.0291	0.0288	0.0284
	5	0.0290	0.0290	0.0290	0.0290	0.0290	0.0290	0.0290	0.0287	0.0282
^{125}I	0.5	0.0278	0.0280	0.0278	0.0280	0.0279	0.0280	0.0280	0.0278	0.0277
	1	0.0277	0.0280	0.0278	0.0280	0.0279	0.0279	0.0280	0.0276	0.0275
	2	0.0275	0.0278	0.0276	0.0278	0.0280	0.0279	0.0277	0.0274	0.0271
	3	0.0275	0.0278	0.0276	0.0277	0.0278	0.0278	0.0278	0.0273	0.0269
	4	0.0275	0.0278	0.0276	0.0277	0.0278	0.0278	0.0278	0.0272	0.0267
	5	0.0275	0.0278	0.0276	0.0278	0.0278	0.0278	0.0278	0.0272	0.0266
^{103}Pd	0.5	0.0210	0.0212	0.0210	0.0212	0.0211	0.0211	0.0212	0.0209	0.0206
	1	0.0210	0.0212	0.0210	0.0211	0.0210	0.0211	0.0212	0.0207	0.0204
	2	0.0208	0.0210	0.0208	0.0210	0.0210	0.0210	0.0210	0.0206	0.0202
	3	0.0207	0.0209	0.0208	0.0210	0.0209	0.0210	0.0210	0.0205	0.0201
	4	0.0207	0.0209	0.0208	0.0210	0.0209	0.0210	0.0209	0.0205	0.0200
	5	0.0207	0.0209	0.0208	0.0210	0.0209	0.0208	0.0209	0.0204	0.0199

An analysis of XCOM (Berger and Hubbell 1987) data shows that the interaction mechanisms at 27 keV photons in water are 46.4% Photoelectric absorption, 41 % Compton scattering and 12.6 % coherent scattering. The predominant primary gamma lines involved in the present study for the low energy brachytherapy sources are 33 keV (^{131}Cs), 27 keV (^{125}I) and 20 keV (^{103}Pd). At these energies, even after multiple Compton scattering in water phantom as well as with solid phantoms, the energy of the scattered photons does not change significantly. For example, a photon of energy 30 keV, after consecutive three Compton scatterings, each scattering through a polar angle of 180^0, would result in a

scattered photon of energy only about 24 keV. Hence, the mean energies of the brachytherapy sources do not change significantly with depth (see Table 3.10).

3.8 Detector-kerma weighted mean energies of photons for brachytherapy sources

The Monte Carlo-calculated detector kerma weighted mean energies of photons, $\overline{E}_k$ were presented in Table 3.11 - 3.14 for high energy brachytherapy sources ^{60}Co, ^{137}Cs, ^{192}Ir and ^{169}Yb, respectively.

Table 3.11 Monte Carlo-calculated detector-kerma weighted mean energies of photons, $\overline{E}_k$ (MeV) of different detectors for ^{60}Co brachytherapy source in different phantoms including water.

Detector Type		Water	PMMA	Polystyrene	Plastic water	RW1	RW3	Virtual water	Solid water	A150	WE210
Solid-state	water	1.0235	0.9878	1.0097	1.0317	1.0246	1.0193	1.0249	1.0227	1.0001	1.0287
	diamond	1.0303	0.9989	1.0206	1.0360	1.0319	1.0270	1.0312	1.0292	1.0086	1.0348
	Al_2O_3	0.9856	0.9285	0.9513	1.0079	0.9844	0.9771	0.9896	0.9870	0.9535	0.9948
	$Li_2B_4O_7$	1.0245	0.9895	1.0114	1.0324	1.0257	1.0205	1.0259	1.0237	1.0014	1.0296
	LiF	1.0182	0.9793	1.0013	1.0284	1.0189	1.0134	1.0200	1.0178	0.9935	1.0240
	Platic Scintillator	1.0311	1.0002	1.0220	1.0365	1.0328	1.0279	1.0320	1.0300	1.0097	1.0355
	Lithium Formate	1.0246	0.9895	1.0114	1.0324	1.0257	1.0205	1.0259	1.0238	1.0014	1.0296
Radio-chromic Films	EBT	1.0238	0.9884	1.0104	1.0319	1.0250	1.0198	1.0252	1.0231	1.0005	1.0290
	EBT2 (lot 020609)	1.0046	0.9595	0.9830	1.0193	1.0050	0.9990	1.0073	1.0049	0.9772	1.0118
	EBT2 (lot 031109)	1.0221	0.9857	1.0078	1.0309	1.0232	1.0179	1.0236	1.0215	0.9985	1.0275
	RTQA	1.0138	0.9726	0.9950	1.0257	1.0144	1.0087	1.0159	1.0137	0.9882	1.0201
	XRT	0.6767	0.5686	0.6072	0.7509	0.6727	0.6600	0.6891	0.6842	0.6168	0.7001
	HS	1.0289	0.9966	1.0184	1.0351	1.0304	1.0255	1.0300	1.0279	1.0069	1.0335
	XRQA	0.5465	0.4405	0.4753	0.6292	0.5418	0.5291	0.5599	0.5549	0.4875	0.5712

For the ^{60}Co source, the values of $\overline{E}_k$ for detectors such as water, $Li_2B_4O_7$, Lithium Formate, EBT, EBT2 (lot 031109) were comparable in water phantom. For a given phantom, detector $\overline{E}_k$ were higher in diamond and Plastic Scintillator detectors, and smaller for XRT and XRQA radiochromic films as compared to other investigated detectors. For example,

$\bar{E}_k$ values were 1.0303, 1.0311, 0.6767 and 0.5465 MeV for diamond, Plastic Scintillator, XRT and XRQA, respectively in water phantom. Among the solid-state detectors, Al_2O_3 detector showed smallest $\bar{E}_k$ values in all the investigated phantoms. $\bar{E}_k$ values were identical for $Li_2B_4O_7$ and Lithium Formate detectors for all the investigated phantoms.

Table 3.12 Monte Carlo-calculated detector-kerma weighted energies of photons, $\bar{E}_k$ (MeV) of different detectors for ^{137}Cs brachytherapy source in different phantoms including water.

Detector Type		Water	PMMA	Polystyrene	Plastic water	RW1	RW3	Virtual water	Solid water	A150	WE210
Solid-state	water	0.4899	0.4645	0.4768	0.4993	0.4899	0.4865	0.4914	0.4653	0.4748	0.4941
	diamond	0.4976	0.4765	0.4889	0.5040	0.4982	0.4952	0.4986	0.4712	0.4842	0.5010
	Al_2O_3	0.4501	0.4071	0.4185	0.4738	0.4476	0.4423	0.4540	0.4345	0.4277	0.4580
	$Li_2B_4O_7$	0.4911	0.4664	0.4787	0.5000	0.4912	0.4878	0.4925	0.4914	0.4762	0.4952
	LiF	0.4840	0.4557	0.4678	0.4956	0.4836	0.4799	0.4859	0.4847	0.4677	0.4888
	Platic Scintillator	0.4985	0.4779	0.4904	0.5046	0.4992	0.4962	0.4994	0.4984	0.4853	0.5018
	Lithium Formate	0.4911	0.4664	0.4787	0.5000	0.4912	0.4878	0.4925	0.4914	0.4762	0.4952
Radio-chromic Films	EBT	0.4902	0.4652	0.4776	0.4995	0.4903	0.4869	0.4917	0.4906	0.4752	0.4944
	EBT2 (lot 020609)	0.4693	0.4358	0.4486	0.4855	0.4684	0.4643	0.4721	0.4707	0.4509	0.4755
	EBT2 (lot 031109)	0.4883	0.4624	0.4747	0.4983	0.4883	0.4848	0.4900	0.4888	0.4730	0.4927
	RTQA	0.4792	0.4488	0.4611	0.4925	0.4786	0.4747	0.4814	0.4802	0.4621	0.4845
	XRT	0.2510	0.2063	0.2178	0.2927	0.2480	0.2427	0.2574	0.2555	0.2271	0.2625
	HS	0.4960	0.4740	0.4864	0.5031	0.4965	0.4934	0.4971	0.4960	0.4822	0.4996
	XRQA	0.2020	0.1647	0.1730	0.2408	0.1991	0.1947	0.2078	0.2062	0.1822	0.2121

For ^{137}Cs source, the values of $\bar{E}_k$ for detectors such as water, $Li_2B_4O_7$, Lithium Formate, EBT, were comparable in water phantom. For a given phantom, $\bar{E}_k$ were higher in diamond and Plastic Scintillator detectors, and smaller for XRT and XRQA radiochromic films as compared to other investigated detectors. For example, $\bar{E}_k$ values were 0.4976, 0.4985, 0.251 and 0.202 MeV for diamond, Plastic Scintillator, XRT and XRQA, respectively in water phantom. Among the solid-state detectors, Al_2O_3 detector showed smallest $\bar{E}_k$ values

in all the investigated phantoms. $\overline{E}_k$ values were identical for $Li_2B_4O_7$ and Lithium Formate detectors for all the investigated phantoms.

Table 3.13 Monte Carlo-calculated detector-kerma weighted mean energies of photons, $\overline{E}_k$ (MeV) of different detectors for ^{192}Ir brachytherapy source in different phantoms including water.

Detector Type		Water	PMMA	Polystyrene	Plastic water	RW1	RW3	Virtual water	Solid water	A150	WE210
Solid-state	water	0.2815	0.2615	0.2670	0.2939	0.2801	0.2783	0.2836	0.2828	0.2711	0.2854
	diamond	0.2911	0.2754	0.2817	0.2996	0.2906	0.2889	0.2925	0.2918	0.2822	0.2941
	Al_2O_3	0.2388	0.2067	0.2095	0.2654	0.2347	0.2322	0.2434	0.2422	0.2240	0.2460
	$Li_2B_4O_7$	0.2830	0.2636	0.2692	0.2948	0.2817	0.2799	0.2850	0.2842	0.2728	0.2868
	LiF	0.2745	0.2518	0.2568	0.2895	0.2726	0.2706	0.2772	0.2763	0.2632	0.2791
	Platic Scintillator	0.2923	0.2771	0.2835	0.3003	0.2918	0.2902	0.2936	0.2929	0.2836	0.2951
	Lithium Formate	0.2830	0.2636	0.2692	0.2948	0.2818	0.2799	0.2850	0.2842	0.2728	0.2868
Radio-chromic Films	EBT	0.2819	0.2623	0.2679	0.2940	0.2806	0.2788	0.2840	0.2832	0.2716	0.2858
	EBT2 (lot 020609)	0.2586	0.2325	0.2374	0.2779	0.2561	0.2538	0.2620	0.2609	0.2459	0.2642
	EBT2 (lot 031109)	0.2797	0.2591	0.2646	0.2926	0.2782	0.2763	0.2819	0.2811	0.2690	0.2837
	RTQA	0.2690	0.2447	0.2495	0.2858	0.2668	0.2647	0.2720	0.2710	0.2571	0.2740
	XRT	0.1300	0.1107	0.1126	0.1541	0.1272	0.1256	0.1336	0.1327	0.1208	0.1354
	HS	0.2891	0.2724	0.2785	0.2984	0.2884	0.2867	0.2907	0.2900	0.2799	0.2923
	XRQA	0.1141	0.0980	0.0990	0.1356	0.1116	0.1103	0.1173	0.1166	0.1066	0.1188

For ^{192}Ir source, the values of $\overline{E}_k$ for detectors such as water, $Li_2B_4O_7$, Lithium Formate, EBT, were comparable in water phantom. For a given phantom, the values of $\overline{E}_k$ are higher in diamond and Plastic Scintillator detectors, and smaller for XRT and XRQA radiochromic films as compared to other investigated detectors. For example, $\overline{E}_k$ values were 0.2911, 0.2923, 0.13 and 0.1141 MeV for diamond, Plastic Scintillator, XRT and XRQA, respectively in water phantom. Among the solid-state detectors, Al_2O_3 detector show

smallest $\overline{E}_k$ values in all the investigated phantoms. $\overline{E}_k$ values were identical for $Li_2B_4O_7$ and Lithium Formate detectors for all the investigated phantoms.

Table 3.14 Monte Carlo-calculated detector-kerma weighted mean energies of photons, $\overline{E}_k$ (MeV) of different detectors for ^{169}Yb brachytherapy source in different phantoms including water.

Detector Type		Water	PMMA	Polystyrene	Plastic water	RW1	RW3	Virtual water	Solid water	A150	WE210
Solid-state	water	0.1022	0.0890	0.0836	0.1280	0.0977	0.0972	0.1060	0.1059	0.0990	0.1065
	diamond	0.1177	0.1056	0.1014	0.1386	0.1141	0.1135	0.1209	0.1208	0.1147	0.1215
	Al_2O_3	0.0721	0.0620	0.0572	0.0981	0.0680	0.0678	0.0753	0.0752	0.0696	0.0757
	$Li_2B_4O_7$	0.1043	0.0911	0.0857	0.1295	0.0998	0.0993	0.1079	0.1079	0.1010	0.1085
	LiF	0.0943	0.0813	0.0757	0.1215	0.0896	0.0892	0.0981	0.0980	0.0911	0.0986
	Platic Scintillator	0.1201	0.1084	0.1045	0.1400	0.1167	0.1161	0.1232	0.1231	0.1172	0.1237
	Lithium Formate	0.1043	0.0911	0.0857	0.1295	0.0998	0.0993	0.1080	0.1079	0.1011	0.1085
Radio-chromic Films	EBT	0.1032	0.0901	0.0848	0.1285	0.0987	0.0982	0.1069	0.1068	0.1000	0.1074
	EBT2 (lot 020609)	0.0840	0.0727	0.0678	0.1104	0.0798	0.0795	0.0875	0.0874	0.0813	0.0879
	EBT2 (lot 031109)	0.1004	0.0873	0.0819	0.1263	0.0958	0.0953	0.1041	0.1040	0.0972	0.1046
	RTQA	0.0898	0.0773	0.0719	0.1171	0.0852	0.0848	0.0935	0.0934	0.0868	0.0940
	XRT	0.0606	0.0556	0.0527	0.0747	0.0583	0.0584	0.0623	0.0623	0.0596	0.0624
	HS	0.1139	0.1013	0.0967	0.1362	0.1100	0.1094	0.1173	0.1172	0.1108	0.1178
	XRQA	0.0592	0.0546	0.0517	0.0725	0.0571	0.0571	0.0608	0.0608	0.0583	0.0609

For ^{169}Yb source, the values of $\overline{E}_k$ for detectors such as water, $Li_2B_4O_7$, Lithium Formate, EBT, were comparable in water phantom. For a given phantom, $\overline{E}_k$ were higher in diamond and Plastic Scintillator detectors, and smaller for XRT and XRQA radiochromic films as compared to other investigated detectors. For example, $\overline{E}_k$ values were 0.1177, 0.1201, 0.0606 and 0.0592 MeV for diamond, Plastic Scintillator, XRT and XRQA, respectively in water phantom. Among the solid-state detectors, Al_2O_3 detector showed smallest $\overline{E}_k$ values (0.0721 in water phantom) in all the investigated phantoms. $\overline{E}_k$ values were identical for

$Li_2B_4O_7$ and Lithium Formate detectors for all the investigated phantoms. For low energy brachytherapy sources such as ^{131}Cs, ^{125}I and ^{103}Pd, it was found that, $\overline{E}_k$ values did not vary significantly with phantom type for any of the investigated detectors.

3.9 Summary and Conclusion

Fluence-weighted mean energies, $\overline{E}_{fl}$ and detector-kerma weighted mean energies, $\overline{E}_k$ were calculated for high energy (^{192}Ir, ^{60}Co, ^{137}Cs and ^{169}Yb) and low energy (^{131}Cs, ^{125}I and ^{103}Pd) brachytherapy sources in the different solid phantoms (PMMA, polystyrene, solid water, virtual water, RW1, RW3, plastic water, A150 and WE210) and water phantom by using the Monte Carlo-based FLURZnrc user-code of EGSnrc code system. It was observed that, for high energy brachytherapy sources (^{60}Co, ^{137}Cs, ^{192}Ir and ^{169}Yb), the values of $\overline{E}_{fl}$ decresases as a function of distance *r* in the above phantoms. For low energy brachytherapy sources such as ^{131}Cs, ^{125}I and ^{103}Pd, it was found that, $\overline{E}_{fl}$ values did not vary significantly with distance for any of the investigated sources and solid phantoms. $Li_2B_4O_7$ and Lithium Formate detectors showed identical $\overline{E}_k$ values for all the investigated phantom materials.

For a given phantom, $\overline{E}_k$ were higher in diamond and Plastic Scintillator detectors, and smaller for XRT and XRQA radiochromic films as compared to other investigated detectors. For low energy brachytherapy sources (^{131}Cs, ^{125}I and ^{103}Pd), $\overline{E}_k$ values did not vary significantly with phantom type for any of the investigated detectors.

CHAPTER 4

Beam quality corrections for brachytherapy sources

4.1 Introduction

Energy Dependence of detector

Energy dependence of radiation detectors is an important property for determination of absorbed dose. The overall energy dependence of a detector is composed of two parts. One is the intrinsic energy dependence and the other is absorbed dose energy dependence. Energy dependence of a detector is the product of intrinsic energy dependence, $k_{bq}(Q)$ and absorbed dose energy dependence, $f(Q)$ (DeWerd et al 2009, Rogers 2009, Sutherland and Rogers 2010).

Intrinsic Energy Dependence

The intrinsic energy dependence, $k_{bq}(Q)$, relates the reading of the detector to the dose to the sensitive volume of the detector (DeWerd et al 2009, Rogers 2009, Sutherland and Rogers 2010). Hence, it can be defined as the ratio of the dose to the sensitive volume of the detector at a given beam quality, $D_{det}(Q)$, to the meter reading of the detector at the same beam quality, $M_{det}(Q)$. i.e,

$$k_{bq}(Q) = D_{det}(Q) / M_{det}(Q) \qquad (4.1)$$

In principle, the intrinsic energy dependence k_{bq} could also be dependent on other factors such as dose, dose rate, temperature and pressure, direction etc. For ionisation chambers used in electron and photon beams, $k_{bq}(Q)$ is generally assumed to be constant (i.e., independent of beam quality Q) because the charge released is directly proportional to the dose to the gas via the quantity W/e, which is taken to be a constant. In case of a TLD detector, the intrinsic energy dependence describes the relationship between the TLD light output and the dose to TLD as a function of photon energy. General-purpose Monte Carlo codes that model radiation transport can be used to calculate the absorbed-dose energy dependence, but cannot be used to calculate the intrinsic energy dependence since the

thermo luminescence process itself is not modeled. Intrinsic energy dependence can be determined through measurements.

Absorbed-Dose Energy Dependence

The absorbed dose energy dependence relates the dose to the detector material to the dose to the medium at the point of measurement of the detector (DeWerd et al 2009, Rogers 2009, Sutherland and Rogers 2010). The absorbed-dose energy dependence *f(Q)* is also called as extrinsic energy dependence. It is the ratio of the dose to the medium at the point of measurement of the detector in the absence of the detector, $D_{\mathrm{med}}(Q)$, to the dose to the sensitive material of the detector,

$$D_{med}(Q) = f(Q) D_{\mathrm{det}}(Q) \qquad (4.2)$$

This factor encompasses the component specific and replacement perturbation effects as well as the absorbed dose energy dependence of the detection material. Absorbed dose energy dependence of the detectors can only be calculated using Monte Carlo methods for different detectors. The absorbed-dose energy dependence of a detector is a function of beam quality but can also be a function of dose, dose rate, and geometry of source and detector location etc.

Beam quality correction

In the present study absorbed dose energy dependence of a given detector at a given beam quality is addressed by beam quality correction, $k_{QQ_0}(r)$. It is the ratio of absorbed dose to the medium at the point of measurement and absorbed dose to the sensitive material of the detector obtained for the beam quality under consideration with respect to the reference radiation. The reference beam quality (Q_0) is generally the telecobalt radiotherapy beam.

$$k_{QQ_0}(r) = \frac{\left[D_{w,Q}(r) / D_{\det,Q}(r)\right]}{\left[D_{w,Q_0} / D_{\det,Q_0}\right]} \tag{4.3}$$

Here, $D_{w,Q}(r)$ and $D_{\det,Q}(r)$ are the absorbed dose to water and absorbed dose to detector in liquid water at a distance *r* along the transverse axis of the photon emitting brachytherapy source of beam quality *Q*, respectively. D_{w,Q_0} and $D_{\det,Q_0}$ are the absorbed dose to water and absorbed dose to detector in water at Q_0 (realistic ^{60}Co teletherapy beam), respectively. The detailed derivation of equation 4.3 is given in Section 4.2. It may be noted that $k_{QQ_0}(r)$ (see equation 4.3) is detector-specific and is defined for photon-emitting brachytherapy sources. It should not be confused with the beam quality correction defined for external radiotherapy beams as per IAEA TRS-398 (Andreo et al 2000) in which ionization chamber is used for measurements.

4.2 Theoretical background of measurement of absorbed dose in water at brachytherapy energies

Following discussion is based on the published study by Adolfsson et al (2010). Primary standards of absolute measurements of absorbed dose to water D_w are based on water calorimetry (Domen 1980). ^{60}Co or megavoltage (MV) photon beam serves as a reference beam quality Q_0 for this purpose. A dosimeter, for example, ionization chamber calibrated to measure D_w at the primary or secondary standards can be used in other beam quality *Q* (example, other clinical MV photon beams) by using the beam quality correction factor k_{QQ_0} (Almond et al 1999, Andreo et al 2000). The other dosimeters such as solid-state dosimeters can therefore be calibrated to measure D_w at *Q* traceable to the primary standard. Note that k_{QQ_0} may be calculated at a brachytherapy beam quality *Q* involving a solid state detector.

Consider a solid state detector is used for measuring D_w at Q_0. This quantity is denoted by D_{w,Q_0}. The output measured by the solid state detector is denoted by M_{det,Q_0}. Absorbed dose to water calibration coefficient N_{D_w,Q_0} can be obtained by using the following the relation:

$$N_{D_w,Q_0} = \frac{D_{w,Q_0}}{M_{\mathrm{det},Q_0}} \tag{4.4}$$

The absorbed dose to the material of the sensitive detector element at Q_0, $D_{\mathrm{det},Q}(r)$ and M_{det,Q_0} are related as follows (DeWerd et al 2009, Rogers 2009, Sutherland and Rogers 2010):

$$D_{\mathrm{det},Q_0} = k_{Q_0} M_{\mathrm{det},Q_0} \tag{4.5}$$

where the function k_{Q_0} is the intrinsic energy-dependence of the detector relates M_{det,Q_0} and D_{det,Q_0} as below:

$$k_{Q_0} = \frac{D_{\mathrm{det},Q_0}}{M_{\mathrm{det},Q_0}} \tag{4.6}$$

Let us now consider a photon emitting brachytherapy source (beam quality Q) is immersed in a liquid water phantom. The absorbed dose to water in the liquid water phantom at r along the transverse axis of the source is denoted by $D_{w,Q}(r)$. The output measured by the detector at r is $M_{\mathrm{det},Q}(r)$. Likewise equation (4.3), absorbed dose to the detector at Q, $D_{\mathrm{det},Q}(r)$ and $M_{\mathrm{det},Q}(r)$ are related by:

$$k_Q(r) = \frac{D_{\mathrm{det},Q}(r)}{M_{\mathrm{det},Q}(r)} \tag{4.7}$$

$D_{w,Q}(r)$ is obtained by using the following relation:

$$D_{w,Q}(r) = M_{\mathrm{det},Q}(r) N_{D_wQ_0} k_{QQ_0}(r), \tag{4.8}$$

where $k_{QQ_0}(r)$ is the beam quality correction and is given by

$$k_{QQ_0}(r) = \frac{D_{w,Q}(r)}{M_{\mathrm{det},Q}(r) N_{D_wQ_0}} \tag{4.9}$$

Using equation (4.1) in (4.6) gives

$$k_{QQ_0}(r) = \frac{D_{w,Q}(r)}{M_{\det,Q}(r)\dfrac{D_{w,Q_0}}{M_{\det,Q_0}}} = \frac{\left[\dfrac{D_w(r)}{M_{\det}(r)}\right]_Q}{\left[\dfrac{D_w}{M_{\det}}\right]_{Q_0}} \tag{4.10}$$

Using equations (4.3) and (4.5) in equation (4.7) gives

$$k_{QQ_0}(r) = \frac{k_Q(r)D_{w,Q}(r)}{D_{\det,Q}(r)\dfrac{D_{w,Q_0}}{D_{\det,Q_0}}k_{Q_0}} = \frac{k_Q(r)}{k_{Q_0}}\frac{\left[D_{w,Q}(r)/D_{\det,Q}(r)\right]}{\left[D_{w,Q_0}/D_{\det,Q_0}\right]} \tag{4.11}$$

$$k_{QQ_0}(r) = f_{QQ_0}\frac{\left[D_{w,Q}(r)/D_{\det,Q}(r)\right]}{\left[D_{w,Q_0}/D_{\det,Q_0}\right]} \tag{4.12}$$

$$k_{QQ_0}(r) = f_{QQ_0}/R_{QQ_0} \tag{4.13}$$

$$R_{QQ_0} = \left[D_{\det}(r)/D_{wat,Q}(r)\right]/\left[D_{\det,Q_0}/D_{wat,Q_0}\right] \tag{4.14}$$

$$f_{QQ_0} = k_{Q_0}(r)/k_{Q_0} \tag{4.15}$$

where R_{QQ_0} is relative absorbed dose energy response correction (Selvam and Biju 2010, DeWerd et al 2009, Rogers 2009). As described previously in Section 4.1 absorbed dose dependence at *Q, f(Q)* relates absorbed dose to medium of interest (usually water), $D_{wat,Q}$ and absorbed dose to detector, $D_{det,Q}$ as below:

$$f(Q) = \frac{D_{wat,Q}}{D_{\det,Q}} \tag{4.16}$$

Similarly at Q_0

$$f(Q_0) = \frac{D_{wat,Q_0}}{D_{\det,Q_0}} \tag{4.17}$$

Equation (4.14) is therefore written as

$$R_{QQ_0} = \left[1/f(Q)\right]/\left[1/f(Q_0)\right] \tag{4.18}$$

Equation (4.13) has two components: (a) f_{QQ_0} relative intrinsic energy dependence of the detector which can be determined experimentally, and (b) $1/R_{QQ_0}$, inverse of relative absorbed dose energy response correction. As mentioned by Adolfsson et al (2010), when an ion chamber is used, $f_{QQ_0} = W/W_0$ where W is the mean energy imparted to air to form an ion pair in air at Q and W_0 is the corresponding quantity at Q_0.

The value of W is usually considered to be independent of the beam quality in MV photon and electron beams but may take other values in beams of protons and heavier charged particles due to the increased ion density along the tracks of the heavy charged particles compared to that along electron tracks (Geithner et al 2006). Note that if the yield of radiation-induced products in the detector is independent of the radiation beam quality, i.e. yield is constant, then $k_Q = k_{Q_0}$. Therefore equation (4.11) becomes

$$k_{QQ_0}(r) \overset{const\ yield}{=} \frac{\left[D_{w,Q}(r)/D_{\det,Q}(r)\right]}{\left[D_{w,Q_0}/D_{\det,Q_0}\right]} \tag{4.19}$$

4.3 Monte Carlo calculations

4.3.1 Calculations of dose ratios for ^{60}Co beam

Detector-to-water dose ratio, $\left(\frac{D_{\det}}{D_{wat}}\right)_{^{60}Co}$ is calculated in the water phantom for each of the investigated detectors and radiochromic films for ^{60}Co beam using the DOSRZnrc user code of EGSnrc code system. Here, D_{det} and D_{wat} represent the dose to active region of the detector and dose to water, respectively. In the Monte Carlo calculation, a realistic ^{60}Co spectrum from a telecobalt unit was used. The ^{60}Co beam was parallel and had a radius of 5.64 cm at the front face of the phantom (equivalent field size is 10x10 cm^2). The beam was incident on a unity density cylindrical water phantom of 20 cm radius and 40 cm height. In the Monte Carlo calculations, solid-state detectors such as diamond, LiF, $Li_2B_4O_7$, Al_2O_3,

Plastic Scintillator and Lithium Formate, of dimensions 0.5 mm high and 0.5 mm thick were positioned at a depth 0.5 cm along the central axis of the water phantom. For the Monte Carlo calculations of radiochrmoic films, the active layer of films was positioned at 0.5 cm depth along the central axis of the water phantom. All layers of the films were modeled as cylindrical discs with radius 0.5 mm.

Table 4.1 presents the values of detector-to-water dose ratios for ^{60}Co beam, $\left(\frac{D_{\text{det}}}{D_{wat}}\right)_{^{60}Co}$ for the investigated detectors and radiochromic films at 0.5 cm depth in water phantom. In this Table, the number shown in parentheses following a value represents the absolute uncertainty on the last digit of the value with a coverage factor k = 1. As shown in the Table, the values of $\left(\frac{D_{\text{det}}}{D_{wat}}\right)_{^{60}Co}$ agree well with the detector-to-water mass energy absorption coefficient ratio $\left[\frac{(\mu_{en}/\rho)_{\text{det}}}{(\mu_{en}/\rho)_{wat}}\right]_{^{60}Co}$ at 1.25 MeV and also with the detector-to-water electron density ratio, $\frac{\langle Z/A\rangle_{\text{det}}}{\langle Z/A\rangle_{wat}}$ for all the investigated detectors and radiochromic films other than XRT (deviation is 3.5% for the XRT film). This suggests that at the ^{60}Co energies, the investigated detectors behave like a photon detector, as Compton scattering is the predominant interaction in all the detector materials. This implies that dose to detector is related to dose to water by the relation:

$$\left(\frac{D_{\text{det}}}{D_{wat}}\right)_{^{60}Co} = \left[\frac{(\mu_{en}/\rho)_{\text{det}}}{(\mu_{en}/\rho)_{wat}}\right]_{^{60}Co}$$

As the difference between the values of $\left[\frac{(\mu_{en}/\rho)_{\text{det}}}{(\mu_{en}/\rho)_{wat}}\right]_{^{60}Co}$ and $\left(\frac{D_{\text{det}}}{D_{wat}}\right)_{^{60}Co}$ is small, $\left[\frac{(\mu_{en}/\rho)_{\text{det}}}{(\mu_{en}/\rho)_{wat}}\right]_{^{60}Co}$ values were used for calculating $k_{QQ_0}(r)$.

Table 4.1 Monte Carlo-calculated ratios of dose to detector and dose to water for different solid state detectors and radiochromic films for ^{60}Co beam are presented. Also shown in this Table are the values of ratio of mass-energy-absorption coefficients of detector to water calculated at the ^{60}Co energy (1.25 MeV) and the values of ratio of <Z/A> of films to water.

Detectors	$\left(\frac{D_{\det}}{D_{wat}}\right)_{^{60}Co}$	$\left[\frac{(\mu_{en}/\rho)_{\det}}{(\mu_{en}/\rho)_{wat}}\right]_{^{60}Co}$	$\frac{\langle Z/A\rangle_{\det}}{\langle Z/A\rangle_{wat}}$
EBT	0.997(3)	0.983	0.982
EBT2 (lot 020609)	0.990(4)	0.981	0.969
EBT2 (lot 031109)	0.989(4)	0.982	0.971
RTQA	0.987(4)	0.976	0.975
XRT	0.985(3)	0.950	0.942
HS	0.992(3)	0.980	0.980
XRQA	0.965(3)	0.950	0.903
Diamond	0.879(5)	0.900	0.894
LiF	0.828(5)	0.833	0.832
$Li_2B_4O_7$	0.865(5)	0.873	0.874
Al_2O_3	0.883(5)	0.882	0.885
Lithium Formate	0.928(4)	0.927	0.926
Plastic Scintillator	0.974(4)	0.976	0.974

4.3.2 FLURZnrc simulations of collision kerma for brachytherapy sources

The calculations of dose ratio of detector-to-water for the brachytherapy sources (numerator of equation 4.19), was based on FLURZnrc user-code of EGSnrc code system. In the Monte Carlo calculations, the photon fluence spectrum was scored in 0.5 mm thick and 0.5 mm high cylindrical shells, along the transverse axis of the sources (distances, 1 cm - 15 cm) in 20 cm radius by 40 cm high cylindrical water phantom. The fluence spectrum was converted to collision kerma to water and collision kerma to detector by using the mass-energy

absorption coefficients of water and detectors. Using the values of collision kerma to water and collision kerma to detectors, the numerator of equation 4.19 was obtained. In the calculations of collision kerma to detectors, no detector was present. It was assumed that the presence of the detector did not affect the photon fluence spectrum and the collision kerma may be approximated to absorbed dose. In order to verify this, auxiliary simulations were carried out using the DOSRZnrc user-code in which all the layers of the XRT film were modeled as cylinders. The active layer of the film is positioned at 1 cm along the transverse axis of the ^{169}Yb source. The height of the layers of the XRT film considered was 1 mm. In another similar simulation the active layer of the film was positioned at 15 cm along the transverse axis of the ^{169}Yb source. The values of absorbed dose to active part of the XRT film obtained at 1 cm and 15 cm compared well to the values of collision kerma to the active part of XRT film obtained in the absence of the XRT film (agreement was within 0.2 %).

4.3.3 Monte Carlo parameters

The PEGS4 dataset needed for Monte Carlo calculations described above was based on XCOM (Berger and Hubbell 1987) compilations. For generating the PEGS4 dataset, AE = 0.521 MeV (kinetic energy of the electron is 0.01 MeV) and AP = 0.01 MeV was set for high energy brachytherapy soureces (^{169}Yb, ^{137}Cs, ^{192}Ir and ^{60}Co) and AE = 0.512 MeV and AP = 0.001 MeV was set for low energy brachytherapy sources (^{131}Cs, ^{125}I and ^{103}Pd), where the parameters AE and AP were the low-energy thresholds for the production of knock-on electrons and secondary bremsstrahlung photons, respectively. All the calculations utilized the PRESTA-II step length and EXACT boundary crossing algorithms. In all calculations, electron range rejection technique was used to save computation time. ESAVE = 2 MeV was set for this purpose. ESAVE was a parameter related to the range rejection technique.

The photon transport cut off energy PCUT was chosen 10 keV for high energy brachytherapy sources and 1 keV for low energy brachytherapy sources in the Monte Carlo calculations. Similarly, ECUT was set 0.521 MeV (10 keV kinetic energy) for high energy brachytherapy sources and 0.512 MeV for low energy brachytherapy sources. In the FLURZnrc calculations, electrons were not transported by setting electron transport cutoff parameter ECUT = 2 MeV (kinetic energy). Up to 10^9 photon histories were simulated. The 1σ statistical uncertainties on the calculated DOSRZnrc-based dose values were within 0.3 %. The 1σ statistical uncertainties on the calculated FLURZnrc-based collision kerma values were less than 0.2 %. The statistical uncertainties on the calculated values of $k_{QQ_0}(r)$ were less than 0.6 %.

4.4 Beam quality corrections for brachytherapy sources

4.4.1 High energy brachytherapy sources

^{60}Co source

The values of $k_{QQ_0}(r)$ of solid state detectors (diamond, LiF, $Li_2B_4O_7$, Al_2O_3, Plastic Scintillator and Lithium Formate) along the transverse axis of the ^{60}Co brachytherapy source were presented in Table 4.2. $k_{QQ_0}(r)$ was about unity and independent of distance (r) for diamond, Plastic Scintillator, LiF, Lithium Formate and $Li_2B_4O_7$ detectors. Whereas, for Al_2O_3 detector $k_{QQ_0}(r)$ decreases with r gradually about 6 % smaller than unity for ^{60}Co source in the distance range of 1-15 cm.

Table 4.2 Beam quality correction, $k_{QQ_0}(r)$, presented for diamond, Al_2O_3, $Li_2B_4O_7$, LiF, Lithium Formate and Plastic Scintillator detectors as a function of distance r along the transverse axis of ^{60}Co brachytherapy source.

Distance r (cm)	Diamond	Al_2O_3	$Li_2B_4O_7$	LiF	Lithium Formate	Plastic Scintillator
1	1	0.998	1	1	1.000	1.001
2	1.001	0.996	1	0.999	1.000	1.001
3	1.001	0.992	1	0.999	1.000	1.002
4	1.002	0.989	1	0.998	1.001	1.003
5	1.003	0.984	1	0.998	1.001	1.003
6	1.003	0.98	1	0.997	1.001	1.004
7	1.004	0.975	1	0.996	1.001	1.005
8	1.005	0.97	1	0.996	1.001	1.006
9	1.006	0.965	1.001	0.995	1.001	1.007
10	1.007	0.96	1.001	0.994	1.001	1.008
11	1.008	0.956	1.001	0.994	1.002	1.009
12	1.009	0.952	1.001	0.993	1.002	1.010
13	1.009	0.949	1.001	0.993	1.002	1.011
14	1.01	0.946	1.001	0.992	1.002	1.012
15	1.01	0.944	1.001	0.992	1.002	1.012

Table 4.3 presents the values of $k_{QQ_0}(r)$ for the investigated radiochromic films along the transverse axis of the ^{60}Co brachytherapy source. Fig. 4.1 (a) presents the Monte Carlo-calculated $k_{QQ_0}(r)$ values as a function of distance along the transverse axis of the ^{60}Co source in water phantom for the XRT and XRQA films. Mass-energy-absorption-coefficient ratio of film-to-water for the investigated radiochromic films as a function of mono-energetic photon energy (from 10 keV - 1.25 MeV) are presented in Fig. 4.1 (b). For the films other than XRT and XRQA the value of $k_{QQ_0}(r)$ in water phantom is about unity and independent of distance for this source. The value of $k_{QQ_0}(r)$ decreases from 0.974 to 0.542 for the XRT film and from 0.956 to 0.401 for the XRQA film when the distance is varied from 1 cm to 15 cm along the transverse axis of the ^{60}Co source (see Fig. 4.1(a)).

Table 4.3 Beam quality correction, $k_{QQ_0}(r)$, presented for radiochromic films EBT, EBT2 (lot 020609 and lot 031109), RTQA and HS film.

Distance r (cm)	EBT	EBT2 (lot 020609)	EBT2 (lot 031109)	RTQA	HS
1	1.000	0.999	1.000	1.000	1.000
2	1.000	0.998	1.000	0.999	1.000
3	1.000	0.996	0.999	0.999	1.001
4	1.000	0.994	0.999	0.998	1.001
5	1.000	0.992	0.999	0.996	1.002
6	1.000	0.989	0.999	0.995	1.002
7	1.000	0.987	0.999	0.994	1.003
8	1.001	0.984	0.999	0.993	1.004
9	1.001	0.982	0.998	0.991	1.005
10	1.001	0.979	0.998	0.990	1.005
11	1.001	0.977	0.998	0.989	1.006
12	1.001	0.975	0.998	0.988	1.007
13	1.001	0.973	0.998	0.987	1.007
14	1.001	0.972	0.998	0.986	1.008
15	1.001	0.971	0.998	0.986	1.008

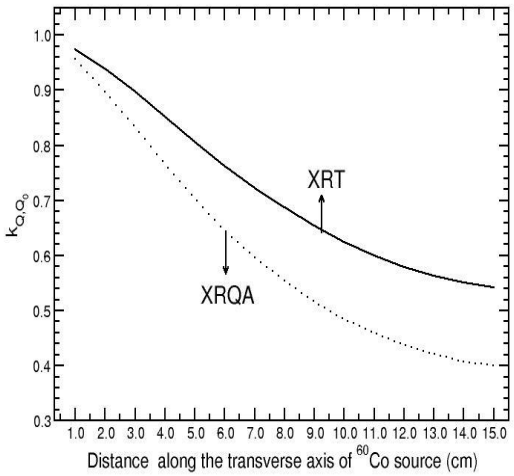

(a)

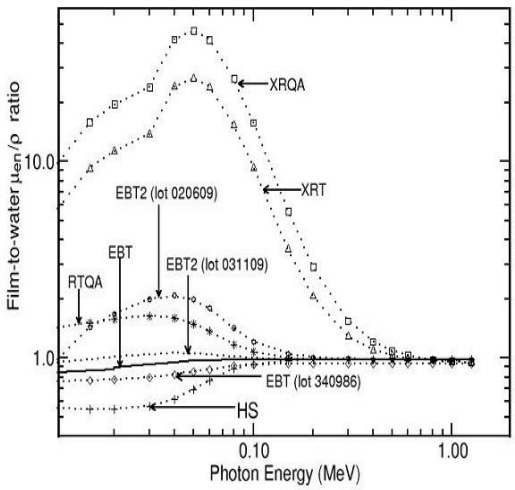

(b)

*Fig. 4.1 (*a) *Monte Carlo-calculated* $k_{QQ_0}(r)$ *values for XRT and XRQA films are shown as a function of distance along the transverse axis of the source* ^{60}*Co source (b) Values of mass-energy-absorption coefficients of film-to-water.*

^{137}Cs source

Figure 4.2 presents the values of $k_{QQ_0}(r)$ for the ^{137}Cs RTR brachytherapy source (a) for solid state detectors and (b) for radiochromic films. For $Li_2B_4O_7$ detector, $k_{QQ_0}(r)$ is about unity and is independent of *r*. The LiF detector showed a gradual decrease in $k_{QQ_0}(r)$ with *r*. The decrease is 2 % over the distance range of 1-15 cm. Diamond detector shows a gradual increase in $k_{QQ_0}(r)$ with *r* (about 3% larger than unity at 15 cm). For the Al_2O_3 detector, $k_{QQ_0}(r)$ decreases with *r* steeply (about 14% over the distance range of 1-15 cm).

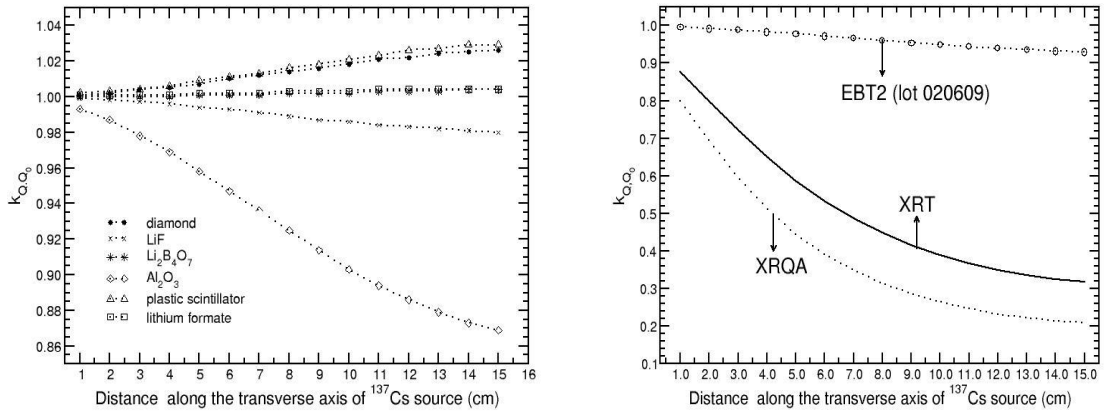

(a) **(b)**

Fig.4.2 Beam quality correction, $k_{QQ_0}(r)$ *for* ^{137}*Cs brachytherapy source (a) solid-state detectors (LiF,* $Li_2B_4O_7$*, diamond, Lithium Formate, Plastic Scintillator,* Al_2O_3*) (b) radiochromic films (EBT2 (lot 020609), XRT, XRQA).*

The numerical values of this Fig. 4.2 (a) are given in Table 4.4. The value of $k_{QQ_0}(r)$ is distance-independent and close to unity (with in 3%) for all the radiochromic films except EBT2 (lot 020609), XRT and XRQA films as shown in Fig. 4.2 (b). $k_{QQ_0}(r)$ values of the remaining radiochromic films are presented in Table 4.5. The value of $k_{QQ_0}(r)$ increases from 1.004 to 1.075 for the EBT2 (lot 020609) film, from 1.142 to 3.155 for the XRT film and from 1.249 to 4.816 for XRQA film when the distance is varied from 1 cm to 15 cm along the transverse axis of the source. For the above films, the increase in with the distance is significant for the XRT and XRQA films, because of their high atomic numbers.

Table 4.4 Monte Carlo-calculated values of beam quality correction, $k_{QQ_0}(r)$ .The data are presented as a function of distance along the transverse axis of the ^{137}Cs RTR source.

Distance, *r* (cm)	$k_{QQ_0}(r)$					
	Diamond	Al_2O_3	$Li_2B_4O_7$	LiF	Plastic Scintillator	Lithium Formate
1	1.001	0.993	1.000	0.999	1.002	1.000
2	1.002	0.987	1.000	0.998	1.003	1.000
3	1.004	0.978	1.000	0.997	1.004	1.000
4	1.005	0.969	1.000	0.996	1.006	0.999
5	1.007	0.958	1.001	0.994	1.009	0.999
6	1.010	0.947	1.001	0.993	1.011	0.999
7	1.012	0.936	1.001	0.991	1.013	0.999
8	1.014	0.925	1.002	0.989	1.016	0.998
9	1.016	0.914	1.002	0.987	1.018	0.998
10	1.018	0.903	1.002	0.986	1.021	0.998
11	1.021	0.894	1.003	0.984	1.023	0.998
12	1.022	0.886	1.003	0.983	1.026	0.997
13	1.024	0.879	1.003	0.982	1.027	0.997
14	1.025	0.873	1.004	0.981	1.029	0.997
15	1.026	0.869	1.004	0.980	1.029	0.998

Table 4.5 Monte Carlo-calculated values of beam quality correction, $k_{QQ_0}(r)$ for EBT, EBT2 (lot 031109), RTQA and HS presented for the ^{137}Cs RTR source.

	$k_{QQ_0}(r)$			
Distance, r (cm)	EBT	EBT (lot 031109)	RTQA	HS
1	1.000	1.000	0.999	1.001
2	1.000	0.999	0.997	1.002
3	1.001	0.999	0.995	1.003
4	1.001	0.999	0.992	1.004
5	1.001	0.998	0.990	1.006
6	1.001	0.998	0.987	1.007
7	1.001	0.997	0.983	1.009
8	1.001	0.997	0.980	1.011
9	1.001	0.996	0.977	1.013
10	1.001	0.996	0.974	1.015
11	1.001	0.996	0.972	1.016
12	1.001	0.995	0.969	1.018
13	1.001	0.995	0.967	1.019
14	1.001	0.995	0.965	1.020
15	1.001	0.994	0.964	1.021

^{192}Ir source

Table 4.6 presents the values of $k_{QQ_0}(r)$ for the investigated solid state detectors for ^{192}Ir source. $k_{QQ_0}(r)$ increases gradually about 6 % and 8 % larger than unity for diamond and Plastic Scintillator but decreases about 4% smaller than unity for LiF detector with r over the distance range of 1-15 cm. For Al_2O_3 detector, $k_{QQ_0}(r)$ decreases with r steeply about 25 % smaller than unity for ^{192}Ir source in the distance range of 1-15 cm. $k_{QQ_0}(r)$ is about unity and distance-independent for Lithium Formate and $Li_2B_4O_7$ detectors.

Table 4.6 Beam quality correction, $k_{QQ_0}(r)$, presented for diamond, Al_2O_3, $Li_2B_4O_7$, LiF, Lithium Formate and Plastic Scintillator detectors as a function of distance r along the transverse axis ^{192}Ir brachytherapy source.

Distance r (cm)	Diamond	Al_2O_3	$Li_2B_4O_7$	LiF	Lithium Formate	Plastic Scintillator
1	1.004	0.973	1.000	0.996	1.001	1.017
2	1.008	0.955	1.001	0.994	1.001	1.022
3	1.012	0.935	1.001	0.991	1.002	1.027
4	1.016	0.913	1.002	0.987	1.003	1.031
5	1.021	0.892	1.003	0.984	1.003	1.037
6	1.026	0.870	1.003	0.980	1.004	1.043
7	1.031	0.849	1.004	0.977	1.005	1.048
8	1.036	0.830	1.005	0.973	1.006	1.055
9	1.041	0.813	1.006	0.970	1.007	1.061
10	1.045	0.797	1.006	0.967	1.007	1.067
11	1.050	0.783	1.007	0.964	1.008	1.071
12	1.054	0.770	1.008	0.961	1.008	1.075
13	1.057	0.760	1.008	0.959	1.009	1.078
14	1.060	0.752	1.009	0.957	1.009	1.083
15	1.062	0.746	1.009	0.956	1.010	1.084

For ^{192}Ir source, the values of $k_{QQ_0}(r)$ are unity (within 1%) and are distance-independent for the films EBT and EBT2 (lot03119). Fig. 4.3 presents the values of $k_{QQ_0}(r)$ as a function of distance along the transverse axis of the ^{192}Ir source in water phantom for the films, EBT2 (lot020609), XRT, XRQA, RTQA and HS. The value of $k_{QQ_0}(r)$ decreases from 0.983 to 0.856, 0.993 to 0.922, 0.631 to 0.174, and 0.492 to 0.106 for EBT2 (lot 020609), RTQA, XRT and XRQA films, respectively when the distance is varied from 1 cm to 15 cm along the transverse axis of the source. For the HS film, the value increases from 1.003 to 1.049 in the above distance range.

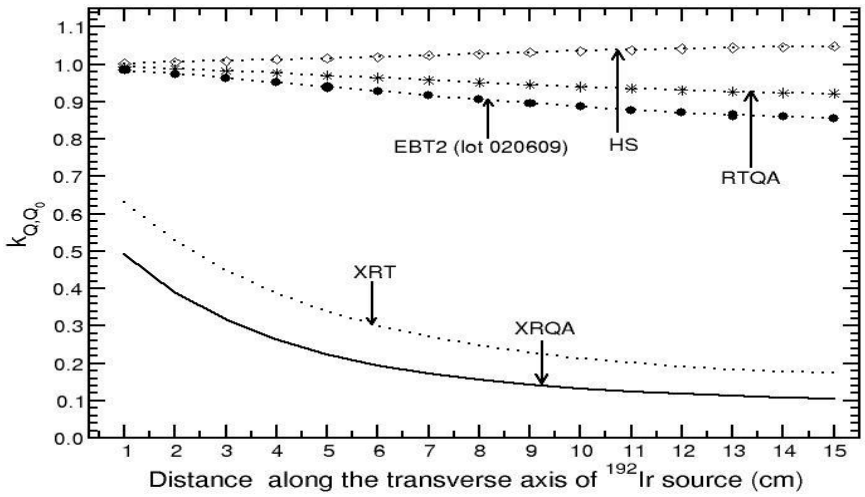

Fig.4.3 Beam quality correction, $k_{QQ_0}(r)$ of radiochromic films (EBT2 (lot 020609),XRT, XRQA, RTQA and HS) presented for ^{192}Ir source.

^{169}Yb source

Selvam and Biju (2010) have reported the relative absorbed dose energy response correction, R of LiF, $Li_2B_4O_7$, Al_2O_3, Diamond, Silicon diode and air detectors for ^{169}Yb and ^{125}I sources Monte Carlo-based EGSnrc code system. Medich and Munro (2010) also reported the absorbed dose energy correction factors of LiF TLD detector ^{169}Yb source as a function of distance *r* and polar angle θ i.e *f(r,θ)* at different locations in the phantom using Monte Carlo-based MCNP5 code. In the present study, $k_{QQ_0}(r)$ values of Plastic Scintillator and Lithium formate are presented in Table 4.7 for ^{169}Yb source. $k_{QQ_0}(r)$ increases gradually about 4 % and 33 % larger than unity for Lithium Formate and Plastic Scintillator detectors, respectively at a distance of 15 cm along the transverse axis of the ^{169}Yb source.

Table 4.7 Beam quality correction, $k_{QQ_0}(r)$, presented for Lithium Formate and Plastic Scintillator detectors for ^{169}Yb brachytherapy source.

Distance r (cm)	Lithium Formate	Plastic Scintillator
1	1.025	1.201
2	1.028	1.233
3	1.031	1.258
4	1.033	1.279
5	1.034	1.294
6	1.036	1.306
7	1.036	1.315
8	1.037	1.322
9	1.037	1.328
10	1.038	1.331
11	1.038	1.332
12	1.038	1.337
13	1.038	1.336
14	1.038	1.337
15	1.038	1.334

For ^{169}Yb source, the value of $k_{QQ_0}(r)$ is distant independent for the radiochromic films EBT and EBT2 (lot 031109). For the EBT film, the value is about unity (within 1%) and about 0.96 for EBT2 (lot 031109). Fig. 4.4 presents the values of $k_{QQ_0}(r)$ for the ^{169}Yb (model 4140) source as a function of distance along the transverse axis of the source in water phantom for the radiochromic films, EBT2 (lot 020609), XRT, XRQA, RTQA and HS. The value of $k_{QQ_0}(r)$ decreases from 0.706 to 0.636, 0.823 to 0.763, 0.082 to 0.067 and 0.048 to 0.039 for EBT2 (lot 020609), RTQA, XRT and XRQA films respectively, when the distance is varied from 1 cm to 15 cm. However, the value of $k_{QQ_0}(r)$ increases from 1.135 to 1.217 for the HS film in the above mentioned distance range.

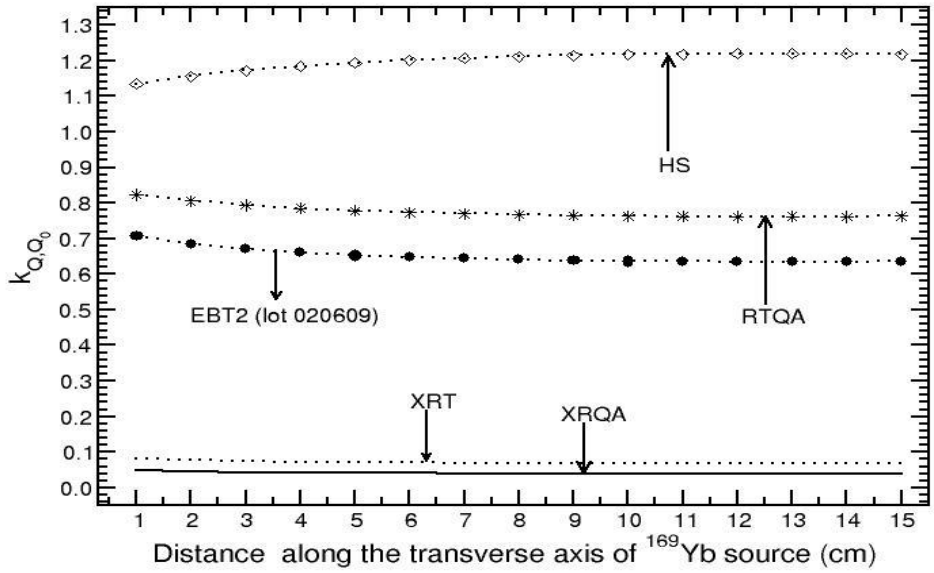

Fig.4.4 Beam quality correction, $k_{QQ_0}(r)$ of radiochromic films (EBT2 (lot 020609),XRT, XRQA, RTQA and HS) presented for ^{169}Yb source.

4.4.2 Low energy brachytherapy sources

Since Selvam and Biju (2010) have already reported the R values of LiF, $Li_2B_4O_7$, Al_2O_3, for ^{125}I source. In the present study, the above detectors were not included for ^{125}I source. $k_{QQ_0}(r)$ is distance-independent for low energy brachytherapy sources, ^{131}Cs, ^{125}I and ^{103}Pd, which were presented in Figs.4.5 (a), (b) and (c), respectively.

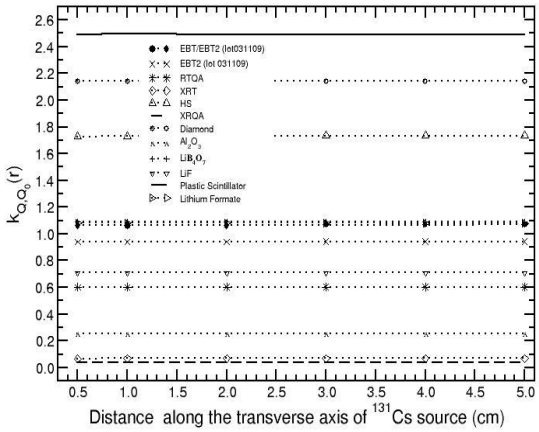

(a)

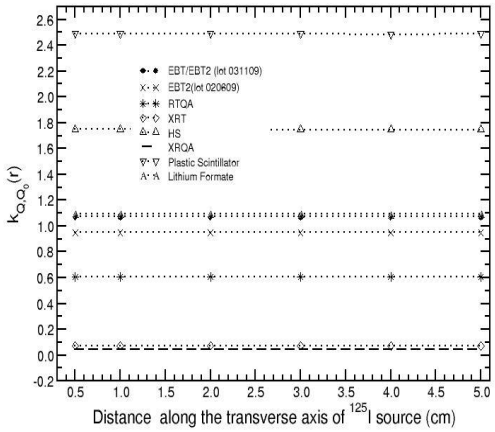

(b)

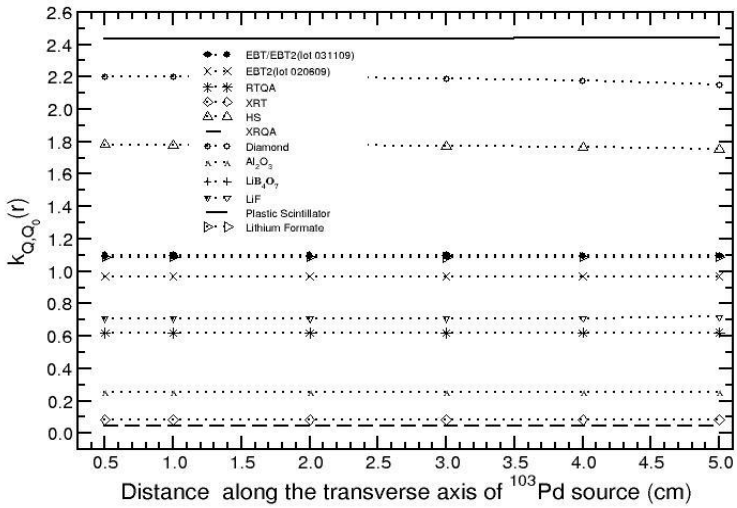

(c)

Fig.4.5 Beam quality correction, $k_{QQ_0}(r)$, presented for the investigated detectors as a function of distance along the transverse axis of (a) ^{131}Cs brachytherapy source (b) ^{125}I brachytherapy source (c) ^{103}Pd brachytherapy source.

For a given detector, $k_{QQ_0}(r)$ is independent of distance for all the investigated low energy sources. Table 4.8 presents the $k_{QQ_0}(r)$ values for the investigated detectors at a distance of 1 cm from the ^{131}Cs, ^{125}I and ^{103}Pd brachytherapy sources. For a given source, $k_{QQ_0}(r)$ values of EBT and EBT2 (lot 031109) are identical for all the above sources. This is because of the fact that these two films have very similar compositions. For EBT and EBT2 (lot 031109) films, $k_{QQ_0}(r)$ values are about 6 %, 5 % and 3 % smaller than unity for ^{131}Cs, ^{125}I and ^{103}Pd sources, respectively. Similarly, $k_{QQ_0}(r)$ values for Lithium Formate and $Li_2B_4O_7$ detectors are identical. For Lithium Formate and $Li_2B_4O_7$ detectors, $k_{QQ_0}(r)$ values are about 8 %, 7 % and 6 % larger than unity for ^{131}Cs, ^{125}I and ^{103}Pd sources, respectively. Except these detectors, remaining investigated detectors such as diamond, LiF, Al_2O_3, EBT2 (lot 020609), RTQA, XRT, XRQA and HS showed significant energy response correction. For example, $k_{QQ_0}(r)$ values are smaller than unity for RTQA, XRT and XRQA films by 40, 93 and 96 %, respectively. Whereas, for HS film and diamond detectors, $k_{QQ_0}(r)$ values are larger than unity by 70 % and a factor of 2.1 for ^{131}Cs brachytherapy source.

Table 4.8 Beam quality correction, $k_{QQ_0}(r)$, presented for the investigated detectors for the brachytherapy sources ^{131}Cs, ^{125}I and ^{103}Pd.

Source	EBT/EBT2 (lot031109)	EBT2 (lot 020609)	RTQA	XRT	HS	XRQA	Diamond	Plastic Scintillator	Lithium Formate	Al_2O_3	$Li_2B_4O_7$	LiF
^{131}Cs	1.065	0.941	0.602	0.068	1.730	0.039	2.145	2.393	1.083	0.252	1.093	0.709
^{125}I	1.075	0.950	0.607	0.073	1.748	0.042	--	2.492	1.095	--	--	--
^{103}Pd	1.098	0.968	0.620	0.084	1.780	0.048	2.201	2.435	1.088	0.252	1.095	0.706

4.5 Discussion

Z_{eff} of detectors and mean energy of photons in the phantom play a major role on the $k_{Q_0}(r)$ values. For detectors with Z_{eff} close to that of water ($Li_2B_4O_7$, Lithium Formate, EBT, EBT2 (lot 031109)), $k_{Q_0}(r)$ values were close to unity (within 6 - 9% depending upon the detector and source). For detectors with lesser Z_{eff} than that of water (diamond, Plastic Scintillator and HS), $k_{Q_0}(r)$ values are much larger than unity and for detectors with higher Z_{eff} than that of water (Al_2O_3, LiF, EBT2 (lot 020609), RTQA, XRT and XRQA), $k_{Q_0}(r)$ values are smaller than unity. It was observed that $k_{Q_0}(r)$ values of Lithium Formate are identical with the corresponding values of $Li_2B_4O_7$ detector at all distances for all the above sources. This is because of the fact that these two detectorss have very similar dosimetric properties. For example, Z_{eff} and $\langle Z/A \rangle$ of Lithium Formate (7.23 and 0.514) are comparable to that of $Li_2B_4O_7$ (7.40 and 0.485) detector. The mass-energy absorption coefficient values of Lithium Formate $\left[\mu_{en}/\rho\right]_{lithiumformate}$ are only 6 % higher to that of $\left[\mu_{en}/\rho\right]_{Li_2B_4O_7}$ in the energy range 10 keV to 1.5 MeV. Although the absolute values differ by 6 %, $k_{Q_0}(r)$ values of these two detectors are identical. Because, $k_{Q_0}(r)$ is the ratio of absorbed dose to water and detector for a given beam quality normalised with the same ratio for the reference beam (see equation 4.18). Hence, the ratio of absorbed dose to Lithium Formate and $Li_2B_4O_7$ at Q is equal to the same ratio at Q_0 which results in identical $k_{Q_0}(r)$ values for these two detectors.

For low energy brachytherapy sources, the mean energies did not change with depth in the phantom significantly. Hence $k_{Q_0}(r)$ values did not change with distance from the source for any of the investigated low energy brachytherapy sources. For these sources,

$k_{QQ_0}(r)$ value mostly depends upon the Z_{eff} of a given detector. As the mean energy does not vary with depth in the phantom for the investigated brachytherapy sources, the mass-energy-absorption data may be sufficient to obtain $k_{QQ_0}(r)$. Hence, simulations were carried out to calculate $\frac{\left[(\mu_{en}/\rho)_{wat}/(\mu_{en}/\rho)_{\det}\right]_Q}{\left[(\mu_{en}/\rho)_{wat}/(\mu_{en}/\rho)_{\det}\right]_{Q_0}}$ using the g user-code of EGSnrc code system. In this Monte Carlo calculation, $(\mu_{en}/\rho)_{wat}$ and $(\mu_{en}/\rho)_{\det}$ (mass-energy absorption coefficients of water and detector materials, respectively) were calculated for beam qualities *Q* and Q_0. For beam quality *Q*, the predominant primary gamma lines 33 keV (^{131}Cs), 27 keV (^{125}I) and 20 keV (^{103}Pd) were considered. For beam quality Q_0 1.25 MeV energy was considered. It was interesting to see that the Monte Carlo-calculated values of $k_{QQ_0}(r)$ agree well with the ratio $\frac{\left[(\mu_{en}/\rho)_{wat}/(\mu_{en}/\rho)_{\det}\right]_Q}{\left[(\mu_{en}/\rho)_{wat}/(\mu_{en}/\rho)_{\det}\right]_{Q_0}}$ (a maximum difference of 1.6 % was observed for the XRT radiochromic film). This suggests that detailed Monte Carlo calculations are not even required for determining $k_{QQ_0}(r)$ for low energy brachytherapy sources such as ^{131}Cs, ^{125}I and ^{103}Pd.

In the Monte Carlo calculations, it was assumed that the detectors do not attenuate the photons and hence they were not modeled. This assumption may be true for high energy photon sources such as ^{60}Co, ^{137}Cs, ^{192}Ir and ^{169}Yb. For example, the study by Selvam and Biju (2010) revealed that self-attenuation by ^{169}Yb for detectors such as LiF and Al_2O_3 was negligible. However, self-attenuation by the detectors is important at low energy photons. Such investigation was carried by Selvam and Biju (2010) for ^{125}I by modeling the detectors (LiF and Al_2O_3) as cylindrical shell due to limitations associated with the DOSRZnrc and FLURZnrc codes to model the detector having their own axes. Their study showed that self-

attenuation of ^{125}I photons in 1-mm-thick x 1-mm-height LiF and Al_2O_3 detectors resulted in decrease in the responses by factors of 0.975 and 0.850, respectively.

In the present investigation, instead of modeling cylindrical source and detector as was modeled by Selvam and Biju (2010), following approach was followed. The source was modeled as a disc. For example, ^{131}Cs source was modeled with inner radius of 2 mm and outer radius of 2.26 mm; overall source thickness of 0.62 mm and active thickness of 0.4 mm. All the encapsulation materials were accounted in the source model. Two separate simulations were carried out by positioning two detectors of thicknesses 0.05 mm and 1 mm/2 mm opposite to each other at the distance of 2 cm from the source centre along the longitudinal axis of the source. In this approach, collisional-kerma was obtained for both the detectors (0.05 mm and 1 mm / 2 mm) in a single run. The ratio of these results gives self-attenuation by the detector. The values of self-attenuation by the LiF detector obtained for the ^{103}Pd and ^{131}Cs sources were 0.953 and 0.989 (independent of distance) for 1 mm-thick and 0.910 and 0.974 for 2 mm-thick, respectively. Similar study was carried out for distances 5 cm and 10 cm. It was found that the self-attenuation by the detector is indepenedent of distance, this is due to the fact that the energy degneration with distance is negligible for low energy brachytherapy sources (as explained in Chapter 3). The result obtained is presented in Table 4.9. The values of self-attenuation by the Al_2O_3 detector obtained for the ^{103}Pd and ^{131}Cs sources were 0.735 and 0.910 (independent of distance) for 1 mm-thick and 0.581 and 0.833 for 2 mm-thick, respectively. It may be noted that, Al_2O_3 detector of nonodots type are generally used (Chen et al 2009) for which the detector self-attenuation will be negligible. This investigation of was carried out to demonstrate the influence of finite dimension of detector on detector response. Hence, detector self-

attenuation should also be accounted along $k_{QQ_0}(r)$ especially for low energy brachytherapy sources.

Table 4.9 Self-attenuation factors for ^{131}Cs and ^{103}Pd sources for LiF and Al_2O_3 detectors.

Detector	^{131}Cs		^{103}Pd	
	1 mm-thick x 2 mm radius	2 mm-thick x 2 mm radius	1 mm-thick x 1.75 mm radius	1 mm-thick x 1.75 mm radius
LiF	0.989	0.974	0.953	0.910
Al_2O_3	0.910	0.833	0.735	0.581

4.6 Summary and conclusion

In summary, detector-specific $k_{QQ_0}(r)$ were calculated for different solid-state detectors (diamond, Al_2O_3, $Li_2B_4O_7$, LiF, Lithium Formate and Plastic Scintillator) and various radiochromic films (EBT, EBT2 (lot 031109), EBT2 (lot 020609), RTQA, XRT, XRQA and HS) as a function of distance along the transverse axis of the ^{60}Co, ^{137}Cs, ^{192}Ir, ^{169}Yb, ^{131}Cs, ^{125}I and ^{103}Pd brachytherapy sources using the Monte Carlo-based EGSnrc code system. Z_{eff} of detectors and mean energy in the phantoms play a major role on the $k_{QQ_0}(r)$ values of high energy brachytherapy sources (^{60}Co, ^{137}Cs, ^{192}Ir and ^{169}Yb). For low energy brachytherapy sources such as ^{131}Cs, ^{125}I and ^{103}Pd, $k_{QQ_0}(r)$ value mostly depends upon the Z_{eff} of a given detector. $k_{QQ_0}(r)$ is distance-dependent for high energy brachytherapy sources and distance-independent for low energy brachytherapy sources. The detectors with Z_{eff} close to that of water, $k_{QQ_0}(r)$ values were close to unity. However, for detectors with lesser Z_{eff} than that of water, $k_{QQ_0}(r)$ values are much larger than unity and for detectors with higher Z_{eff} than that of water, $k_{QQ_0}(r)$ values are smaller than unity. For a given

brachytherapy source, $Li_2B_4O_7$, Lithium Formate, EBT and EBT2 detectors showed lesser energy response corrections than other investigated detectors.

CHAPTER 5

Phantom scatter corrections for brachytherapy sources

5.1 Introduction

As per TG 43 recommendations (Nath et al 1995, Rivard et al 2004), water should be the reference medium for dosimetry of brachytherapy sources. Water provides excellent reproducibility and comparability of measurements worldwide. However, the precise and reproducible placement of radiation detectors in water is a challenge and may cause measurement errors. Hence, water phantom is often replaced by solid phantoms for measurement purposes. Solid phantom have several advantages over water phantom for example solid phantoms can be machined, to accommodate the source and detectors in a precise geometrical configuration, facilitating an accurate measurement and reproducibility in source-detector geometry, water proofing, precise positioning of detectors etc. However, a solid phantom will alter the attenuation and scattering characteristics of photons as compared to the water phantom especially for low energy photons. The energies used in brachytherapy applications are in general much lower compared to the External beam therapy. Hence, the dose distributions of brachytherapy sources are highly sensitive to phantom compositions and solid phantoms are not truly water equivalent for brachytherapy sources. In the present study, water equivalence of solid phantoms is addressed by phantom scatter correction and is calculated for different brachytherapy sources.

Phantom scatter correction

Phantom scatter correction, $k_{phan}(r)$ can be calculated at a brachytherapy beam quality Q for a given solid-state detector by using the following relation:

$$k_{phan}(r) = \left[D_{\mathrm{det},Q}(r) / D_{\mathrm{det},\,phan,Q}(r) \right] \tag{5.1}$$

where, $D_{\det,Q}(r)$ and $D_{\det,phan,Q}(r)$ are the absorbed dose to a given detector material in water and in the solid phantom at a distance *r* for brachytherapy source of beam quality *Q*, respectively. Note that, $k_{phan}(r)=1$ means the phantom is water-equivalent. The phantoms where the $k_{phan}(r)$ values deviate from unity within $\pm 3\%$ at clinically relevant distances i.e up to 10 cm for high energy brachytherapy sources and 5 cm for low energy brachytherapy sources were also considered as water-equivalent phantoms (Schoenfeld et al 2017).

Brachytherapy Sources, phantoms and detectors investigated

The brachytherapy sources (^{60}Co, ^{137}Cs, ^{192}Ir, ^{169}Yb, ^{131}Cs, ^{125}I and ^{103}Pd) and the detectors (diamond, LiF, $Li_2B_4O_7$, Al_2O_3, Plastic Scintillator, Lithium Formate and various radiochromic films) investigated in the present study are the same as used for calculation of $k_{QQ_0}(r)$. The details of the brachytherapy sources and detectors are outlined in Sections 3.3 and 3.4 of Chapter 3. The solid phantoms investigated are PMMA, polystyrene, solid water, virtual water, RW1, RW3, plastic water, plastic water (LR), A150 and WE210. The details of the solid phantoms are outlined in Section 3.5 of Chapter 3.

5.2 Monte Carlo calculations

The Monte Carlo calculations of absorbed dose to detectors in water and in solid water phantoms were based on the FLURZnrc user-code of EGSnrc code system. The phantom dimensions used in the calculations were 40 cm dia x 40 cm height. The photon fluence spectrum was scored in the investigated phantoms along the transverse axis of the source in 0.5 mm high and 0.5 mm-thick cylindrical shells. The fluence spectrum was converted to the collision kerma to water and the collision kerma to detectors using the mass-energy absorption coefficients of water and detector, respectively. In the calculation of the collision

kerma to films, no detector was present. We assumed that the presence of the detector did not affect the photon fluence spectrum and the collision kerma may be approximated to absorbed dose. This was also verified by an auxiliary simulation using the DOSRZnrc user-code which was explained in Section 4.3.2 of Chapter 4.

Up to 10^9 photon histories were simulated. The 1 σ statistical uncertainties for the calculated absorbed dose and collision kerma values were about 0.2%. The statistical uncertainties for the calculated values of $k_{phan}(r)$ were less than 0.5%. The Monte Carlo parameters are same as those used in the calculation for $k_{QQ_0}(r)$ which was described in Section 4.3.3 of Chapter4.

5.3 Phantom scatter corrections of brachytherapy sources

5.3.1 High energy brachytherapy sources

^{60}Co source

Phantoms such as solid water, virtual water, RW1, RW3 and WE210 are water-equivalent at all distances (1-15 cm) for all the solid-state detectors (maximum deviation from unity is about 1% at 15 cm for Al_2O_3 detector in solid water, RW1 and RW3). Polystyrene and plastic water phantoms are water-equivalent at all distances for all the detectors (with a maximum deviation of about 1% from unity for LiF) other than Al_2O_3. Fig. 5.1 presents the distance-dependent $k_{phan}(r)$ values for the Al_2O_3 detector in plastic water and polystyrene phantoms.

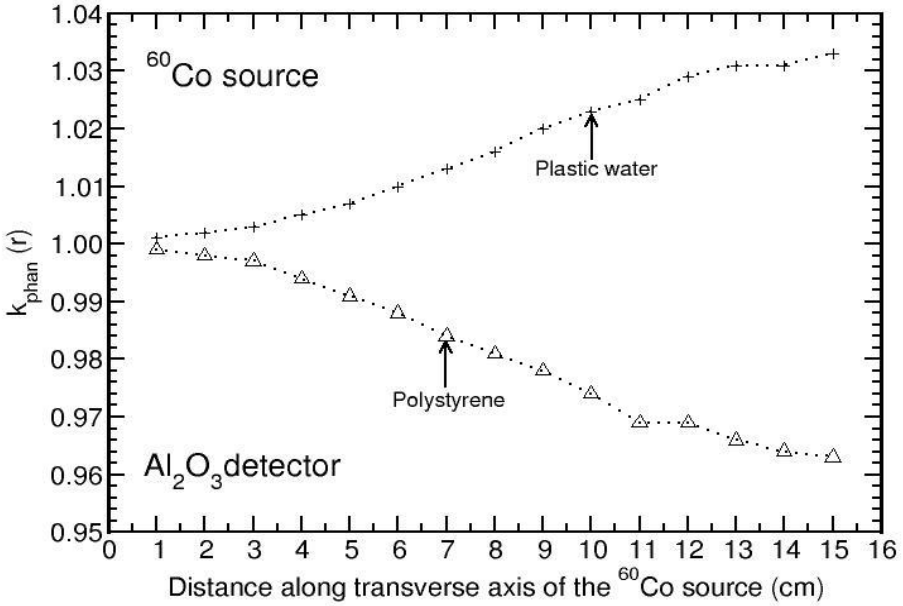

Fig.5.1 Phantom scatter correction, $k_{phan}(r)$, presented for Al_2O_3 detector in polystyrene and plastic water phantoms as a function of distance along the transverse axis of the ^{60}Co source.

PMMA is water-equivalent at all distances for Al_2O_3 detector (larger than unity by about 1% at 15 cm) whereas $k_{phan}(r)$ increases with *r* for remaining detector materials including water (see Fig. 5.2 (a)). In this phantom, $k_{phan}(r)$ values are comparable for diamond, Plastic Scintillator, $Li_2B_4O_7$, LiF, Lithum Formate and water detectors at all distances. For A150 phantom, $k_{phan}(r)$ increases with *r* for all the detectors including water (see Fig. 5.2 (b)). For this phantom, $k_{phan}(r)$ values are comparable for the detectors diamond, Plastic Scintillator, Lithium Formate, $Li_2B_4O_7$, LiF and water at all distances, with a maximum value of about 1.045 at 15 cm. For Al_2O_3, the maximum value of $k_{phan}(r)$ is 1.027 at 15 cm.

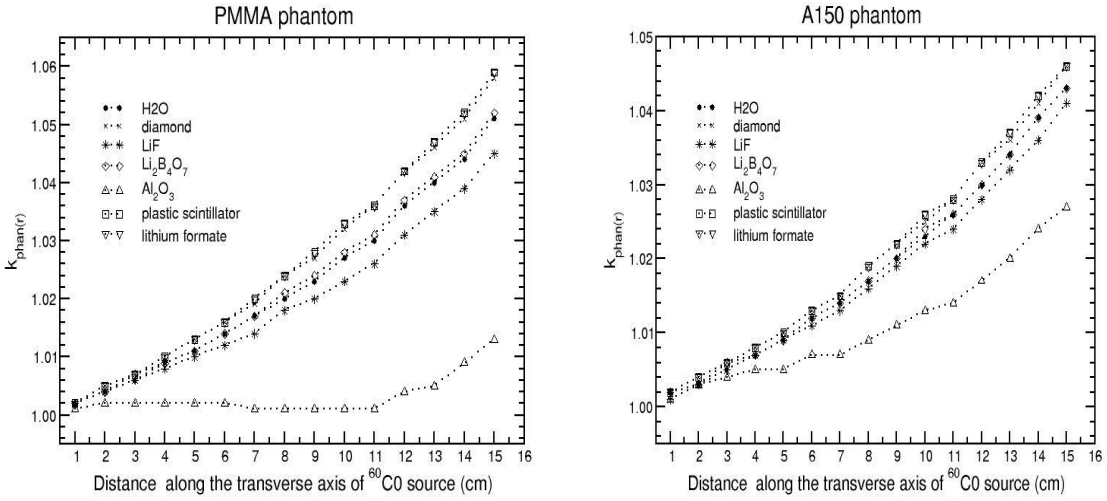

(a) (b)

Fig.5.2 Phantom scatter correction, $k_{phan}(r)$*, presented as a function of distance along the transverse axis of the* ^{60}*Co brachytherapy source for different solid-state detectors LiF,* $Li_2B_4O_7$*, diamond, Lithium Formate, Plastic Scintillator and water (a) PMMA, (b) A150.*

Phantoms such as polystyrene, plastic water, solid water, virtual water, RW1, RW3 and WE210 are water-equivalent at all distances (1-15 cm) for the investigated radiochromic films other than XRT and XRQA. Z_{eff} of XRQA and XRT films were higher compared to that of the other films. Hence these two films showed a different trend. Table 5.1 presents the $k_{phan}(r)$ values of XRT and XRQA films for the above phantoms. PMMA and A150 showed distance-dependent $k_{phan}(r)$ values for all of the radiochromic films, which were presented in Fig. 5.3 (a) and (b), respectively. For these phantoms, $k_{phan}(r)$ decreased with *r*, for the XRT and XRQA films and increases with *r* for the remaining radiochromic films.

Table 5.1 Monte Carlo-calculated phantom scatter correction, $k_{phan}(r)$, for XRT and XRQA films for polystyrene, plastic water, RW1, RW3, virtual water, solid water and WE210 phantoms.

Distance	Polystyrene		Plastic water		RW1		RW3		Virtual water		Solid water		WE210	
r (cm)	XRT	XRQA	XRT	XRQA	XRT	XRQA	XRT	XRQA	XRT	XRQA	XRT	XRQA	XRT	XRQA
1	0.997	0.994	1.003	1.006	1.000	1.000	0.999	0.999	1.001	1.001	1.001	1.001	1.001	1.002
2	0.990	0.983	1.010	1.017	1.000	1.001	0.998	0.997	1.002	1.004	1.002	1.002	1.004	1.006
3	0.980	0.968	1.020	1.033	1.000	1.000	0.996	0.994	1.004	1.007	1.003	1.005	1.007	1.012
4	0.969	0.951	1.033	1.053	0.999	1.000	0.994	0.990	1.006	1.010	1.005	1.007	1.010	1.017
5	0.956	0.934	1.046	1.072	0.998	0.998	0.991	0.986	1.009	1.014	1.007	1.010	1.014	1.022
6	0.944	0.918	1.061	1.093	0.997	0.996	0.989	0.983	1.011	1.017	1.009	1.013	1.018	1.028
7	0.931	0.903	1.077	1.114	0.995	0.994	0.986	0.979	1.014	1.021	1.011	1.016	1.022	1.033
8	0.919	0.888	1.091	1.133	0.993	0.991	0.982	0.975	1.016	1.023	1.012	1.017	1.025	1.037
9	0.910	0.878	1.106	1.152	0.992	0.990	0.980	0.972	1.020	1.027	1.014	1.019	1.029	1.042
10	0.900	0.868	1.120	1.170	0.990	0.988	0.979	0.971	1.022	1.029	1.018	1.023	1.032	1.045
11	0.891	0.858	1.132	1.184	0.988	0.986	0.976	0.968	1.023	1.031	1.018	1.024	1.033	1.047
12	0.886	0.854	1.142	1.196	0.987	0.984	0.976	0.968	1.024	1.032	1.021	1.027	1.036	1.050
13	0.880	0.847	1.151	1.207	0.984	0.980	0.973	0.964	1.025	1.034	1.022	1.028	1.036	1.050
14	0.877	0.844	1.159	1.216	0.983	0.981	0.973	0.965	1.027	1.036	1.022	1.028	1.038	1.052
15	0.874	0.841	1.164	1.222	0.983	0.980	0.972	0.964	1.028	1.036	1.024	1.031	1.038	1.052

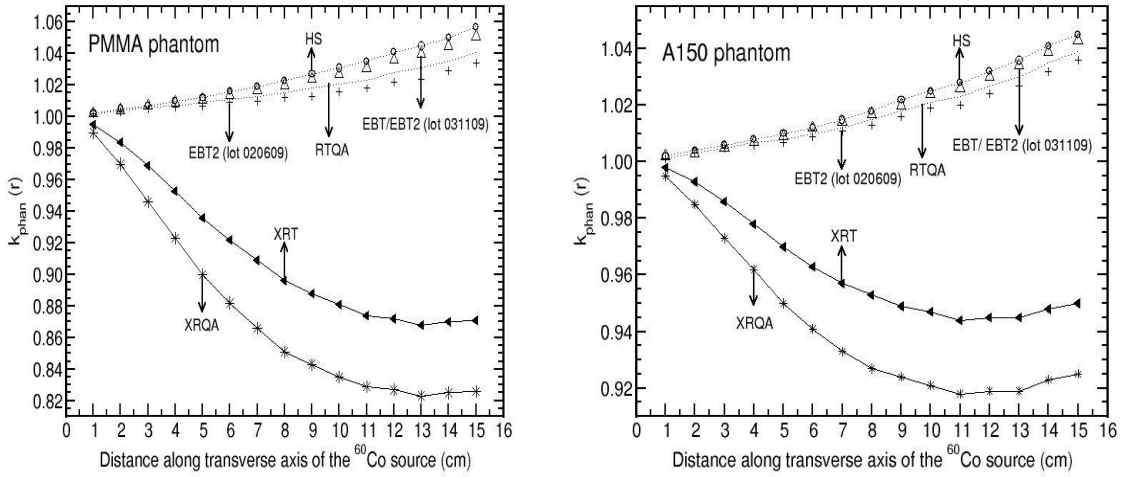

(a) (b)

Fig.5.3 Phantom scatter correction, $k_{phan}(r)$, presented as a function of distance along the transverse axis of the ^{60}Co source for different radiochromic films (a) PMMA (b) A150.

^{137}Cs source

For PMMA and plastic water phantoms, $k_{phan}(r)$ increases with *r* for the diamond detector. The value increases to 1.061 in PMMA and 1.021 in plastic water at 15 cm for the diamond detector. For the LiF and $Li_2B_4O_7$ detectors, virtual water, RW1, solid water are water-equivalent (within 1 %). Note that $Li_2B_4O_7$ and Lithium Formate detectors behave like water detector at all distances for all the solid phantoms investigated. For A150 and plastic water phantoms, $k_{phan}(r)$ values of diamond and LiF detectors are identical to that of Lithium Formate. However, for PMMA and polystyrene phantoms, the values differ with a maximum deviation of about 2 % to that of Lithium Formate, which is not significant. For the Al_2O_3 detector the phantoms such as Polystyrene, PMMA and RW1 show decrease in $k_{phan}(r)$ with *r* and the degree of decrease is higher for polystyrene phantom. For example,

the value decreases to 0.908, 0.970 and 0.982 at 15 cm for the phantoms polystyrene, PMMA and RW1, respectively. The degree of decrease is higher in polystyrene phantom. Figs. 5.4 (a) - (d) present the distance-dependent $k_{phan}(r)$ values for solid-state detectors in polystyrene, plastic water, PMMA, and A150 phantoms.

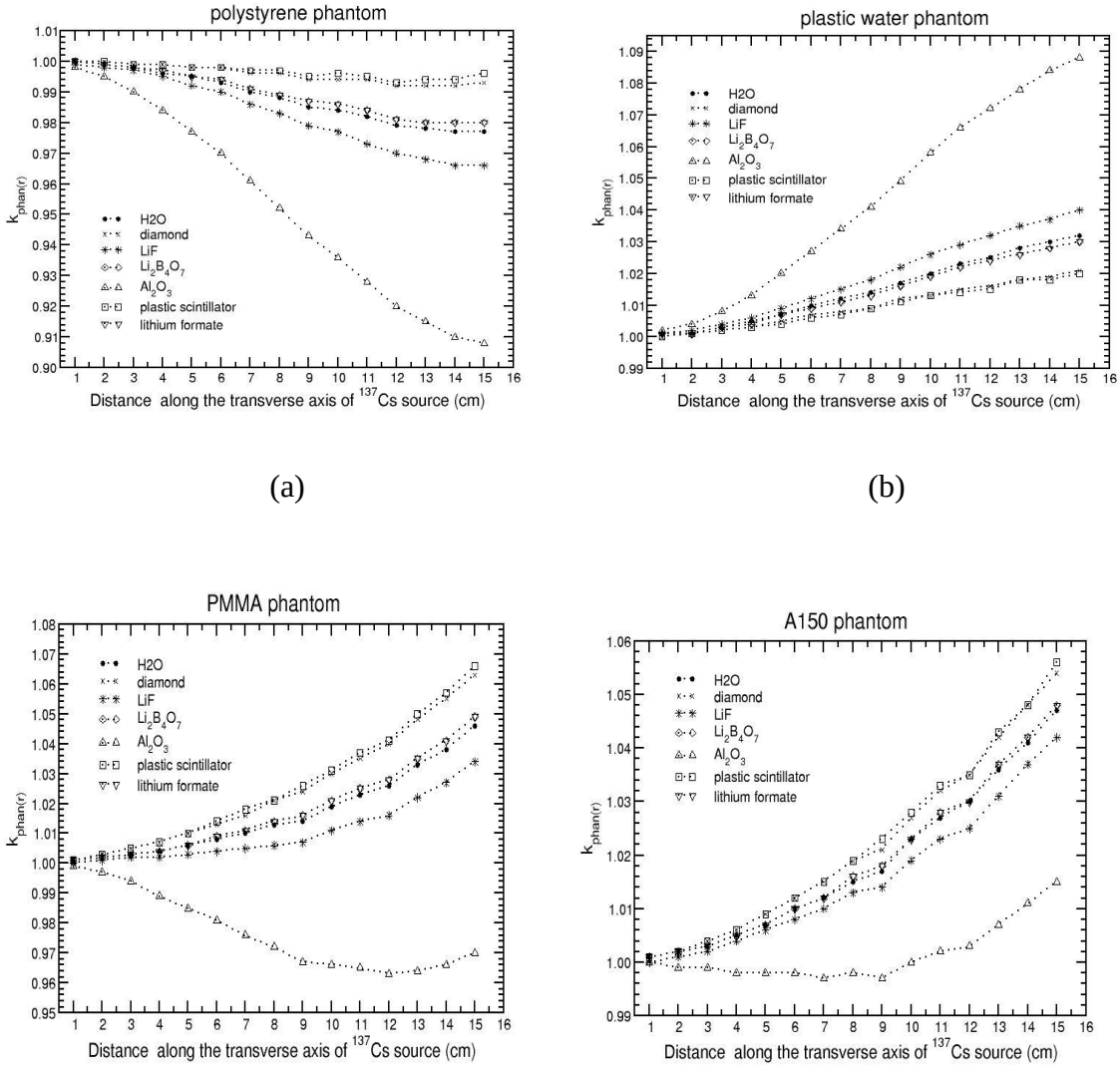

Fig.5.4 Phantom scatter correction, $k_{phan}(r)$, presented as a function of distance along the transverse axis of the ^{137}Cs source for different solid-state detectors (a) Polystyrene, (b) plastic water, (c) PMMA, and (d) A150

Phantoms such as solid water, virtual water, RW1, RW3 and WE210 are water-equivalent at all distances (1-15 cm) for all the solid state detectors and radiochromic films other than XRT and XRQA. Table 5.2 presents the $k_{phan}(r)$ values of XRT and XRQA films for all of these phantoms. The remaining phantoms, polystyrene, plastic water, PMMA, and A150 showed distance-dependent $k_{phan}(r)$ values, which were presented in Figs. 5.5 (a) - (d) for radiochromic films (EBT, EBT2 (lot 031109), EBT2 (lot 020609), RTQA, XRT, XRQA and HS).

Table 5.2 Monte Carlo-calculated phantom scatter correction, $k_{phan}(r)$, for XRT and XRQA films shown as a function of distance along the transverse axis of the ^{137}Cs source.

Distance	RW1		RW3		Virtual water		Solid water		WE210	
r (cm)	XRT	XRQA	XRT	XRQA	XRT	XRQA	XRT	XRQA	XRT	XRQA
1	1.000	1.001	0.998	0.997	1.002	1.002	1.001	1.001	1.003	1.005
2	1.000	1.000	0.995	0.992	1.004	1.007	1.002	1.004	1.008	1.013
3	0.998	0.998	0.991	0.987	1.008	1.012	1.005	1.007	1.014	1.020
4	0.996	0.995	0.986	0.980	1.012	1.016	1.008	1.011	1.021	1.029
5	0.994	0.993	0.981	0.975	1.017	1.022	1.012	1.015	1.027	1.037
6	0.992	0.991	0.978	0.972	1.021	1.027	1.016	1.020	1.033	1.044
7	0.988	0.985	0.973	0.966	1.023	1.029	1.018	1.022	1.037	1.047
8	0.985	0.982	0.970	0.963	1.026	1.032	1.020	1.024	1.042	1.053
9	0.982	0.979	0.966	0.959	1.029	1.035	1.022	1.027	1.045	1.056
10	0.980	0.977	0.965	0.959	1.032	1.039	1.027	1.032	1.049	1.060
11	0.978	0.975	0.962	0.956	1.034	1.040	1.028	1.033	1.050	1.061
12	0.975	0.972	0.960	0.954	1.037	1.043	1.031	1.036	1.052	1.063
13	0.974	0.971	0.959	0.952	1.037	1.044	1.032	1.037	1.055	1.066
14	0.971	0.968	0.957	0.950	1.039	1.045	1.035	1.039	1.054	1.064
15	0.971	0.968	0.958	0.952	1.043	1.049	1.037	1.042	1.057	1.067

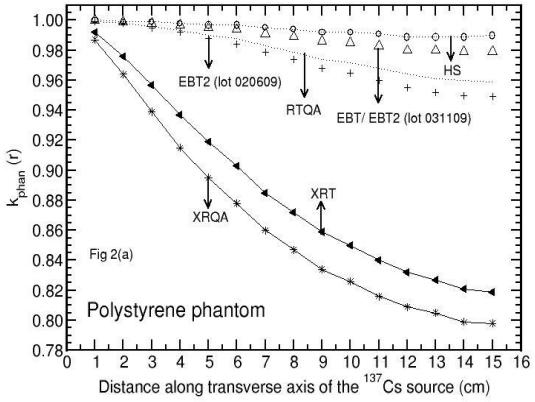

(a)

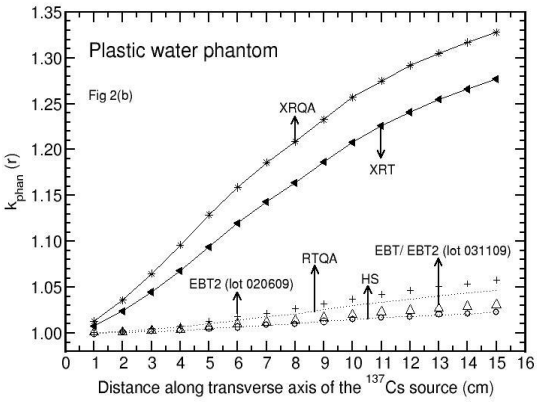

(b)

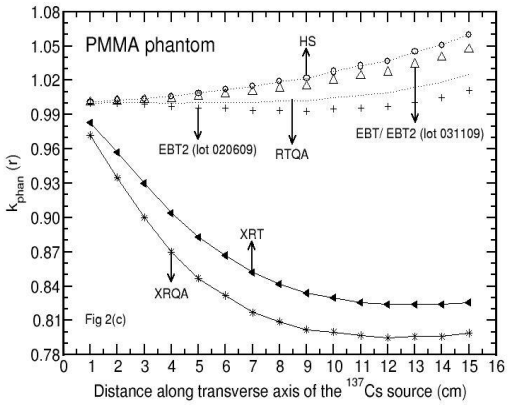

(c)

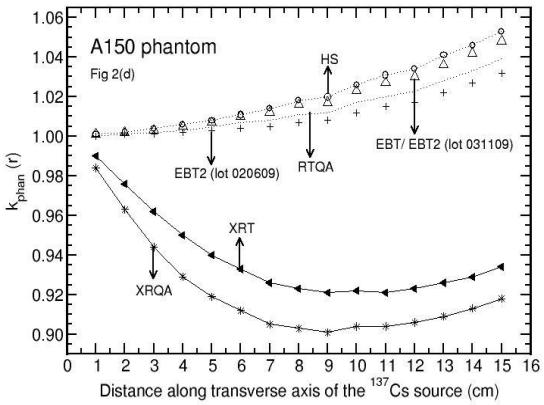

(d)

Fig.5.5 Phantom scatter correction, $k_{phan}(r)$, presented for the ^{137}Cs brachytherapy source for different radiochromic films (a) Polystyrene, (b) plastic water, (c) PMMA, and (d) A150.

^{192}Ir source

Phantoms such as solid water, virtual water, RW3 and WE210 are water-equivalent in the distance range of 1-15 cm for all the solid state detectors other than Al_2O_3 (with a maximum deviation of about 2 % at 15 cm for solid water and RW3 phantoms). Fig. 5.6 (a) presents

the distance-dependent $k_{phan}(r)$ values of Al_2O_3 detector for the above four phantoms. For this detector, $k_{phan}(r)$ increases with *r* for solid water, virtual water and WE210 phantoms and decreases with *r* for RW3 phantom. $k_{phan}(r)$ is comparable for solid water, virtual water and WE210 phantoms. In A150 phantom, for Al_2O_3 detector, $k_{phan}(r)$ decreases from 0.997 (at 1 cm) to 0.978 (at 7 cm) and thereafter increases to unity at a distance of 15 cm. In order to verify this trend beyond 15 cm, auxiliary simulations are carried out to calculate $k_{phan}(r)$ for *r* = 1 - 20 cm using the FLURZnrc user-code for larger dimensions. Fig. 5.6 (b) compares $k_{phan}(r)$ values obtained in 50 cm dia x 50 cm height and 40 cm dia x 40 cm height phantoms for Al_2O_3 detector.

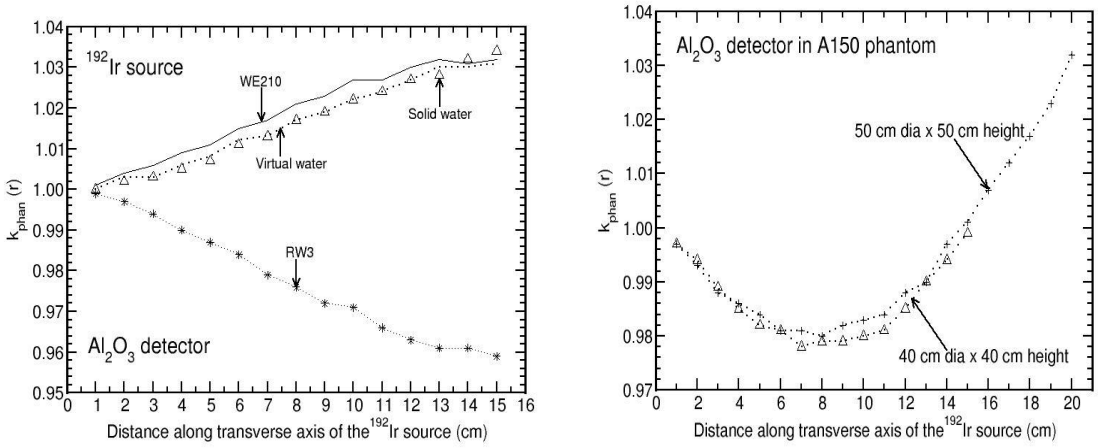

(a) (b)

Fig.5.6 Phantom scatter correction, $k_{phan}(r)$, presented as a function of distance along the transverse axis of the ^{192}Ir source for Al_2O_3 detector (a) virtual water, solid water, RW3 and WE210 phantoms (b) in 40 cm dia x 40 cm height and 50 cm dia x 50 cm height A150 phantoms.

Up to 15 cm $k_{phan}(r)$ values are comparable in both the phantom dimension. For 50 cm diameter x 50 cm height phantom, $k_{phan}(r)$ reaches the value of 1.032 at *r* = 20 cm. To verify any possible influence of the detector dimensions on $k_{phan}(r)$, separate auxiliary simulations are also carried out with 50 cm diameter x 50 cm height phantom by using the DOSRZnrc user-code, in which Al_2O_3 detector is modeled as a 1 mm thick x 2 mm high cylinder. The values of $k_{phan}(r)$ are calculated along the transverse axis of the ^{192}Ir source for *r* = 1, 5, 10, 15 and 20 cm. The study shows that DOSRZnrc-based $k_{phan}(r)$ values are statistically identical to the corresponding FLURZnrc-based $k_{phan}(r)$ values. PMMA phantom is water-equivalent for LiF detector. Fig. 5.7 (a) presents $k_{phan}(r)$ values for all the solid state detector in PMMA phantom. The phantoms polystyrene, RW1, plastic water and A150 show distance-dependent $k_{phan}(r)$ values, which are presented in Figs. 5.7 (b) - (e). For PMMA phantom, $k_{phan}(r)$ decreases with *r* for Al_2O_3 detector (about 10 % at 15 cm) whereas $k_{phan}(r)$ increases with *r* for all the other detectors. The degree of increase is higher for diamond detector and Plastic Scintillator (maximum deviation from unity at 15 cm is about 5 % and 6 % respectively). $k_{phan}(r)$ decreases with *r* for all the detector materials in polystyrene and RW1 phantoms (Figs. 5.7 (b) and (c)). However the degree of decrease is higher for Al_2O_3 detector compared to all other detectors. For example, the value decreases to 0.821 and 0.960 at 15 cm for polystyrene and RW1 phantoms, respectively. For plastic water phantom, $k_{phan}(r)$ values increase with *r* for all the detectors including water (Fig. 5.7 (d)). The degree of increase is higher for Al_2O_3 detector (about 20 % larger than unity at 15 cm) compared to all other detectors (minimum deviation of about 5 % from unity

at 15 cm for diamond and plastic scintillator detector). In case of A150 phantom, $k_{phan}(r)$ value increases with *r* for all the detector materials (maximum deviation of about 6 % from unity at 15 cm for diamond detector) other than Al_2O_3 detector (Fig. 5.7 (e)).

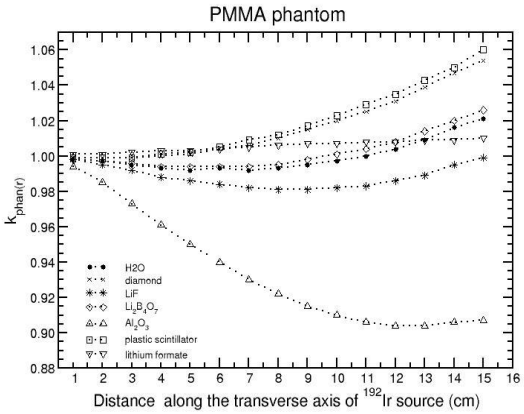

(a)

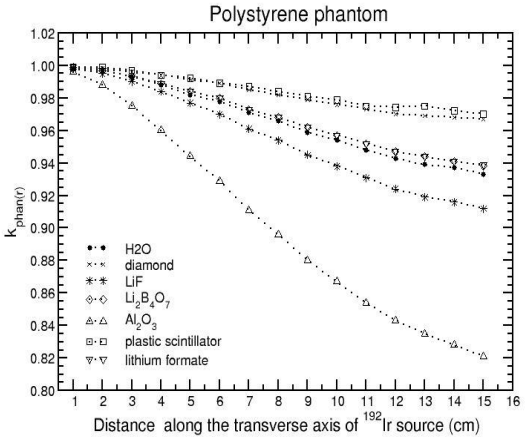

(b)

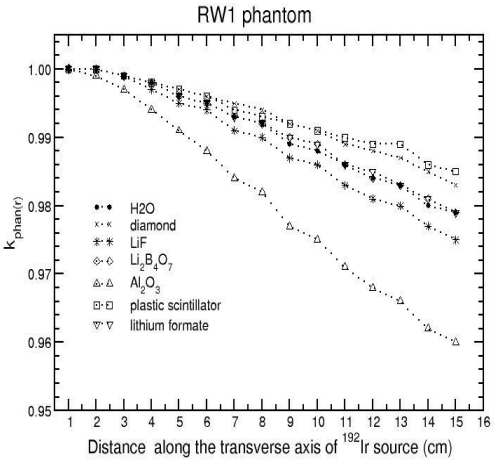

(c)

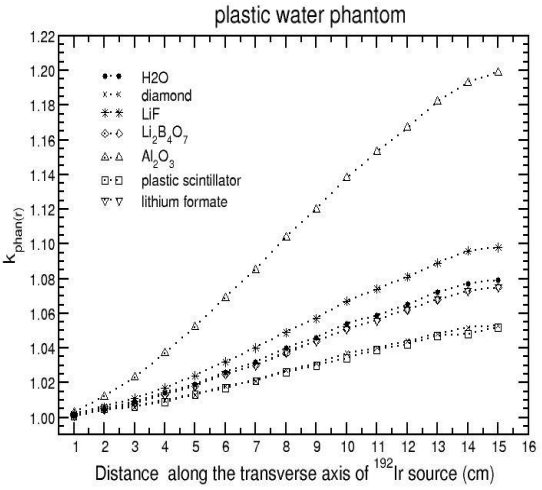

(d)

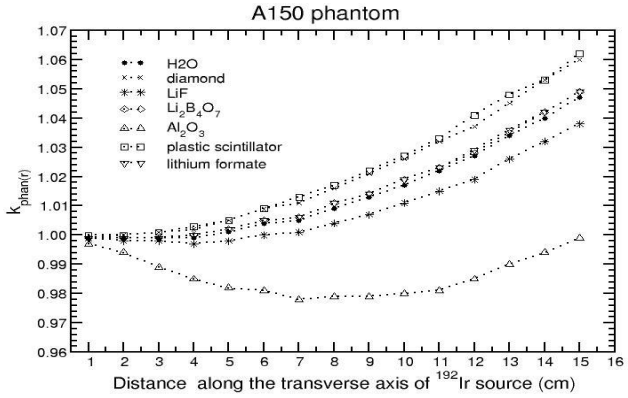

(e)

Fig.5.7 Phantom scatter correction, $k_{phan}(r)$*, presented as a function of distance along the transverse axis of the* ^{192}*Ir brachytherapy source for solid-state detectors* $Li_2B_4O_7$*, LiF, diamond, Plastic Scintillator, Lithium Formate,* Al_2O_3 *and water in (a) PMMA (b) polystyrene (c) RW1 (d) plastic water (e) A150 phantom.*

Phantoms such as solid water, virtual water, RW1, RW3 and WE210 are water-equivalent at all distances (1-15 cm) for the investigated radiochromic films other than XRT and XRQA. Table 5.3 presents the $k_{phan}(r)$ values of the XRT and XRQA films for all of these phantoms. The polystyrene, plastic water, PMMA, and A150 phantoms show distance-dependent $k_{phan}(r)$ values for the investigated radiochromic films, which are presented in Figs. 5.8 (a) - (d), respectively. $k_{phan}(r)$ decreased with *r* for all of the radiochromic films in the polystyrene phantom (see Fig. 5.8 (a)). However, the degree of decrease is significant for the XRT and XRQA films compared to all other films. For example, the value decreased to 0.779 and 0.767 at 15 cm for the XRT and XRQA films, respectively. For the plastic-water phantom, $k_{phan}(r)$ increased with *r* for all of the investigated films (see Fig. 5.8 (b)). The degree of increase was significant for the XRT and XRQA films (about 40 % larger

than unity at 15 cm) compared to all other films. For the PMMA phantom, $k_{phan}(r)$ decreased with *r* for EBT2 (lot 020609), RTQA, XRT and XRQA films and increased with *r* for the remaining radiochromic films (see Fig. 5.8 (c)). However, for the A150 phantom, $k_{phan}(r)$ decreases with *r* for XRT and XRQA films and increased with *r* for the remaining radiochromic films (see Fig. 5.8 (d)). The higher atomic numbers of the XRT and XRQA films gave higher $k_{phan}(r)$ values in solid phantoms.

Table 5.3 Monte Carlo-calculated phantom scatter correction, $k_{phan}(r)$, for XRT and XRQA films shown as a function of distance along the transverse axis of the ^{192}Ir source.

Distance	RW1		RW3		Virtual water		Soild water		WE210	
r (cm)	XRT	XRQA	XRT	XRQA	XRT	XRQA	XRT	XRQA	XRT	XRQA
1	1.001	1.001	0.996	0.995	1.003	1.004	1.001	1.002	1.007	1.009
2	1.001	1.001	0.992	0.990	1.011	1.014	1.007	1.009	1.018	1.023
3	0.995	0.994	0.983	0.979	1.013	1.016	1.009	1.011	1.024	1.030
4	0.992	0.990	0.976	0.972	1.019	1.023	1.014	1.016	1.033	1.040
5	0.987	0.985	0.972	0.967	1.025	1.029	1.018	1.020	1.039	1.046
6	0.983	0.982	0.967	0.963	1.030	1.034	1.023	1.026	1.047	1.054
7	0.979	0.976	0.963	0.958	1.033	1.037	1.027	1.030	1.050	1.057
8	0.977	0.975	0.960	0.956	1.038	1.042	1.032	1.036	1.056	1.063
9	0.971	0.969	0.957	0.953	1.040	1.044	1.035	1.038	1.058	1.064
10	0.970	0.968	0.956	0.952	1.044	1.048	1.040	1.043	1.063	1.070
11	0.965	0.963	0.952	0.948	1.045	1.049	1.039	1.042	1.062	1.068
12	0.962	0.960	0.950	0.946	1.050	1.054	1.044	1.047	1.065	1.071
13	0.961	0.959	0.948	0.945	1.053	1.057	1.046	1.049	1.068	1.074
14	0.957	0.955	0.948	0.944	1.052	1.056	1.049	1.052	1.068	1.074
15	0.955	0.953	0.947	0.943	1.055	1.058	1.051	1.054	1.068	1.074

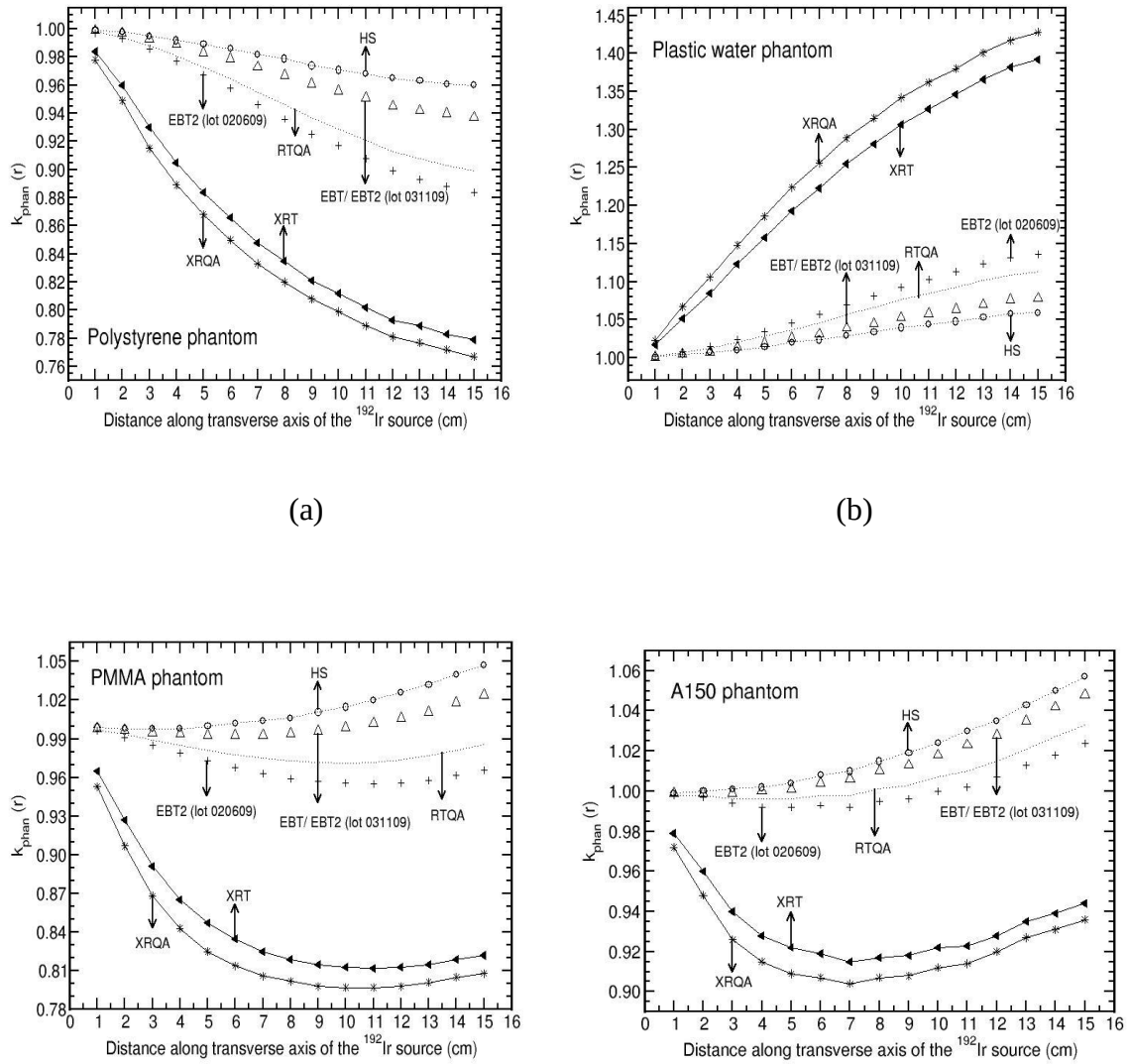

Fig.5.8 Phantom scatter correction, $k_{phan}(r)$*, presented as a function of distance along the transverse axis of the* ^{192}*Ir brachytherapy source for different radiochromic films (a) Polystyrene, (b) plastic water, (c) PMMA, and (d) A150.*

^{169}Yb source

For ^{169}Yb brachytherapy source, none of the investigated phantoms is water-equivalent. For a given *r*, phantoms such as solid water, virtual water and WE210 show statistically

identical values of $k_{phan}(r)$ which are shown in Fig. 5.9 (a). This is because at ^{169}Yb energies, Compton scattering is the predominant interaction and the cross section values of these phantoms are comparable. Distance-dependent $k_{phan}(r)$ values of remaining phantoms are presented in Figs. 5.9(b) - (g) for all the investigated solid state detectors including water detector.

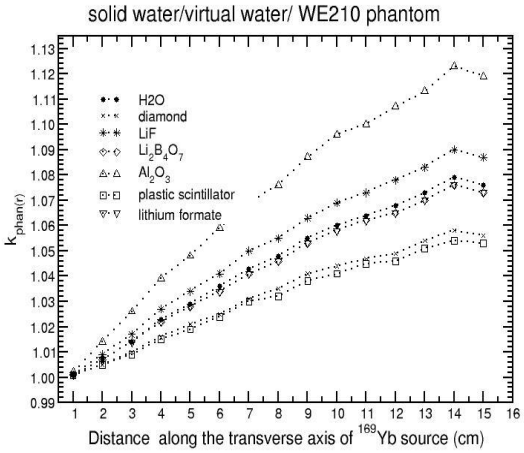

(a)

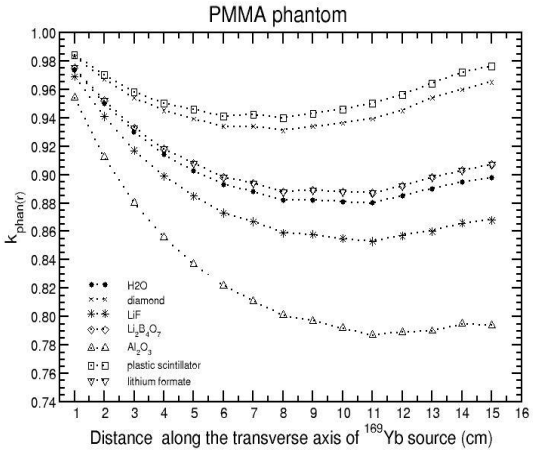

(b)

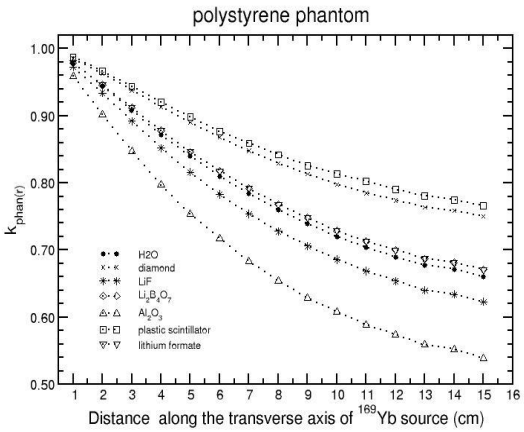

(c)

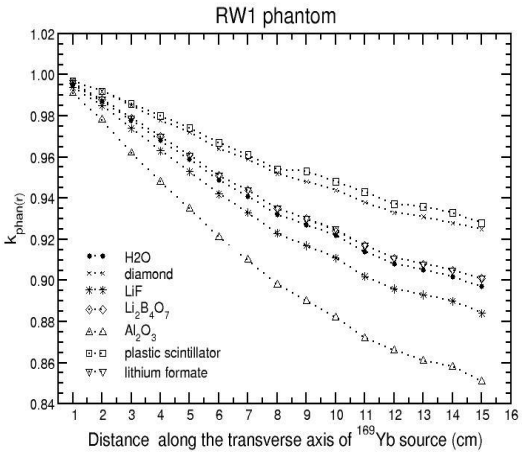

(d)

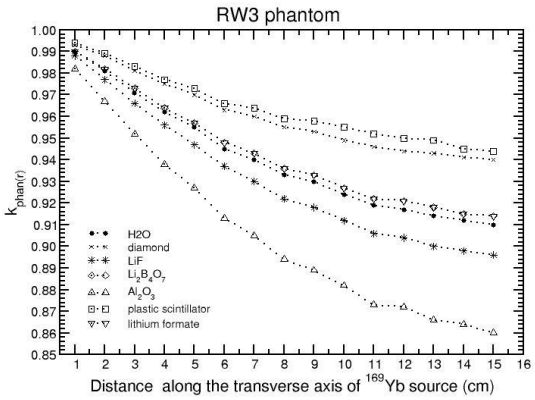

(e)

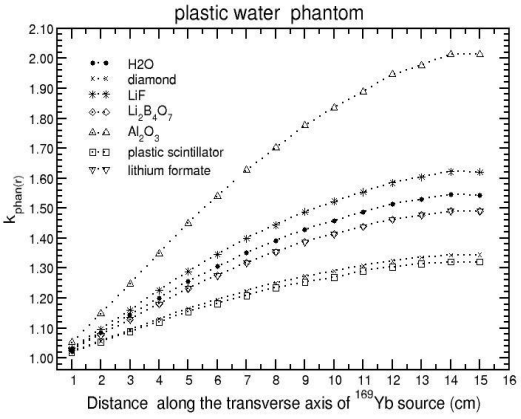

(f)

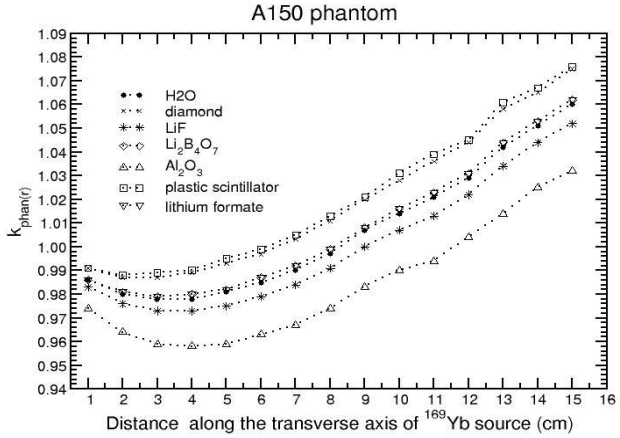

(g)

Fig.5.9 Phantom scatter correction, $k_{phan}(r)$*, presented as a function of distance along the transverse axis of the* ^{169}*Yb source for different solid-state detectors (a) solid water/ virtual water/ WE210 (b)PMMA (c) polystyrene (d) RW1(e) RW3 (f) plastic water (g) A150.*

Phantoms such as PMMA, polystyrene, RW1 and RW3 show decrease in $k_{phan}(r)$ values with *r* for all the investigated solid state detectors. The degree of decrease in $k_{phan}(r)$ values with *r* is significant for polystyrene phantom (about 47 % smaller than unity for Al_2O_3

detector at 15 cm). This is because, for this phantom: (a) linear attenuation coefficient, μ values at 50 keV are smaller than water, and (b) Compton scattering cross section is higher than water. RW1 and RW3 phantoms show a similar trend, as these two phantoms have comparable μ values and Compton scattering cross section at the ^{169}Yb energies. Plastic water and A150 phantoms show increase in $k_{phan}(r)$ values with r for all the investigated solid state detectors. The degree of increase is significant for plastic water phantom (about 34 % at a distance of 15 cm for diamond detector). This is because for this phantom at typical energy 50 keV of ^{169}Yb: (a) μ values are higher than water (factor is 1.24), (b) Compton scattering cross section is smaller than water (factor is 0.80), and (c) Photoelectric absorption cross section is higher than by a factor of 2.34.

Phantoms such as solid water, virtual water, and WE210 showed statistically identical $k_{phan}(r)$ values for the investigated radiochromic films. However, the RW1 and RW3 phantoms also showed identical $k_{phan}(r)$ values (with a maximum deviation of about 2.0 % at 15 cm for XRQA film). The $k_{phan}(r)$ values of the EBT and EBT2 (lot 031109) films were statistically identical for all of the investigated phantoms and were presented in Fig.5.10 (a). Figs.5.10 (b) - (f) present the $k_{phan}(r)$ values for EBT2 (lot 020609), RTQA, HS, XRT and XRQA radiochromic films for the investigated phantoms. Phantoms including PMMA, polystyrene, RW1 and RW3, showed a decrease in $k_{phan}(r)$ values with r for all of the investigated films. However, the degree of decrease was significant for the polystyrene phantom (about 40 % smaller than unity at 15 cm for XRT and XRQA films). The remaining phantoms, including solid water, virtual water, plastic water, A150 and WE210 showed an increase in $k_{phan}(r)$ values with r for all of the investigated films. The degree of

increase was significant for the plastic water phantom (about a factor of 2 at 15 cm for XRT and XRQA films) compared to all other phantoms.

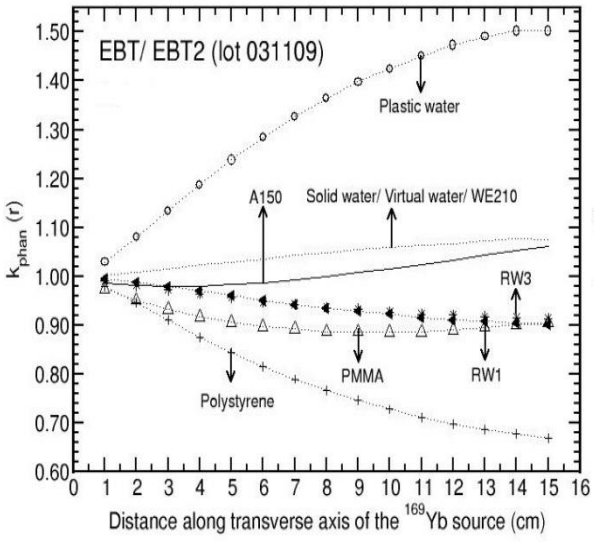

(a)

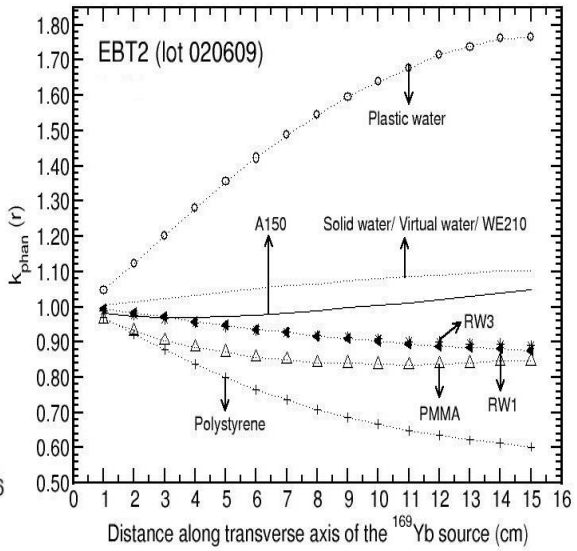

(b)

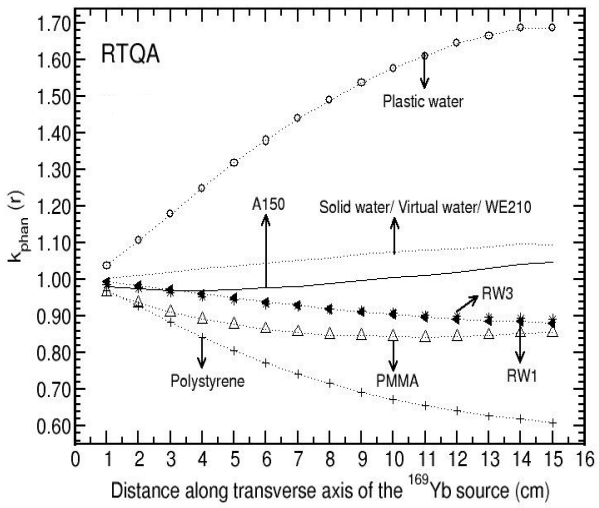

(c)

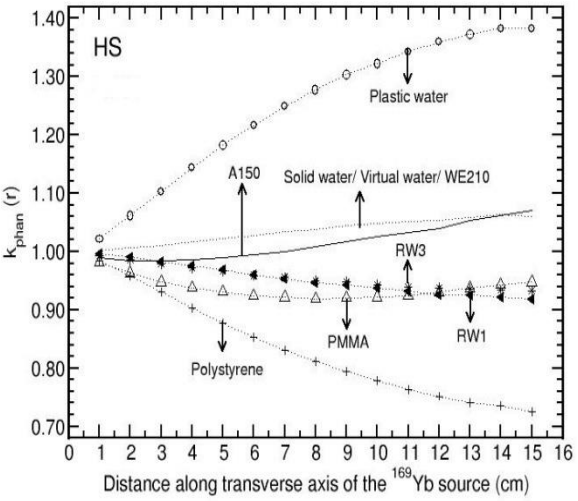

(d)

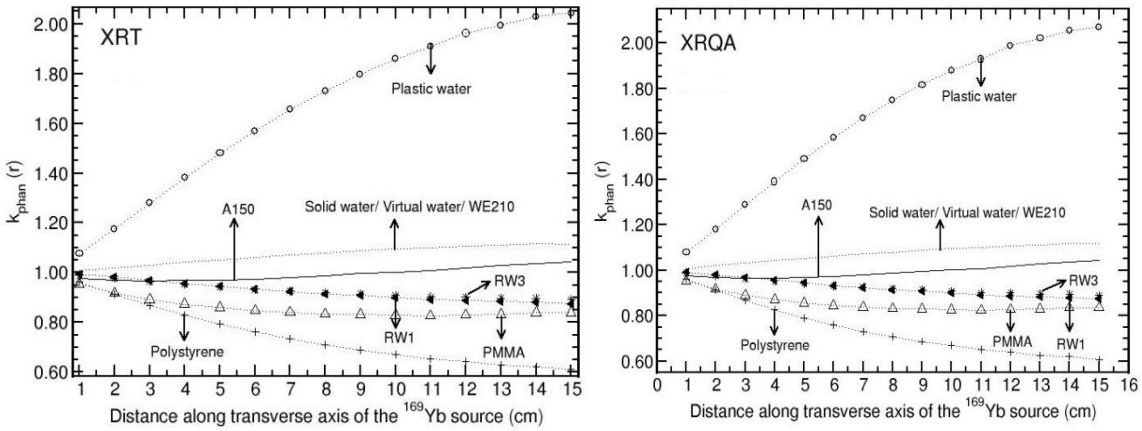

(e) (f)

Fig.5.10 Phantom scatter correction, $k_{phan}(r)$*, presented as a function of distance along the transverse axis of the* ^{169}*Yb brachytherapy source for different phantoms (a) EBT and EBT2 (lot 031109) (b) EBT2 (lot 020609), (c) RTQA (d) HS (e) XRT (f) XRQA.*

5.3.2 Low energy brachytherapy sources (^{131}Cs, ^{125}I and ^{103}Pd)

For a given detector, $k_{phan}(r)$ depends on distance from the source for the investigated phantoms, but the degree of deviation from unity depends on the type of solid phantom and the brachytherapy source. For all the investigated detectors and sources, $k_{phan}(r)$ decreases with *r* for polystyrene, PMMA, RW1 and RW3 phantoms and increases with *r* for the remaining phantoms. As discussed in the previous Section 5.3.1, for a given solid phantom, $k_{phan}(r)$ values change with detector type for high energy brachytherapy sources such as ^{60}Co, ^{137}Cs, ^{192}Ir and ^{169}Yb. However, the results for low energy brachytherapy sources (^{131}Cs, ^{125}I and ^{103}Pd.) show that for a given solid phantom and given source, $k_{phan}(r)$ value does not change with detector type. Figs. 5.11 (a), (b), (c) present the $k_{phan}(r)$ values for the

investigated solid-state detectors including water detectorin PMMA phantom for ^{131}Cs, ^{125}I and ^{103}Pd brachytherapy sources, respectively. $k_{phan}(r)$ values are presented for EBT2 film for ^{131}Cs, ^{125}I and ^{103}Pd brachytherapy sources, in Figs. 5.12 (a) - (c), respectively for different solid phantoms. For a given phantom, $k_{phan}(r)$ values change about 20 % among the sources. For example, for solid water phantom, $k_{phan}(r)$ values are 1.15, 1.03 and 1.26 at a distance of 5 cm from the ^{131}Cs, ^{125}I and ^{103}Pd sources, respectively. Similarly, for polystyrene phantom, $k_{phan}(r)$ values are 0.446, 0.371 and 0.166 at a distance of 5 cm from the ^{131}Cs, ^{125}I and ^{103}Pd sources, respectively.

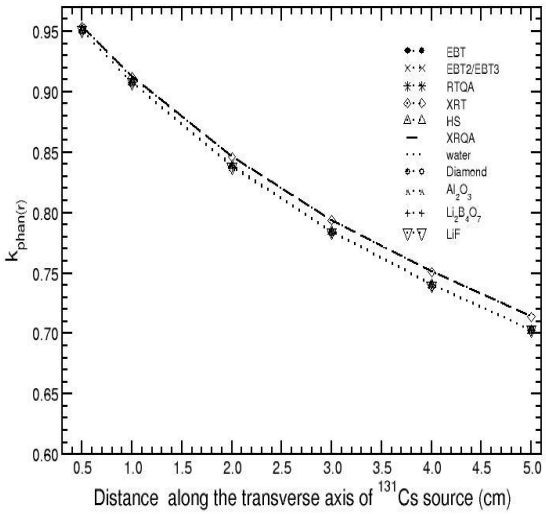

(a)

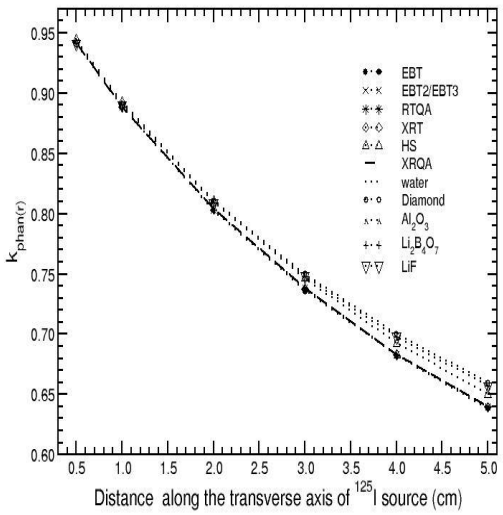

(b)

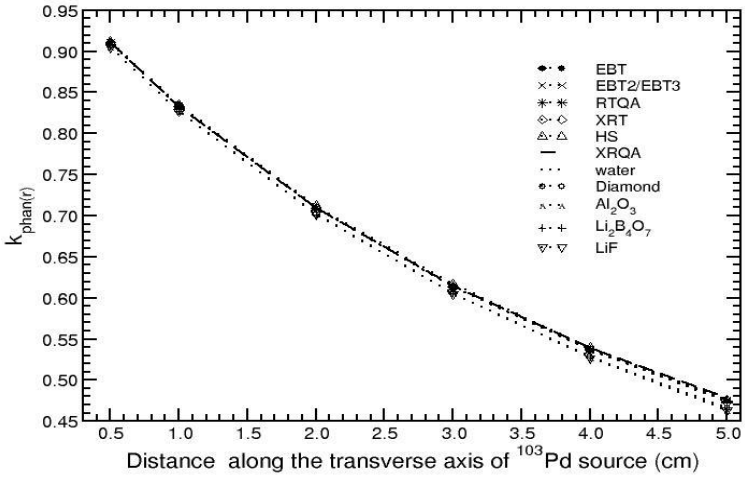

(c)

Fig.5.11 Phantom scatter correction, $k_{phan}(r)$*, presented for the investigated detectors as a function of distance along the transverse axis (a)* ^{131}Cs *(b)* ^{125}I *(c)* ^{103}Pd *brachytherapy sources.*

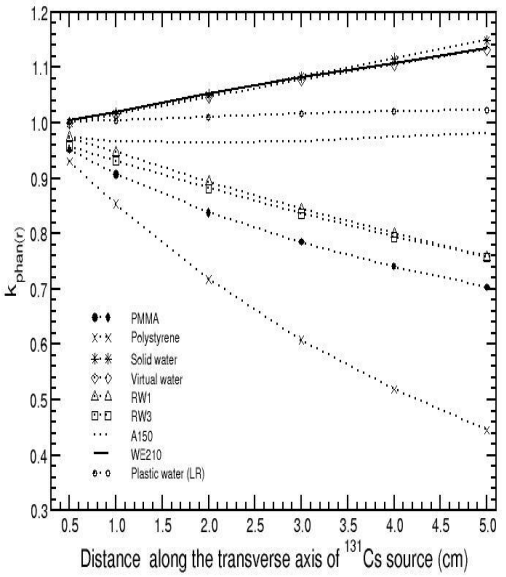

(a)

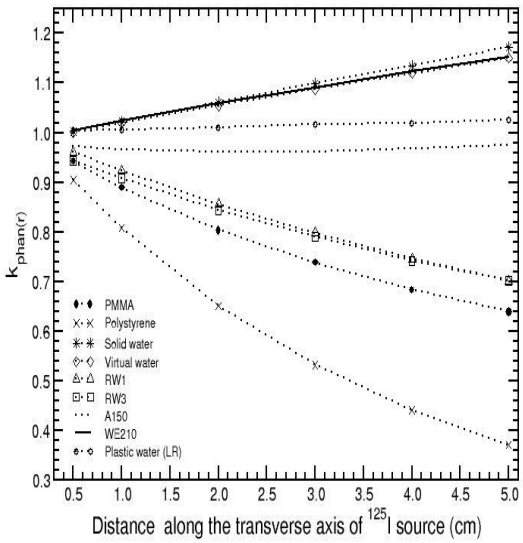

(b)

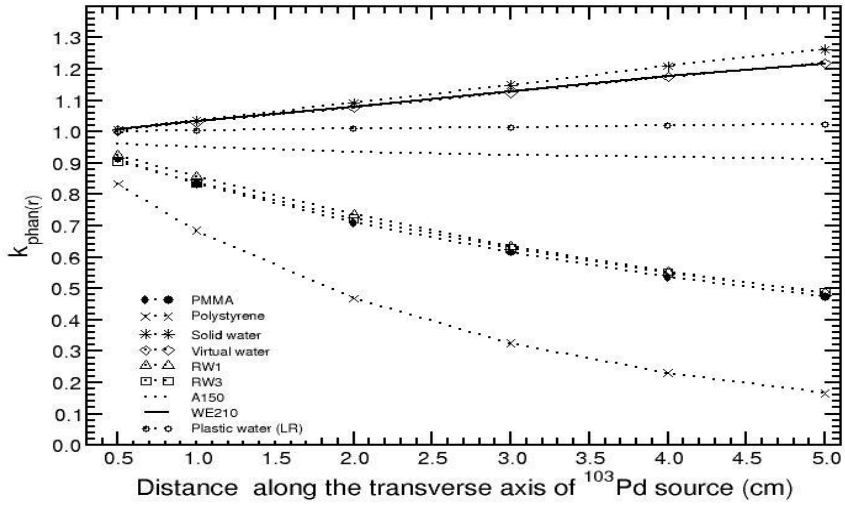

(c)

Fig.5.12 Phantom scatter correction, $k_{phan}(r)$*, presented for EBT2 film in the investigated phantoms as a function of distance along the transverse axis (a)* ^{131}Cs *(b)* ^{125}I *(c)* ^{103}Pd *brachytherapy sources.*

Plastic water (LR) and A150 solid phantoms are the water-equivalent among the investigated phantoms. The maximum deviation is about 2.5 % at a distance of 5 cm from the source for these two phantoms. However, phantoms such as solid water, virtual water and WE210 are water-equivalent at short distances (up to1 cm) for all the investigated detectors and brachytherapy sources. However, as the distances increases these phantoms tend towards non-water-equivalence (at 5 cm, $k_{phan}(r)$ value is about 24 % larger than unity). Remaining phantoms such as PMMA, polystyrene, RW1 and RW3 showed $k_{phan}(r)$ values significantly larger than unity. For example, polystyrene and PMMA showed

$k_{phan}(r)$ values lesser than unity of about 80 % and 50 %, respectively at 5 cm distance from the ^{103}Pd brachytherapy source.

5.4 Discussion

The collision-kerma to the detector at a distance *r* from the source in a phantom is due to both primary and scattered photons. The collision-kerma due to primary photons is characterized by exponential attenuation of the primary photons and the mass-energy-absorption coefficient (μ_{en}/ρ) of the detector at the primary photon energy. In order to understand the variations in the primary component of collision-kerma, (μ) data of photons in the energy range 10 keV – 1.25 MeV were analysed for the investigated solid phantoms and water using the state-of-the art XCOM (Berger and Hubbell 1987). Table 5.4 presents the values of μ for all the investigated phantoms for photons in the range 10 keV – 1.25 MeV. Table 5.5 presents the ratio of μ values of the phantoms normalized to water for the above energy range. Note that the predominant primary gamma lines involved in the present study are 50 keV (^{169}Yb), 300 keV (^{192}Ir), 662 keV (^{137}Cs), 1.25 MeV (^{60}Co) 20 keV and 30 keV for low energy brachytherapy sources. An analysis of exponential attenuation of photons in water and the phantoms suggests that for photon energy 50 keV and above, phantoms other than plastic water produce comparable attenuation at 1 cm. However, at 15 cm, the low energy photons (below 50 keV) show significant variations in exponential attenuation by the phantoms (other than WE210 at 50 keV) as compared to water. At 300 keV and above, all the phantoms other than PMMA, A150 and WE210 demonstrate comparable attenuation as compared to water (attenuation by Polystyrene is larger by 5 % at 300 keV when compared to water).

Table 5.4 Values of linear attenuation coefficient μ (cm^{-1}) presented for different phantoms as a function of photon energy.

Energy (MeV)	Water	Polystyrene	PMMA	A150	Plastic Water	Solid Water	Virtual Water	RW1	RW3	WE210
0.01	5.3300	2.3521	3.9948	4.7199	10.7581	5.2929	5.2324	3.7801	3.5122	5.2362
0.02	0.8098	0.4626	0.6800	0.7969	1.6228	0.8517	0.8425	0.6464	0.6201	0.8391
0.03	0.3756	0.2798	0.3608	0.3924	0.6258	0.3936	0.3895	0.3286	0.3252	0.3858
0.04	0.2683	0.2314	0.2797	0.2887	0.3747	0.2773	0.2746	0.2473	0.2489	0.2709
0.05	0.2269	0.2105	0.2468	0.2477	0.2811	0.2323	0.2300	0.2148	0.2180	0.2265
0.06	0.2059	0.1982	0.2290	0.2263	0.2368	0.2094	0.2073	0.1976	0.2014	0.2039
0.08	0.1837	0.1829	0.2084	0.2032	0.1961	0.1857	0.1840	0.1785	0.1826	0.1807
0.10	0.1707	0.1721	0.1953	0.1893	0.1767	0.1722	0.1706	0.1668	0.1709	0.1675
0.15	0.1505	0.1535	0.1733	0.1674	0.1517	0.1516	0.1502	0.1477	0.1514	0.1474
0.20	0.1370	0.1401	0.1580	0.1525	0.1373	0.1380	0.1367	0.1347	0.1381	0.1341
0.30	0.1186	0.1216	0.1371	0.1322	0.1183	0.1195	0.1183	0.1168	0.1198	0.1161
0.40	0.1061	0.1089	0.1227	0.1182	0.1058	0.1069	0.1059	0.1046	0.1072	0.1039
0.50	0.0969	0.0994	0.1120	0.1080	0.0965	0.0975	0.0966	0.0954	0.0979	0.0948
0.60	0.0896	0.0919	0.1035	0.0998	0.0892	0.0902	0.0893	0.0883	0.0905	0.0877
0.80	0.0787	0.0807	0.0909	0.0876	0.0783	0.0792	0.0784	0.0775	0.0795	0.0770
1.00	0.0707	0.0726	0.0818	0.0788	0.0704	0.0712	0.0705	0.0697	0.0714	0.0692
1.25	0.0632	0.0649	0.0731	0.0705	0.0629	0.0637	0.0631	0.0623	0.0639	0.0619

The phantoms PMMA and A150 show higher attenuation than water. For example, even at photon energy 1.25 MeV, PMMA and A150, at 15 cm, demonstrate attenuation larger by factors of 1.16 and 1.11, respectively, when compared to water. Note that, the above analysis of exponential attenuation of photons in the phantoms has direct influence on the primary component of the collision-kerma.

Table 5.5 Values of linear attenuation coefficient μ (cm^{-1}) normalized to that of water presented for different phantoms as a function of photon energy.

Energy (MeV)	Polystyrene	PMMA	A150	Plastic Water	Solid Water	Virtual Water	RW1	RW3	WE210
0.010	0.441	0.749	0.886	2.018	0.993	0.982	0.709	0.659	0.982
0.020	0.571	0.840	0.984	2.004	1.052	1.040	0.798	0.766	1.036
0.030	0.745	0.961	1.045	1.666	1.048	1.037	0.875	0.866	1.027
0.040	0.862	1.042	1.076	1.397	1.034	1.023	0.922	0.928	1.010
0.050	0.928	1.088	1.092	1.239	1.024	1.014	0.946	0.961	0.998
0.060	0.963	1.112	1.099	1.150	1.017	1.007	0.960	0.978	0.990
0.080	0.995	1.134	1.106	1.068	1.011	1.001	0.972	0.994	0.984
0.100	1.008	1.144	1.109	1.035	1.009	0.999	0.977	1.001	0.981
0.150	1.020	1.151	1.112	1.008	1.007	0.998	0.982	1.006	0.979
0.200	1.023	1.154	1.113	1.002	1.007	0.998	0.983	1.008	0.979
0.300	1.025	1.156	1.115	0.998	1.007	0.998	0.985	1.010	0.979
0.400	1.026	1.156	1.114	0.997	1.008	0.998	0.986	1.011	0.979
0.500	1.026	1.156	1.114	0.996	1.007	0.997	0.985	1.010	0.979
0.600	1.026	1.156	1.115	0.996	1.007	0.997	0.985	1.010	0.979
0.800	1.026	1.156	1.114	0.995	1.007	0.997	0.985	1.010	0.978
1.000	1.026	1.156	1.114	0.995	1.007	0.997	0.985	1.010	0.978
1.250	1.026	1.156	1.114	0.995	1.007	0.997	0.985	1.010	0.978

Quantification of collision-kerma due to scattered photons is complex it would depend upon several factors such as fraction of photons that would undergo interactions such as photo electric effect, Rayleigh Scattering, Compton Scattering and Pair Production (for the photon energies investigated in the present study, Pair Production is not important). For example, a

photon with an initial energy $h\nu_0$ making a contribution at the detector location through Compton scattering depends upon: (a) the spatial point the in the phantom at which Compton scattering occurs, (b) probability that the scattered photon passes through the detector location which includes exponential attenuation of scattered photon energy between the scattering point and the detector, and (c) mass energy absorption coefficient of the detector material at the scattered photon energy. Note that μ values at both primary and scattered photon energies play an important role on response of detector.

Following discussion is based on an analysis of macroscopic cross section data of photons based on XCOM (Berger and Hubbell 1987). In this analysis, the macroscopic cross sections such as photoelectric and Compton scattering were normalized to the total cross section. This normalization was done for all the phantoms. The normalized Compton scattering cross sections of all the phantoms are comparable to that of water at photon energies 150 keV and above. A similar analysis shows that A150, solid water, virtual water, WE210 are comparable to that of water in the entire photon energy range of 10 keV - 1.25 MeV, and RW1 and RW3 in the energy range of 80 keV - 1.25 MeV. At low energies, the phantoms such as polystyrene, PMMA, A150, plastic water, RW1 and RW3 show significantly higher values of Compton scattering cross sections. Fig. 5.13 (a) presents values of Compton scattering macroscopic cross section normalized to total cross section for the investigated phantoms in the photon energy range 30 keV - 150 keV. At 30 keV, the normalized Compton scattering cross section values are higher by factors of 1.40, 1.20, 1.08, 1.18 and 1.15, respectively, for the phantoms polystyrene, PMMA, A150, RW1 and RW3, when compared to that of water. For solid water, virtual water and WE210, the factor is about 0.97. Due to the presence of high atomic number elements in the plastic water, the

Compton scattering cross section at 30 keV is significantly less as compared to water (factor is 0.6). At 50 keV, the above comparison provides a factor of 1.11 for Polystyrene, 1.05 - 1.07 for PMMA, RW1 and RW3, 1.03 for A150, 0.99 for solid water, WE210 and virtual water. The photoelectric absorption cross section data of all the phantoms were analyzed. The Photoelectric absorption is important only at low photon energies. Hence, the comparison is restricted only in the energy range of 30 – 100 keV (see Fig. 5.13(b)). The analysis shows that the Photoelectric cross sections are higher for phantoms plastic water, solid water, virtual water and WE210. However, the Photoelectric absorption is important only for the ^{169}Yb source as it principal gamma line is at 50 keV (about 53% of total emission). At his energy, probability that the photon will undergo Photoelectric absorption is 0.12 for water and A150, 0.14 for solid water, virtual water and WE210, about 0.10 for RW1 and RW3 and about 0.29 for plastic water. At 30 keV, the Photoelectric absorption is significant for all phantoms. For example, the fractions of photons that will undergo Photoelectric absorption are 0.39 for water, 0.20 for polystyrene, 0.3 for PMMA, 0.37 for A150, 0.63 for plastic water, 0.42 for solid water, virtual water and WE210, and 0.34 for RW1. In the present study, Rayleigh scattering is important. At 30 keV, water, PMMA and Polystyrene show normalized Rayleigh cross section value of about 0.12, A150, solid water, virtual water, RW1, RW3 and WE210 show a value of about 0.10. At this energy, the normalized Rayleigh scattering cross section for plastic water is 0.08. At 50 keV, all phantoms show significantly smaller cross section than water (smaller by factor of 0.75 – 0.86 depending upon the phantom).

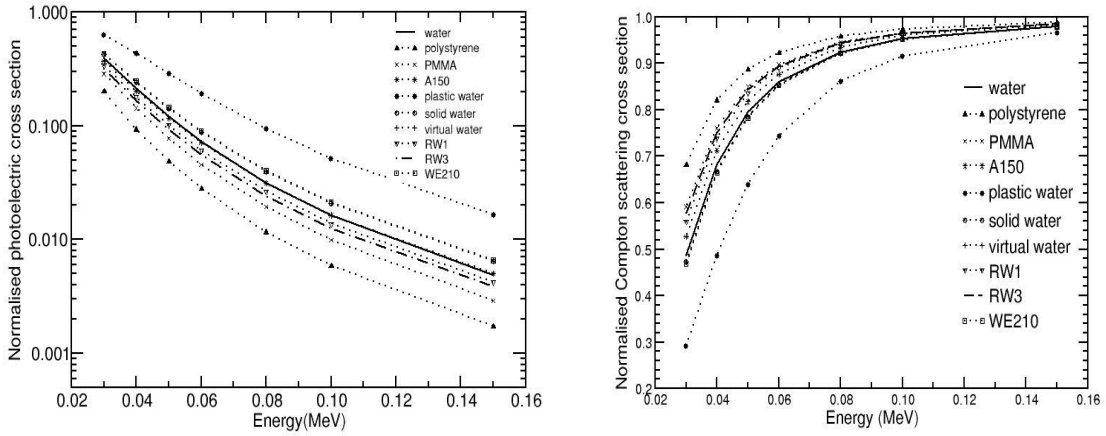

(a) (b)

Fig.5.13 Macroscopic cross section normalized to total macroscopic cross section as a function of photon energy (a) Photoelectric absorption (b) Compton scattering. Data are based on XCOM (Berger and Hubbell 1987).

$k_{phan}(r)$ decreases with *r* for polystyrene phantom which is due to increased contribution from multiple scattered photons. Note that at low energy, polystyrene has high Compton scattering cross section than water. For plastic water, PMMA and A150 phantom, $k_{phan}(r)$ increases with *r*. Note that both PMMA and A150 phantoms have higher μ for a wide range of photon energies (40 keV - 1.25 MeV). Hence, $k_{phan}(r)$ increases with *r*. For plastic water, the scatter contribution is affected by: (a) higher values of μ at low energy photons, (b) smaller Compton scattering cross section at low energy photons, and (c) higher values of Photoelectric absorption cross section at low energy photons. Phantoms such as polystyrene, plastic water, solid water, virtual water, RW1, RW3 and WE210 are water-equivalent (i.e $k_{phan}(r)$ is unity) at all distances (1-15 cm) for Lithium Formate detector. This is because, for these phantoms: (a) exponential attenuation of ^{60}Co photons at these distances are same,

and (b) Compton scattering cross section is comparable for wide range of photon energies (150 keV - 1.25 MeV). Whereas, PMMA and A150 phantoms show increase in $k_{phan}(r)$ values with distance. Although these phantoms have similar Compton scattering cross section values as that of water (80 keV - 1.25 MeV), differences in the exponential attenuation of primary photons (see Tables 5.5 and 5.6 at 1.25 MeV) result in deviation of $k_{phan}(r)$ values from unity (up to about 1.05 for PMMA and 1.04 for A150 at 15 cm) as the distance increases. For a given *r*, phantoms such as solid water, virtual water and WE210 show statistically identical values of $k_{phan}(r)$.This is because for high energy brachytherapy sources, Compton scattering is the predominant interaction and the cross section values of these phantoms are comparable. As the distance increases, $k_{phan}(r)$ increases to about 1.07 for these phantoms. Phantoms such as PMMA, polystyrene, RW1 and RW3 show decrease in $k_{phan}(r)$ values with *r*. However, RW1 and RW3 phantoms show a similar trend, as these two phantoms have comparable μ values and Compton scattering cross section at the ^{169}Yb energies. For PMMA, $k_{phan}(r)$ decreases initially, from 0.988 to 0.901 when *r* is increased from 1- 5 cm, and thereafter itis almost constant with a value of about 0.90. For PMMA, at ^{169}Yb energies, values of μ and Compton scattering cross section are higher when compared to water. It appears that scattering is a major contributor of $k_{phan}(r)$ than the exponential attenuation of primary photons for PMMA. Although values of μ and Compton scattering cross section for A150 phantom are comparable to that of PMMA, A150 shows a different trend on $k_{phan}(r)$ values. $k_{phan}(r)$ is constant (about 0.98) up to *r* = 6 cm and thereafter it increases to 1.06 at *r* = 15 cm. Thus there is a tendency on compensation of exponential attenuation of primary photons by scatter contribution up to a

distance of about 10 cm and there after exponential attenuation of primary photons is a major contributor of $k_{phan}(r)$. This is because, density of PMMA (1.19 g/cm^3) is higher than A150 (1.127 g/cm^3) which results in more number of atoms present in PMMA than in A150. As a result there will be more number of electrons present in PMMA than in A150 which enhances number of Compton scattering events comparatively more in PMMA.

For polystyrene, degree of decrease in $k_{phan}(r)$ with *r* is significant (about 36 % smaller than unity at 15 cm). This is because, for this phantom: (a) μ values at 50 keV are smaller than water, and (b) Compton scattering cross section is higher than water. The phantom plastic water shows increase in $k_{phan}(r)$ values with *r*. The degree of increase is significant for plastic water phantom (about 52 % at a distance of 15 cm). This is because for this phantom at typical energy 50 keV of ^{169}Yb: (a) μ values are higher than water (factor is 1.24), (b) Compton scattering cross section is smaller than water (factor is 0.80), and (c) photo electric cross section is higher than by a factor of 2.34. $k_{phan}(r)$ values of diamond detector are higher by 6 % and 11 % for PMMA and polystyrene phantoms, respectively to that of Lithium Formate detector at a distance of 15 cm. Whereas for plastic water phantom, it is lower by 10 % as compared to Lithium Formate detector. For LiF detector, $k_{phan}(r)$ values are lower by 4 % and 7 % for PMMA and polystyrene phantoms, respectively to that of Lithium Formate detector. However for plastic water phantom, it is higher by 9% as compared to Lithium Formate detector. $Li_2B_4O_7$ detector shows $k_{phan}(r)$ values identical to that of water detector and diamond detector shows

$k_{phan}(r)$ values identical to that of plastic scintillator detector for all the investigated phantoms for high energy sources.

For photon energy 30 keV, phantoms such as water, A150, solid water, virtual and WE210 produce comparable attenuation. RW1 and RW3 phantoms demonstrate a comparable attenuation which is lesser by 13% as compared to water at 30 keV. PMMA and polystyrene showed 4 % and 25 % lesser attenuation than water, respectively. Similarly, for photon energy 20 keV, A150 phantom demonstrated comparable attenuation to that of water. Solid water, virtual and WE210 showed comparable attenuation which is larger by 5 % as compared to water at this energy. RW1 and RW3 phantoms also showed comparable attenuation which is lesser by 20 % as compared to water. PMMA and polystyrene showed 17 % and 63 % lesser attenuation than water, respectively. Hence, $k_{phan}(r)$ value decreases with r for polystyrene, PMMA, RW1 and RW3 phantoms and increases with r for the remaining phantoms. Plastic water (LR) and A150 phantom were the water-equivalent among the investigated phantoms. Additionally, phantoms such as solid water, virtual water and WE210 are also water-equivalent at short distances (up to 1 cm). Schoenfeld et al (2017) also concluded that plastic water (LR) was the only water-equivalent phantom material among their investigated phantoms which is consistent with the observation made in the present study. Similarly, results obtained by Schoenfeld et al (2017) for other solid phantoms such as solid water, virtual water, RW1, RW3, PMMA and polystyrene compare well with the present study. Note that, A150 and WE210 phantoms were not included in their study.

Unlike high energy brachytherapy sources, $k_{phan}(r)$ value is independent of detector for the investigated low energy sources. This is due to the fact that the mean energy does not change significantly with distance from the source for low energy brachytherapy sources. Hence, (μ_{en}/ρ) of the detector material does not play any role on $k_{phan}(r)$ values for low energy brachytherapy sources. An auxiliary simulation was carried out to confirm it in which photon fluence was scored at distances 1 cm and 5 cm for ^{131}Cs source in water and PMMA phantom. It was found that, the ratio of photon fluence in water and photon fluence in PMMA phantom was identical with the corresponding $k_{phan}(r)$ values. This investigation reveals that $k_{phan}(r)$ is independent of detector material and photon fluence information is sufficient to determine $k_{phan}(r)$ for low energy brachytherapy photon sources.

5.5 Summary and conclusion:

$k_{phan}(r)$ for various solid phantoms (PMMA, polystyrene, solid water, virtual water, RW1, RW3, plastic water, A150 and WE210) are calculated for different solid state detectors (diamond, H_2O, Al_2O_3, $Li_2B_4O_7$, LiF, Lithium Formate and Plastic Scintillator) and various radiochromic films (EBT, EBT2 (lot 031109), EBT2 (lot 020609), RTQA, XRT, XRQA and HS) as a function of distance along the transverse axis of the ^{60}Co, ^{137}Cs, ^{192}Ir, ^{169}Yb, ^{131}Cs, ^{125}I and, ^{103}Pd brachytherapy sources using the Monte Carlo-based EGSnrc code system. For a given detector, $k_{phan}(r)$ depends on distance from the source for the investigated phantoms, but the degree of deviation from unity depends on the type of solid phantom and the brachytherapy source. It is interesting to note that, unlike for high energy sources (^{60}Co, ^{137}Cs, ^{192}Ir and ^{169}Yb), $k_{phan}(r)$ values did not change with detector type for low energy sources (^{131}Cs, ^{125}I and ^{103}Pd) at all distances. Summary of $k_{phan}(r)$ results for the

investigated solid-state detectors and radiochromic films are shown in Table 5.6 and 5.7, respectively for high energy brachytherapy sources.

Table 5.6 Summary of $k_{phan}(r)$ results presented for diamond, Al_2O_3, $Li_2B_4O_7$, LiF, Lithium Formate and Plastic Scintillator detectors for the ^{60}Co, ^{137}Cs, ^{192}Ir and ^{169}Yb sources.

Solid	Diamond / Plastic scintillator				Lithium Formate / /H_2O/ $Li_2B_4O_7$				Al_2O_3				LiF			
Phnatoms	^{60}Co	^{137}Cs	^{192}Ir	^{169}Yb	^{60}Co	^{137}Cs	^{192}Ir	^{169}Yb	^{60}Co	^{137}Cs	^{192}Ir	^{169}Yb	^{60}Co	^{137}Cs	^{192}Ir	^{169}Yb
PMMA	No	No	No	No	No	No	No	No	Yes	No	No	No	No	No	Yes	No
Polystyrene	Yes	No	No	No	Yes	No	No	No	No	No	No	No	Yes	No	No	No
Plastic water	Yes	No	No	No	Yes	No	No	No	No	No	No	No	Yes	No	No	No
RW1	Yes	Yes	No	No	Yes	Yes	No	No	Yes	Yes	No	No	Yes	Yes	No	No
RW3	Yes	Yes	Yes	No	Yes	Yes	Yes	No	Yes	Yes	No	No	Yes	Yes	Yes	No
Virtual water	Yes	Yes	Yes	No	Yes	Yes	Yes	No	Yes	Yes	No	No	Yes	Yes	Yes	No
Solid water	Yes	Yes	Yes	No	Yes	Yes	Yes	No	Yes	Yes	No	No	Yes	Yes	Yes	No
A150	No	No	No	No	No	No	No	No	No	No	No	No	No	No	No	No
WE210	Yes	Yes	Yes	No	Yes	Yes	Yes	No	Yes	Yes	No	No	Yes	Yes	Yes	No

Table 5.7 Summary of $k_{phan}(r)$ results presented for radiochromic films (EBT, EBT2, RTQA, HS XRQA and XRT) for the ^{60}Co, ^{137}Cs, ^{192}Ir and ^{169}Yb sources.

Solid	EBT/ EBT2 (lot 031109)				HS				RTQA/ EBT2 (lot 020609)				XRT/XRQA			
Phnatoms	^{60}Co	^{137}Cs	^{192}Ir	^{169}Yb	^{60}Co	^{137}Cs	^{192}Ir	^{169}Yb	^{60}Co	^{137}Cs	^{192}Ir	^{169}Yb	^{60}Co	^{137}Cs	^{192}Ir	^{169}Yb
PMMA	No	No	No	No	No	No	No	No	No	No	No	No	No	No	No	No
Polystyrene	Yes	No	No	No	Yes	No	No	No	Yes	No	No	No	No	No	No	No
Plastic water	Yes	No	No	No	Yes	No	No	No	Yes	No	No	No	No	No	No	No
RW1	Yes	Yes	Yes	No	Yes	Yes	Yes	No	Yes	Yes	Yes	No	No	No	No	No
RW3	Yes	Yes	Yes	No	Yes	Yes	Yes	No	Yes	Yes	Yes	No	No	No	No	No
Virtual water	Yes	Yes	Yes	No	Yes	Yes	Yes	No	Yes	Yes	Yes	No	No	No	No	No
Solid water	Yes	Yes	Yes	No	Yes	Yes	Yes	No	Yes	Yes	Yes	No	No	No	No	No
A150	No	No	No	No	No	No	No	No	No	No	No	No	No	No	No	No
WE210	Yes	Yes	Yes	No	Yes	Yes	Yes	No	Yes	Yes	Yes	No	No	No	No	No

In this table, “Yes” implies the phantom is water-equivalent and “No” implies that the phantoms show distance-dependent $k_{phan}(r)$ values.

For low energy brachtherapy sources, plastic water (LR) and A150 phantoms were water equivalent solid phantoms among the investigated phantoms. However, solid phantoms such as solid water, virtual water and WE210 are not water-equivalent phantoms for distances larger than 1 cm. Hence, for measurements involving brachytherapy sources care should be taken for selection of solid phantom, detector type (high energy sources) and should also account for the depth of measurement.

CHAPTER 6

Response of solid-state detectors for radiotherapy electron beams

6.1 Introduction

In general, detectors are calibrated in ^{60}Co beam and used for measurements in megavoltage photon and electron beams. Therefore, the energy response correction factor needs to be applied if the detector is used in a different beam quality. For radiotherapy photon beams such as ^{60}Co, 4 MV – 18 MV, Compton scattering is the predominant interaction in water and the detector materials. Hence, the response of the detector can be understood by using electron density information of the detectors. However, in case of electron beams, electron density information of the detectors is not sufficient to understand the response of the detector as the electrons will undergo multiple scattering in the detector. The detector response may also depend upon the electron beam energy, size and density of the detector, depth of measurement in the phantom etc. Hence, for electron beams, investigation of cavity theory is important to understand the response of the detector. Thin detectors mostly behave like an ideal Spencer-Attix (1955) cavity and intermediate size detectors which fall in neither large nor small category cavities, general cavity theory proposed by Burlin (1966) holds good. Such investigations can be done using Monte Carlo methods.

The present study was aimed at determining the energy correction factors of different solid-state detectors such as diamond, LiF, $Li_2B_4O_7$, Al_2O_3, Plastic Scintillator and Lithium Formate for the radiotherapy electron beams as a function of depth in water using Monte Carlo-based EGSnrc code system. In addition the most appropriate Δ (the kinetic energy of an electron that is sufficient to cross the cavity, i.e the electron energy that corresponds to a CSDA range or the mean chord length of the detector thickness) parameter was investigated for thin micro diamond detector and electron fluence perturbation correction factors were studied for other solid-state detectors (LiF, $Li_2B_4O_7$, Al_2O_3, Plastic Scintillator and Lithium Formate) for radiotherapy electron beams.

6.2 Energy response correction factor

The energy response correction factor is defined as the ratio of the medium to detector dose ratio for an electron beam energy E, to the medium to detector dose ratio for ^{60}Co beam. It can be written as below:

$$f_{60_{Co}}^{E} = \frac{\left(\left(\overline{D}_{med}(E)\right)/\left(\overline{D}_{\det}(E)\right)\right)}{\left(\left(\overline{D}_{\det}(E)\right)/\left(\overline{D}_{\det}(^{60}Co)\right)\right)} \qquad (6.1)$$

where, $f_{60_{Co}}^{E}$ is the energy response correction, $\overline{D}_{med}(E)$ and $\overline{D}_{med}(^{60}Co)$ are the average absorbed dose to medium for electron beam energy E and ^{60}Co beam, respectively, $\overline{D}_{\det}(E)$ and $\overline{D}_{\det}(^{60}Co)$ are the average absorbed dose to detector for electron beam energy E and ^{60}Co beam, respectively.

6.3 Cavity theory

In order to measure the absorbed dose in a medium, it is necessary to introduce a radiation sensitive device (dosimeter) into the medium. Generally, the sensitive medium of the dosimeter will not be of the same material asthat of the medium in which it is embedded. For a radiation detector to be useful as a dosimeter the signal must be proportional to the energy absorbed in the detector's sensitive material and thus proportional to the absorbed dose in this material. Cavity theory relates the absorbed dose in the dosimeter's sensitive medium (cavity) to the absorbed dose in the surrounding medium containing the cavity.

Bragg–Gray cavity theory

The Bragg-Gray cavity theory was the first cavity theory (Bragg 1912, Gray 1929 and 1936) developed to provide a relation between the absorbed dose in a dosimeter and the absorbed dose in the medium containing the dosimeter. The conditions for application of the Bragg–Gray cavity theory are: 1) The cavity must be small when compared with the range of charged particles incident on it, so that its presence does not perturb the fluence of charged particles in the medium; 2) The absorbed dose in the cavity is deposited solely by charged particles crossing it. Under these two conditions, according to the Bragg–Gray cavity theory, the dose to the medium D_{med} is related to the dose in the cavity D_{cav} as follows:

$$D_{med} = D_{cav}\left(\frac{\overline{S}}{\rho}\right)_{med,cav} \qquad (6.2)$$

where $\left(\frac{\overline{S}}{\rho}\right)_{med,cav}$ is the ratio of the average unrestricted mass collision stopping powers of the medium and the cavity. The use of unrestricted stopping powers rules out the production of secondary charged particles (or delta electrons) in the cavity and the medium.

Spencer-Attix cavity theory

The Bragg–Gray cavity theory does not take into account the creation of secondary (delta) electrons generated as a result of hard collisions in the slowing down of the primary electrons in the sensitive volume of the dosimeter. Spencer-Attix proposed a cavity theory (Spencer and Attix 1955, Spencer 1965) that accounts for the creation of these electrons that have sufficient energy to produce further ionization on their own account. Some of these

electrons released in the gas cavity would have sufficient energy to escape from the cavity, carrying some of their energy with them. This reduces the energy absorbed in the cavity and requires modification of the stopping power of the gas. The Spencer–Attix theory operates under the two Bragg-Gray conditions; however, these conditions now even apply to the secondary particle fluence in addition to the primary particle fluence. The secondary electron fluence in the Spencer Attix theory is divided into two components based on a user defined energy threshold Δ. Secondary electrons with kinetic energies E_K less than Δ are considered slow electrons that deposit their energy locally; secondary electrons with energies larger than or equal to Δ are considered fast (slowing down) electrons and are part of the electron spectrum. Consequently, this spectrum has a low energy threshold of Δ and a high energy threshold of E_{K0}, where E_{K0} represents the initial electron kinetic energy. Since the lowest energy in the spectrum is Δ, the maximum energy loss of a fast electron with kinetic energy E_K larger than or equal to 2Δ cannot be larger than Δ, and the maximum energy loss of a fast electron with kinetic energy less than 2Δ cannot be larger than $E_K/2$ (where $\Delta < E_K < 2\Delta$). Spencer-Attix relation between the dose to the medium and the dose in the cavity is thus written as:

$$\frac{D_{med}}{D_{cav}} = \frac{S_{med}}{S_{cav}} = \frac{\int_{\Delta}^{E_{K_0}} \Phi_{med,E_K}(E_K)(L_{\Delta,med}/\rho)d(E_K) + TE_{med}}{\int_{\Delta}^{E_{K_0}} \Phi_{med,E_K}(E_K)(L_{\Delta,cav}/\rho)d(E_K) + TE_{cav}} \tag{6.3}$$

Where, S_{med} ans S_{cav} are the mean restricted mass collision stopping powers of the medium and cavity, respectively. $\Phi_{med,Ek}$ is the medium electron fluence spectrum. $L_{\Delta,med}$ and $L_{\Delta,cav}$ are the restricted stopping powers of medium and cavity evaluated at energy Δ, respectively.

The terms TE_{med} and TE_{cav} are called the track end terms and are approximated by Nahum (1978) as:

$$TE_{med} = \Phi_{med,E_k}(\Delta)\frac{S_{med}(\Delta)}{\rho}\Delta \tag{6.4}$$

$$TE_{cav} = \Phi_{med,E_k}(\Delta)\frac{S_{cav}(\Delta)}{\rho}\Delta \tag{6.5}$$

Note that, the unrestricted collision stopping powers are used here, because the maximum energy transfer for an electron with energy less than 2Δ is less than Δ.

Burlin cavity theory

Burlin (1966) extended the Bragg-Gray and Spencer-Attix cavity theories to cavities of intermediate dimensions by introducing a large cavity limit to the Spencer-Attix equation using a weighting technique. The Burlin cavity theory for incident photon beam can be written as follows:

$$\frac{D_{med}}{D_{cav}} = dS_{med,cav} + (1-d)\left(\frac{\overline{\mu_{en}}}{\rho}\right)_{cav}^{med} \tag{6.6}$$

where d is a parameter related to cavity size, approaching unity for small cavities and zero or large cavities, $S_{med,cav}$ is the mean ratio of the restricted mass stopping powers

medium and cavity and $\left(\overline{\frac{\mu_{en}}{\rho}}\right)_{med.cav}$ is the mean ratio of the mass–energy absorption coefficients for the medium and cavity. Burlin and Snelling (1969) derived the expression for electron beams from the general cavity theory of ionisation for photons as below:

$$\frac{D_{med}}{D_{cav}} = d(1/S_{med,cav}) \qquad (6.7)$$

where $S_{med,cav}$ is the mass collision stopping power ratio of the medium to the cavity calculated by Spencer-Attix theory, d is a dimensionless weighting factor which accounts for the decrease of the electron spectrum characteristic of the medium inside the cavity. Almond and Monte CarloCray (1970) extended Burlin's expression to include the production of delta rays within the cavity by introducing an additional term to equation 6.6 as below:

$$\frac{D_{med}}{D_{cav}} = d(1/S_{med,cav}) + (1-d)\left(\frac{Z}{A}\right)_{cav,med} \qquad (6.8)$$

where $(Z/A)_{cav,med}$ is ratio of the electron densities of the cavity to the wall medium.

6.4 Radiotherapy electron beams

The electron beams investigated in the present study were 6 MeV, 9 MeV, 12 MeV, 15 MeV and 18 MeV. The incident electron beam is circular with a radius of 5.64 cm (equivalent field size of 10x10 cm^2) at the depth of measurement in the phantom. The spectra of incident electron beams were taken from the source model of a Varian Clinac 2100C reported by Ding and Rogers (1995). The reference depth, $d_{ref} = 0.6R_{50}-0.1$ (where R_{50} is the depth at which the dose falls to 50 % of its maximum), d_{max} (the depth of

maximum dose) and the projected range R_p (obtained by extrapolating the maximum slope line to intercept the bremsstrahlung tail) were taken from the published study (Wang and Rogers 2007) and were presented in Table 6.1.

Table 6.1 Calculated values of d_{max}, d_{ref}, R_{50} and R_p for parallel incident electron beams of various energies.

Depth	Electron energy (MeV)				
(cm)	6	9	12	15	18
d_{max}	1.42 ± 0.02	2.18 ± 0.02	2.98 ± 0.02	3.55 ± 0.05	4.05 ± 0.05
R_{50}	2.645 ± 0.001	4.03 ± 0.001	5.207 ± 0.001	6.543 ± 0.001	7.806 ± 0.001
d_{ref}	1.487	2.318	3.024	3.826	4.584
R_p	3.3	5	6.3	7.8	9.4

6.5 Detectors and phantom

The detectors investigated in the present study were diamond, LiF, $Li_2B_4O_7$, Al_2O_3, Plastic Scintillator and Lithium Formate. The composition, and values of Z_{eff}, $<Z/A>$ and ρ of these solid-state detectors were already listed in Table 3.2 of Chapter 3. The dimensions of the above investigated detectors were presented in Table 6.2. In the Monte Carlo calculations, each detector was modeled as cylinders (of given radius and height as per the dimensions listed in Table 6.2) and placed at different depths in a unity density water phantom of dimension 20 cm radius and 30 cm height.

Table 6.2 Dimensions of Diamond, LiF, $Li_2B_4O_7$, Al_2O_3, Plastic Scintillator and Lithium Formate detectors used in the present study.

Height/radius	Detector Type					
(mm)	Diamond	$Li_2B_4O_7$	Al_2O_3	LiF	Lithium Formate	Plastic scintillator
Height	0.033	0.25	0.3	0.25	2.0	1.0
Radius	1.1	1.8	2.0	1.8	2.5	2.0

6.6 Monte Carlo calculations

6.6.1 Calculations of water to detector dose ratio

In the Monte Carlo calculations, absorbed dose to each detector was scored as a function of central axis depth (d_{max}, d_{ref}, $0.1R_{50}$, $0.2R_{50}$, $0.3R_{50}$, $0.4R_{50}$, $0.5R_{50}$, $0.6R_{50}$, $0.7R_{50}$, $0.8R_{50}$, $0.9R_{50}$ and R_{50}) where R_{50}, is the depth at which the dose falls to 50 % of its maximum and is a function of beam energy, d_{max} is the depth of maximum dose and d_{ref} is the reference depth in the water phantom using the Monte Carlo-based DOSRZnrc (Rogers et al 2010) user-code of EGSnrc code system (Kawrakow et al 2010). Absorbed dose to water, D_{wat} and absorbed dose to detector, D_{det} were scored as a function the above-mentioned depths in the water phantom for the investigated radiotherapy electron beams. The detector response i.e the numerator of equation 6.1 was calculated by taking the ratio of absorbed dose to water and absorbed dose to detector for a given electron beam energy. For calculation of the denominator of equation 6.1 a realistic ^{60}Co spectrum from a telecobalt unit was used. The ^{60}Co beam was parallel and had a radius of 5.64 cm at the front face of the phantom (equivalent field size is 10x10 cm^2). The Monte Carlo calculations were carried out to calculate the water to detector dose ratio for ^{60}Co beam with the same phantom and detectors as used in the calculations for the investigated radiotherapy electron beams.

6.6.2 Calculations of water to detector stopping power ratio

As explained in Section 6.3, the response of the detector i.e the water to detector dose ratio is closely related to the water to detector stopping power ratios. In this study Spencer-Attix water to detector mass-collision stopping power ratios were calculated using the Monte Carlo-based SPRRZnrc (Rogers et al 2010) user-code of EGSnrc code system (Kawrakow et al 2010, Rogers et al 2010). Water to detector Spencer-Attix stopping power ratios were

calculated in the water phantom with the same radiation sources and depths as used in the dose ratio calculations.

Thin detectors such as diamond (micro), mostly behave like an ideal Spencer-Attix cavity. For this detector, to find the suitable Δ, (the Spencer-Attix cavity characterized by this parameter Δ and is the kinetic energy of an electron that is sufficient to cross the cavity), that best characterizes the detector thickness, the electron energy that corresponds to the CSDA range and mean chord length of the detector were considered. The thickness of the diamond detector investigated in this study was 33 μm (Woodings et al 2018). The electron energy that corresponds to a CSDA range of 33 μm in diamond was about 80 keV. On the other hand, the mean chord length, L, calculated using the standard formula of L=4V/S (Attix 1986), where V is the volume and S is the surface area of the cavity, gives 64 μm, which corresponds to an energy of about 120 keV. But the penetration depth, could be substantially less than the CSDA range due to extensive multiple scattering. Hence a variety of Δ were investigated ranging from 80 to 500 keV. By comparing the results with the dose-ratio calculations as a function of depth, the most appropriate Δ was determined for the diamond detector.

For intermediate size detectors such as LiF, $Li_2B_4O_7$, Al_2O_3, Plastic Scintillator and Lithium Formate (dimensions were shown in Table 6.2), the total electron fluence (primary electrons and δ-rays) in these solid-state detectors is significantly different from that in water for the same incident electron energy and depth of irradiation. Thus the Spencer-Attix assumption that the electron fluence energy spectrum in the cavity was identical in shape to that in the medium was violated for these detectors. Differences in the total electron fluence give rise to electron fluence perturbation correction factors which were calculated for the above

detectors in the present study for the investigated radiotherapy electron beams. The perturbation correction factor can be expressed as below (Mobit et al 2000):

$$\gamma(p) \approx \frac{D^{SA}_{med,\det}}{S^{SA}_{med,\det}} \tag{6.9}$$

where $\gamma(p)$ is the perturbation correction factor, $D^{SA}_{med,\det}$ is the absorbed dose ratio of medium to detector calculated using the Spencer-Attix formalism, $S^{SA}_{med,\det}$ is the Spencer-Attix mass collision stopping power ratio of medium to detector.

6.6.3 Monte Carlo parameters

The photon transport cut off energy PCUT was chosen 10 keV and electron transport cut off energy ECUT was set 0.521 MeV (10 keV kinetic energy) in the Monte Carlo calculations. For generating the PEGS4 dataset, AE = 0.521 MeV (kinetic energy of the electron is 0.01 MeV) and AP = 0.01 MeV was set, where the parameters AE and AP were the low-energy thresholds for the production of knock-on electrons and secondary bremsstrahlung photons, respectively. All the calculations utilized the PRESTA-II step length and EXACT boundary crossing algorithms. Up to 10^9 histories were simulated. The 1σ statistical uncertainties on the calculated DOSRZnrc-based dose values were within 0.3 %. The 1σ statistical uncertainties on the calculated SPRRnrc-based dose values were within 0.2 %. The statistical uncertainties on the calculated values of response of the detector and energy response correction were less than 0.4 %.

6.7 Energy response correction and response of solid-state detectors

Enegy response corrections (see equation 6.1) and detector response (numerator of equation 6.1) of the investigated detectors (diamond, LiF, $Li_2B_4O_7$, Al_2O_3, Plastic Scintillator and Lithium Formate) were calculated as a function of central axis depths (d_{max}, d_{ref}, $0.1R_{50}$,

$0.2R_{50}$, $0.3R_{50}$, $0.4R_{50}$, $0.5R_{50}$, $0.6R_{50}$, $0.7R_{50}$, $0.8R_{50}$, $0.9R_{50}$ and R_{50}) and were presented in Table 6.3 – Table 6.7 for the radiotherapy electron beams 6 MeV, 9MeV, 12 MeV, 15 MeV and 18 MeV, respectively.

Table 6.3 Energy response correction, $f^{E}_{^{60}Co}$ and detector response, $\frac{\overline{D}_{med}(E)}{\overline{D}_{det}(E)}$ of diamond, LiF, $Li_2B_4O_7$, Al_2O_3, Plastic Scintillator and Lithium Formate detectors calculated at different depths for 6 MeV electron beam.

Depth	diamond		$Li_2B_4O_7$		Al_2O_3		LiF		Plastic Scintillator		Lithium Formate	
(cm)	$\frac{\overline{D}_{med}(E)}{\overline{D}_{det}(E)}$	$f^{E}_{^{60}Co}$	$\frac{\overline{D}_{med}(E)}{\overline{D}_{det}(E)}$	$f^{E}_{^{60}Co}$	$\frac{\overline{D}_{med}(E)}{\overline{D}_{det}(E)}$	$f^{E}_{^{60}Co}$	$\frac{\overline{D}_{med}(E)}{\overline{D}_{det}(E)}$	$f^{E}_{^{60}Co}$	$\frac{\overline{D}_{med}(E)}{\overline{D}_{det}(E)}$	$f^{E}_{^{60}Co}$	$\frac{\overline{D}_{med}(E)}{\overline{D}_{det}(E)}$	$f^{E}_{^{60}Co}$
$0.1R_{50}$	1.150	1.035	1.207	1.054	1.198	1.056	1.260	1.049	1.090	1.010	1.078	1.052
$0.2R_{50}$	1.148	1.033	1.201	1.049	1.194	1.053	1.258	1.048	1.090	1.010	1.080	1.054
$0.3R_{50}$	1.147	1.032	1.208	1.055	1.203	1.061	1.261	1.050	1.087	1.008	1.081	1.055
$0.4R_{50}$	1.148	1.033	1.198	1.046	1.201	1.059	1.252	1.043	1.088	1.009	1.085	1.059
$0.5R_{50}$	1.148	1.033	1.195	1.043	1.202	1.060	1.250	1.041	1.088	1.009	1.082	1.056
$0.6R_{50}$	1.158	1.043	1.202	1.050	1.209	1.066	1.256	1.047	1.087	1.008	1.093	1.067
$0.7R_{50}$	1.161	1.045	1.201	1.048	1.207	1.064	1.253	1.044	1.091	1.011	1.095	1.069
$0.8R_{50}$	1.166	1.049	1.190	1.039	1.220	1.076	1.241	1.034	1.096	1.016	1.100	1.074
$0.9R_{50}$	1.161	1.045	1.181	1.031	1.224	1.079	1.235	1.029	1.096	1.016	1.109	1.083
R_{50}	1.142	1.028	1.152	1.005	1.244	1.098	1.199	0.998	1.112	1.031	1.124	1.097
d_{max}	1.151	1.036	1.198	1.046	1.204	1.062	1.252	1.043	1.087	1.008	1.087	1.061
d_{ref}	1.156	1.040	1.2	1.048	1.207	1.065	1.255	1.045	1.086	1.007	1.09	1.064

Table 6.4 Energy response correction, $f^{E}_{^{60}Co}$ and detector response, $\frac{\bar{D}_{med}(E)}{\bar{D}_{det}(E)}$ of diamond, LiF, $Li_2B_4O_7$, Al_2O_3, Plastic Scintillator and Lithium Formate detectors calculated at different depths for 9 MeV electron beam.

Depth	diamond		$Li_2B_4O_7$		Al_2O_3		LiF		Plastic Scintillator		Lithium Formate	
(cm)	$\frac{\bar{D}_{med}(E)}{\bar{D}_{det}(E)}$	$f^{E}_{^{60}Co}$	$\frac{\bar{D}_{med}(E)}{\bar{D}_{det}(E)}$	$f^{E}_{^{60}Co}$	$\frac{\bar{D}_{med}(E)}{\bar{D}_{det}(E)}$	$f^{E}_{^{60}Co}$	$\frac{\bar{D}_{med}(E)}{\bar{D}_{det}(E)}$	$f^{E}_{^{60}Co}$	$\frac{\bar{D}_{med}(E)}{\bar{D}_{det}(E)}$	$f^{E}_{^{60}Co}$	$\frac{\bar{D}_{med}(E)}{\bar{D}_{det}(E)}$	$f^{E}_{^{60}Co}$
$0.1R_{50}$	1.168	1.051	1.192	1.041	1.194	1.053	1.250	1.041	1.081	1.002	1.078	1.052
$0.2R_{50}$	1.170	1.053	1.189	1.038	1.197	1.056	1.247	1.039	1.087	1.007	1.081	1.055
$0.3R_{50}$	1.172	1.055	1.196	1.044	1.205	1.063	1.250	1.041	1.081	1.002	1.081	1.055
$0.4R_{50}$	1.169	1.052	1.200	1.048	1.199	1.058	1.256	1.046	1.087	1.008	1.081	1.055
$0.5R_{50}$	1.169	1.053	1.196	1.044	1.202	1.060	1.254	1.045	1.092	1.013	1.084	1.058
$0.6R_{50}$	1.170	1.053	1.196	1.044	1.206	1.064	1.254	1.044	1.097	1.017	1.089	1.063
$0.7R_{50}$	1.172	1.055	1.191	1.040	1.199	1.058	1.244	1.036	1.095	1.015	1.095	1.068
$0.8R_{50}$	1.166	1.050	1.186	1.036	1.216	1.072	1.243	1.036	1.098	1.018	1.097	1.071
$0.9R_{50}$	1.168	1.051	1.179	1.029	1.215	1.072	1.230	1.025	1.095	1.016	1.105	1.078
R_{50}	1.161	1.045	1.159	1.011	1.232	1.087	1.211	1.009	1.104	1.023	1.105	1.079
d_{max}	1.169	1.052	1.196	1.044	1.204	1.062	1.254	1.045	1.094	1.015	1.086	1.060
d_{ref}	1.170	1.053	1.197	1.045	1.205	1.063	1.254	1.045	1.096	1.016	1.088	1.062

Table 6.5 Energy response correction, $f^{E}_{^{60}Co}$ and detector response, $\frac{\bar{D}_{med}(E)}{\bar{D}_{det}(E)}$ of diamond, LiF, $Li_2B_4O_7$, Al_2O_3, Plastic Scintillator and Lithium Formate detectors calculated at different depths for 12 MeV electron beam.

Depth	diamond		$Li_2B_4O_7$		Al_2O_3		LiF		Plastic Scintillator		Lithium Formate	
(cm)	$\frac{\bar{D}_{med}(E)}{\bar{D}_{det}(E)}$	$f^{E}_{^{60}Co}$	$\frac{\bar{D}_{med}(E)}{\bar{D}_{det}(E)}$	$f^{E}_{^{60}Co}$	$\frac{\bar{D}_{med}(E)}{\bar{D}_{det}(E)}$	$f^{E}_{^{60}Co}$	$\frac{\bar{D}_{med}(E)}{\bar{D}_{det}(E)}$	$f^{E}_{^{60}Co}$	$\frac{\bar{D}_{med}(E)}{\bar{D}_{det}(E)}$	$f^{E}_{^{60}Co}$	$\frac{\bar{D}_{med}(E)}{\bar{D}_{det}(E)}$	$f^{E}_{^{60}Co}$
$0.1R_{50}$	1.164	1.048	1.192	1.040	1.203	1.061	1.249	1.040	1.095	1.015	1.085	1.059
$0.2R_{50}$	1.170	1.053	1.189	1.038	1.199	1.057	1.248	1.039	1.084	1.005	1.082	1.056
$0.3R_{50}$	1.166	1.049	1.197	1.045	1.205	1.062	1.253	1.044	1.091	1.011	1.082	1.056
$0.4R_{50}$	1.168	1.051	1.204	1.051	1.199	1.058	1.259	1.048	1.087	1.007	1.083	1.057
$0.5R_{50}$	1.167	1.050	1.203	1.050	1.205	1.063	1.258	1.048	1.090	1.011	1.082	1.056
$0.6R_{50}$	1.176	1.059	1.193	1.041	1.195	1.054	1.247	1.039	1.094	1.014	1.080	1.054
$0.7R_{50}$	1.157	1.041	1.198	1.046	1.208	1.066	1.253	1.044	1.092	1.012	1.091	1.064
$0.8R_{50}$	1.148	1.033	1.186	1.035	1.212	1.069	1.243	1.035	1.089	1.010	1.096	1.070
$0.9R_{50}$	1.158	1.042	1.174	1.025	1.213	1.069	1.220	1.017	1.103	1.023	1.101	1.075
R_{50}	1.161	1.045	1.158	1.011	1.227	1.082	1.210	1.008	1.105	1.025	1.113	1.086
d_{max}	1.171	1.054	1.198	1.046	1.199	1.058	1.152	0.960	1.093	1.013	1.081	1.055
d_{ref}	1.174	1.056	1.192	1.041	1.194	1.053	1.145	0.954	1.094	1.014	1.081	1.055

Table 6.6 Energy response correction, $f^{E}_{^{60}Co}$ *and detector response,* $\frac{\bar{D}_{med}(E)}{\bar{D}_{det}(E)}$ *of diamond, LiF,* $Li_2B_4O_7$*,* Al_2O_3*, Plastic Scintillator and Lithium Formate detectors calculated at different depths for 15 MeV electron beam.*

Depth	diamond		$Li_2B_4O_7$		Al_2O_3		LiF		Plastic Scintillator		Lithium Formate	
(cm)	$\frac{\bar{D}_{med}(E)}{\bar{D}_{det}(E)}$	$f^{E}_{^{60}Co}$	$\frac{\bar{D}_{med}(E)}{\bar{D}_{det}(E)}$	$f^{E}_{^{60}Co}$	$\frac{\bar{D}_{med}(E)}{\bar{D}_{det}(E)}$	$f^{E}_{^{60}Co}$	$\frac{\bar{D}_{med}(E)}{\bar{D}_{det}(E)}$	$f^{E}_{^{60}Co}$	$\frac{\bar{D}_{med}(E)}{\bar{D}_{det}(E)}$	$f^{E}_{^{60}Co}$	$\frac{\bar{D}_{med}(E)}{\bar{D}_{det}(E)}$	$f^{E}_{^{60}Co}$
$0.1R_{50}$	1.160	1.044	1.201	1.048	1.194	1.053	1.261	1.051	1.095	1.015	1.084	1.058
$0.2R_{50}$	1.168	1.051	1.200	1.047	1.202	1.060	1.258	1.048	1.088	1.009	1.082	1.056
$0.3R_{50}$	1.158	1.042	1.195	1.043	1.198	1.057	1.256	1.046	1.094	1.015	1.078	1.052
$0.4R_{50}$	1.171	1.054	1.202	1.049	1.205	1.063	1.254	1.045	1.092	1.013	1.084	1.058
$0.5R_{50}$	1.173	1.056	1.194	1.042	1.201	1.060	1.251	1.042	1.089	1.009	1.085	1.059
$0.6R_{50}$	1.149	1.034	1.197	1.045	1.205	1.063	1.252	1.043	1.093	1.013	1.088	1.062
$0.7R_{50}$	1.148	1.033	1.204	1.051	1.203	1.061	1.261	1.050	1.097	1.017	1.086	1.060
$0.8R_{50}$	1.155	1.039	1.195	1.043	1.206	1.063	1.249	1.040	1.098	1.018	1.091	1.065
$0.9R_{50}$	1.165	1.049	1.183	1.033	1.220	1.076	1.237	1.030	1.099	1.019	1.099	1.073
R_{50}	1.166	1.049	1.153	1.007	1.216	1.072	1.203	1.002	1.106	1.025	1.105	1.078
d_{max}	1.160	1.044	1.195	1.043	1.203	1.061	1.251	1.042	1.091	1.012	1.086	1.060
d_{ref}	1.153	1.037	1.196	1.044	1.204	1.062	1.252	1.043	1.092	1.013	1.085	1.059

Table 6.7 Energy response correction, $f^{E}_{^{60}Co}$ *and detector response,* $\frac{\bar{D}_{med}(E)}{\bar{D}_{det}(E)}$ *of diamond, LiF,* $Li_2B_4O_7$*,* Al_2O_3*, Plastic Scintillator and Lithium Formate detectors calculated at different depths for 18 MeV electron beam.*

Depth	diamond		$Li_2B_4O_7$		Al_2O_3		LiF		Plastic Scintillator		Lithium Formate	
(cm)	$\frac{\bar{D}_{med}(E)}{\bar{D}_{det}(E)}$	$f^{E}_{^{60}Co}$	$\frac{\bar{D}_{med}(E)}{\bar{D}_{det}(E)}$	$f^{E}_{^{60}Co}$	$\frac{\bar{D}_{med}(E)}{\bar{D}_{det}(E)}$	$f^{E}_{^{60}Co}$	$\frac{\bar{D}_{med}(E)}{\bar{D}_{det}(E)}$	$f^{E}_{^{60}Co}$	$\frac{\bar{D}_{med}(E)}{\bar{D}_{det}(E)}$	$f^{E}_{^{60}Co}$	$\frac{\bar{D}_{med}(E)}{\bar{D}_{det}(E)}$	$f^{E}_{^{60}Co}$
$0.1R_{50}$	1.155	1.040	1.193	1.041	1.195	1.054	1.251	1.042	1.094	1.014	1.084	1.058
$0.2R_{50}$	1.162	1.045	1.198	1.046	1.199	1.057	1.255	1.045	1.087	1.008	1.083	1.057
$0.3R_{50}$	1.161	1.045	1.194	1.042	1.198	1.057	1.252	1.043	1.088	1.009	1.083	1.057
$0.4R_{50}$	1.160	1.044	1.187	1.036	1.196	1.055	1.243	1.035	1.094	1.014	1.086	1.060
$0.5R_{50}$	1.161	1.045	1.200	1.047	1.206	1.064	1.259	1.049	1.094	1.014	1.082	1.056
$0.6R_{50}$	1.160	1.044	1.193	1.042	1.202	1.060	1.255	1.046	1.092	1.012	1.085	1.059
$0.7R_{50}$	1.164	1.048	1.190	1.039	1.205	1.063	1.243	1.036	1.089	1.009	1.084	1.058
$0.8R_{50}$	1.159	1.043	1.189	1.038	1.208	1.065	1.245	1.037	1.094	1.014	1.090	1.063
$0.9R_{50}$	1.153	1.038	1.190	1.038	1.216	1.072	1.245	1.037	1.097	1.016	1.092	1.066
R_{50}	1.147	1.032	1.200	1.047	1.229	1.084	1.222	1.018	1.102	1.021	1.101	1.075
d_{max}	1.160	1.044	1.195	1.044	1.204	1.062	1.257	1.047	1.094	1.014	1.083	1.057
d_{ref}	1.160	1.044	1.194	1.043	1.203	1.061	1.254	1.045	1.093	1.013	1.084	1.058

It was observed that, for a given electron beam energy and for a given detector, the response of the detector does not change significantly with depth. The maximum variation in the response as a function of depth was about 4 % for Al_2O_3 detector for 6 MeV electron beam. Detectors such as diamond, $Li_2B_4O_7$ and LiF showed decrease in response when compared with the $0.1R_{50}$ value with that of the R_{50} value. Whereas detectors such as Al_2O_3, Plastic scintillator and Lithium Formate showed increase in response when compared with the $0.1R_{50}$ value with that of the R_{50} value for all the investigated radiotherapy electron beams. However, it may be noted that the change in detector response with depth is not significant for any of the investigated detectors. Although the absolute values of absorbed to detector increases with increase in electron beam energy, the detector response (which is the ratio of absorbed dose to water and absorbed dose to detector) does not change with change in electron beam energy for any of the investigated detectors.

The results of the present study are in agreement (with in 6 %) with the published results of Mobit et al (1998) for $Li_2B_4O_7$ detector and Mobit et al (1996) for LiF detector. Mobit et al (1996) investigated two different dimensions of LiF (1 mm diameter x 6 mm height rod and 3.62 mm diameter x 1 mm thick chip) and monoenergetic electron beams (2 MeV, 5 MeV, 10 MeV, 15 MeV and 20 MeV). The dimension of $Li_2B_4O_7$ detector investigated by Mobit et al (1996) was 3.61 dia x 0.9 mm thick disc. In both of their studies the centre of the detector was placed at the depth of d_{max} (of each electron beam). The dimensions of the detectors, beam energy and depth of calculation used in the present study were different from Mobit et al (1996 and 1998). This may lead to the variation of 6 % in the results with published values of Mobit et al (1998, 1996). However, the results of the present study do not differ significantly (with in 6 %) from the reported values of Mobit et al (1996, 1998),

this may be due to the fact that, detector response itself has very little dependence on detector dimension, electron beam energy and depth of measurement.

6.8 Detector response versus cavity theory

The Monte Carlo-calculated Spencer-Attix stopping power ratios and the detector response i.e, water-to-diamond dose ratio as a function depth in water phantom was compared for the investigated radiotherapy electron beams 6, 9 12, 15 and 18 MeV. Comparison of water to diamond dose ratio and Spencer-Attix stopping power ratios for four different Δ values i.e 10, 100, 300 and 500 keV at the depth of d_{max} were presented in Table 6.8 for the investigated radiotherapy electron beams. Δ=10 keV, which is the value normally used in ion chamber dosimetry calculations, was included for comparison only. The Spencer-Attix stopping power ratios for value Δ=300 keV were found to coincide closely with the corresponding dose ratio values near the d_{max} for the investigated radiotherapy electron beams for diamond detector.

Table 6.8 Diamond detector response $\left(\frac{\overline{D}_{water}(E)}{\overline{D}_{diamond}(E)}\right)_{d_{max}}$ *at a depth of* d_{max} *and Spencer-Attix stopping power ratios at different* Δ *values for radiotherapy electron beams.*

		Spencer-Attix stopping power ratios			
Energy (MeV)	$\left(\frac{\overline{D}_{water}(E)}{\overline{D}_{diamond}(E)}\right)_{d_{max}}$	Δ=10 keV	Δ=100 KeV	Δ=300 keV	Δ=500 keV
6	1.151	1.161	1.158	1.150	1.147
9	1.169	1.164	1.163	1.166	1.165
12	1.171	1.167	1.161	1.168	1.165
15	1.16	1.171	1.165	1.163	1.166
18	1.16	1.169	1.167	1.160	1.163

It was observed that the variation of Spencer-Attix stopping power ratios as a function Δ was not significant. A maximum deviation of about 1 % was found for all the investigated radiotherapy electron beams.

For intermediate size detectors such as LiF, $Li_2B_4O_7$, Al_2O_3, Plastic Scintillator and Lithium Formate electron fluence perturbation correction factors were calculated (see equation 6.9). Δ was chosen as 300 keV for all the above detectors which was consistent with Δ values considered in the study of Mobit et al (2000). However, the dependence of the Spencer-Attix mass collision stopping power ratios on Δ values were also investigated in the similar manner as discussed for diamond detector. It was found that no significant difference (about 0.4 %) between the Spencer-Attix mass collision stopping power ratios evaluated for $\Delta \geq$ 300keV. Hence Δ = 300 keV was chosen for all above the detectors. Electron fluence perturbation correction factors calculated for LiF, $Li_2B_4O_7$, Al_2O_3, Plastic Scintillator and Lithium Formate detectors were presented in Table 6.9 at a depth of d_{max} for the investigated radiotherapy electron beams.

Table 6.9 Electron fluence perturbation correction factors $\gamma(p)$ calculated for LiF, $Li_2B_4O_7$, Al_2O_3, Plastic Scintillator and Lithium Formate detectors calculated at a depth of d_{max}, for Δ=300 keV for the investigated radiotherapy electron beams.

Energy (MeV)	$Li_2B_4O_7$	Al_2O_3	LiF	Plastic Scintillator	Lithium Formate
6	0.972	0.940	0.935	1.118	1.049
9	0.987	0.943	0.939	1.132	1.065
12	0.988	0.946	0.936	1.133	1.065
15	0.979	0.950	0.939	1.128	1.066
18	0.978	0.950	0.940	1.125	1.063

It was observed that, electron fluence perturbation correction factors were smaller than unity for LiF, $Li_2B_4O_7$, Al_2O_3, detectors and larger than unity for Plastic Scintillator and Lithium Formate detectors. Since electron fluence perturbation correction factors deviate significantly from unity for the above investigated detectors, Spencer-Attix cavity equation cannot be applied directly to these investigated detectors. The electron fluence perturbation

correction factors should be applied in order to determine absorbed in a medium for LiF, $Li_2B_4O_7$, Al_2O_3, Plastic Scintillator and Lithium Formate detectors using Spencer-Attix cavity theory.

6.9 Summary and Conclusion

The energy response correction factors of different solid-state detectors such as diamond, LiF, $Li_2B_4O_7$, Al_2O_3, Plastic Scintillator and Lithium Formate for the radiotherapy electron beams as a function of depth in water was calculated using Monte Carlo-based EGSnrc code system. The response of the detector does not change significantly with depth for the radiotherapy electron beam energy. These calculated detector responses were compared with the Spencer-Attix mass collision stopping power ratios. For thin diamond detector, Δ=300 keV was the most suitable at which the diamond detector response agrees well with the Spencer-Attix mass collision stopping power ratios. For other solid-state detectors (LiF, $Li_2B_4O_7$, Al_2O_3, Plastic Scintillator and Lithium Formate) electron fluence perturbation correction factors were calculated for radiotherapy electron beams. The values of electron fluence perturbation correction factors were significantly different from unity (maximum deviation was found about 13 % for Plastic Scintillator) for the investigated radiotherapy electron beams. Hence for these detectors electron fluence perturbation correction factors should be applied in order to determine absorbed in a medium for the investigated radiotherapy electron beams.

CHAPTER 7

Summary, conclusion and future work

7.1 Summary & Conclusion

This Chapter summarizes the major findings of the thesis and outlines the scope for future work. In general, detectors are calibrated in ^{60}Co beam and used for measurements in megavoltage photon and electron beams. Therefore, the energy response correction factor needs to be applied if the detector is used in a different beam quality. Although water is recommended as the reference medium of dosimetry, various solid phantoms are used for measuremet purposes. However, the scattering and attenuation properties of these phantoms may differ from that of water phantom which need to be accounted for accurate dosimetry.

Mean energies (both fluence-weighted and detector-kerma weighted) of photons were calculated for various solid-state detectors (diamond, Al_2O_3, $Li_2B_4O_7$, LiF, Lithium Formate and Plastic Scintillator) and radiochromic films (EBT, EBT2 (lot 031109), EBT2 (lot 020609), RTQA, XRT, XRQA and HS) as a function of distance along the transverse axis of the ^{60}Co, ^{137}Cs, ^{192}Ir, ^{169}Yb, ^{131}Cs, ^{125}I and ^{103}Pd brachytherapy sources in various solid phantoms (PMMA, polystyrene, solid water, virtual water, RW1, RW3, plastic water, plastic water (LR), A150 and WE210). This Chapter is helpful to understand and discuss the results of following two Chapters (4 and 5). It was observed that, for high energy brachytherapy sources (^{60}Co, ^{137}Cs, ^{192}Ir and ^{169}Yb), the values of $\bar{E}_{fl}$ decreases as a function of distance *r* in the above phantoms. For low energy brachytherapy sources such as ^{131}Cs, ^{125}I and ^{103}Pd, it was found that, $\bar{E}_{fl}$ values did not vary significantly with distance for any of the investigated sources and solid phantoms. $Li_2B_4O_7$ and Lithium Formate detectors showed identical $\bar{E}_k$ values for all the investigated phantom materials. For a given phantom, detector kerma weighted mean energies, $\bar{E}_k$ were higher in diamond and Plastic Scintillator detectors, and smaller for XRT and XRQA radiochromic films as compared to other investigated detectors.

Detector-specific, $k_{QQ_0}(r)$ were calculated for different solid-state detectors and various radiochromic films using the Monte Carlo-based EGSnrc code system. Z_{eff} of detectors and mean energy in the phantoms play a major role on the $k_{QQ_0}(r)$ values of high energy brachytherapy sources (^{60}Co, ^{137}Cs, ^{192}Ir and ^{169}Yb). For low energy brachytherapy sources such as ^{131}Cs, ^{125}I and ^{103}Pd, $k_{QQ_0}(r)$ value mostly depends upon the Z_{eff} of a given detector. $k_{QQ_0}(r)$ is distance-dependent for high energy brachytherapy sources and distance-independent for low energy brachytherapy sources. The detectors with Z_{eff} close to that of water, $k_{QQ_0}(r)$ values were close to unity. However, for detectors with lesser Z_{eff} than that of water, $k_{QQ_0}(r)$ values are much larger than unity and for detectors with higher Z_{eff} than that of water, $k_{QQ_0}(r)$ values are smaller than unity. For a given brachytherapy sources, $Li_2B_4O_7$, Lithium Formate, EBT and EBT2 detectors showed lesser energy response corrections than other investigated detectors.

Phantom scatter correction, $k_{phan}(r)$ for various solid phantoms were calculated for different solid state detectors and various radiochromic films as a function of distance along the transverse axis of the ^{60}Co, ^{137}Cs, ^{192}Ir, ^{169}Yb, ^{131}Cs, ^{125}I and, ^{103}Pd brachytherapy sources using the Monte Carlo-based EGSnrc code system. For a given detector, $k_{phan}(r)$ depends on distance from the source for the investigated phantoms, but the degree of deviation from unity depends on the type of solid phantom and the brachytherapy source. It is interesting to note that, unlike for high energy sources (^{60}Co, ^{137}Cs, ^{192}Ir and ^{169}Yb), $k_{phan}(r)$ values did not change with detector type for low energy sources (^{131}Cs, ^{125}I and ^{103}Pd) at all distances. For low energy brachtherapy sources, plastic water (LR) and A150 phantoms were water

equivalent solid phantoms among the investigated phantoms. However, solid phantoms such as solid water, virtual water and WE210 are not water-equivalent phantoms for distances larger than 1 cm. In order to understand the results the variations in the primary and scattered component of collision-kerma, were studied. The total linear attenuation coefficient (μ) data and the macroscopic cross section data of individual photon interactions (photoelectric, Compton scattering, pair production and Rayleigh scattering) were analysed in the energy range of 10 keV - 1.25 MeV for the investigated solid phantom materials using the state-of-the art XCOM. Hence, for measurements involving brachytherapy sources care should be taken for selection of solid phantom, detector type (high energy sources) and should also account for the depth of measurement.

The energy response correction factors of different solid-state detectors (diamond, LiF, $Li_2B_4O_7$, Al_2O_3, Plastic Scintillator and Lithium Formate) were calculated as a function of depth for the radiotherapy electron beams using Monte Carlo-based EGSnrc code system. The response of the detector does not change significantly with depth for the radiotherapy electron beam energy. These calculated detector responses were compared with the Spencer-Attix mass collision stopping power ratios. For thin diamond detector, Δ=300 keV was the most suitable at which the diamond detector response agrees well with the Spencer-Attix mass collision stopping power ratios. For other solid-state detectors (LiF, $Li_2B_4O_7$, Al_2O_3, Plastic Scintillator and Lithium Formate) electron fluence perturbation correction factors were calculated for radiotherapy electron beams. The values of electron fluence perturbation correction factors were significantly different from unity (maximum deviation was found about 13% for Plastic Scintillator) for the investigated radiotherapy electron beams. Hence,

for these detectors electron fluence perturbation correction factors should be applied in order to determine absorbed dose in medium for the investigated radiotherapy electron beams.

7.2 Future work

The scope for future work includes:

(1) Energy response studies can be extended for various detectors used in hardontherapy (proton, carbon ion beams etc)

(2) Intrinsic energy dependence can be studied for different detectors and brachytherapy sources. This study can be extended for other detectors and brachytherapy sources. General-purpose Monte Carlo codes that model radiation transport can be used to calculate the absorbed-dose energy dependence, but cannot be used to calculate the intrinsic energy dependence since the process of detection can not be modeled. Intrinsic energy dependence can therefore be determined through measurements.

References

Adolfsson E, Carlsson G A, Grindbard J, Gustaffson H, Lund E, Tedgren A C 2010 Response of lithium formate EPR dosimeters at photon energies relevant to the dosimetry of brachytherapy *Med. Phys.* **37** 4956-59

Almond P R and Monte Carlo Cray K 1970 The energy response of LiF, CaF_2 and $Li_2B_4O_7$:Mn to high energy radiations *Phys. Med. Biol.* **15** 335-42

Almond P R, Biggs P J, Coursey B M, Hanson W F, Huq M S, Nath R, Rogers D W O 1999 AAPM's TG-51 protocol for clinical reference dosimetry of high-energy photon and electron beams *Med. Phys.* **26** 1847-70

Agostinelli S, Allison J, Amako K, Apostolakis J, Araujo H, Arce P et al 2003 Geant4—a simulation toolkit *Nucl. Instrum. Methods Phys. Res. A* **506** 250-303

Akselrod M S, Kortov V S and Gorelova E A 1993 Preparation and Properties of Alpha-Al_2O3:C *Radiat. Prot. Dosimetry* **47** 159- 64

Andreo P 1991 Monte Carlo techniques in medical radiation physics *Phys. Med. Biol.* **36** 861-920

Andreo P, Burns D T, Hohlfeld H, Huq M S, Kanai T, Laitano F, Smyth V, Vynckier S 2000 IAEA Technical Report Series No. 398 (International Atomic Energy Agency, Vienna)

Attix F H 1986 Introduction to Radiological Physics and Radiation Dosimetry New York Wiley U.S.A.

Azam N R, Robert B C, Coursey B M et al 1998 Radiochromic film dosimetry: Recommendations of AAPM Radiation Therapy Committee Task Group 55 *Med. Phy.***25** 2093-115

Aznar M C, Medin J, Hemdal B, Thilander Klang A, Bøtter-Jensen L and Mattsson S 2005 A Monte Carlo study of the energy dependence of Al2O3:C crystals for real-time in vivo dosimetry in mammography *Radiat. Pro.t Dosimetry* **114** 444-9

Ballester F, Lluch J L, Limami Y, Serrano M A, Casal E, Pérez-Calatayud J and Lliso F 2000 A Monte Carlo investigation of the dosimetric characteristics of CSM11 ^{137}Cs sources from CIS *Med. Phys.* **27** 2182-9

Ballester F, Puchades V, Lluch J L, Serrano-Andrés M A, Limami Y, Pérez-Calatayud J and Casal E 2001 Technical note: Monte-Carlo dosimetry of the HDR 12i and Plus ^{192}Ir sources *Med. Phys.***28** 2586-91

Ballester F, Puchades V, Cluch J L, Serrano-Andrés M A, Limami Y, Pérez-Calatayud J and Casal E 2004 Technical note: Monte-Carlo dosimetry of the HDR 12i and Plus ^{192}Ir sources (erratum) *Med. Phys.* **31** 2372

Ballester F, Granero D, Perez-Calatayud J, Casal E, Agramunt S and Cases R 2005 Monte Carlo dosimetric study of the BEBIG Co-60 HDR source *Phys. Med. Biol.* **50** N309-16

Baro J, Sempau J, Fernandez-Varea J M and Salvat F 1995 PENELOPE: an algorithm for Monte Carlo simulation of the penetration and energy loss of electrons and positrons in matter *Nucl. Instrum. Methods Phys. Res. B* **100** 31-46

Barton M B, Gebski V, Manderson C, Langlands A O 1995 Radiation Therapy: are we getting value for money? *Clin. Oncol.* **7** 287-92

Beaulieu L, Tedgren A C, Carrier J, Davis S D, Mourtada F, Rivard M J, Thomson R M, Verhaegen F, Wareing T A and Williamson J F 2012 Report of the Task Group 186 on model-based dose calculation methods in brachytherapy beyond the TG-43 formalism: current status and recommendations for clinical implementation *Med. Phys.* **39** 6208-36

Beddar A S, Briere T M, Mourtada F A, Vassiliev O N, Liu H H and Mohan R 2005 Monte Carlo calculations of the absorbed dose and energy dependence of plastic scintillators *Med. Phys.* **32** 1265-9

Berger M J 1963 Monte Carlo Calculation of the penetration and diffusion of fast charged particles in *Methods in Computational Physics* edited by Alder B, Fernbach S and Rotenberg M Academic Pres New York **1**135-215

Berger M J and Hubbell J H 1987 XCOM, Photon cross sections on a personal computer Report No. NBSIR87–3597. Gaithersburg, MD: NIST Available from: http://physics.nist.gov/PhysRefData/Xcom/html/xcom1.html

Bethe H. and Ashkin J 1953 Experimental Nuclear Physics. Vol 1 edited by Segr E and Wiley J New York 253

Bielajew A F and Rogers D W O 1987 PRESTA: The Parameter Reduced Electron-Step Transport Algorithm for electron Monte Carlo transport *Nucl. Instrum. Methods Phys.Res. B* **18** 165-181

Bielajew A F 2000 Fundamentals of the Monte Carlo method for neutral and charged particle transport. The University of Michigan U.S.A

Bielajew A F 2001 Fundamentals of the Monte Carlo method for neutral and charged particle transport (The University of Michigan, 2001)

Bradshaw W W, Cadena D G, Crawford G W and Spetzler H A 1962 The use of alanine as a solid dosimeter *Radiat. Res.* **17** 11-21

Bragg W H 1912 *Studies in Radioactivity* (London: MacMillan)

Brenner D J 1997 Radiation biology in brachytherapy *J. Surg. Oncol.* **65** 66-70

Briesmeister J F (ed) 1988 MCNP-A General Monte Carlo N-Particle Transport Code Version **4A** LA-12625-M (Los Alomos, NM: Los Alamos National Laboratory)

Briesmeister J F (ed) 1997 MCNP-A General Monte Carlo N-Particle Transport Code Version **4B** LA-12625-M (Los Alamos, NM: Los Alamos National Laboratory).

Bucciolini M, Buonamici F B, Mazzocchi S, De Angelis C, Onori S and Cirrone G A 2003 Diamond detector versus silicon diode and ion chamber in photon beams of different energy and field size *Med. Phys.* **30** 2149-54.

Burlin T E 1966 A general theory of cavity ionizations *Br. J. Radiol.* **39** 727–34

Burlin T E and Snelling R J 1969 The application of general cavity theory to the dosimetry of electron fields *Proc. 2nd Symp. on Microdosimetry* 455–73

Butson M J, Cheung T, Yu P K 2004 Radiochromic film: the new x-ray dosimetry and imaging tool *Australas. Phys. Eng. Sci. Med*. **27** 230

Butson M J, Cheung T, Yu P K 2005 XR type-R radiochromic film x-ray energy response *Phys. Med. Biol.* **50** 195-99

Butson M J, Cheung T, Yu P K 2006a Measurement of energy dependence for XRCT radiochromic film *Med. Phys.* **33** 2923-25

Butson M J, Cheung T, Yu P K 2006b Weak energy dependence of EBT gafchromic film dose response in the 50 kVp-10MVp X-ray range *Appl. Radiat. Isot.* **64** 60-62

Butson M J, Cheung T and Yu P K N 2007 Measuring energy response for RTQA radiochromic film to improve quality assurance procedures *Phys. Med. Biol.* **52** 3931-48

Cameron J R, Suntharalingam N and Kenney G K 1968 *Thermoluminescent dosimetry*, (University of Wisconsin Press, Madison, Wisconsin, U.S.A.)

Cashwell E D and Everett C J 1959 A practical Manual on the Monte-Carlo Method for Random Walk Problems Oxford: Pergamon Press

Chen Z and Nath R 2001 Dose rate constant and energy spectrum of interstitial brachytherapy sources *Med. Phys.* **28** 86- 96

Chen S W, Wang X T, Chen L X, Tang Q and Liu X W 2009 Monte Carlo evaluations of the absorbed dose and quality dependence of Al_2O_3 in radiotherapy photon beams *Med. Phys.* **32** 3350-54

Chiu-Tsao S T, Ho Y, Shankar R, Wang L and Harrison L B 2005 Energy dependence of response of new high sensitivity radiochromic films for megavoltage and kilovoltage radiation energies *Med. Phys.* **36** 4421-4424

Colemon W A 1968 Mathematical verification of a certain Monte Carlo sampling technique and applications of the technique to radiation problems *Nucl. Sci. Eng.* **32** 76-81

Crook J 2011 The role of brachytherapy in the definitive management of prostate cancer *Cancer/Radiotherapie* **15** 230-37

Dale R G and Jones B 1998 The clinical radiobiology of brachytherapy *Br. J. Radiol.* **71** 465-83

Daskalov G M, Loffler E and Williamson JF 1998 Monte Carlo-aided dosimetry of a new high dose-rate brachytherapy source *Med. Phys.* **25** 2200-08

Del Sol Fernandez S, Garcia-Salcedo R, Sanchez-Guzman D, Ramirez-Rodriguez G, Gaona E, de Leon-Alfaro M A and Rivera-Montalvo T 2016 Thermoluminescent dosimeters for low dose X-ray measurements *App. Rad. Isot.* **107** 340-45

Desrosiers M F, Publ J M and Cooper S L 2008 An absorbed-dose/dose-rate dependence for the alanine-EPR dosimetry system and its implications in high-dose ionizing radiation metrology J.*Res. NIST.* **113** 79-95

Devic S, Seuntjens J, Hegyi G, Podgorsak E B, Soares C G, Kirov A S, Ali I, Williamson J F, Elizondo A 2004 Dosimetric properties of improved Gafchromic films for seven different digitizers *Med. Phys.* **31** 2392-401

Devic S, Seuntjens J, Abdel-Rahman W, Evans M, Olivares M, Podgorsak E B, Vuong T, Soares C G 2006 Accurate skin dose measurements using radiochromic film in clinical applications *Med. Phys.* **33** 1116-24

DeWerd L A, Bartol L J and Davis S D 2009 Thermoluminescence dosimetry in *Clinical Dosimetry Measurements in Radiotherapy* Madison WI: Medical Physics Publishing Available from: http://www.aapm.org/meetings/09SS/documents/2.pdf

Domen S R 1980 Absorbed dose to water calorimeter *Med. Phys.* **7** 157-9

Dutreix A and Wambersie A 1975 Specification of gamma-ray brachytherapy sources *Br. J. Radiol.* **48** 1034-58

Ebenau M, Radeck D, Bambynek M, Sommer H, Flühs D, Spaan B and Eichmann M 2016 Energy dependent response of plastic scintillation detectors to photon radiation of low to medium energy *Med. Phys.***43** 4598-606.

Ebert M, Asad A and Siddiqui A 2009 Suitability of radiochromic films for dosimetry of low energy X-rays *J. Appl. Clin. Med. Phys.* **10** 232-40.

Eckhardt R 1987 Stan Ulam, John von Neumann and the Monte Carlo method Los Alamos

Science, Special Issue **15** 131-41

Essers M and Mijnheer B J 1999 In Vivo dosimetry during external photon beam radiotherapy *Int. J. Radiat. Oncol. Biol. Phys.* **43** 245-59

Evans R D 1955 *The Atomic Nucleus* (MCGraw-Hill, New York)

Ferrari A, Sala P R, Fassò A and Ranft J 2005 FLUKA: A Multi-Particle Transport Code. Technical Report CERN-2005-10, INFN/TC 05/11, SLAC-R-773, CERN, INFN, SLAC.

Fishman G S 1996 Monte Carlo: concepts, algorithms, and applications (Springer Series in Operations Research and Financial Engineering) Springer

Gamboa-deBueny I, Buenfilz A E, Ruizz C G, Rodrıguez-Villafuertez M, Floresx A and Brandanz M E 1998 Thermoluminescent response and relative efficiency of TLD-100 exposed to low-energy x-rays *Phys. Med. Biol.* **43** 2073–83

Geithner O, Andreo P, Sobolevsky N, Hartmann G, Jäkel O 2006 Calculation of stopping power ratios for carbon ion dosimetry *Phys. Med. Biol.* **51** 2279-92

Gerig L, Soubra M and Salhani D 1994 Beam characteristics of the Therapax DXT300 orthovoltage therapy unit *Phys. Med. Biol.* **39** 1377-92

Goudsmit S and Saunderson J L 1940 Multiple Scattering of Electrons *Phys. Rev* **57** 24-29

Granero D, Perez-Calatayud J and Ballester F 2007 Technical note: Dosimertic study of a new Co-60 source used in brachytherapy *Med. Phys.* **34** 3485-8

Gray L H 1929 The absorption of penetrating radiation *Proc. R. Soc. Lond. A* **122** 647-68

Gray L H 1936 An ionization method for the absolute measurement of gamma ray energy Proc. *R. Soc. Lond. A* **156** 578–98

Greening J R 1985 Fundamentals of Radiation Dosimetry in *Medical Physics handbook*, No 15 2nd ed. (Adam Hilger, Bristol.)

Gupta T and Anand N C 2012 Image-guided radiation therapy: Physician's perspectives. *J. Med. Phy.* **37** 174-82

Hale J 1974 *The Fundamentals of Radiological Science (*Thomas, Springfield, IL)

Halbleib J 1988 Structure and Operation of the ITS code system in *Monte Carlo Transport of Electrons and Photons* edited by Jenkins T M, Nelson W R and Rindi A, Nahum AE and Rogers D W O Plenum Press, New York, 249-262

Holt J G, Edelstein G R and Clark T E 1975 Energy dependence of the response of LiF TLD rods in high energy electrons fields *Phys. Med. Biol.* **4** 559-70

Horowitz Y S 1981 The theoretical and microdosimetric basis of thermoluminescence and applications to dosimetry *Phys. Med. Biol.* **26** 765-824

Horton J L 1987 *Handbook of radiation therapy physics*, (Prentice Hall, New York, U.S.A.)

Hubbell J H and Seltzer S M 1995 Tables of x-ray mass attenuation coefficients and mass energy absorption coefficients. Gaithersburg, MD: National Institute of Standards and Technology Available from: http://physics.nist.gov/physRefData/XrayMassCoef.

ICRU 1980 Fundamental Quantities and Units for Ionizing Radiation ICRU Report No. 33 (Bethesda, MD: ICRU)

ICRU 1984 Stopping Powers for Electrons and Positrons ICRU Report No. 37 (Bethesda, MD: ICRU)

ICRU 1993 Stopping Powers and Ranges for Protons and Alpha Particles ICRU Report No. 49 (Bethesda, MD: ICRU)

ICRU 1998 Fundamental Quantities and Units for Ionizing Radiation ICRU Report No. 60 (Bethesda, MD: ICRU)

Jackson S M 1970 The clinical application of electron beam therapy with energies up to 10MeV *Br. J. Radiol.* **43** 431-44

Jakel O, Schulz-Ertner D, Karger C P, Nikoghosyan A and Debus J 2003 Heavy ion therapy: status and perspectives *Technol. Cancer Res. Treat.* **2** 377- 87

Johns H E and Cunningham J R 1983 *The Physics of Radiology,* 4th ed. (Thomas C C Publisher Ltd. Springfield IL)

Joslin C A F, Flyn A and Hall E J 2001 *Principles and practice of brachytherapy – using afterloading systems* (Arnold, London, UK)

Karaiskos P, Angelopoulos A, Sakelliou L, Sandilos P, Antypas C, Vlachos L, Koutsouveli E 1998 Monte Carlo and TLD dosimetry of an ^{192}Ir high dose-rate brachytherapy source *Med. Phys.* **25** 1975-84

Karaiskos P, Papagiannis P, Sakelliou L, Anagnostopoulos G and Baltas D 2001 Monte Carlo dosimetry of the selectSeed ^{125}I interstitial brachytherapy seed *Med. Phys.* **28** 1753-60

Karzmark C J 1987 Total Skin Electron Therapy: Technique and Dosimetry AAPM Report No. 23 Published by the American Institute of Physics, Inc. New York

Kawrakow I 2000a Accurate condensed history Monte Carlo simulation of electron transport (Part I) *Med. Phys.* **27** 485-98

Kawrakow I 2000b Accurate condensed history Monte Carlo simulation of electron transport (Part II) *Med. Phys.* **27** 499-513

Kawrakow I, Mainegra-Hing E, Rogers D W O, Tessier F and Walters B R B 2010 The EGSnrc Code System: Monte Carlo simulation of electron and photon transport. NRCC Report PIRS–701. Ottawa, ON: National Research Council of Canada. Available from: http://www.irs.inms.nrc.ca/EGSnrc/pirs701.pdf

Keller B, Sankreacha R, Rakovitch E, O'Brien P and Pignol J 2005 A permanent breast seed implant as partial breast radiation therapy for early-stage patients: a comparison of

palladium-103 and iodine-125 isotopes based on radiation safety considerations *Int. J. Radiat. Oncol. Biol. Phys.* **62** 358-65

Kent W, Gregory M, Lawrence T, Steven S, William C, Wayne B 2003 ^{125}I versus ^{103}Pd for low-risk prostate cancer: preliminary PSA outcomes from a prospective randomized multicenter trial *Int. J. Radiat. Oncol. Biol. Phys.* **57** 1297-1303

Khan F M 2010 *The Physics of Radiation Therapy*, 4th ed. (Lippincott Williams & Wilkins, Baltimore MD)

Klein O and Nishina Y 1929 On the Scattering of Radiation by Free Electrons According to Dirac's New Relativistic Quantum Dynamics *Z. Phys.* **52** 853-69

Knoll G F 2000 Radiation Detection and Measurement, 3rd ed. (John Wiley & sons. New York)

Knöös T and MClean B 2007 Dose calculations for external photon and electron beam therapy 9th Biennial ESTRO meeting. Barcelona, Spain.

Laub W U, Kaulich T W and Nüsslin F 1997 Energy and dose rate dependence of a diamond detector in the dosimetry of 4-25 MV photon beams *Med. Phys.* **24** 535-6

Lazarescu G R and Battista J J 1997 Analysis of the radiobiology of ytterbium-169 and iodine-125 permanent brachytherapy implants *Phys. Med. Biol.* **42** 1727-36

Loft S M, Coles I P and Dale R G 1992 The potential for ytterbium 169 in brachytherapy: A brief physical and radiobiological assessment *Br. J. Radiol.* **65** 252-7

Mackie T R 1990 Applications of the Monte Carlo Method in Radiotherapy Vol. III of *Dosimetry of Ionizing Radiation* edited Kase K, Bjarngard B E and. Attix F H (Academic Press, New York) 541-620

Massillon J L G, Cabrera-Santiago A, Minniti R, O'Brien M and Soares C G 2014 Influence of phantom materials on the energy dependence of LiF:Mg,Ti thermoluminescent dosimeters exposed to 20-300 kV narrow x-ray spectra, ^{137}Cs and ^{60}Co photons *Phys. Med. Biol.* **59** 4149-66

Medich D C, Tries M A and Munro J J 2006 Monte Carlo characterization of an ytterbium-169 high dose rate brachytherapy source with analysis of statistical uncertainty *Med. Phys.* **33** 163-72

Medich D C and Munro J J 2010 Dependence of Yb-169 absorbed dose energy correction factors on self-attenuation in source material and photon buildup in water *Med. Phys.* **37** 2135-44

Meigooni A S, Meli J A and Nath R 1988a Influence of the variation of energy spectra with depth in the dosimetry of ^{192}Ir using LiF TLD *Phys. Med. Biol.* **33** 1159-70

Meigooni AS, Meli J A and Nath R 1988b A comparison of solid phantoms with water for dosimetrty of ^{125}I brachytherapy sources *Med. Phys.* **15** 695-701

Meli J A, Meigooni A S and Nath R 1988 On the choice of phantom material for the dosimetry of ^{192}Ir sources *Int. J. Radiat. Oncol. Biol. Phys.* **14** 587-94

Metropolis N 1987 The beginning of the Monte Carlo method, Los Alamos Science (1987 Special Issue dedicated to Stanislaw Ulam) 125-130

Mobit P N, Mayles P and Nahum A E 1996a Quality-dependence of LiF TLD in megavoltage photon beams: Monte Carlo simulation and experiments *Phys. Med. Biol.* **41** 387-98

Mobit P N, Nahum A E and Mayles P 1996b The energy correction factor of LiF thermoluminescent dosemeters in megavoltage electron beams: Monte Carlo simulations and experiments *Phys. Med. Biol.* **41** 979-93

Mobit P N, Nahum A E and Mayles P 1997 An EGS4 Monte Carlo examination of general cavity theory *Phys. Med. Biol.* **42** 1319-34

Mobit P N, Nahum A E and Mayles P 1998 A Monte Carlo study of the quality dependence factors of common TLD materials in photon and electron beams *Phys. Med. Biol.* **43** 2015-32

Mobit P N, Sandison G A and Nahum A E 2000 Electron fluence perturbation correction factors for solid state detectors irradiated in megavoltage electron beams *Phys. Med. Biol.* **45** 255-65

Mohan R 1997 Why Monte Carlo? XII Int. Conf. on the Use of Computers in Radiation Therapy (Salt Lake City, Utah, May 1997) 16-18

Moliere G 1948 Moliere's Theory of Multiple Scattering *Z Naturforsch* **3a** 78-85

Morgan G, Ward R, Barton M 2004 The contribution of cytotoxic chemotherapy to 5-year survival in adult malignancies. *Clin. Onc.* **16** 549-60

Murphy M K, Piper R K, Greenwood, L R, Mitch M G, Lamperti P J, Seltzer S M, Bales M J, Phillips M H 2004 Evaluation of the new cesium-131 seed for use in low-energy x-ray brachytherapy *Med. Phys.* **31** 1529-38

Nahum A E 1978 Water/air mass stopping power ratios for megavoltage photon and electron beams *Phys. Med. Biol.* **23** 24-38.

Nahum A E 1996 Perturbation effects in dosimetry: Part I. kilovoltage x-rays and electrons Phys. Med. Biol. 41 1531–80

Nath R, Anderson L L, Luxton G, Weaver K A, Williamson J F and Meigooni A S 1995 Dosimetry of interstitial brachytherapy sources: Recommendations of the AAPM Radiation Therapy Committee Task Group No. 43 *Med. Phys.* **22** 209-34

Nelson W R, Hirayama H and Rogers D W O 1985 The EGS4 Code System, Report SLAC–265, Stanford Linear Accelerator Center, Stanford, California

Olivera G H, Kessler C, Sonsogne R A and Saravi M 1994a Energy dependence response of thermoluminescence dosemeters to photons and electrons beams *Nucl. Instrum. Methods B* **84** 89-94

Olivera G H, Sonsogne R A, Papadopulos S and Saravi M 1994b Thermoluminescent dosemeter response in high energy photon and electron beams *Proc. Int. Symp. on Measurement Assurance in Dosimetry* (Vienna, 1993) (Vienna: IAEA) 555–62

Papoulis A and Pillai S U 1965 Probability Theory, Random Variables and Stochastic Processes 4th Edition (Publisher: MCgraw Higher Ed)

Perez C A, Camel H M, Kuske R R et al 1986 Radiation therapy alone in the treatment of carcinoma of the uterine cervix: A 20 year experience *Gynecol. Oncol.* **23** 127-40

Perez-Calatayud J, Granero D, Ballester F, Casal E, Cases R, Agramunt S 2005 Technical note: Monte Carlo derivation of TG43 dosimetric parameters for radiation therapy resources and 3M ^{137}Cs sources *Med. Phys.* **32** 2464-70

Perez-Calatayud J 2009 Monte Carlo Application in Brachytherapy Dosimetry in *Radiotherapy and Brachytherapy* NATO Science for Peace and Security Series B: Physics and Biophysics Springer: Netherlands 239.

Peter D G, John C B, John E, Robert M M, William C 2001 10-year biochemical (prostate-specific antigen) control of prostate cancer with ^{125}I brachytherapy *Int. J. Radiat. Oncol. Biol. Phys.* **51** 31-40

Pierquin B, Wilson J F and Chassagne D 1987 *Modern Brachytherapy Baltimore London*

Planskoy B 1980 Evaluation of diamond radiation dosimeters *Phys. Med. Biol.* **25** 519-32

Podgorsak E B 2005 *Radiation Oncology Physics: A Handbook for Teachers and Students* International Atomic Energy Agency, Vienna

Podgorsak E B 2006 *Radiation Physics for Medical Physicists* (Springer Berlion Heidelberg New York)

Pradhan A S and Quast U 2000 In-phantom response of LiF TLD-100 for dosimetry of ^{192}Ir HDR source *Med. Phys.* **27** 1025-9

Pradhan A S 2010 A concern on in-phantom photon energy response of luminescence dosimeters for clinical applications *J. Med. Phys.* **35** 187-9

Reco C and Clifton Ling C 2008 Broadening the scope of image-guided radiotherapy (IGRT). *Acta Oncol.* **47** 1193-200

Reniers B, Verhaegen F and Vynckier S 2004 The radial dose function of low-energy brachytherapy seeds in different solid phantoms: comparison between calculations with the EGSnrc and MCNP4C Monte Carlo codes and measurements *Phys. Med. Biol.* **49** 1569-82

Rink A, Vitkin I A and Jaffray D A 2007 Energy dependence (75 kVp to 18 MV) of radiochromic films assessed using a real-time optical dosimeter *Med. Phys.* **34** 458-63

Rivard M J, Coursey B M, DeWerd L A, Hanson W, Saiful Huq M, Ibbott J S, Mitch M G, Nath R and Williamson J F 2004 Update of AAPM Task Group No. 43 Report: A revised AAPM protocol for brachytherapy dose calculations *Med. Phys.* **31** 633-74

Rivard M J 2007 Brachytherapy dosimetry parameters calculated for a ^{131}Cs source *Med. Phys.* **34** 754-762

Rogers D W O 1984 Low energy electron transport with EGS *Nucl. Inst. Meth.* **227** 535-48

Rogers D W O and Bielajew A F 1986 Differences in Electron Depth Dose Curves Calculated with EGS and ETRAN and Improved Energy Range Relationships *Med. Phys.* **13** 687-94

Rogers D W O and Bielajew A F 1990 Monte Carlo techniques of electron and photon transport for radiation dosimetry in *The Dosimetry of Ionizing Radiation* Vol III edited by Kase K R, Bjarngard B E and Attix F H San Diego, CA: Academic Press 427-539

Rogers D W O 2002 Monte Carlo techniques in radiotherapy *Phys. Canada* **58** 63-70

Rogers D W O 2006 Fifty years of Monte Carlo simulations in medical physics *Phys. Med. Biol.* **51** 287-301

Rogers D W O 2009 General characteristics of radiation dosimeters and a terminology to describe them in *Clinical Dosimetry Measurements in Radiotherapy* Madison, WI: Medical Physics Publishing

Rogers D W O, Kawrakow I, Seuntjens J P, Walters B R B and Mainegra-Hing E 2010 NRC User Codes for EGSnrc. NRCC Report PIRS-702 (revB). Ottawa, ON: National Research Council of Canada. Available from: http://www.irs.inms.nrc.ca/EGSnrc/pirs702.pdf

Rogers D W O, Walters B and Kawrakow I 2016 BEAMnrc users Manual. PIRS 509(A) Rev. Ottawa, ON: National Research Council of Canada; 2016.

Rohlf J W 1994 Modern Physics from α to Z^0 Wiley: New York

Rustgi S N 1995 Evaluation of the dosimetric characteristics of a diamond detector for photon beam measurements *Med. Phys.* **22** 567-70.

Sadeghi M, Hosseinib S H and Raisali G 2008 Experimental measurements and Monte Carlo calculations of dosimetric parameters of the IRA1-103Pd brachytherapy source *Appl. Radia. Isot.* **66** 1431-7

Scarboro S B and Kry S F 2013 Characterisation of energy response of Al2O3:C optically stimulated luminescent dosemeters (OSLDs) using cavity theory *Radiat. Prot. Dosimetry* **153** 23–31

Schoenfeld A A, Harder D, Poppe B and Chofor N 2015 Water equivalent phantom materials for ^{192}Ir brachytherapy *Phys. Med. Biol.* **60** 9403-20

Schoenfeld A A, Thieben M. Harder D, Poppe B and Chofor N 2017 Evaluation of water-mimicking solid phantom materials for use in HDR and LDR brachytherapy dosimetry *Phys. Med. Biol.* **62** N561-72

Seco J and Evans P M 2006 Assessing the effect of electron density in photon dose calculations *Med. Phys.* **33** 540-52.

Seltzer S M 1988 An Overview of ETRAN Monte Carlo Methods in *Monte Carlo Transport of Electrons and Photons* edited by Jenkins T M, Nelson W R and Rindi A Ettore Majorana International Science Series, vol **38**. Springer, Boston, MA

Selvam T P and Biju K 2010 Monte Carlo investigation of energy response of various detector materials in ^{125}I and ^{169}Yb brachytherapy dosimetry *J. Appl. Clin. Med. Phys.* **11** 70-82

Sipila P 1994 Quality assurance of treatment planning systems: Radiation Dose in Radiotherapy from Prescription to Delivery IAEA-TECDOC-734, IAEA, Vienna 341-34

Simon N 1963 Radium substitutes in the interstitial implantation of tumours with particular reference to iridium-192 *J. Okla State Med. Assoc.* **56**: 371-6

Song H, Chen Z, Yue N, Wu Q and Yin F F 2009 Ice as a water-equivalent solid medium for brachytherapy dosimetric measurements Radiat *Environ. Biophys.***48** 145-5

Spencer L V and Attix F H 1955 A theory of cavity ionization *Radiat. Res.* **3** 239-354

Spencer L V 1965 Note on the theory of cavity ionizatiion chambers *Radiat. Res.* **25** 352-358

Strohmaier S and Zwierzchowski G 2011 Comparison of ^{60}Co and ^{192}Ir sources in HDR brachytherapy *J. Contemp Brachytherapy* **4** 199-208

Sujatha P, Indra J D, James F D et al 2007 TG-69: Radiographic film for megavoltage beam dosimetry *Med. Phy.* **34** 2228-258

Sutherland H and Rogers D W O 2010 Monte Carlo calculated absorbed-dose energy dependence of EBT and EBT2 film *Med. Phys.* **37** 1110-16

Svensson H 1984 1st international symposium on quality assurance in radiation therapy *Int. J. Radiat. Oncol. Biol. Phys.* **10** 59-65

Tedgren A C and Carlsson G A 2009 Influence of phantom materials and dimensions on experimental ^{192}Ir dosimetry *Med. Phys.* **36** 2228-35

Tedgren A C, Angelica H, Jan-Erik G and Gudrum A C 2011 Response of LiF:Mg,Ti thermoluminescent dosimeters at photon energies relevant to the dosimetry of brachytherapy (<1 MeV) *Med. Phys.* **38** 5539-50

Teh B S, Woo S Y and Butler E B 1999 Intensity Modulated Radiation Therapy (IMRT): A New Promising Technology in Radiation Oncology *The Oncologist* **4** 433-42

Turesson I 1990 Radiobiological aspects of continuous low dose rate irradiation and fractionated high dose rate irradiation *Radiother. Oncol*. **19** 1-16

Walters B R B, Kawrakow I and Rogers D W O 2002 History by history statistical estimators in the BEAM code system *Med. Phys.* **29** 2745-52

Walters B, Kawrakow I, Rogers D W O 2016 DOSXYZnrc users Manual. PIRS 794(B) Rev. Ottawa, ON: National Research Council of Canada; 2016.

Wang L L W and Rogers D W O 2007 Monte Carlo study of Si diode response in electron beams *Med. Phys.* **34** 1734-42

Webb S 2003 The physical basis of IMRT and inverse planning *Br. J. Radiol.* **76** 678-89

Williamson J F 1977 Physics of Brachytherapy in Principles and Practice of Radiation Oncology, 3rd ed. (Lippincott-Raven Press, Philadelphia, USA)

Williamson J F 1991 Comparison of measured and calculated dose rates in water near I-125 and Ir-192 seeds *Med. Phys.***18** 776-86

Williamson J F 1998 Monte Carlo–based dose-rate tables for the Amersham CDCS.J and 3M model 6500 ^{137}Cs tubes *Int. J. Radiat. Oncol. Biol. Phys.* **41** 959-70

Williamson J F, Dempsey J F, Kirov A S, Monroe J I, Binns W R and Hedtjarn H 1999 Plastic scintillator response to low-energy photons *Phys. Med. Biol.* **44** 857-71

Wilson R R 1946 Radiological use of fast protons *Radiology* **47** 487- 91

Wilson R R 1952 Monte Carlo of shower production *Phys. Rev.* **86** 261-9

Yin Z, Hugtenburg R P and Beddoe A H 2002 Response of silicon diode dosimeters to scattered radiation from megavoltage photon beams *Rad. Prot. Dos.* **101** 415-18

Original Article

Monte Carlo Calculation of Beam Quality and Phantom Scatter Corrections for Lithium Formate Electron Paramagnetic Resonance Dosimeter for High-energy Brachytherapy Dosimetry

Subhalaxmi Mishra, T. Palani Selvam

Bhabha Atomic Research Centre, Radiological Physics and Advisory Division, Health, Safety and Environment Group, Mumbai, Maharashtra, India

Abstract

Purpose: To investigate beam quality correction, K_{QQ0} (r) and phantom scatter correction, K_{phan} (r) for lithium formate dosimeter as a function of distance r along the transverse axis of the high-energy brachytherapy sources ^{60}Co, ^{137}Cs, ^{192}Ir and ^{169}Yb using the Monte Carlo-based EGSnrc code system. **Materials and Methods:** The brachytherapy sources investigated in this study are BEBIG High Dose Rate (HDR) ^{60}Co (model Co0.A86), ^{137}Cs (model RTR), HDR ^{192}Ir (model Microselectron) and HDR ^{169}Yb (model 4140). The solid phantom materials investigated are PMMA, polystyrene, solid water, virtual water, plastic water, RW1, RW3, A150 and WE210. **Result:** K_{QQ0} (r) is about unity and distance independent for ^{60}Co, ^{137}Cs and ^{192}Ir brachytherapy sources, whereas for the ^{169}Yb source, K_{QQ0} (r) increases gradually to about 4 % larger than unity at a distance of 15 cm along the transverse axis of the source. For ^{60}Co source, phantoms such as polystyrene, plastic water, solid water, virtual water, RW1, RW3 and WE210 are water-equivalent but PMMA and A150 phantoms show distance-dependent K_{phan} (r) values. For ^{137}Cs and ^{192}Ir sources, phantoms such as solid water, virtual water, RW1, RW3 and WE210 are water-equivalent. However, phantoms such as PMMA, plastic water, polystyrene and A150 showed distance-dependent K_{phan} (r) values, for these sources. For ^{169}Yb source, all the investigated phantoms show distance-dependent K_{phan} (r) values. **Conclusion:** K_{QQ0} (r) is about unity and distance independent for ^{60}Co, ^{137}Cs and ^{192}Ir brachytherapy sources. Phantoms such as solid water, virtual water, RW1, RW3 and WE210 are water-equivalent for ^{60}Co, ^{137}Cs and ^{192}Ir brachytherapy sources. For ^{169}Yb source, all the investigated phantoms show distance-dependent K_{phan} (r) values.

Keywords: Beam quality correction, brachytherapy, lithium formate, Monte Carlo, phantom scatter correction

Received on: 14-09-2016 **Review completed on: 28-12-2016** **Accepted on: 21-02-2017**

Introduction

Quantity of interest in brachytherapy dosimetry is absorbed dose to water in liquid water phantom. For measurement purposes, the precise and reproducible placement of detectors in water phantom is a challenge, so various detectors and solid phantoms are used which are probably not water equivalent. At the brachytherapy photon energies, a given solid phantom will alter the attenuation and scattering characteristics of photons as compared to the liquid water phantom. Hence, detector response changes with the type of the solid phantom and the distance from the source to the point of measurement in the phantom.

Selvam *et al.*[1] reported methodologies for calculating beam quality correction, K_{QQ0} (r), and phantom scatter correction K_{phan} (r), for different solid phantoms. Using these methodologies, the authors calculated the above corrections for various detector materials and solid phantoms at the ^{137}Cs energy.[1] In another study by Subhalaxmi and Selvam,[2] correction factors K_{QQ0} (r) and K_{phan} (r) were reported for various solid-state detectors for ^{60}Co and ^{192}Ir brachytherapy sources.

Recently, electron paramagnetic resonance (EPR) studies have shown that lithium formate monohydrate (hereafter

Access this article online

Quick Response Code:

Website: www.jmp.org.in

DOI: 10.4103/jmp.JMP_95_16

Address for correspondence: Subhalaxmi Mishra, Bhabha Atomic Research Centre, Radiological Physics and Advisory Division, Health, Safety and Environment Group, Mumbai - 400 094, Maharashtra, India.
E-mail: b.subwu@gmail.com

How to cite this article: Mishra S, Selvam TP. Monte carlo calculation of beam quality and phantom scatter corrections for lithium formate electron paramagnetic resonance dosimeter for high-energy brachytherapy dosimetry. J Med Phys 2017;42:72-9.

Radiol Phys Technol
DOI 10.1007/s12194-015-0310-9

Phantom scatter corrections of radiochromic films in high-energy brachytherapy dosimetry: a Monte Carlo study

Mishra Subhalaxmi · T. Palani Selvam

Received: 25 July 2014 / Revised: 23 February 2015 / Accepted: 24 February 2015

Abstract Our aim in this study was to calculate Monte Carlo-based phantom scatter corrections of various radiochromic films for different solid phantoms for high-energy brachytherapy sources. Brachytherapy sources ^{60}Co, ^{137}Cs, ^{192}Ir, and ^{169}Yb and radiochromic films EBT, EBT2 (lot 020609 and lot 031109), RTQA, XRT, XRQA, and HS were investigated in this study. The solid phantom materials investigated were PMMA (polymethylmethacrylate), polystyrene, solid water, virtual water, plastic water, RW1, RW3, A150, and WE210. Monte Carlo-based user codes DOSRZnrc and FLURZnrc of the EGSnrc code system were employed in the present work. For the ^{60}Co source, the polystyrene, plastic water, solid water, virtual water, RW1, RW3, and WE210 phantoms were water equivalent for the investigated films, but showed distance-dependent values for XRT and XRQA films. For the ^{137}Cs and ^{192}Ir sources, the solid water, virtual water, RW1, RW3, and WE210 phantoms were water equivalent for the investigated films, but showed distance-dependent values for XRT and XRQA films. For these sources, the remaining phantoms showed distance-dependent values for all of the films investigated. For the ^{169}Yb source, all of the investigated phantoms showed distance-dependent values for the investigated films. This study suggests that radiochromic films demonstrate distance-dependent values, but the degree of dependence is related to the types of solid phantom and film. Hence, for brachytherapy dosimetry involving radiochromic films and solid phantom materials, phantom scatter corrections need to be applied.

M. Subhalaxmi (✉) · T. Palani Selvam
Radiological Physics and Advisory Division, Health, Safety and Environment Group, Bhabha Atomic Research Centre, Mumbai 400 094, Maharashtra, India
e-mail: b.subwu@gmail.com

Published online: 10 March 2015

Keywords Monte Carlo · Brachytherapy · Phantom scatter correction · Radiochromic film

1 Introduction

A quantity of interest in brachytherapy dosimetry is the absorbed dose to water. Water is recommended as the reference medium for dosimetry of brachytherapy sources [1, 2]. However, different solid phantoms were also used for brachytherapy dosimetry for overcoming the practical problems such as water proofing and precise positioning of detectors. Radiochromic films were in extensive use for brachytherapy dosimetry because of their high spatial resolution and small detecting volume [3–6].

An article by Palani Selvam et al. [7] reports on a beam quality correction for different solid-state detectors at the ^{137}Cs energy. Their study included the basis for calculating detector-specific phantom scatter corrections, $k_{\text{phan}}(r)$, for various solid phantoms. In another study by Subhalaxmi and Palani Selvam [8], $k_{\text{phan}}(r)$ values were reported for different solid-state detectors for ^{60}Co and ^{192}Ir brachytherapy sources. Subhalaxmi and Palani Selvam [9] also reported on the relative absorbed dose energy response correction, R, for different radiochromic films for high-energy brachytherapy sources such as ^{60}Co, ^{137}Cs, ^{192}Ir, and ^{169}Yb. Their study also included the influence of the solid phantoms PMMA and polystyrene on R. The present study was aimed at calculating film-specific phantom scatter corrections for different solid phantoms for ^{60}Co, ^{137}Cs, ^{192}Ir, and ^{169}Yb brachytherapy sources. The detector materials considered in this work were various radiochromic films. The EGSnrc-based [10] user codes DOSRZnrc and FLURZnrc [11] were used in our study.

Monte Carlo-based beam quality and phantom scatter corrections for solid-state detectors in ^{60}Co and ^{192}Ir brachytherapy dosimetry

Mishra Subhalaxmi[a] and T. Palani Selvam
Radiological Physics & Advisory Division, Health, Safety & Environment Group, Bhabha Atomic Research Centre, Mumbai – 400 094, Maharashtra, India
b.subwu@gmail.com

Received 20 January, 2014; accepted 19 June, 2014

Beam quality correction, $k_{QQ_0}(r)$, for solid-state detectors diamond, LiF, $Li_2B_4O_7$, Al_2O_3, and plastic scintillator are calculated as a function of distance, r, along the transverse axis of the ^{60}Co and ^{192}Ir brachytherapy sources using the Monte Carlo-based EGSnrc code system. This study also includes calculation of detector-specific phantom scatter correction, $k_{phan}(r)$, for solid phantoms such as PMMA, polystyrene, solid water, virtual water, plastic water, RW1, RW3, A150, and WE210. For ^{60}Co source, $k_{QQ_0}(r)$ is about unity and distance-independent for diamond, plastic scintillator, $Li_2B_4O_7$ and LiF detectors. For this source, $k_{QQ_0}(r)$ decreases gradually with r for Al_2O_3 detector (about 6% smaller than unity at 15 cm). For ^{192}Ir source, $k_{QQ_0}(r)$ is about unity and distance-independent for $Li_2B_4O_7$ detector (overall variation is about 1% in the distance range of 1–15 cm). For this source, $k_{QQ_0}(r)$ increases with r for diamond and plastic scintillator (about 6% and 8% larger than unity at 15 cm, respectively). Whereas $k_{QQ_0}(r)$ decreases with r gradually for LiF (about 4% smaller than unity at 15 cm) and steeply for Al_2O_3 (about 25% smaller than unity at 15 cm). For ^{60}Co source, solid water, virtual water, RW1, RW3, and WE210 phantoms are water-equivalent for all the investigated solid-state detectors. Whereas polystyrene and plastic water phantoms are water-equivalent for diamond, plastic scintillator, $Li_2B_4O_7$ and LiF detectors, but show distance-dependent $k_{phan}(r)$ values for Al_2O_3 detector. PMMA phantom is water-equivalent at all distances for Al_2O_3 detector, but shows distance-dependent $k_{phan}(r)$ values for remaining detectors. A150 phantom shows distance-dependent $k_{phan}(r)$ values for all the investigated detector materials. For ^{192}Ir source, solid water, virtual water, RW3, and WE210 phantoms are water-equivalent for diamond, plastic scintillator, $Li_2B_4O_7$ and LiF detectors, but show distance-dependent $k_{phan}(r)$ values for Al_2O_3 detector. All other phantoms show distance-dependent $k_{phan}(r)$ values for all the detector materials.

PACS numbers: 87.10.Rt, 87.53.Bn, 87.53.Jw

Key words: Monte Carlo, brachytherapy, beam quality correction, phantom scatter correction

I. INTRODUCTION

^{192}Ir and ^{60}Co sources are used in high-dose-rate (HDR) brachytherapy.[1-4] Dosimetry of a brachytherapy source is generally carried out using various solid-state detectors. The response of the detector is required to be corrected for absorbed dose energy dependence, when it is not water-equivalent. Although water is recommended as the reference medium for dosimetry of

[a] Corresponding author: Mishra Subhalaxmi, Radiological Physics & Advisory Division, Health, Safety & Environment Group, Bhabha Atomic Research Centre, Mumbai – 400 094, Maharastra, India; phone: (91) 22-25598654; fax: (91) 22-25519209; email: b.subwu@gmail.com

Monte Carlo-based investigation of absorbed-dose energy dependence of radiochromic films in high energy brachytherapy dosimetry

Mishra Subhalaxmi,[a] T. Palani Selvam
Radiological Physics & Advisory Division, Health, Safety & Environment Group, Bhabha Atomic Research Centre, Mumbai – 400 094, Maharashtra, India
b.subwu@gmail.com

Received 8 March, 2013; accepted 26 August, 2013

Relative absorbed dose energy response correction, R, for various radiochromic films in water phantom is calculated by the use of the Monte Carlo-based EGSnrc code system for high energy brachytherapy sources ^{60}Co, ^{137}Cs, ^{192}Ir and ^{169}Yb. The corrections are calculated along the transverse axis of the sources (1–15 cm). The radiochromic films investigated are EBT, EBT2 (lot 020609 and lot 031109), RTQA, XRT, XRQA, and HS. For the ^{60}Co source, the value of R is about unity and is independent of distance in the water phantom for films other than XRT and XRQA. The XRT and XRQA films showed distance-dependent R values for this source (the values of R at 15 cm from the source in water are 1.845 and 2.495 for the films XRT and XRQA, respectively). In the case of ^{137}Cs and ^{192}Ir sources, XRT, XRQA, EBT2 (lot 031109), and HS films showed distant-dependent R values. The rest of the films showed no energy dependence (HS film showed R values less than unity by about 5%, whereas the other films showed R values higher than unity). In the case of ^{169}Yb source, the EBT film showed no energy dependence and EBT2 film (lot 031109) showed a distance-independent R value of 1.041. The rest of the films showed distance-dependent R values (increases with distance for the films other than HS). The solid phantoms PMMA and polystyrene enhance the R values for some films when compared the same in the water phantom.

PACS number: 87.53.Jw

Key words: brachytherapy, Monte Carlo, energy response, phantoms

I. INTRODUCTION

Accurate dose measurement in the vicinity of brachytherapy source is difficult mainly due to existence of steep dose gradients.[1,2] Hence requirements of a suitable dosimeter for measuring accurate dose in vicinity of brachytherapy source are high spatial resolution, energy independency, tissue equivalency, and convenience of use. The introduction of radiochromic films has solved some of the problems associated with conventional 2D radiation detectors such as ionization chambers, thermoluminescence dosimetry (TLD), diodes, plastic scintillators, diamond detectors, radiographic films, and polymer gels. The high spatial resolution with small detecting volume makes them suitable for measurement of dose distributions in radiation fields with high-dose gradients. Radiochromic films change color directly upon irradiation; hence, they do not require chemical processing. These dosimeters are insensitive to visible light, and thus can be handled in room light.[3-5] Radiochromic films are in use extensively for radiation dosimetry in conventional radiation therapy, including external-beam, brachytherapy, and radiosurgery.[6-13] Varieties of radiochromic films are commercially available and, depending upon the type of

[a] Corresponding author: Mishra Subhalaxmi, Radiological Physics & Advisory Division, Health, Safety & Environment Group, Bhabha Atomic Research Centre, Mumbai – 400 094, Maharastra, India; phone: (91) 22-25598653; fax: (91)22-25519209; email: b.subwu@gmail.com

Monte Carlo calculation of beam quality correction for solid-state detectors and phantom scatter correction at ^{137}Cs energy

T. Palani Selvam, Subhalaxmi Mishra, R.S. Vishwakarma[a]
Radiological Physics and Advisory Division, Health, Safety and Environment Group, Bhabha Atomic Research Centre, Mumbai – 400 085, India
pselvam66@yahoo.co.in

Received 8 March, 2013; accepted 6 September, 2013

Beam quality correction $k_{QQ_0}(r)$, which reflects the absorbed energy dependence of the detector, is calculated for solid-state detector materials diamond, LiF, $Li_2B_4O_7$, and Al_2O_3 for the ^{137}Cs RTR brachytherapy source using the Monte Carlo-based EGSnrc code system. The study also includes calculation of detector-specific phantom scatter corrections $k_{phan}(r)$ for solid phantoms such as PMMA, polystyrene, RW1, solid water, virtual water, and plastic water. Above corrections are calculated as a function of distance r along the transverse axis of the source. $k_{QQ_0}(r)$ is about unity for the $Li_2B_4O_7$ detector. LiF detector shows a gradual decrease in $k_{QQ_0}(r)$ with r (decrease is about 2% over the distance range of 1–15 cm). Diamond detector shows a gradual increase in $k_{QQ_0}(r)$ with r (about 3% larger than unity at 15 cm). In the case of Al_2O_3 detector, $k_{QQ_0}(r)$ decreases with r steeply (about 14% over the distance range of 1–15 cm). The study shows that some solid-state detectors demonstrate distance-dependent $k_{phan}(r)$ values, but the degree of deviation from unity depends on the type of solid phantom and the detector.

PACS number: 87.10.Rt, 87.53.Bn, 87.53.Jw, 87.56.Bg

Key words: Monte Carlo, brachytherapy, energy response, phantom scatter

I. INTRODUCTION

American Association of Physicists in Medicine (AAPM) Task Group reports AAPM TG43[1] and TG43U1[2] recommend water as a reference medium for dosimetry of interstitial brachytherapy sources. Due to high-dose gradients near brachytherapy sources and specification of the dose parameters within few centimeters of the source, source-detector distance should be specified very accurately for dosimetric measurements. Precise positioning of detectors, reproducibility of source and detectors in reference liquid water medium, and water proofing of detectors posses a practical problem. Solid phantom materials can be easily machined to accommodate the source and detectors in a precise geometrical configuration, facilitating an accurate measurement and reproducibility in source-detector geometry.

In a previously published article, relative absorbed-dose energy response corrections R for detector materials such as air, LiF, $Li_2B_4O_7$, Si diode, diamond, and Al_2O_3 were presented for ^{169}Yb and ^{125}I brachytherapy sources.[3] The corrections were calculated using the EGSnrc-based[4] Monte Carlo code system for liquid water, PMMA, and polystyrene phantom materials. The present study is aimed at investigating absorbed-dose energy dependence of solid-state detector materials such as diamond, LiF, $Li_2B_4O_7$, and Al_2O_3 at the ^{137}Cs energy. This investigation also includes calculation of detector-specific phantom scatter correction for different solid phantoms such as PMMA, polystyrene, RW1, solid water, virtual water, and plastic water. The EGSnrc-based[4] user-codes DOSRZnrc and FLURZnrc[5] are used in the study.

[a] Corresponding author: R.S. Vishwakarma, Radiological Physics & Advisory Division, Health, Safety & Environment Group, Bhabha Atomic Research Centre, Mumbai – 400 094, India; phone: (91) 22-25598653; fax: (91)22-25519209; email: vishwakarma_ram@yahoo.com

Original Article

Monte Carlo-based investigation of water-equivalence of solid phantoms at ^{137}Cs energy

Ramkrushna S. Vishwakarma, T. Palani Selvam, Sridhar Sahoo, Subhalaxmi Mishra, Ghanshyam Chourasiya

Radiological Physics and Advisory Division, Health, Safety and Environment Group, Bhabha Atomic Research Centre, Anushaktinagar, Mumbai, Maharastra, India

Received on: 04.06.13 Review completed on: 31.07.13 Accepted on: 01.08.13

ABSTRACT

Investigation of solid phantom materials such as solid water, virtual water, plastic water, RW1, polystyrene, and polymethylmethacrylate (PMMA) for their equivalence to liquid water at ^{137}Cs energy (photon energy of 662 keV) under full scatter conditions is carried out using the EGSnrc Monte Carlo code system. Monte Carlo-based EGSnrc code system was used in the work to calculate distance-dependent phantom scatter corrections. The study also includes separation of primary and scattered dose components. Monte Carlo simulations are carried out using primary particle histories up to 5×10^9 to attain less than 0.3% statistical uncertainties in the estimation of dose. Water equivalence of various solid phantoms such as solid water, virtual water, RW1, PMMA, polystyrene, and plastic water materials are investigated at ^{137}Cs energy under full scatter conditions. The investigation reveals that solid water, virtual water, and RW1 phantoms are water equivalent up to 15 cm from the source. Phantom materials such as plastic water, PMMA, and polystyrene phantom materials are water equivalent up to 10 cm. At 15 cm from the source, the phantom scatter corrections are 1.035, 1.050, and 0.949 for the phantoms PMMA, plastic water, and polystyrene, respectively.

Key words: Brachytherapy; Monte Carlo simulations; solid phantom

Introduction

Brachytherapy refers to a method of treatment in which sealed radioactive sources are used to deliver radiation at short distances by interstitial, intracavitary, or surface mould applications. Brachytherapy delivers a high dose in the tumor and an acceptable low dose to surrounding normal tissue due to rapid dose fall-off with distance. American Association of Physicists in Medicine (AAPM) Task Group reports, AAPM TG43[1] and TG43U1[2] recommend water as a reference medium for dosimetry of interstitial brachytherapy sources. Due to high dose gradients near brachytherapy sources and specification of the dose parameters within few centimetres of the source, source-detector distance should be specified very accurately for dosimetric measurements. Precise positioning of detectors, reproducibility of source and detectors in reference liquid water medium, and water proofing of detectors poses a practical problem. Solid phantom materials can be easily machined, to accommodate the source and detectors in a precise geometrical configuration, facilitating an accurate measurement and reproducibility in source-detector geometry.

Suitable solid phantom material should be selected to mimic the absorption and scattering of radiation as that in liquid water.[3] Constantinou *et al.*,[4] had studied the

Address for correspondence:
Mr. Ramkrushna S. Vishwakarma,
Radiological Physics and Advisory Division, Health, Safety and Environment Group, Bhabha Atomic Research Centre, Anushaktinagar, Mumbai - 400 094, Maharastra, India

In-phantom depth-dependent photon energy response and phantom scatter corrections for low energy brachytherapy sources

Subhalaxmi Mishra[1,2] and Palani Selvam T. [1,2]

[1]Radiological Physics & Advisory Division, Health, Safety & Environment Group,

Bhabha Atomic Research Centre, Mumbai – 400 094, Maharashtra, India

[2]Homi Bhabha National Institute, Training School Complex, Anushaktinagar, Mumbai, India

Abstract

Introduction

Generally, in brachytherapy, absorbed dose measurements involving various detectors are carried out in solid phantoms. These detectors are calibrated at ^{60}Co beam energy and need correction while being used other than reference beam energy. Similarly, influence of solid phantoms should also be taken into account when phantoms other than water phantom are used for measurement purposes. In the present study, depth-dependent absorbed-dose energy response corrections, $k_{QQ_0}(r)$ and phantom scatter correction $k_{phan}(r)$ were determined in-phantom.

Methods

Absorbed-dose energy response corrections, $k_{QQ_0}(r)$ for various solid-state detectors such as diamond, LiF, $Li_2B_4O_7$, Al_2O_3 and radiochromic films such as HS, EBT, EBT2, EBT3, RTQA, XRT and XRQA and phantom scatter correction $k_{phan}(r)$ for different solid phantoms involving the above detectors were calculated using the Monte Carlo-based EGSnrc code system . The above corrections were calculated as a function of distance along the transverse axis of the low energy brachytherapy sources (up to 5 cm) such as ^{131}Cs, ^{125}I and ^{103}Pd. The solid phantoms investigated were PMMA, polystyrene, solid water, virtual water, plastic water (LR), RW1, RW3, A150 and WE210.

Results and Discussion

For a given detector and brachytherapy source, values of $k_{QQ_0}(r)$ is independent of distance. For a given detector $k_{phan}(r)$ depends on distance from the source for the investigated phantom materials, but the degree of

Monte Carlo study of water-equivalence of various solid phantom materials for ^{131}Cs, ^{125}I and ^{103}Pd low energy brachytherapy sources

Subhalaxmi Mishra[1,2] and T. Palani Selvam[1,2]

[1]Radiological Physics & Advisory Division, Bhabha Atomic Research Centre, Mumbai,
[2]Homi Bhabha National Institute, Training School Complex, Anushaktinagar, Mumbai, India
(Email: b.subwu@gmail.com , Mobile: 9324696805)

Introduction: Experimental brachytherapy dosimetry is a challenge in terms of positional accuracy due to steep gradients in dose and dose rate, low photon energies, and spectral changes with distance from the source. Solid phantom materials can be easily machined to accommodate the source and detector in a precise position, facilitating an accurate measurement and reproducibility in source-detector geometry. Several solid phantom materials are being used for the dosimetric measurements of brachytherapy sources. However, for low energy brachytherapy sources (less than 50 keV), the dose distributions are highly sensitive to phantom compositions due to the predominance of photoelectric effect.

Objective: The aim of this work is to study the water-equivalence of various solid phantom materials for low energy brachytherapy sources such as ^{131}Cs, ^{125}I and ^{103}Pd using Monte Carlo-based EGSnrc code system.

Materials and Methods: The brachytherapy sources included in this study are ^{125}I (model Selectseed), ^{103}Pd (model IRA1) and ^{131}Cs (Isoray model Cs-1). The solid phantom materials investigated are PMMA, polystyrene, solid water, virtual water, RW1, RW3, A150 and WE210. The detectors investigated in this study are diamond, $Li_2B_4O_7$ and LiF.

Phantom scatter correction at distance (r) along the transverse axis of the source, $k_{phan}(r)$, can be calculated at a brachytherapy beam quality Q for solid-state detector by using the following relation:

$$k_{phan}(r) = \left[D_{\det, Q}(r) / D_{\det,\ phan, Q}(r) \right]$$

Where, $D_{\det,Q}(r)$ and $D_{\det,phan,Q}(r)$ are the absorbed dose to a given detector material in liquid water and in the solid phantom at a distance *r* along the transverse axis of the photon emitting

Influence of phantom materials on ^{192}Ir brachytherapy dosimetry using air as a detector material: a Monte Carlo study

Subhalaxmi Mishra and T. Palani Selvam

[1]Radiological Physics & Advisory Division, Bhabha Atomic Research Centre, Mumbai, India

(Email: b.subwu@gmail.com , Mobile: 9324696805)

Purpose: Accurate dosimetry of ^{192}Ir brachytherapy source is a challenge due to steep dose gradients and spectral changes with distance from the source. Although American Association of Physicists in Medicine (AAPM) Task Group reports, AAPM TG43[(1)] and TG43U1[(2)] recommend water as a reference medium for dosimetry of interstitial brachytherapy sources, various solid phantoms are also used to maintain the positional accuracy and reproducibility in dosimetry. The purpose of this investigation is to study the influence of solid phantoms regarding their use in ^{192}Ir brachytherapy dosimetry for an air detector.

Materials and Methods: The brachytherapy source investigated in this study is HDR ^{192}Ir (model MicroSelectron; Elekta, Stockholm, Sweden)[(3)] and the detector considered is an air detector. The solid phantoms investigated are PMMA, polystyrene, solid water, virtual water, plastic water, RW1, RW3, A150 and WE210.

Phantom correction factor, $k_{phan}(r)$[(4)], is detector specific. It converts absorbed dose to detector at a distance r along the transverse axis of the brachytherapy source in a solid phantom to absorbed dose to detector in a water phantom at the same r and can be defined as:

$$k_{phan}(r) = \left[D_{\det,Q}(r) / D_{\det,phan,Q}(r) \right]$$

where $D_{det,wat}(r)$ and $D_{det,phan}(r)$ are the absorbed dose to detector in water phantom and absorbed dose to detector in solid phantom respectively. In this study the detector material is air. Note that, if $k_{phan}(r)$ value is unity the phantom can be considered as water-equivalent for the given detector.

In the Monte Carlo calculations, the source is positioned at the centre of a 40 cm diameter and 40 cm height cylindrical phantoms (water and solid phantoms). The photon fluence spectrum is scored along the transverse axis of the source (r = 1-15 cm) in 0.5 mm high and 0.5 mm thick cylindrical shells which is converted to water kerma and air kerma using the mass-energy absorption coefficients of water and air, respectively. The statistical uncertainty on the calculated values of is $k_{phan}(r)$ less than 0.5%. The above calculations are based on the assumption that charged particle equilibrium exists and the presence of detector does not affect the above corrections. The EGSnrc-based [(5)] user-codes DOSRZnrc and FLURZnrc[(6)] are used in this study.

Absorbed dose energy dependence of radiochromic films in high energy brachytherapy dosimetry – an EGSnrc study

Subhalaxmi Mishra and T. Palani Selvam
Radiological Physics & Advisory Division,
Bhabha Atomic Research Centre, Mumbai- 400 085
e-mail: subhalaxmi_bhola@yahoo.co.in

Objective: The objective of present study is to calculate the relative absorbed dose energy response correction *R* for various radiochromic films in different phantom materials for high-energy brachytherapy sources by the use of Monte Carlo-based EGSnrc code system.

Materials and Methods: The brachytherapy sources investigated in this study are BEBIG High Dose Rate (HDR) ^{60}Co (model Co0.A86), ^{137}Cs (model RTR), HDR ^{192}Ir (model Microselectron), HDR ^{169}Yb (model 4140) and radiochromic films models investigated are EBT, EBT2 (lot 031109), EBT2 (lot 020609), RTQA, HS, XRT and XRQA. The phantom materials included in this study are liquid water, polystyrene and PMMA. For the study of relative absorbed dose-energy dependence of films, dose ratio of film-to-water is calculated at the beam quality Q (^{60}Co, ^{137}Cs, ^{192}Ir and ^{169}Yb) and normalized with respect to the reference Q_0 (^{60}Co beam). *R* can be written as:

$$R = [D_{film} / D_{wat}]_Q / [D_{film} / D_{wat}]_{Q0}$$

In this Monte Carlo calculations, photon fluence spectrum is scored in 0.5 mm thick and 0.5 mm high cylindrical shells, along the transverse axis of the sources (distances, 1 cm–15 cm) in 20 cm radius by 40 cm high cylindrical phantoms (liquid water, PMMA and Polystyrene). The fluence spectrum is converted to collision kerma to water and collision kerma to films by using the mass-energy absorption coefficients of water and films. Using the values of collision kerma to water and collision kerma to films, the numerator of the above equation is obtained for the ^{60}Co, ^{137}Cs, ^{192}Ir and ^{169} Yb sources. The denominator i.e film-to-water ratio at Q_0 is calculated in a unity density cylindrical water phantom of 20 cm radius and 40 cm height for each of the investigated

Monte Carlo-based energy response study of indigenously developed $LiMgPO_4$: Tb phosphor in radiotherapy photon beams

Subhalaxmi Mishra, T. Palani Selvam, Bhushan Dhabekar, A. K. Singh and
M. Chaougaonkar
Radiological Physics & Advisory Division
Bhabha Atomic Research Centre, Mumbai - 400 094
e-mail: subhalaxmi_bhola@yahoo.co.in

Aim: A reasearch group in Radiological Physics & Advisory Division of Bhabha Atomic Reasearch Centre (BARC) has developed indigenously a new phosphor, $LiMgPO_4$:Tb, for applications in radiation dosimetry. It is essential that characteristics of the dosimeter including its energy dependence are studied. Towards this goal, absorbed dose energy response of this phosphor was studied using the Monte Carlo-based EGSnrc code system.

Materials and Methods: To study the energy response, radiotherapy photon beams such as ^{60}Co, 4 MV - 24 MV were considered. In this Monte Carlo calculation, central axis depth dose values for each beam were obtained in a 20 cm radius x 40 cm height cylindrical water phantom. Absorbed dose to detector was calculated by positioning the detector (1 cm diameter x 0.5 cm thickness) at various depths (0.5 cm - 10 cm) along the central axis of the water phantom. The incident beam of was modeled as a parallel circular beam with a radius of 5.6 cm. Using the calculated dose results, absolute energy response (ratio between absorbed dose to detector and absorbed dose to water) and relative response (normalized at ^{60}Co energy) were calculated. The 1 σ statistical uncertainties on the calculated dose values were usually less than 0.5%

Results and Discussion: Analysis of relative response values suggests that the relative response is nearly flat (within 3%) at the investigated photon beam qualities and depths. However, the response at smaller depths could possibly be different due to electron contamination, which was not included in our study. Such a study requires a full modeling of medical linear accelerator.

Conclusions: Although, Monte Carlo-based investigation suggests that indigenously developed $LiMgPO_4$:Tb phosphor can be used for radiotherapy dose measurements, its practical usability is required to be investigated by carrying our measurements in radiotherapy photon beams. The experimental work is in progress.